

Design and synthesis of biofunctional magnetic/fluorescent *glyco*-nanoparticles and quantum dots and their application as specific molecular imaging probes

Cover: TEM micrograph of Fe₃O₄@Au@PbSe nanostars obtained in an attempt to prepare quantum dots-magnetic hybrid nanoparticles.

Design and synthesis of biofunctional magnetic/fluorescent *glyco*-nanoparticles and quantum dots and their application as specific molecular imaging probes

Juan Gallo Páramo
San Sebastian, 2011

**AUTORIZACION DE LAS DIRECTORAS DE TESIS
PARA SU PRESENTACION**

Prof. Soledad Pénades Ullate con N.I.F. 02683273R y Dra. Isabel García Martín con N.I.F. 05425331E como Directoras de la Tesis Doctoral: Design and synthesis of biofunctional magnetic/fluorescent *glyco*-nanoparticles and quantum dots and their application as specific molecular imaging probes, realizada en el Laboratorio de Gliconanotecnología en el Centro de Investigación Cooperativa en Biomateriales (CIC biomaGUNE) y en el departamento de Física de Materiales, por el Doctorando Don Juan Gallo Páramo, autorizamos la presentación de la citada Tesis Doctoral, dado que reúne las condiciones necesarias para su defensa.

En San Sebastian, a de de 2011

LAS DIRECTORAS DE LA TESIS

Fdo.:

Fdo.:

**AUTORIZACION DEL PONENTE DE TESIS
PARA SU PRESENTACION**

Dr. Angel Alegría como Ponente de la Tesis Doctoral:

Design and synthesis of biofunctional magnetic/fluorescent *glyco*-nanoparticles and quantum dots and their application as specific molecular imaging probes, realizada en el Laboratorio de Gliconanotecnología en el Centro de Investigación Cooperativa en Biomateriales (CIC biomaGUNE) y el departamento de Física de Materiales por el Doctorando Don Juan Gallo Páramo, y dirigida por Prof. Soledad Penadés Ullate y Dra. Isabel García Martín, autorizo la presentación de la citada Tesis Doctoral en el Departamento de Física de Materiales dado que reúne las condiciones necesarias para su defensa.

En San Sebastian, a de de 2011

EL PONENTE DE LA TESIS

Fdo.:

CONFORMIDAD DEL DEPARTAMENTO

El Consejo del Departamento de Física de Materiales,
en reunión celebrada el día de de 2011 ha acordado dar la
conformidad a la admisión a trámite de presentación de la Tesis Doctoral titulada:
Design and synthesis of biofunctional magnetic/fluorescent *glyco*-nanoparticles and
quantum dots and their application as specific molecular imaging probes, dirigida por la
Prof. Soledad Penadés Ullate y la Dra. Isabel García Martín, y presentada por Don Juan
Gallo Páramo ante este Departamento.

En San Sebastian, a de de 2011

Vº Bº DIRECTOR/A DEL DEPARTAMENTO

SECRETARIO/A DEL DEPARTAMENTO

Fdo.:

Fdo.:

ACTA DE GRADO DE DOCTOR
ACTA DE DEFENSA DE TESIS DOCTORAL

DOCTORANDO: Don Juan Gallo Páramo

TITULO DE LA TESIS: Design and synthesis of biofunctional magnetic/fluorescent *glyco*-nanoparticles and quantum dots and their application as specific molecular imaging probes

El Tribunal designado por la Subcomisión de Doctorado de la UPV/EHU para calificar la Tesis Doctoral arriba indicada y reunido en el día de la fecha, una vez efectuada la defensa por el doctorando y contestadas las objeciones y/o sugerencias que se le han formulado, ha otorgado por _____ la calificación de:
unanimidad ó mayoría



En San Sebastian, a de de 2011

EL/LA PRESIDENTE/A,

EL/LA SECRETARIO/A,

Fdo.:

Fdo.:

Dr/a:

Dr/a:

VOCAL 1º,

VOCAL 2º,

VOCAL 3º,

Fdo.:

Fdo.:

Fdo.:

Dr/a:

Dr/a:

Dr/a:

EL/LA DOCTORANDO/A,

Fdo.:

This thesis has been carried out in the Laboratory of Glyconanotechnology, Biofunctional Nanomaterials Unit of the Centro de Investigación Cooperativa en Biomateriales (CIC biomaGUNE). The research was financially supported by a fellowship from CIC biomaGUNE, the Spanish Ministry of Science and Innovation (grant CTQ2008-04638), and the Department of Industry of the Basque Country (grant ETORTEK 2009 IE09-257).

Table of contents

Abstract

Resumen

Introduction, aim and scope

Part 1. Preparation and characterization of magnetic/fluorescent biofunctional nanoparticles

Chapter 1. Water-soluble magnetic glyconanoparticles based on metal-doped ferrites coated with gold: Preparation and characterization

Introduction

Preparation and characterization of core@shell magnetic nanoferrites with 3-6 nm magnetic cores

Attempts to prepare bigger magnetite cores

Preparation and characterization of water soluble magnetic *glyco*-nanoferrites

Conclusion

References

Experimental part

Materials and methods

Standard preparation of $\text{Fe}_3\text{O}_4@Au$ nanoparticles

Preparation of $X\text{Fe}_2\text{O}_4@Au$ nanoparticles

Preparation of bigger size $\text{Fe}_3\text{O}_4@Au$ nanoparticles

Preparation and characterization of water soluble magnetic *glyco*-nanoferrites

Chapter 2. Preparation and characterization of CdTe-based quantum dots

Introduction

Aqueous preparation of CdTe quantum dots

Aqueous preparation of CdTe@ZnTe core@shell quantum dots

Cytotoxicity studies on CdTe and CdTe@ZnTe quantum dots

References

Experimental part

Materials and methods
Aqueous preparation of CdTe quantum dots
Aqueous preparation of CdTe@ZnTe core@shell quantum dots
Cytotoxicity studies on CdTe and CdTe@ZnTe quantum dots

Chapter 3. Water soluble DNA-magnetic glyconanoparticles

Introduction
DNA-functionalised magnetic glyconanoparticles as probes for biosensors
Preparation and characterization of DNA-functionalised magnetic glyconanoparticles
Hybridization of DNA-magnetic glyconanoparticles
References
Experimental part
 Materials and methods
 Preparation and characterization of DNA-functionalised magnetic glyconanoparticles

Chapter 4. Fluorescent-magnetic *immuno*-glyconanoparticles and quantum dots

Introduction
Preparation and characterization of magnetic *immuno*-glyconanoparticles
Preparation and characterization of multifunctional fluorescent-magnetic *immuno*-glyconanoparticles
Preparation of *immuno*-CdTe quantum dots for fluorescent labelling of cells
References
Experimental part
 Materials and methods
 Preparation and characterization of *immuno*-magnetic glyconanoparticles
 Preparation and characterization of multifunctional fluorescent-magnetic *immuno*-glyconanoparticles
 Applications of CdTe quantum dots in standard immunostainings

Part 2. Applications of biofunctional nanoparticles

Chapter 5. *In vitro* and *ex vivo* applications of *immuno*-nanoparticles

Uptake and intracellular fate of dual fluorescent-magnetic glyconanoparticles

In vitro specific cellular labelling with *immuno*-magnetic glyconanoparticles

Specific dual labelling of blood cell populations

Application of *immuno*-quantum dots as potential anti-cancer agents

References

Experimental part

Materials and methods

Uptake and intracellular fate of dual fluorescent-magnetic glyconanoparticles

Specific *in vitro* cellular labelling with *immuno*-glyconanoparticles

Specific dual labelling of blood cell populations with *immuno*-fluorescent-magnetic glyconanoparticles

Application of CdTe quantum dots in specific cell labelling and as potential anti-cancer agents

Chapter 6. *In vivo* tracking of endogenous neural progenitor migration towards brain damaged sites with *immuno*-magnetic glyconanoparticles

Introduction

Neural stem cells tracking with *immuno*-magnetic glyconanoparticles

References

Experimental part

Materials and methods

Concluding remarks

Contributors

Acknowledgements

Appendix (publications)

Appendix (curriculum vitae)

Abstract

Nanotechnology presents very promising characteristics for its application in the biomedicine area. By now the most advanced application of nanoparticles in medicine is the use of iron oxide nanoparticles embedded in biocompatible polymers as magnetic resonance imaging (MRI) contrast agents. Nowadays MRI application relies either on inherent tissue contrast differences or on the unspecific accumulation of contrast agents in certain tissues. This status can be extended to other imaging techniques. These limitations do not enable the application of imaging techniques to many diagnostic problems such as the imaging of small or diffuse populations of tumour cells, or require the administration of large amounts of the contrast agents to achieve a clear diagnostic. Considering this, there is a clear need for the development of new probes able to target specifically cells, organs or tissues for high resolution imaging.

In this thesis, we have first prepared nanomaterials with suitable properties to be used as imaging probes; on one hand magnetic nanoparticles based on water soluble gold-coated *glyco*-nanoferrites to be used as MRI T₂ contrast agents, and on the other, CdTe-based quantum dots with fluorescent emissions in the visible to the near infrared spectra to be used in optical molecular imaging. The biofunctionalization of these nanoprobe with different biomolecules has been explored. Magnetic glyconanoparticles and quantum dots (QDs) coupled to protein G and IgG antibodies have been prepared to get specific targeted imaging probes (*immuno*-nanoparticles) for MRI and optical imaging. Functionalised magnetic glyconanoparticles with single chain DNA molecules have also been produced as potential specific probes for genetic material sensing.

Both kinds of *immuno*-nanoparticles have been applied *in vitro* for the specific labelling of a cell population within a simple mixture, or of sub-cellular structures (cytoskeleton). The application of *immuno*-magnetic glyconanoparticles (*immuno*-MGNPs) has been taken further with specific *ex vivo* labelling experiments in whole human blood. Finally, the *immuno*-MGNPs have been applied in *in vivo* studies to label and track endogenous neural stem cells to answer a fundamental question in neurobiology: Do neural stem cells migrate towards damaged brain areas?

In conclusion, we have been able to design, prepare, and apply, specific biofunctional nanoprobe as targeted contrast agents for *in vivo* imaging techniques, especially for MRI.

Resumen

La nanotecnología en general presenta características muy prometedoras para su aplicación en el área de biomedicina. Hasta el momento, la aplicación más avanzada en este área es el uso de nanopartículas de óxido de hierro encapsuladas en polímeros biocompatibles como agentes de contraste en resonancia magnética de imagen (MRI). Actualmente la aplicación de MRI confía, bien en diferencias inherentes de contraste entre tejidos, o bien en una acumulación inespecífica del agente de contraste en ciertos tejidos. Esta misma situación es compartida por otras técnicas de imagen. Estas limitaciones no permiten la aplicación de técnicas de imagen a muchos problemas diagnósticos, como por ejemplo la visualización de poblaciones pequeñas o difusas de células tumorales, o requiere de la administración de grandes cantidades del agente de contraste para la obtención de un diagnóstico claro. Considerando esto, hay una necesidad clara de desarrollo de nuevas sondas capaces de hacer un marcaje específico de células, tejidos u órganos para su uso en técnicas de imagen de alta resolución.

En esta tesis, hemos preparado primero nanomateriales con propiedades adecuadas para su utilización como sondas de imagen; por una parte nanopartículas magnéticas basadas en *glico*-nanoferritas recubiertas con oro solubles en agua para ser usadas como agentes de contraste T_2 en MRI, y por otra parte quantum dots derivados de CdTe con emisión de fluorescencia en la zona del visible al infrarrojo cercano para ser usados en imagen óptica molecular. También hemos explorado la biofuncionalización de estas nanosondas con diferentes biomoléculas. Gliconanopartículas magnéticas (MGNPs) y quantum dots (QDs) unidos a proteína G y anticuerpos IgG han sido preparadas para obtener sondas de imagen específicas (*immuno*-nanopartículas) para MRI e imagen óptica. MGNPs funcionalizadas con moléculas de DNA de una cadena también han sido preparadas como sondas para la potencial detección de material genético.

Ambas clases de *immuno*-nanopartículas han sido aplicadas *in vitro* al marcaje específico de una población celular dentro de una mezcla simple de células, o al marcaje de estructuras sub-celulares (citoesqueleto). La aplicación de *immuno*-gliconanopartículas magnéticas (*immuno*-MGNPs) se ha llevado más lejos con experimentos de marcaje específico *ex vivo* en sangre humana. Finalmente, las *immuno*-MGNPs han sido aplicadas en estudios *in vivo* para marcar y hacer un seguimiento de células madre neuronales endógenas para contestar una pregunta fundamental en

Resumen

neurobiología: Migran las células madre neuronales hacia lugares en los que se produce un daño cerebral?

En conclusión, hemos sido capaces de diseñar, preparar y aplicar nanosondas biofuncionales específicas como agentes de contraste dirigidos para su uso en técnicas de imagen *in vivo*, especialmente MRI.

Introduction, aim and scope

Introduction, aim and scope of this thesis

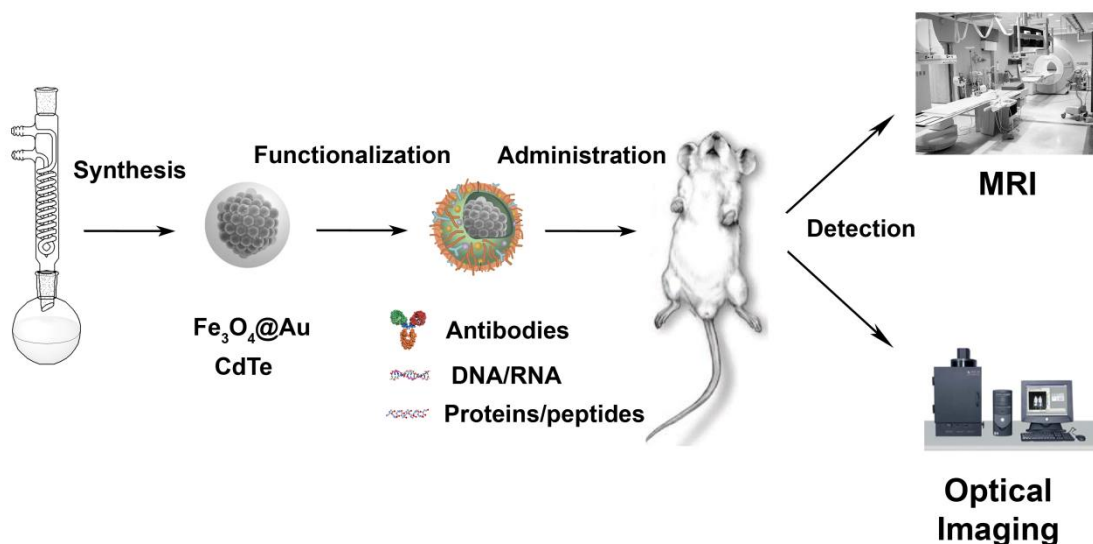
Nanoparticles in general have long been proposed to play an important role in future medicine [1] [2] [3] [4]. The most advanced application of nanoparticles so far is the use of magnetic nanoparticles (MNPs) as magnetic resonance imaging (MRI) contrast agents [5] [6]. Superparamagnetic iron oxide nanocrystals are being developed as promising probes that provide enormous possibilities for improving the efficiency and efficacy of medical diagnosis. In this multidisciplinary field, discovering, developing and understanding the underlying chemistry for particle size, surface control and behaviour into complex biological media are of the outmost importance.

For *in vivo* applications, the physical/chemical characteristics of non-targeted nanoparticles, especially the hydrodynamic size, govern their biodistribution and toxicology. Passive targeting iron oxide nano-probes named SPIO (hydrodynamic size 40 nm) are typical liver contrast agents [7] [8], and nanoparticles smaller than 40 nm, called USPIO, have been widely developed to detect lymph node metastases [9] [10] and inflammatory and degenerative diseases due to their uptake by macrophages [11]. However, disease detection through iron oxide-enhanced MRI, especially for early tumour detection, is being gradually shifted from passive targeting modes to active targeting modes by taking advantage of specific molecular recognition. Various types of targeting ligands such as proteins, peptides, aptamers and small molecules demonstrate active targeting of tumours via specific molecular recognition [12] [13] [14] [15] [16] [17] [18]. The success of a specific targeting of pathological sites *in vivo* via particle surface coupled targeting molecules involves mandatory a specific labelling of a cell population inside a multicellular environment present in the human organism. Probes must be able to discriminate tumoural cells in the presence of the same healthy ones and others. Despite careful design of the nanoplatforms, prediction of their effect, in terms of biodistribution in the body, is usually complicated.

The same trend, a shift from passive to specific labelling of target organs, tissues or cells, is observed not only in nanomedicine in general but also in pharmaceutical drug design. The scientific community is doing great efforts in this field from different approaches. For example, Chen *et al.* [19] conjugated a cyclic peptide (cRGD) to nanoparticles to target $\alpha_v\beta_3$ integrin that plays a vital role in tumour angiogenesis and

metastasis. Similarly, the group of Sailor [20] functionalised magnetic nanoparticles with a linear peptide (F3 = KDEPQRRSARLSAKPAPPKPEPKPKKAPAKK) that selectively targets cell-surface nucleolin in tumour cells and tumour endothelial cells to image tumours in mice by MRI. Apart from peptides also small molecules are been used to achieve specificity. For example Shi and co-workers [21] have used folic acid to target dendrimers to human epithelial carcinoma cells. Folic acid is one of the most widely used cancer targeting molecules. It targets folic acid receptors that are overexpressed in several human carcinomas including breast, ovary, endometrium, kidney, lung, head and neck, brain, and myeloid cancers. Other kind of biological markers that are been explored as specificity providers are nucleic acids derivatives. The group of Liu [22] has modified DNA short sequences to make them more stable (phosphorothioate derivatives) and so use them attached by means of biotin-neutravidin interactions to nanoparticles to specifically detect gliosis or abnormal growth of cells in the brain. The DNA sequence chosen was complementary to the cerebral mRNA of glial fibrillary acidic protein (GFAP) found in glia and astrocytes in elevated levels after gliosis. There is also a completely different methodology for the achievement of specificity. In this case instead of functionalising the probes, target cells are explanted from the study subject, incubated *ex vivo* with the probes, and finally re-implanted in the subject. This protocol has been followed for example by Schwaiger *et al.* [23] to follow the fate of human endothelial progenitor cells transplanted in rats' heart after myocardial infarction. Other methods rely on the coadministration of certain drugs together with nonspecific probes. The group of Kataoka [24] has demonstrated that the coadministration of nonspecific polyethyleneglycol-polybenzyl L-aspartate functionalised nanoparticles together with TGF- β inhibitor can be used to image by MRI experimental human pancreatic adenocarcinoma in mice.

Considering the precedents together with the previous experience of the laboratory in the preparation of biofunctional nanoparticles, we have tried in this thesis to **design and prepare versatile biofunctional nano-probes for the specific targeting at sub-cellular level of organs, tissues or cells, and investigate their potential as *in vitro* and *in vivo* probes by means of molecular imaging techniques** (Scheme 1).



Scheme 1. From the synthesis to the applications as imaging probes of specific functionalised fluorescent/magnetic nanoparticles.

In the last 10 years our laboratory has been successful in the preparation of metallic nanoparticles (Au, [25] Au/Fe, [26] QDs [27]) coated with biologically relevant carbohydrates, and in their application to study carbohydrate-carbohydrate interactions [28] [29] or biomedical issues [30] [31] [32]. In all of these examples the functionalization and biocompatibility of the nanocrystals was achieved by means of thiol chemistry. To take advantage from our experience in Au-thiol chemistry, we have designed our nano-probes in such a way that this chemistry is still possible. With the QDs the direct functionalization of cadmium based nanocrystals with thiols is well established; but for the case of the magnetic nanoparticles, a coating step of the magnetic material with gold had to be introduced.

In our design, the core of the nano-probes was thought to be a nanoparticle with magnetic properties for its application in MRI (iron oxide based magnetic nanoparticles) or with emission abilities for its use in fluorescence imaging techniques (organic fluorophores or CdTe-based quantum dots). Ideally, all these nanoparticles should not be cytotoxic and they should not give rise to an immune response when used *in vivo*. To achieve this last point we have coated the nanocrystals with natural carbohydrate derivatives that apart from fulfilling the two prerequisites above mentioned, will also protect our nanoparticles from aggregation and nonspecific interactions. To get specificity we have used antibodies (immunoglobulins G, IgG) raised against the target

of interest. The application of this kind of molecules to give specificity to a nanoplatform has already been proposed by other groups with promising results [33] [34]. Finally, to link the antibody (Ab) to the nanoplatform and at the same time to give versatility to the system, we have profited from protein G, a bacterial protein known to have high affinity and specificity for the constant fraction of IgGs from different species. The interaction between protein G and the constant fraction of the IgG will leave the epitopes of the antibody free to recognize their target.

This design is common to the fluorescent/magnetic nanoparticles and the quantum dots, and has been performed, especially in the case of the magnetic nanoparticles with the idea of developing a universal tool to target and label specifically cells, tissues and organs and to contribute to the understanding of concrete fundamental physiological questions.

This thesis is divided into two parts. The first one describes the design and preparation of biofunctional nanoparticle probes for their use as targeted molecular imaging probes. The second one summarizes the applications, from *in vitro* to *in vivo*, of these specific probes in different biological systems.

To achieve the goals of this thesis, we have developed first new protocols for the preparation and detailed characterization of water-soluble nanoferrites (*glyco-ferrites*). The results are described in **Chapter 1**.

In an attempt to obtain biocompatible quantum dots (QDs) with emissions in the visible to near infrared (NIR) wavelengths for optical imaging both *in vitro* and *in vivo*, we have prepared CdTe-based QDs. **Chapter 2** describes these attempts.

Chapter 3 describes the work carried out in collaboration with Dr. Briones' group of the Instituto de Microelectrónica (CSIC) in Madrid on the preparation of DNA-functionalized magnetic glyconanoparticles as probes for biosensors based on optomagnetic detection.

The preparation of targeted fluorescent/magnetic nanoparticles (*immuno-glyconanoparticles*) as well as the validation of their functionality is summarized in **Chapter 4**. In this chapter the attempts to prepare *immuno-QDs* are also described.

The evaluation *in vitro* and *ex vivo* of the ability of the *immuno-nanoparticles* (magnetic glyconanoparticles and quantum dots) as specific labelling agents of cellular systems and complex biological fluids are presented in **Chapter 5**.

Together with the laboratory of Dr Augusto Silva at the Centro de Investigaciones Biológicas (CSIC) in Madrid, and the group of Dr. Manuel Desco (Hospital Universitario Gregorio Marañón) also in Madrid, we have tried to answer a fundamental question in neurobiology: Do neural stem cells migrate towards damaged brain areas? Whether there is or not an involvement of adult neurogenesis in brain repair is still an open question that we have tried to clarify *in vivo* with the help of the *immuno-nanoprobes* and MRI. The results obtained are presented in **Chapter 6**.

References

1. S.S. Agasti, S.R., M-H. Park, C.K. Kim, C-C. You, V.M. Rotello, *Nanoparticles for detection and diagnosis*. Adv Drug Deliv Rev, 2010. **62**: p. 316-328.
2. M. De, P.S.G., V.M. Rotello, *Applications of nanoparticles in biology*. Adv. Mater., 2008. **20**: p. 1-17.
3. C.J. Murphy, A.M.G., J.W. Stone, P.N. Sisco, A.M. Alkilany, E.C. Goldsmith, S.C. Baxter, *Gold nanoparticles in biology: beyond toxicity to cellular imaging*. Acc Chem Res, 2008. **41**(12): p. 1721-1730.
4. K. Douma, L.P., D.W. Sllaf, C.P.M. Reutelingsperger, E.A.L. Biessen, T.M. Hackeng, M.J. Post, M.A. van Zandvoort, *Nanoparticles for optical molecular imaging of atherosclerosis*. Small, 2009. **5**(5): p. 544-557.
5. Jun, Y.W., J.H. Lee, and J. Cheon, *Chemical design of nanoparticle probes for high-performance magnetic resonance imaging*. Angew Chem Int Ed Engl, 2008. **47**(28): p. 5122-35.
6. Gao, J., H. Gu, and B. Xu, *Multifunctional magnetic nanoparticles: design, synthesis, and biomedical applications*. Acc Chem Res, 2009. **42**(8): p. 1097-107.
7. Semelka, R.C. and T.K. Helmlberger, *Contrast agents for MR imaging of the liver*. Radiology, 2001. **218**(1): p. 27-38.
8. Reimer, P. and B. Tombach, *Hepatic MRI with SPIO: detection and characterization of focal liver lesions*. Eur Radiol, 1998. **8**(7): p. 1198-204.
9. Weissleder, R., et al., *Ultrasmall superparamagnetic iron oxide: characterization of a new class of contrast agents for MR imaging*. Radiology, 1990. **175**(2): p. 489-93.
10. Harisinghani, M.G., et al., *Noninvasive detection of clinically occult lymph-node metastases in prostate cancer*. N Engl J Med, 2003. **348**(25): p. 2491-9.
11. Corot, C., et al., *Recent advances in iron oxide nanocrystal technology for medical imaging*. Adv Drug Deliv Rev, 2006. **58**(14): p. 1471-504.
12. F. Hu, L.W., Z. Zhou, Y. Ran, Z. Li, M. Gao, *Preparation of Biocompatible Magnetite Nanocrystals for In Vivo Magnetic Resonance Detection of Cancer*. Adv. Mater., 2006. **18**: p. 2553-2556.

13. Lee, J.H., et al., *Artificially engineered magnetic nanoparticles for ultra-sensitive molecular imaging*. Nat Med, 2007. **13**(1): p. 95-9.
14. Zhao, M., et al., *Differential conjugation of tat peptide to superparamagnetic nanoparticles and its effect on cellular uptake*. Bioconjug Chem, 2002. **13**(4): p. 840-4.
15. Zhang, C., et al., *Specific targeting of tumor angiogenesis by RGD-conjugated ultrasmall superparamagnetic iron oxide particles using a clinical 1.5-T magnetic resonance scanner*. Cancer Res, 2007. **67**(4): p. 1555-62.
16. Xie, J., et al., *Ultrasmall c(RGDyK)-coated Fe₃O₄ nanoparticles and their specific targeting to integrin alpha(v)beta3-rich tumor cells*. J Am Chem Soc, 2008. **130**(24): p. 7542-3.
17. Kircher, M.F., et al., *In vivo high resolution three-dimensional imaging of antigen-specific cytotoxic T-lymphocyte trafficking to tumors*. Cancer Res, 2003. **63**(20): p. 6838-46.
18. Chen, T.J., et al., *Targeted folic acid-PEG nanoparticles for noninvasive imaging of folate receptor by MRI*. J Biomed Mater Res A, 2008. **87**(1): p. 165-75.
19. Chen K., X.J., Xu H., Behera D., Michalski M.H., Biswal S., Wang A., Chen X., *Triblock copolymer coated iron oxide nanoparticle conjugate for tumor integrin targeting*. Biomaterials, 2009. **30**: p. 6912-6919.
20. Park J-H., v.M.G., Zhang L., Schwartz M.P., Ruoslahti E., Bhatia S.N., Sailor M.J., *Magnetic iron oxide nanoworms for tumor targeting and imaging*. Adv. Mater., 2008. **20**: p. 1630-1635.
21. Shi X., W.S.H., Swanson S.D., Ge S., Cao Z., Van Antwerp M.E., Landmark K.J., Baker J.R., *Dendrimer-functionalized shell-crosslinked iron oxide nanopartilces for in-vivo magnetic resonance imaging of tumors*. Adv. Mater., 2008. **20**(9): p. 1671-1678.
22. Liu C.H., Y.Z., Ren JQ., Kim Y.R., Eikermann-Haerter K., Liu P.K., *Noninvasive delivery of gene targeting probes to live brains for transcription MRI*. FASEB J., 2008. **22**: p. 1193-1203.
23. Higuchi T., A.M., Dumler K., Seidl S., Pelisek J., Saraste A., Welling A., Hofmann F., Oostendrof R.A.J., Gansbacher B., Nekolla S.G., Bengel F.M., Botnar R.M., Schwaiger M., *Combined reporter gene PET and iron oxide MRI for monitoring survival and localization of transplanted cells in rat heart*. J. Nuc. Med., 2009. **50**(7): p. 1088-1094.
24. Kumagai M., K.M.R., Morishita Y., Ota M., Imai Y., Nishiyama N., Sekino M., Ueno S., Miyazono K., Kataoka K., *Enhanced magnetic resonance imaging of experimental pancreatic tumor in vivo by block copolymer-coated magnetite nanoparticles with TGF- β inhibitor*. J. Control. Release, 2009. **140**: p. 306-311.
25. J.M. de la Fuente, S.P., *Glyconanoparticles: Types, synthesis and applications in glycoscience, biomedicine and material science*. Biochimica et Biophysica Acta, 2006. **1760**: p. 636-651.
26. J.M. de la Fuente, D.A., P. Eaton, P. Crespo, T.C. Rojas, A. Fernandez, A. Hernando, S. Penadés, *Gold and Gold-Iron oxide magnetic glyconanoparticles: synthesis, characterization and magnetic properties*. J. Phys. Chem. B, 2006. **110**: p. 13021-13028.
27. J.M. de la Fuente, S.P., *Glyco-quantum dots: a new luminescent system with multivalent carbohydrate display*. Tetrahedron: asymmetry, 2005. **16**: p. 387-391.
28. de La Fuente, J.M., et al., *Gold Glyconanoparticles as Water-Soluble Polyvalent Models To Study Carbohydrate Interactions*. Angew Chem Int Ed Engl, 2001. **40**(12): p. 2257-2261.

Introduction, Aim and Scope

29. de la Fuente, J.M. and S. Penades, *Understanding carbohydrate-carbohydrate interactions by means of glyconanotechnology*. Glycoconj J, 2004. **21**(3-4): p. 149-63.
30. Ojeda, R., et al., *Preparation of multifunctional glyconanoparticles as a platform for potential carbohydrate-based anticancer vaccines*. Carbohydr Res, 2007. **342**(3-4): p. 448-59.
31. J. Rojo, V.D., J.M. de la Fuente, I. Segura, A.G. Barrientos, H.H. Riese, A. Bernad, S. Penadés, *Gold Glyconanoparticles as new tools in antiadhesive therapy*. Chembiochem, 2004. **5**: p. 291-297.
32. Martínez-avila, O., et al., *Multivalent Manno-Glyconanoparticles inhibit DC-SIGN-mediated HIV-1 trans-infection of human T cells*. Chembiochem, 2009. **10**: p. 1806-1809.
33. Amstad E., Z.S., Mashaghi A., Wong J.Y., Textor M., Reimhult E., *Surface functionalization of single superparamagnetic iron oxide nanoparticles for targeted magnetic resonance imaging*. Small, 2009. **5**(11): p. 1334-1342.
34. Lin P-C., C.S.-H., Wang K-Y., Chen M-L., Adak A.K., Hwu J-R., Chen Y-J., Lin C-C., *Fabrication of oriented antibody-conjugated magnetic nanoprobe and their immunoaffinity application*. Anal. Chem., 2009. **81**(21): p. 8774-8782.

PART 1:

Preparation and characterization of magnetic/fluorescent biofunctional nanoparticles

CHAPTER 1

Water-soluble magnetic glyconanoparticles based on metal-doped ferrites coated with gold: Preparation and characterization

Water-soluble magnetic glyconanoparticles based on metal-doped ferrites coated with gold: Synthesis and characterization

Introduction

Integration of nanomaterials research and biology is expected to produce major perspectives in molecular biology, bioengineering, medical diagnostics, and therapeutics [1] [2] [3]. Recent advances include the development of functional nanoparticles (electronic, optical, or magnetic) that are conjugated to biological molecules such as peptides, proteins, and nucleic acids [4] [5] [6] [7] [8] [9]. Magnetic nanocrystals, including magnetite (Fe_3O_4) and maghemite (Fe_2O_3), have already shown great potential in biomedical applications. There are few well established approaches to produce high quality magnetic nanoparticles suitable for *in vivo* applications [10] [11] [12] [13]. Because of their size-dependent properties and dimensional similarities to biomolecules, these nanoparticles and bioconjugates, will be well suited as contrast agents for *in vivo* Magnetic Resonance Imaging (MRI). Superparamagnetic iron oxide and ferrite nanoparticles allow researchers and clinicians to enhance tissue contrast of an area of interest by increasing the relaxation rate of water [14] [15] [16]. Those systems affect T_2 relaxation time more significantly than T_1 , resulting in a darkening of the image where the nanocrystals are located. With variations in the size, coating thickness, surface chemistry, and targeting ligands, these nanoparticle probes can be tailored to target and label specific organs, cells, or even molecular markers of different diseases *in vivo*.

For the preparation of iron oxide nanoparticles, the thermal decomposition method recently developed [17] [18] [19] [20] [21] [22] [23], has been demonstrated to be the most convenient approach for the preparation of high quality magnetic nanocrystals. The use of high boiling point solvents as reaction media can effectively separate the nucleation and subsequent growth process. This method allows precise control over the size of the final nanoparticles (with variation minor of 5%), controlling the experimental conditions (temperature, stoichiometry, metallic salts, surfactants, etc...). There are several considerations for the design of the scaffold nanoparticles. For example, an

adequate size (5 - 10 nm) and the presence of ligands onto the surface which increase blood half-life, avoid opsonisation and have good biokinetics characteristics.

Magnetic resonance was discovered around 60 years ago. In 1946, independently one from the other, two American scientists (E. Purcell and F. Bloch), discovered a physico-chemical process based on the magnetic properties of certain nuclei. They found that when they placed the nuclei in a magnetic field, they absorbed energy in the region of radiofrequency and then reemit this energy during the transition to their original orientation [24] [25]. Due to the existing relationship between the strength of the magnetic field and the radiofrequency, this phenomenon was called Nuclear Magnetic Resonance (NMR). In Bloch's work, it was the first time that a paramagnetic catalyser was mentioned [24] that accelerated the T_1 process of relaxation and it was immediately applied in imaging studies when MRI was developed [26]. In 1972 Lauterbur [27] obtained the first 2D image of water molecule protons and in 1974 produced the first images of a living animal [28]. From here on numerous groups began to contribute to the development of this technique. P. C. Lauterbur shared the Nobel Prize in Physiology or Medicine in 2003 with Peter Mansfield for his work which made the development of magnetic resonance imaging (MRI) possible.

Using MRI different images can be obtained of one tissue based on three parameters; protonic density (ρ), given by the concentration of water in the tissue, the longitudinal relaxation time (T_1), and the transversal relaxation time (T_2) of water protons. However, if the intrinsic contrast is low, contrast agents should be used to improve the quality of the resulting images.

Even though the inherent contrast of tissues can be manipulated in MRI in a more flexible way than in the case of other imaging techniques, in many cases giving a diagnosis based on this kind of images require the use of contrast agents. In general, the manipulation of the contrast in magnetic resonance applying contrast agents is only used when the inherent contrast can not be changed. The most important objectives for the development and uses of new contrast agents are summarized in table 1 [29].

As it is impossible to change the water content of tissues, commercial contrast agents or the ones employed in clinical research are based on changes in the relaxation rates T_1 and T_2 of water protons and in the magnetic susceptibility of water in tissues. Most of the contrast agents are para- or superparamagnetic.

Many of the efforts devoted to the development of contrast agents are more focused on simplifying the synthesis of the compounds than on achieving a specific medical

application. The contrast agents available currently in the market for routine diagnosis are secure and good contrast enhancers, but the main problem is that they are highly unspecific. These contrast agents are only valid to localize pathologic changes in the tissues, but not specific pathologies. The development of specific contrast agents is a crucial research line.

Table 1. Main objectives pursued in the development of MRI contrast agents.

Objectives	Requirements
Improvement of tissue contrast	Good relaxivity
Tissue characterization	Good susceptibility
Improvement of general sensitivity	Good osmolarity
Improvement of general specificity	Good biodistribution
Diagnosis	Good tolerance
Therapy	Adequate metabolism
Function screening	Good stability
Reduction of artefacts	Easy wash-out
Reduction of imaging times	Low toxicity
Reduction of general costs	

Classification of contrast agents [30]. Contrast agents are classified in ‘T₁’ or ‘T₂’ agents depending on whether they reduce the longitudinal (T₁) or the transversal relaxation rates (T₂ or T₂^{*}) of water in subject tissues. The ability of the agent to reduce T₁ or T₂ is described by a parameter called relaxivity (r₁ or r₂ respectively). The relaxivity is defined as the slope of the straight line that is obtained when 1/T₁₍₂₎ (s⁻¹) is plotted against the concentration of the contrast agent (mM). Higher relaxivity corresponds with a stronger increase of (T₁) or decrease of (T₂) signal.

T₁ contrast agents are based on paramagnetic atoms, mainly Gd³⁺, while T₂ contrast agent use magnetic materials. In this case the most common ones are iron oxide based. This thesis describes the preparation of T₂ agents so we will focus on these last ones. Iron oxide nanoparticles are classified regarding their magnetic properties among the superparamagnetic agents. These nanoparticles, with a diameter between 3 and 200 nm, are constituted of thousands of magnetic ions. Iron oxide nanocrystals display a property defined as superparamagnetism. They have crystal-containing regions of unpaired spins (figure 1). These magnetic domains are disordered in the absence of a

magnetic field, but when a field is applied, the magnetic domains align to create a magnetic moment much greater than the sum of the individual unpaired electrons. This does not, however, result in residual magnetization of the particles.

Depending on their sizes they can be classified in several groups:

- diameter above 50 nm: SPIO (SuperParamagnetic Iron Oxide)
- diameter under 50 nm: USPIO (Ultrasmall SPIO)

The particles have permanent magnetic moment that increases when they are exposed to an external magnetic field. This magnetic moment is much higher than the one from gadolinium chelates that are commercial paramagnetic agents. In most of the cases SPIO and USPIO are both used as T_2 agents, and result in a reduction of the signal on T_2 -weighed images (negative contrast agents). Basically, the magnetic moment origins a heterogeneous magnetic field through which the water molecules diffuse [31]. The diffusion induces a diphas in the magnetic moments of the protons, which finally results in a reduction of T_2 . These contrast agents are also called susceptibility agents due to their effect over the magnetic fields.

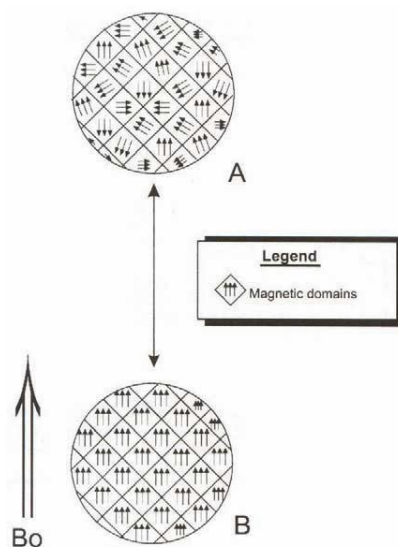


Figure 1. **A**, superparamagnetic iron oxide (SPIO) crystal in the absence of an external magnetic field (B_0); the orientation of the magnetic domains is random. **B**, the application of an external magnetic field aligns the magnetic domains with B_0 (image taken from ref. [32])

Magnetic nanoparticles (mainly iron oxide nanoparticles) were developed at the beginning of the 80s as contrast agents for MRI. Iron oxide nanoparticles coated with dextran were used for the first time in *in vitro* studies in 1978 by Ohgushi [33]. In those

first experiments they demonstrated a dramatic reduction of T_2 of an aqueous solution of the contrast agent. The first *in vivo* images by MRI using iron oxide nanoparticles were obtained by Prof. Lauterbur [34] (dog models). During the next years numerous researchers used iron oxide superparamagnetic nanoparticles as contrast agent for MRI [35] [36] [37] [38]. Nowadays, this kind of nanocrystals are functionalized with starch [36], dextran [37] [39], and even with specific biomolecule markers like antibodies [40]. Weissleder *et al.* developed monocrystalline iron oxide nanoparticles (MION) [41] and their application on magnetic resonance angiography (MRA) [42] and to label asialoglycoprotein membrane receptor [43].

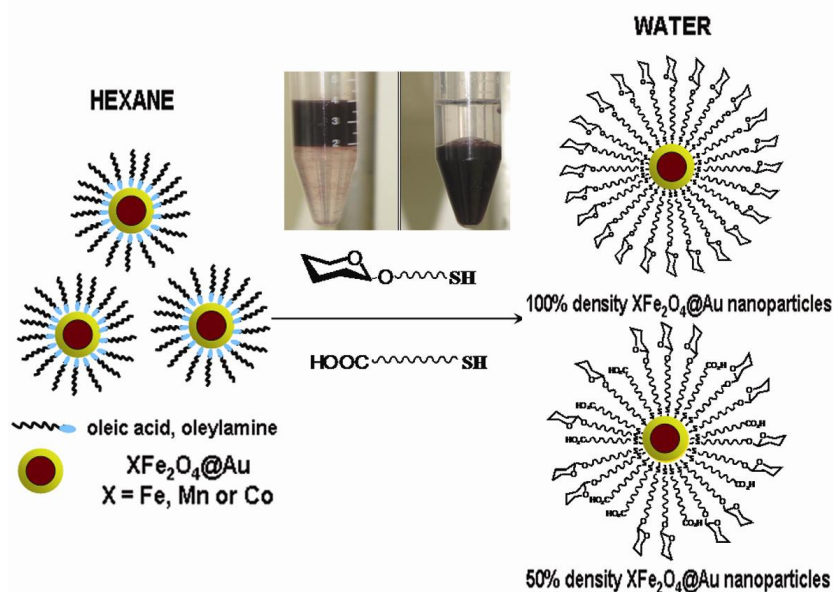
Currently, some of these superparamagnetic materials are commercially available. Examples of commercial iron oxide nanoparticles are Lumirem® (iron oxides covered with silica), Endorem® (iron oxide coated with dextran), Sinerem® (used to detect metastasis in lymphatic nodes).

In this chapter we present the preparation and characterization of water-soluble magnetic glyconanoparticles (glyco-nanoferrites). In our design, we started from well-defined ferrite cores and coated them with a gold shell. We have chosen the gold coating for the magnetic cores instead of any of the other possibilities (silica, polymers ...) because of our experience on the functionalization of gold nanoparticles with biomolecules. This approach requires optimization of the preparation protocols and also a careful characterization of the resulting particles because of their bimetallic nature. These ferrites were converted into water-soluble ferrites by a ligand exchange reaction with the help of thiol-ending amphiphilic carbohydrates and linkers (Scheme 2).

Preparation and characterization of core@shell magnetic nanoferrites with 3-6 nm magnetic cores

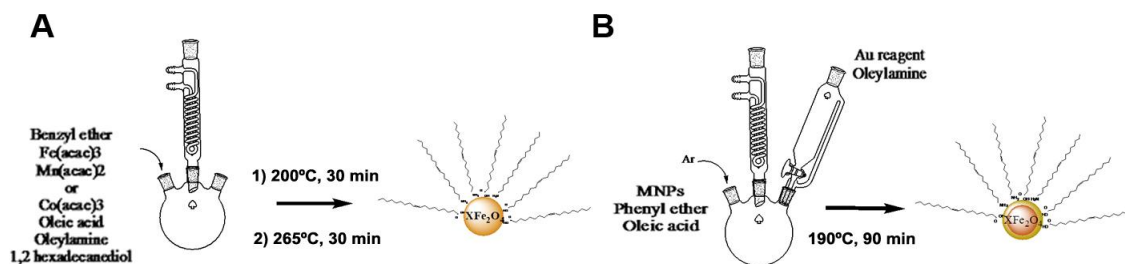
Considerable efforts have been devoted to the preparation of monodispersed magnetic nanocrystals with a controlled size and shape. One of the most successful routes involves the thermal decomposition of organometallic M^{2+} and Fe^{3+} complexes in high boiling point solvents and in the presence of surfactants (oleic acid, oleylamine and others) [21] [44] [45] [46]. At this respect we have followed Sun's protocol to prepare well-defined monodisperse magnetite and ferrite (XFe_2O_4) nanoparticles [21]. In a second step we have coated these magnetic cores with a gold shell by a modified

protocol based on [47]. By the addition of this gold shell we can profit from the experience of the group on gold nanoparticles functionalization and characterization.



Scheme 2. General design for the preparation of water soluble *glyco*-nanoferrites.

We began with the synthesis of 3.2 nm-sized Fe_3O_4 magnetic cores by thermal decomposition of iron acetylacetonate [$Fe(acac)_3$]. We prepared using the same methodology manganese and cobalt ferrite cores ($MnFe_2O_4$ and $CoFe_2O_4$) with a narrow size distribution centred on 6.1 nm and 6.2 nm respectively, to get an improvement of the magnetic properties and to evaluate the effect of the different magnetic atoms in the final relaxivity properties, as described in the bibliography [48]. Finally, Fe_3O_4 nanoparticles with bigger sizes were also prepared (see next section). The ferrite cores were characterized by TEM. The presence of the different elements, Fe, Mn or Co was confirmed by EDX spectroscopy. Once the magnetic core was synthesized, a gold coating was performed in a controlled reduction process with gold acetate [$Au(Ac)_3$] in the presence of oleic acid and oleylamine. These core@shell $XFe_2O_4@Au$ nanostructures are the scaffolds over which we will modify the shell by ligand exchange with the appropriate amphiphilic molecules, to reach high biocompatibility, low toxicity, water solubility and specific targeting (see chapter 3 and 4).



Scheme 3. A, preparation of magnetic cores in benzyl ether from $\text{Fe}(\text{acac})_3$ and $\text{Mn}(\text{acac})_2$ or $\text{Co}(\text{acac})_3$, in the presence of 1, 2 hexadecanediol, oleic acid and oleylamine. B, gold coating reaction of the magnetic cores in phenyl ether, with $\text{Au}(\text{Ac})_3$ as gold reagent.

Zhong's protocol [47] allowed us to obtain $\text{Fe}_3\text{O}_4@Au$ monodispersed nanoparticles in nonpolar solvents with a size of 5.8 nm. In the case of $\text{MnFe}_2\text{O}_4@Au$ (13.5 nm) and $\text{CoFe}_2\text{O}_4@Au$ (12.5 nm) an extensive modification of the protocol has to be made in order to obtain a uniform shell of gold. The main problems when Zhong's protocol was applied to obtain the new structures were the incomplete coating of the population of magnetic nanocrystals and at the same time the formation of pure gold nanoparticles. Several changes were applied. First, gold reagent was added very slowly, drop by drop, over the preheated (at 190°C) reaction mixture of ferrite cores. Second, and more important, only a weak reducing agent, oleylamine, was used to reduce slowly the gold precursor onto the ferrite seeds to form a shell and not gold nanocrystals, since the heterogeneous nucleation requires less activation energy according to the Classical Nucleation Theory (CNT) [49]. The mild reducing conditions together with the high temperature force gold to grow over the magnetic seeds.

In order to control the thickness of the gold shell, gold deposition was extensively studied. This coating process was monitored using UV-Vis spectroscopy. Before the addition of gold (III) acetate reagent, the extinction properties of the superparamagnetic particles (XFe_2O_4) are consistent with subwavelength sized dielectric spheres (figure 2 left) but upon addition of the gold layer onto the magnetic core, the extinction spectrum changes drastically appearing a typical plasmon resonance peak (around 520 nm) (figure 2 left). The controlled coating of Au can tune the plasmonic properties of the core@shell structure [50]. Three different ratios Fe: Au (1:7, 1:1.75, 1:0.5) in the case of magnetite, were used with a consequent decrease in the Au layer thickness. Figure 2 right shows a series of UV-Vis spectra corresponding to $\text{Fe}_3\text{O}_4@Au$ prepared at

different ratios. The $\text{Fe}_3\text{O}_4@Au$ nanoparticles at a proportion Fe:Au 1:0.5 (not sufficient for the complete coating of all the magnetic cores) have an absorption peak at 513 nm. Deposition of more Au on the seed nanoparticles leads to a red shift of the absorption peak to 526 and 530 nm for 1:1.75 and 1:7 (Fe/Au) respectively. This shift towards the red when we increase the dimensions of the Au coating is in accordance with data from the bibliography [50].

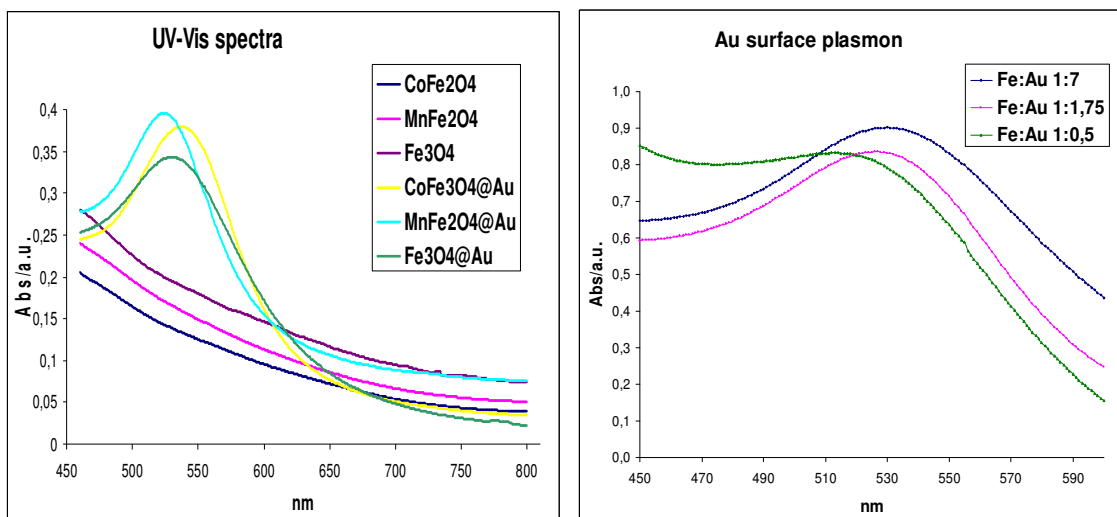


Figure 2. Left, UV-Vis spectra of Fe_3O_4 , MnFe_2O_4 , CoFe_2O_4 before and after the gold coating. Right, UV-Vis spectra of the core@shell $\text{Fe}_3\text{O}_4@Au$ nanoparticles with three Au coating thicknesses.

Core@shell characterization. For the complete characterization of this core@shell structure several analytical techniques were used. TEM is the easiest way to characterize core@shell nanostructures [51] [52]. However, it is impossible to use TEM to precisely characterize these structures (in the range of sizes prepared herein) because of the fact that the gold atom is electronically much denser than iron or oxygen. Gold gives such dark contrast that nothing can be imaged underneath. A similar problem appears when High Angle Annular Dark Field-Scanning Transmission Electron Microscopy (HAADF-STEM) technique is used. We have tried to demonstrate unequivocally the presence of magnetic material and gold in the same nanoparticle. Measurements like X-Ray Diffraction (XRD) and X-Ray Photoelectron Spectroscopy (XPS) have been used to propose core@shell structures. But these are measurements held over a whole sample, not over individual nanoparticles, so the results are the average of a wide population. Besides, there is some controversy in the interpretation of

the results, especially XRD data, concerning the presence or absence of Fe_3O_4 peaks when the gold shell is built [47] [53] [54].

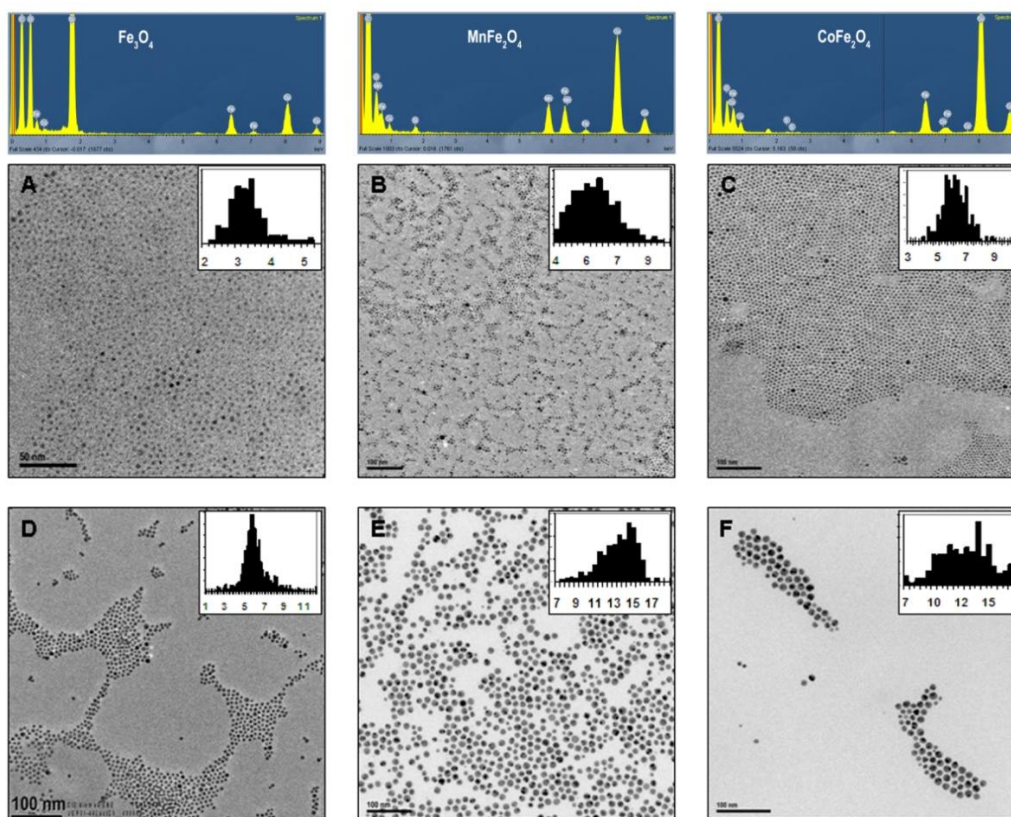


Figure 3. Comparative data of XFe_2O_4 and $\text{XFe}_2\text{O}_4@Au$. **Upper row**, EDX spectra of Fe_3O_4 (left), MnFe_2O_4 (centre) and CoFe_2O_4 (right). Peaks from Cr (around 5.5 KeV) and Si (around 1.7 KeV) are present in the three spectra coming from the sample holder. TEM micrographs of Fe_3O_4 (**A**, **D**), MnFe_2O_4 (**B**, **E**), and CoFe_2O_4 (**C**, **F**), before (**A**, **B**, **C**), and after (**D**, **E**, **F**) the gold coating.

TEM micrographs of the prepared nanoferrites $\text{XFe}_2\text{O}_4@Au$ (figure 3D-F, figure 4IV) show gold contrast and monodispersity. The sizes measured by TEM before and after the coating show a growth in the diameter. Before coating, the magnetic Fe_3O_4 nanoparticles presented a diameter of 3.2 nm, while MnFe_2O_4 and CoFe_2O_4 cores showed 6.1 and 6.2 nm of diameter respectively. After the coating under the conditions of an excess of $\text{Au}(\text{Ac})_3$ (X: Au 1/7) and 190°C , the diameter grew to 5.8 nm, 13.5 nm, and 12.5 nm for Fe, Mn and Co respectively (figure 3D-F). This fact already points towards a core@shell structure or at least to an alloy structure. We have designed several chemical protocols to confirm that the prepared structures were core@shell. Several control experiments were performed to elucidate if the nanoparticles obtained (figure 3D-F) present in the same nanoparticle gold and a magnetic component.

Results and Discussion

The first protocol was to grow gold nanoparticles exactly under the same conditions as in the coating reaction before, but without the presence of iron oxide seeds. The corresponding TEM micrographs showed gold nanoparticles with high polydispersity (figure 4I). In the absence of Fe_3O_4 magnetic seeds, and under high temperature conditions, the size of gold nanoparticles can not be controlled; then a high degree of dispersion was obtained in comparison with the monodispersed nanoparticles obtained under standard conditions (figure 4IV). In a second protocol, the coating reaction of the Fe_3O_4 seeds was carried out in a defect of Au reagent ($\text{Au}(\text{Ac})_3$, 0.25 eq.). A mixture of small iron oxide nanoparticles and bigger gold coated nanoparticles was obtained (figure 4II). Both populations present in electron microscopy a remarkable difference in their contrast. A third experiment was performed in order to assess whether gold and iron present a tendency to form alloys. When formation of magnetite cores was performed in a one-step reaction in the presence of the gold reagent used for the coating, $\text{Au}@Fe_3O_4$ core@shell nanoparticles were clearly produced (figure 4III). The strong contrast indicates gold in the core and iron oxide in the shell. Under these conditions, it seems that there is no tendency to form alloys and the materials remain separated from each other. These same control experiments were repeated for Mn ferrite with similar results.

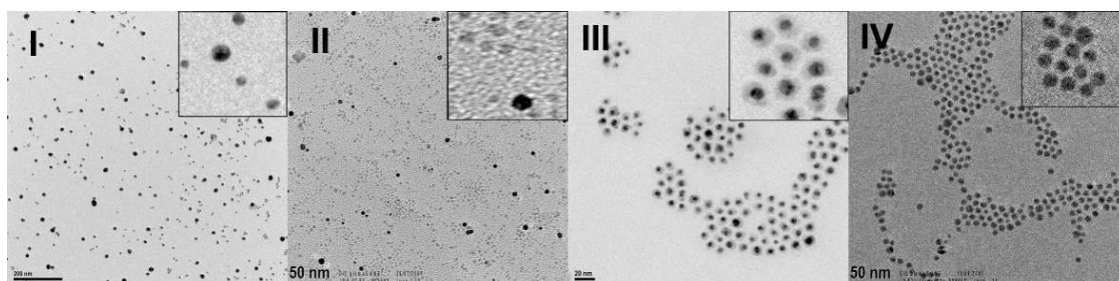


Figure 4. TEM micrographs of nanoparticles obtained in the different control experiments. **I**, Au nanoparticles obtained from the coating reaction without the magnetic seeds. **II**, nanoparticles from the coating reaction with insufficient Au reagent. **III**, core@shell $\text{Au}@Fe_3O_4$ structure obtained when the synthesis of the magnetic cores was performed in the presence of Au reagent. **IV**, $Fe_3O_4@Au$ nanoparticles obtained under the standard gold coating conditions.

We want to emphasize in this point that in spite of the progress on nanomaterials synthesis, the random nucleation of mixing nanocomponents provides limited control in the synthesis of magnetic hybrid materials. In this context, the one-step method described above represents a straightforward and easy way to obtain in one step

Au@Fe₃O₄ core@shell nanoparticles (figure 4III) *versus* other strategies that involve several steps [55] [56] [57].

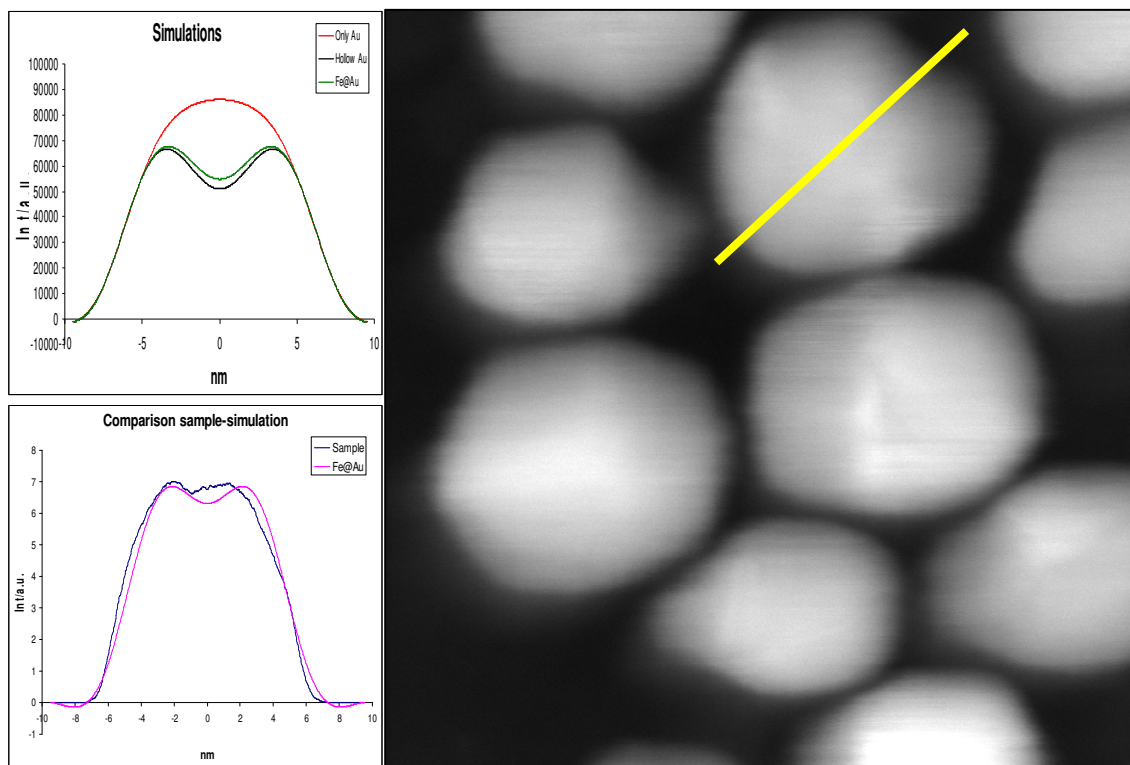


Figure 5. Left, intensity profiles of a single nanoparticle: **Up**, simulations of pure Au nanoparticle (**red**); hollow Au nanoparticle (**black**); and Fe core Au shell nanoparticle (**green**). **Bottom**, comparison between the experimental intensity profile of the sample and the calculated for an iron@gold core@shell structure. **Right**, HAADF image of MnFe₂O₄@Au nanoparticles.

STEM or HAADF (high angle annular dark field), and STEM-EDXS analysis were used to estimate the internal distribution of Au and Fe within a single nanoparticle. HAADF technique, provides what is called chemical contrast, i.e. the intensity of the crystals imaged depends on the electronic density of the containing atoms. With an electron beam probe of 0.5 nm in diameter the sample was scanned and the intensity of the resulting image (figure 5) was analyzed and compared with a theoretical approximation. This approximation considers the nanoparticles to be spherical, the intensity of the image in each point proportional to the square of the atomic number of the constituting elements (for simplicity only Fe and Au), and takes into account the finite size effect of the probe [58]. From the results, (figure 5) two conclusions can be extracted; first, the nanocrystals are not built up of a homogeneous material, and second, that there is clearly a less dense area in the core of the nanoparticles as expected.

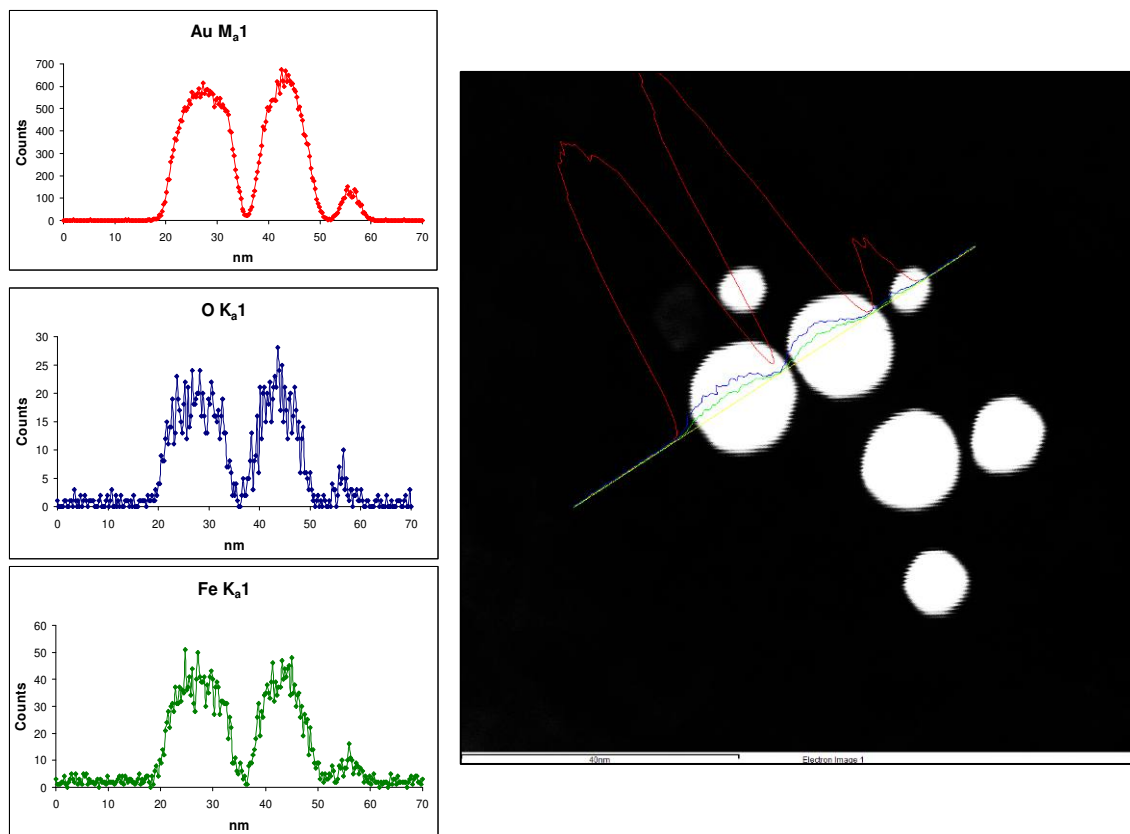


Figure 6. STEM-EDX analysis of $\text{MnFe}_2\text{O}_4@Au$ nanoparticles. **Left**, linescans of the three elements of interest, Au (**red**), Fe (**blue**), and O (**green**). **Right**, STEM image of a group of $\text{MnFe}_2\text{O}_4@Au$ nanoparticles.

Combining STEM with EDXS, with a scanning probe of 1.0 nm it is possible to distinguish the component elements in bimetallic particles. Figure 6 shows the annular dark field STEM image of several nanoparticles and the individual chemical profiles of the elements Au, Fe and O obtained from linescans across three nanoparticles. The EDXS-image and the chemical profiles show that Fe, Au and O are present in the same nanoparticle. Unluckily, the lateral resolution of this technique under the conditions used is not enough to determine, whether the structure is a core@shell or an alloy. However, according to previous control experiments, the TEM micrograph in figure 4III, and the intensity profiles of individual crystals by HAADF (figure 5), the most probable structure is the core@shell one. Using this same technique, chemical maps of the elements of interest (Fe, Au and O) were also obtained, and the results confirm the presence of gold and iron oxide in the same nanoparticle.

These results evident STEM-EDXS as a straightforward and powerful technique for the characterization of new nanostructured hetero-materials. Furthermore, it can help to understand the relationship between the atomic structure of the cluster and their final physical properties. In fact, several authors have used these combined analytical STEM-EDXS data to propose their structures especially with heavy atoms [59] [60] [61] [62]. The result obtained by STEM-EDXS technique on its own allows us to ensure that the magnetic material and gold are part of the same crystal. We can conclude from these data together with the results obtained in the chemical control experiments, that the structure of $XFe_2O_4@Au$ is a core@shell one.

Magnetic characterization. The magnetic properties of the ferrites were determined and compared with the data already published. The hysteresis loops of the ferrites were measured using a vibrating sample magnetometer (VSM). All the synthesised nanoparticles showed a superparamagnetic behaviour. The magnetic properties measured for the magnetite core are in total accordance with bibliography data [21] [63]. The magnetization curves of $MnFe_2O_4$ and $CoFe_2O_4$ display high saturation magnetization at 300 K of around 115 and 130 emu/g of magnetic material, respectively (figure 7). For the cobalt ferrite, a higher magnetization value (130 emu/g) was observed related to the values described in the literature (80-100 emu/g) [64] [46]. The coercivity of Fe_3O_4 and $MnFe_2O_4$ has similar values, but $CoFe_2O_4$ nanocrystal display a markedly higher coercivity of aprox. 12.000 Oe at 5K versus 175 Oe at 5H for $MnFe_2O_4$ (figure 7) likely due to its higher magnetocrystalline anisotropy. This observed value is within the range reported in the literature [21] [46]. As indicated by the ZFC-FC curves in the figure 7, $MnFe_2O_4$ presents a lower blocking temperature (~25 K) as compared with $CoFe_2O_4$. The magnetism of the core@shell ferrites was measured after converting them in water-soluble *glyco*-ferrites.

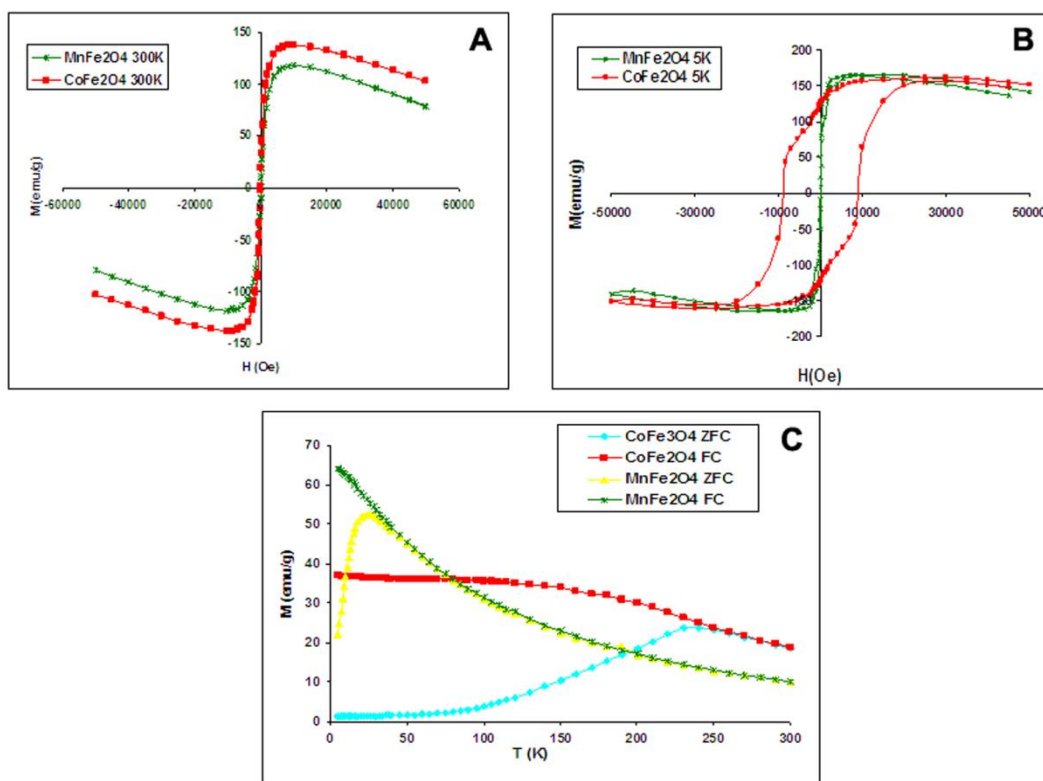


Figure 7. Magnetic measurements of MnFe_2O_4 and CoFe_2O_4 . **Top-left**, room temperature magnetization hysteresis. **Top-right**, magnetization hysteresis at low temperature (5K). **Bottom**, zero field cooled (ZFC) and field cooled (FC) magnetization.

Attempts to prepare bigger magnetite cores

The synthesis of $\text{Fe}_3\text{O}_4@Au$ nanoparticles with bigger magnetite cores, which would in theory enhance the performance of the final nanoparticles as T_2 contrast agents, resulted much difficult than expected. The first attempt to obtain bigger Fe_3O_4 nanoparticles was following a seeded growth protocol [21]. In this case first 6 nm Fe_3O_4 nanoparticles were prepared by a thermal decomposition method, and then the size of these nanoparticles was increased in a second step. Following this protocol we were not able to obtain a final monodispersed population of magnetite nanoparticles (Figure 8, A and B). Then, Sun's protocol [65] was followed to obtain 8 nm Fe_3O_4 nanoparticles in one step, with good results (Figure 8, C). According to this methodology final nanoparticles are protected only by oleylamine (instead of by the usual mixture oleylamine/oleic acid). We have confirmed that this represents a problem for the subsequent coating of the magnetic cores with a gold shell. If the coating reaction is

Results and Discussion

performed directly with the nanoparticles obtained (Figure 8, D), gold grows on its own rather than over the existing seeds. If this same reaction is performed after exchanging part of the oleylamine in the nanoparticles surface by oleic acid molecules, gold grows over iron oxide seeds, although the final nanoparticles are not homogeneous (Figure 8, E). A completely different protocol using a gold salt, HAuCl_4 , as Au reagent [50] was also applied for the gold coating of these nanoparticles, but this methodology gives a mixture of iron oxide nanoparticles and small pure gold nanoparticles (Figure 8, F).

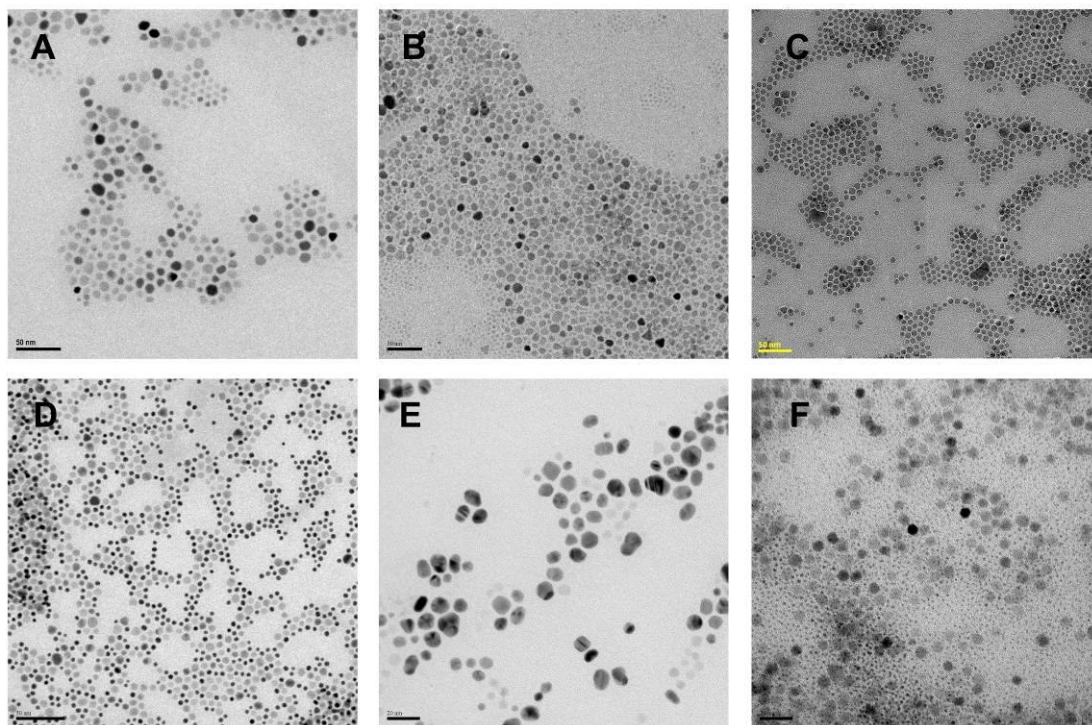


Figure 8. TEM micrographs showing the resulting products from the attempts to synthesize of bigger magnetite core gold coated nanoparticles. **A**, Fe_3O_4 nanoparticles obtained following a protocol to obtain 6 nm particles. **B**, Fe_3O_4 nanoparticles obtained after the seeded growth procedure using nanoparticles from A as seeds. **C**, 8 nm Fe_3O_4 obtained following a protocol without oleic acid. **D**, mixture of 8 nm Fe_3O_4 nanoparticles and smaller Au nanoparticles obtained using our standard coating protocol with nanoparticles from C. **E**, mixture of Fe_3O_4 nanoparticles and $\text{Fe}_3\text{O}_4@$ Au nanoparticles obtained from our standard coating reaction with nanoparticles from C after exchanging part of the oleylamine ligands for oleic acid. **F**, mixture of Fe_3O_4 nanoparticles and really small Au nanoparticles obtained using HAuCl_4 as gold coating reagent. All scale bars are 50 nm except E and F, 20 nm.

After these failures a closer control of the reaction temperature was tried in the standard synthesis of 4 nm magnetite nanoparticles inserting the temperature controller inside the reaction mixture. Under these conditions 4.5 nm diameter Fe_3O_4 nanoparticles were

obtained. The gold coating of these nanoparticles was straightforward using our standard conditions (Figure 9).

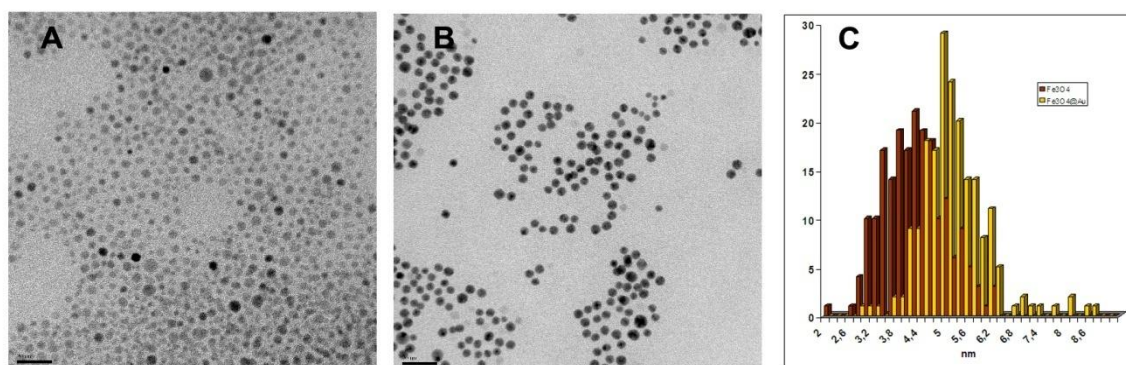
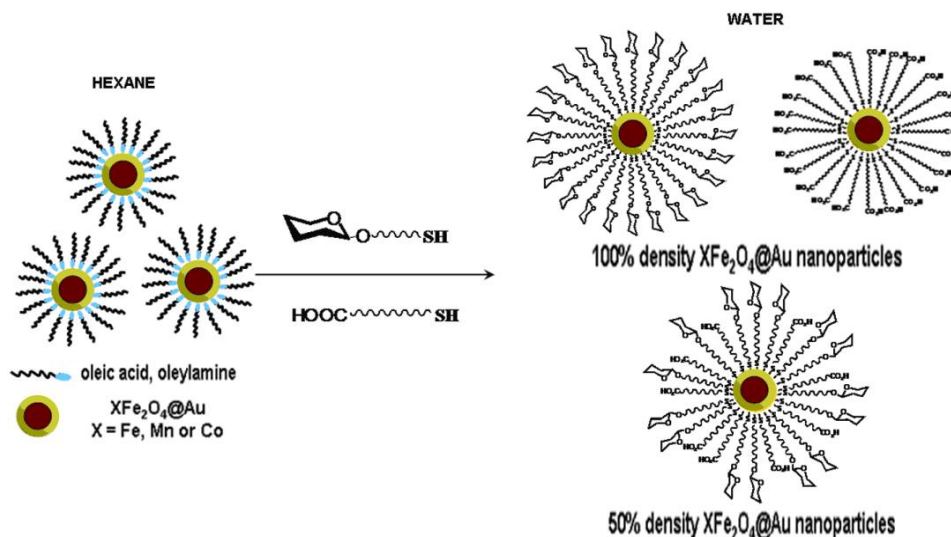


Figure 9. **A**, TEM micrograph of 4.5 nm Fe_3O_4 nanoparticles. **B**, TEM micrograph of $\text{Fe}_3\text{O}_4@Au$ nanoparticles. **C**, size distribution comparison of nanoparticles from A and B.

Preparation and characterization of water soluble magnetic glyco-nanoferrites

To use previously prepared magnetic nanoparticles in biological applications their surface coatings must be somehow transformed into hydrophilic and ideally biocompatible.



Scheme 4. Ligand exchange reaction for the preparation of the 100 % (carbohydrate or linker) and hybrid families (50 %) of glyco-ferrites.

In our approach (scheme 4), the previous prepared oleylamine and oleic acid protected $\text{XFe}_2\text{O}_4@Au$ magnetic nanoparticles were capped with different modified saccharides

Results and Discussion

and/or with a linker ended in a carboxylic group (figure 10) by a two-phases ligand exchange reaction which strips the original hydrophobic coating and replaces it with biofunctional capping molecules.

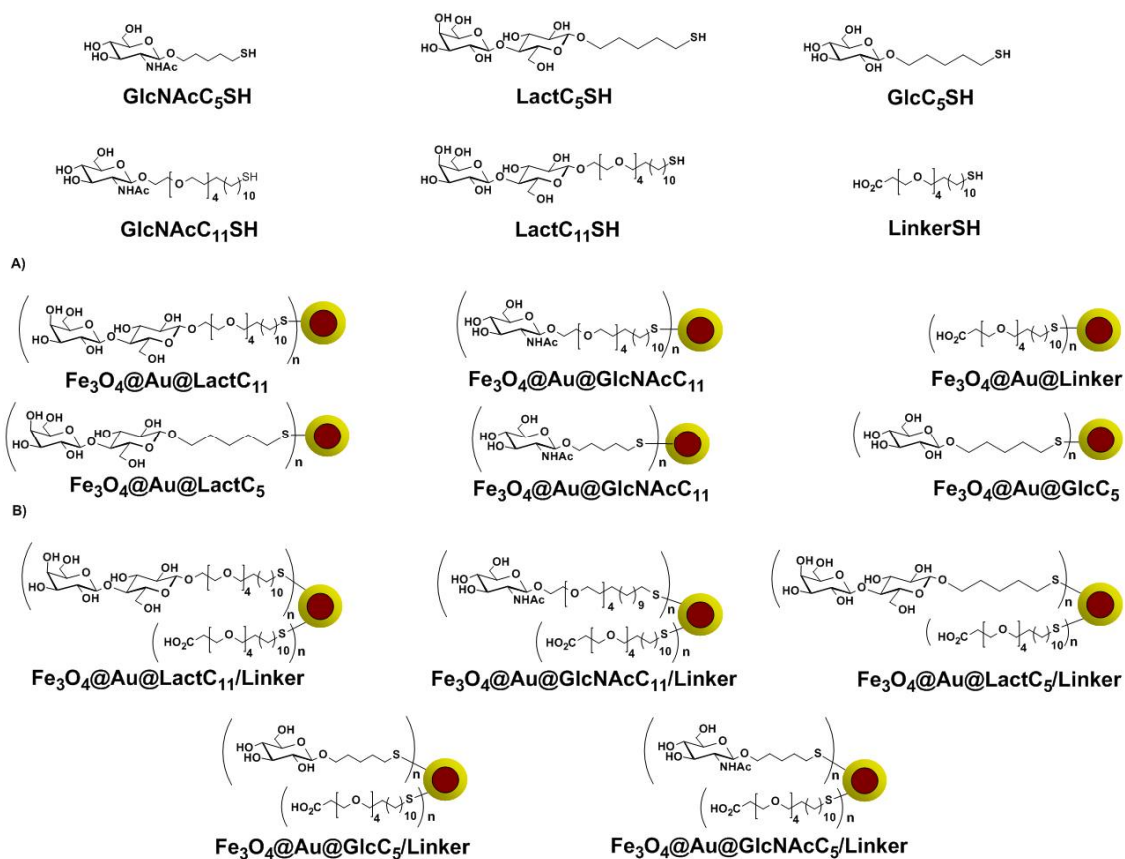


Figure 10. Glycoconjugates and carboxylic linker used for the preparation of water soluble nanoferrites, and the corresponding families of magnetic glyconanoparticles (MGNPs) obtained by the ligand exchange reaction. **A**, glyco-ferrites with 100% density of sugar, and **B**, glyco-ferrites with 50% density of sugar.

As ligands, we have prepared a series of amphiphilic carbohydrates by glycosidation of the disaccharide lactose (β -D-galactopyranosyl-(1 \rightarrow 4)-D-glucose, Lact), the monosaccharides D-glucose (Glc), and N-acetyl D-glucosamine (GlcNAc) with linkers to obtain 5-mercaptopentyl β -D-galactopyranosyl(1 \rightarrow 4)- β -D-glucopyranoside (LactC₅SH), 5-mercaptopentyl β -D-glucopyranoside (GlcC₅SH), 5-mercaptopentyl 2-acetamido β -D-glucopyranoside (GlcNAcC₅SH), 22-mercapto [3,6,9,12-tetraoxadecanyl]-1-oic acid (LinkerSH), 22-mercapto [3,6,9,12-tetraoxadecanyl (β -D-galactopyranosyl)(1 \rightarrow 4) β -D-glucopyranoside] (LactC₁₁SH), and 22-mercapto [3,6,9,12-tetraoxadecanyl-2-acetamido(β -D-glucopyranoside)] (GlcNAcC₁₁SH).

Results and Discussion

Linkers with different lengths and chemical natures, aliphatic $[\text{HS}(\text{CH}_2)_5 \equiv \text{C}_5\text{SH}]$ or amphiphilic linker $[\text{HS}(\text{CH}_2)_{11}(\text{OCH}_2\text{CH}_2)_4 \equiv \text{C}_{11}\text{SH}]$, ended in a thiol moiety to attach them to the Au coating were selected to evaluate the effectiveness and versatility of the methodology.

The water soluble glyconanoparticles (MGNPs) were obtained by mixing $\text{XFe}_2\text{O}_4@Au$ hexane solutions and an aqueous solution of the glycoconjugates or the linker and shaking overnight at room temperature until any colour was observed in the hexane phase (figure 11 I). Glycoconjugates or the carboxylic linker were coupled to the gold shell by the formation of thiol-Au bond giving Lact-, Glc-, GlcNAc- or Linker-protected glyconanoparticles with 100% density.

The presence of the tetraethylenglycol-undecene linker (TEG- C_{11}SH) in some of these conjugates with more amphiphilic character than the pentane linker (C_5SH), makes the transfer reaction more rapid. In fact, for the later ligands it was necessary to evaporate slowly the hexane phase for a complete transfer into the aqueous layer. In all the cases, this transfer process had a nearly 100% efficiency. To remove possible large contaminants (micelles), the solutions were filtered through $0.2 \mu\text{m}$ Nylon syringe filters. The nanoparticles were lyophilized, dissolved in water, washed three times (usually with ethanol and/or methanol) with magnetic separation and finally purified by dialysis. Finally, after lyophilizing a dark purple powder was obtained. This methodology is quite general and can be applied to other bimetallic cores as we have demonstrated for the transfer to water of FePt nanostars with the lactose conjugate and the liker without a change in the properties nor in the shape of the nanostarts [66].

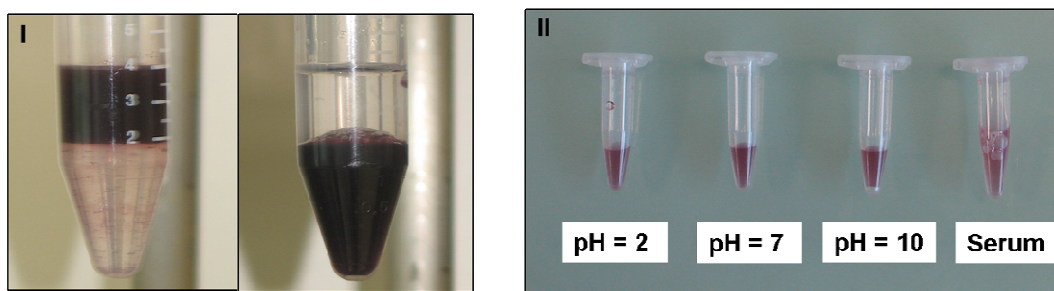


Figure 11. I, two phase (hexane/water) ligand exchange reaction before (left) and after (right) overnight shaking in the presence of the glycoconjugates. II, colloidal stability of $\text{Fe}_3\text{O}_4@Au@LactC_{11}$ in PBS at various pH values and in serum.

The water-soluble nanoparticles were very stable in water and physiological buffers. There was no precipitation in water over a wide pH range of 2-10 (adjusted by HCl or

NaOH), nor when dissolved in serum (figure 11 II) and they could be re-dissolved after centrifugation.

This methodology allows also the preparation of hybrid nanoparticles with different density of sugars. To prepare nanoparticles of differing density, aqueous solutions containing a 1:1 mixture of glycoconjugate and linker were shaken together with the hexane soluble nanomaterial. The composition of the ligands on the resulting hybrid magnetic nanoparticles was determined by comparison of the $^1\text{H-NMR}$ of the original mixture and the integration of the $^1\text{H-NMR}$ spectrum of the mixture after the ligand exchange. The integration of the signals directly in the $^1\text{H-NMR}$ of the *glyco*-ferrites was not possible due to broadening of the signals caused by the magnetic cores. The structure of these shells profit benefits from the carbohydrates and from the linker. The presence of multiple carboxylic groups allows further bioconjugation with other important targets like proteins, peptides and others while the carbohydrates confer biocompatibility, solubility in aqueous buffers, and lack of immunogenicity.

Structural characterization of water soluble magnetic *glyco*-nanoferrites. The glyconanoparticles were extensively characterised. UV-visible, FT-IR (figure 12 left) and $^1\text{H-NMR}$ spectroscopies were used to characterize the organic coating of the nanoparticles, while TEM, STEM (figure 13 C), EDXS analysis, and contact mode AFM were used to characterise mainly the metallic core of the nanoferrites.

UV-Vis spectra showed no changes after the ligand exchange, while changes in FT-IR spectra are clear (figure 12 left). The characteristic peaks of oleic acid (near 2854 and 2924 cm^{-1}) [67] are clearly reduced after ligand exchange.

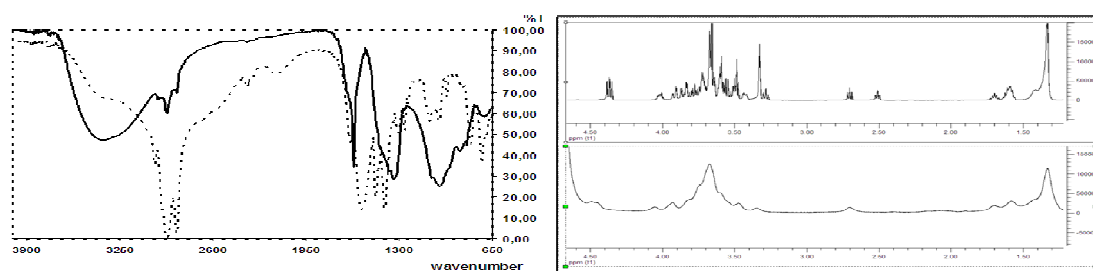


Figure 12. Left, FT-IR spectra of $\text{Fe}_3\text{O}_4@Au@LactC_{11}/\text{Linker}$ nanoparticles before (dotted line) and after the ligand exchange reaction (black line). Right, $^1\text{H-NMR}$ of glyconanoparticle $\text{Fe}_3\text{O}_4@Au@LactC_{11}$ and the corresponding glycoconjugate.

In the case of water soluble nanoparticles derived from $\text{Fe}_3\text{O}_4@Au$ core, it was possible to detect signals in their $^1\text{H-NMR}$ spectra. In fact, the $^1\text{H-NMR}$ spectra in D_2O of the

Results and Discussion

prepared *glyco*-Fe₃O₄@Au (figure 12 right) differ from the corresponding glycoconjugates in the line broadening (typical for macromolecules in solution) being especially broad in these systems due to the effect of the magnetic core. In order to detect the proton signal from the samples, the spectra were recorded at high dilution (0.05 µg nanoparticle/ml D₂O).

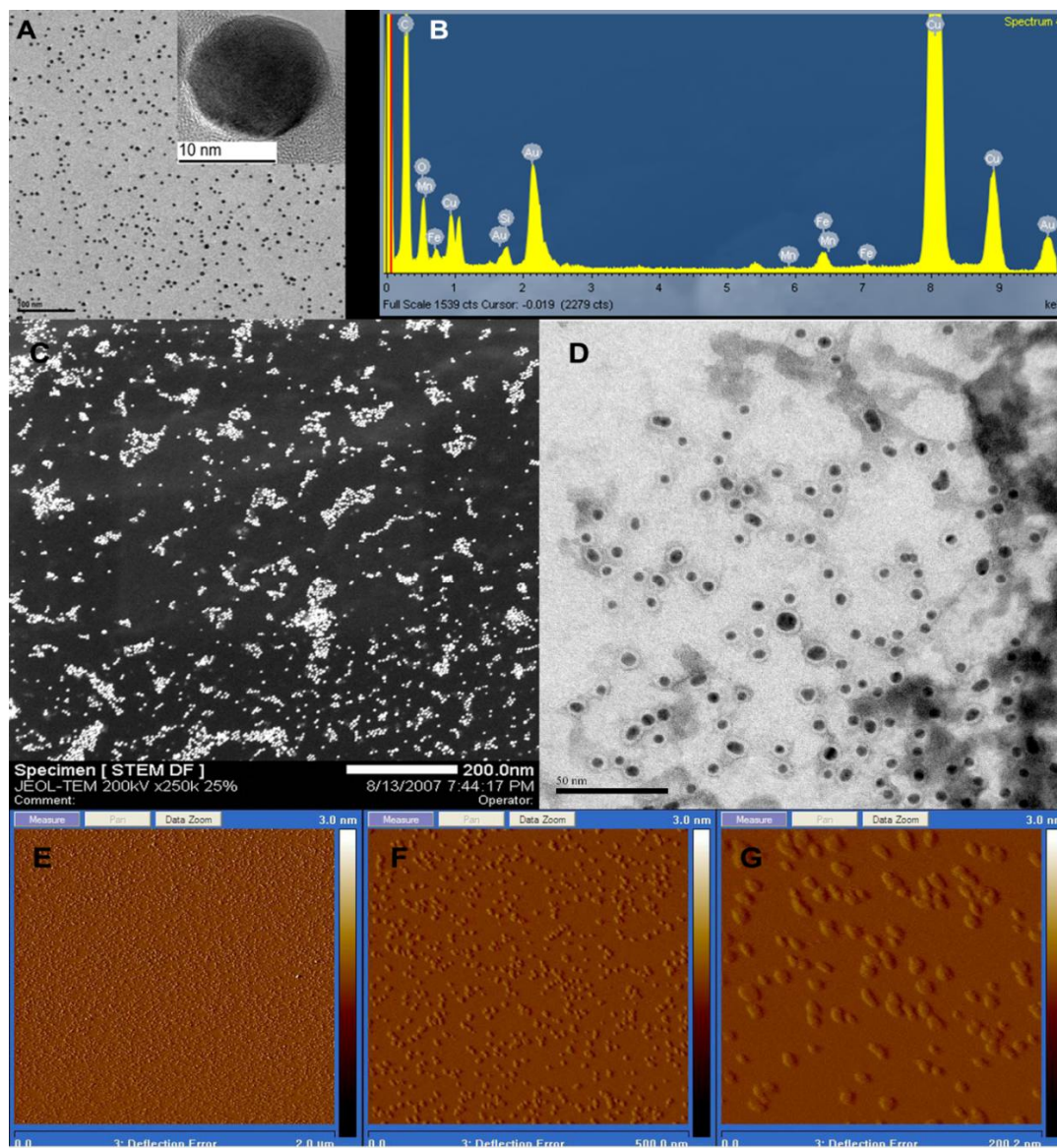


Figure 13. A, TEM micrograph of water-soluble MnFe₂O₄@Au@LactC₁₁/Linker nanoparticles. Inset: HRTEM image of one of these nanoparticles. B, EDXS spectra of the same nanoparticles showing peaks from Au, Fe and Mn. Signals of Cu and Si come from the sample holder. C, STEM image of Fe₃O₄@Au@LactC₁₁/Linker nanoparticles. D, TEM image of Fe₃O₄@Au@LactC₁₁/Linker nanoparticles negatively stained with 3% uranyl acetate. E, F, and G, contact AFM images at different magnifications of Fe₃O₄@Au@Linker nanoparticles loaded over mica surface pre-treated with 1 mM NiCl₂ solution. Transmission electron micrographs of the *glyco*-ferrites show dispersed nanoparticles with no changes in shape or size compared with the water-insoluble ferrites. The

presence of the inorganic elements Au, Fe, and Mn or Co was confirmed by EDXS (figure 13 B). Micrographs of the glyconanoparticles under negative staining (figure 13 D) show a light area surrounding each nanoparticle corresponding to the carbohydrate coating. AFM images (figure 13 E-G) of these nanoparticles also show well-defined and monodisperse population of particles. Chemical analysis using inductively coupled plasma atomic emission spectroscopy (ICP-OES) showed a Mn:Fe and Co:Fe ratio close to 1:2 (Table 2).

Table 2. ICP-OES analysis results from the three different nature *glyco*-nanoferrites.

ICP-OES analysis	Fe	Mn	Co	Au
Fe₃O₄@Au@LactC₁₁/Linker	3.69 %	0 %	0 %	96.31 %
MnFe₂O₄@Au@LactC₁₁/Linker	6.04 %	2.54 %	0 %	91.42 %
CoFe₂O₄@Au@LactC₁₁/Linker	6.72 %	0 %	2.87 %	90.43 %

Magnetic characterization of water soluble magnetic *glyco*-nanoferrites. All the nanoparticles here prepared had, as expected, a superparamagnetic nature. The magnetization hysteresis of water-soluble *glyco*-XFe₂O₄@Au nanoferrites were similar to those of the non-soluble XFe₂O₄ when referred to the content of magnetic material (Fe or Fe+Mn or Co) (figure 14 A, B). This is in contrast with the results obtained by other authors where a decrease in the maximum magnetization values were observed [47]. The blocking temperatures of the gold coated *glyco*-ferrites have slightly lower values than those for the non-coated ferrites (25 K for MnFe₂O₄ vs 22 K for MnFe₂O₄@Au@LactC₁₁/Linker, Figure 14, C). This same effect has been observed by other authors [47] [68], and can be explained in terms of a decrease in the coupling of the magnetic moments as a result of the increased interparticle spacing of the magnetic cores.

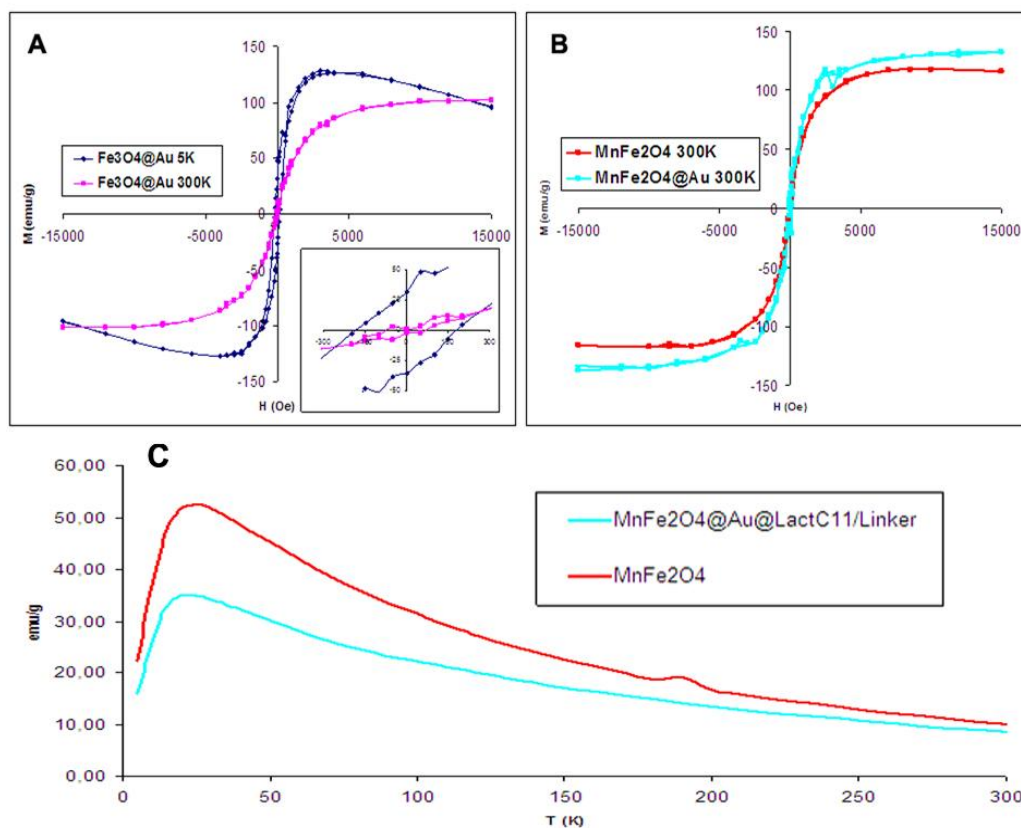


Figure 14. A, magnetic hysteresis of $\text{Fe}_3\text{O}_4@Au@LactC_{11}/Linker$ at low temperature (blue) and at room temperature (pink). **Inset**, enlarged view of the graph from -300 to 300 Oe and -50 and 50 emu/g. B, magnetic hysteresis of MnFe_2O_4 and $\text{MnFe}_2\text{O}_4@Au@LactC_{11}/Linker$ at room temperature. C, comparison of blocking temperature (T_B) for MnFe_2O_4 (red) and $\text{MnFe}_2\text{O}_4@Au@LactC_{11}/Linker$ (blue) at $H = 100$ Oe.

Relaxivity values determination. In order to test the potential of *glyco*-nanoferrites as contrast agents in magnetic resonance imaging (MRI), the longitudinal T_1 and transversal T_2 relaxation times of the 100 % and the hybrid nanoparticle probes were measured and their relaxivity (slope of $1/T$ versus Fe concentration mM) r_1 and r_2 calculated (table 3). In general, these new glyconanoparticles exhibit relaxivity values in the range of commercially available contrast agents or even superior as it is the case of $\text{Fe}_3\text{O}_4@Au@LactC_{11}/Linker$ and $\text{MnFe}_2\text{O}_4@Au@LactC_{11}/Linker$ (table 3). The observed relaxivity values order between the *glyco*-ferrites is $\text{MnFe}_2\text{O}_4@Au > \text{Fe}_3\text{O}_4@Au > \text{CoFe}_2\text{O}_4@Au$ as expected, although the difference between MnFe_2O_4 and Fe_3O_4 was expected to be more significant. Comparison of the r_2 values for the hybrid $\text{Fe}_3\text{O}_4@Au@LactC_{11}/Linker$ nanoparticles and $\text{Fe}_3\text{O}_4@Au@LactC_5$ or

Results and Discussion

$\text{Fe}_3\text{O}_4@Au@Linker$ revealed no contribution of the ligands or ligand density on the final relaxivities.

Table 3. Relaxivity values of commercially available nanoparticle-based MRI contrast agents and the new prepared water-soluble $glyco\text{-Fe}_3\text{O}_4@Au$, $\text{-MnFe}_2\text{O}_4@Au$, and $\text{-CoFe}_2\text{O}_4@Au$ measured in 10 mM PBS pH 7.4 buffer at 25 °C and 1.47 Tesla.

Name	Magnetic Core size (nm)	Total size (nm)	Coating material	$r_1^{[a]}$ [$\text{mM}^{-1}\text{s}^{-1}$]	$r_2^{[a]}$ [$\text{mM}^{-1}\text{s}^{-1}$]	B (T)
AMI-25 (Feridex; Endorem) [38]	5-6	80-150	Dextran	$10^{[b]}$	Ca. 100/91 ^[b]	1.47
SHU 555A (Resovist) [69]	ca. 4.2	ca. 62	Carbodextran	--	151	0.47
AMI-227, (Sinerem) [70]	4-6	20-40	Dextran	--	53	0.47
CLIO, MION [14]	ca. 2.8	10-30	Dextran	--	ca. 69	1.47
$\text{Fe}_3\text{O}_4@Au$	3.2	12 ^[c]	LactC ₅	10	155	1.47
$\text{Fe}_3\text{O}_4@Au$	3.2	12 ^[c]	Linker	10	158	1.47
$\text{Fe}_3\text{O}_4@Au$	3.2	12 ^[c]	LactC ₁₁ /Linker	11	157	1.47
$\text{MnFe}_2\text{O}_4@Au$	6.1	20 ^[c]	LactC ₁₁ /Linker	4	183	1.47
$\text{CoFe}_2\text{O}_4@Au$	6.2	19 ^[c]	LactC ₁₁ /Linker	2	66	1.47
$\text{Fe}_3\text{O}_4@Au$	4.5	11.6	LactC ₁₁ /Linker	1	52	1.47

[a] r values are variable depending on the field strength and MR pulse sequences.

[b] This value has been measured by us.

[c] Calculated values from metallic core sizes as measured by TEM plus the calculated size of the ligands.

Surprisingly, the relaxivity values r_1 and r_2 from the glyconanoparticles with bigger Fe_3O_4 magnetic core resulted much worse than those from smaller nanoparticles. This supports the idea that size is not the only factor that affects the final performance of iron oxide nanoparticles as contrast agent (Figure 15) [44]. Relaxivity r_2 values are strongly related to the magnetic moment of the nanoparticles. This magnetic moment is dependent not only on the size, but also on the composition and the magneto-crystalline phase of the nanocrystals. Therefore, trying to modify only one of these parameters without careful control of the rest can lead to unexpected results.

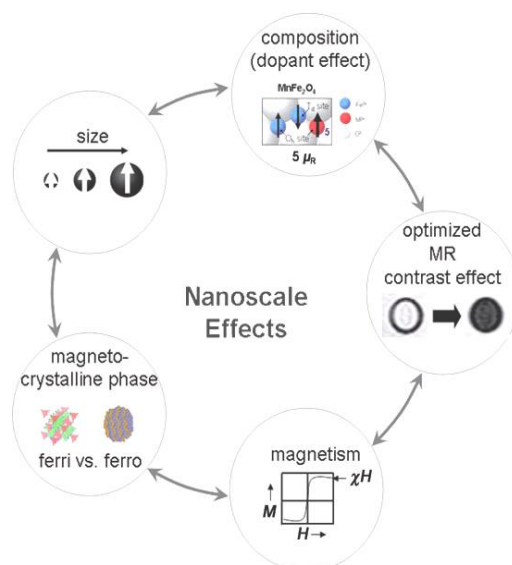


Figure 15. Important parameters of MNPs for MR contrast-enhancement effects. Taken from ref. [44]

Evaluation of the cytotoxicity and internalization behaviour of water soluble magnetic glyco-nanoferrites. With the idea to apply the glyco-ferrites as contrast agents for in vivo labelling of progenitor and tumour cells, the cytotoxicity of selected $Fe_3O_4@Au$ glyconanoparticles was tested by evaluating the viability of rat glioma C6 cellular line after 3 days culture in the presence of increasing concentrations of the glyco-ferrites by a MTT assay [71]. None of the glyco-ferrites tested showed cytotoxicity even at $100 \mu g/mL$ concentration (figure 16).

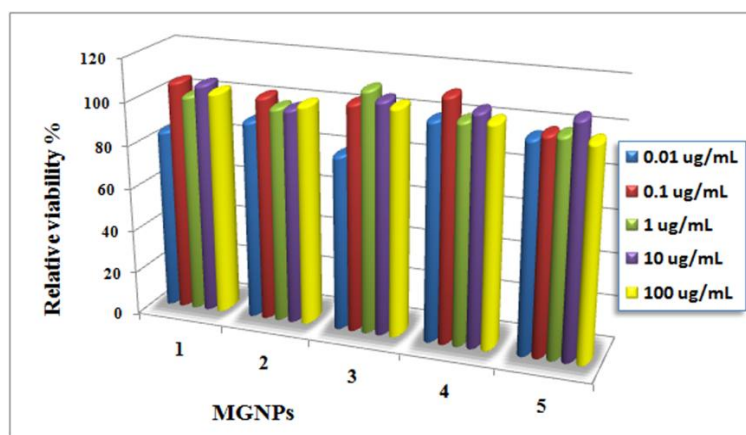


Figure 16. Viability of C6 cells incubated for 72 hours at $37^\circ C$ with increasing concentrations of: 1: $Fe_3O_4@Au@GlcC_5$. 2: $Fe_3O_4@Au@LactC_{11}/Linker$. 3: $Fe_3O_4@Au@Linker$. 4: $Fe_3O_4@Au@LactC_5/Linker$. 5: $Fe_3O_4@Au@GlcNAcC_{11}/Linker$, as measured by MTT assays.

Results and Discussion

The discrete sugar molecules capping the magnetic nanoparticles provide two major requirements for the successful integration of the nanoparticles in biological media, i.e. small nanoparticle size (core 6 nm, sugars 1.3 nm), minimization of non-specific adsorptions that may drastically reduce the efficiency of molecular recognition processes, and the avoidance of immunogenic responses. At the same time, different carbohydrate binding proteins (lectins, selectins) present on the cell membrane can recognize the multivalent presentation of the carbohydrate molecules [72] [73]. A significant advantage of the presence of sugars on the cluster surface is an easier uptake of the nanoclusters by cells related to nanoclusters capped with synthetic polymers. MGNPs capped with lactose glycoconjugate are internalized by C33 cells in 1 hour at 37 °C, while MGNPs functionalized only with the carboxylic linker were not able to enter the cells under the same conditions as indicated by silver staining (Figure 17).

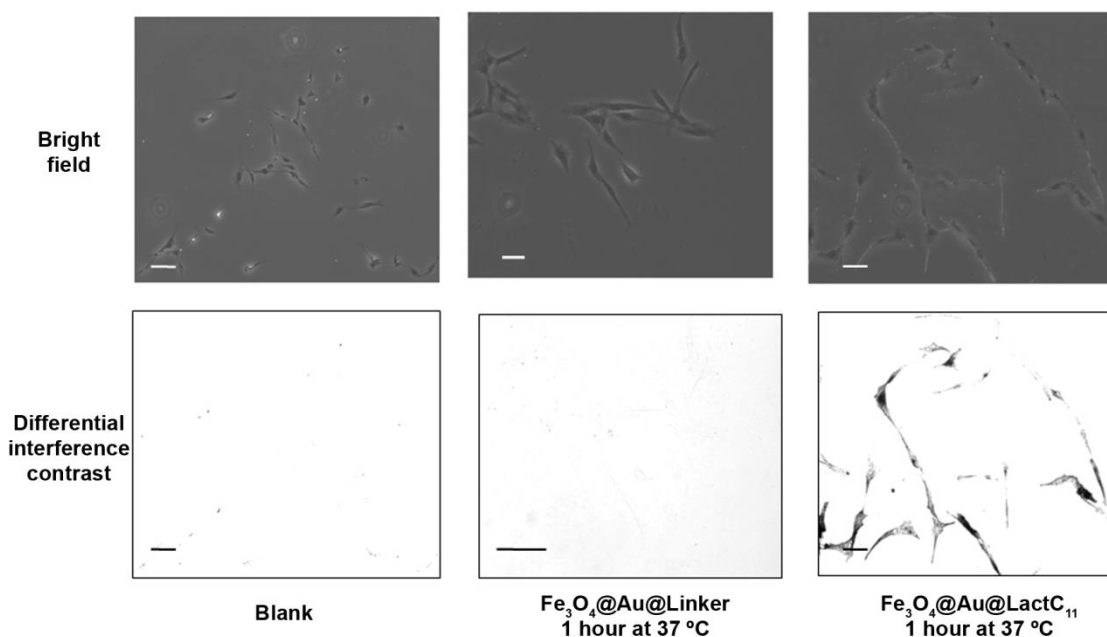











Figure 17. Differential interference contrast and bright field optical images of silver staining of C33 cells incubated (from left to right) without MGNPs; with 25 $\mu\text{g/mL}$ of $\text{Fe}_3\text{O}_4\text{@Au@Linker}$, and with 25 $\mu\text{g/mL}$ of $\text{Fe}_3\text{O}_4\text{@Au@LactC}_{11}$ for 1 hour at 37 °C.

Evaluation of water soluble magnetic *glyco*-nanoferrites as magnetic resonance imaging contrast agents. The efficiency of some selected *glyco*-ferrites as contrast agent by phantom imaging at 11.7 T was also tested. The T_2 -weighted MRI images at two different concentrations (250, 62.5 μM in Fe) are shown in table 4. The results confirm that the glyconanoparticles at the lowest concentration enhance significantly the

Results and Discussion

contrast and that this enhancement is similar for the different *glyco*-ferrites as indicated by the T_2 values obtained under this conditions (281.07 ms for $\text{MnFe}_2\text{O}_4@Au@LactC_{11}/\text{Linker}$, 240.07 ms for $\text{Fe}_3\text{O}_4@Au@LactC_{11}/\text{Linker}$, and 295.19 ms for $\text{CoFe}_2\text{O}_4@Au@LactC_{11}/\text{Linker}$).

Table 4. T_2 -weighted MRI images of phantoms from the three different *glyco*-ferrites in 10 mM PBS pH 7.4 buffer at 21 °C and 11.7 Ts.

	250 μM^*	62.5 μM^*	0.00 μM^*
$\text{MnFe}_2\text{O}_4@Au@LactC_{11}/\text{Linker}$			
$\text{Fe}_3\text{O}_4@Au@LactC_{11}/\text{Linker}$			
$\text{CoFe}_2\text{O}_4@Au@LactC_{11}/\text{Linker}$			

*concentrations referred to magnetic material.

Conclusion

To sum up, until here we have described a synthetic pathway and characterization protocols to get monodispersed water-soluble core@shell $X\text{Fe}_2\text{O}_4@Au$ nanoparticles ($X = \text{Fe}, \text{Mn}, \text{or Co}$) capped with carbohydrates and functional linkers (*glyco*-nanoferrites). We have also demonstrated the bimetallic nature of our hetero-nanoparticles in an unequivocal way using TEM-related techniques. The ferrite core and the gold coating are in the same nanoparticle working in a cooperative way: the ferrite provides the magnetic properties and the gold supplies biocompatibility, protection from further oxidation of the magnetic core and the possibility to attach ligands for specific targeting in a simple way without reducing the magnetization values or the relaxivity rates. From the point of view of their future application as magnetic resonance imaging (MRI) probes, carbohydrates on the surface protect the nanocrystals from aggregation and nonspecific biomolecular interactions better than other ligands and can provide targeted recognition for different proteins (lectins) at the cell surface involved in important pathological processes (inflammation, infection, etc.). The control of size, nucleation of hybrid materials, crystallinity and surface functionalization is an important

feature to achieve the best results in the generation of new magnetic probes with improved properties as contrast agents for MRI. The properties shown by the *glyco-ferrites* validate them as potential contrast agents for in vivo imaging. In addition, the carboxyl group of the linker provides the functionality for further attaching biomolecules onto the shell surface.

References

1. LaVan D.A., L.D.M., Langer R., *Moving smaller in drug discovery and delivery*. Nat. Rev. Drug Discov., 2002. **1**: p. 77-84.
2. Chan W C, M.D.J., Gao X, Bailey R E, Han M., Nie S., *Luminescent QDs for multiplexed biological detection and imaging*. Curr. Opin. Biotechnol., 2002. **13**(1): p. 40-46.
3. Niemeyer, C.M., *Nanoparticles, proteins, and nucleic acids: biotechnology meets materials science*. Angew. Chem. Int. Ed., 2001. **40**(22): p. 4128-4158.
4. Hamad-Schifferli K., S.J.J., Santos A.T., Zhang S., Jacobson J.M., *Remote electronic control of DNA hybridization through inductive coupling to an attached metal nanocrystal antenna*. Nature, 2002. **415**: p. 152-155.
5. Clapp A.R., M.I.L.J., Mauro M., Fisher B.R., Bawendi M.G., Mattoussi H., *Fluorescence resonance energy transfer between QD donors and dye-labelled protein acceptors*. J. Am. Chem. Soc., 2004. **126**: p. 301-310.
6. Chan W.C., N.S., *Quantum dot bioconjugates for ultrasensitive nonisotopic detection*. Science, 1998. **281**: p. 2016-2018.
7. Pathak S., C.S.K., Arnheim N., Thompson M.E., *Hydroxylated quantum dots as luminescent probes for in situ hybridization*. J Am Chem Soc, 2001. **123**: p. 4103-4104.
8. Mirkin C.A., L.R.L., Mucic R.C., Storhoff J.J., *A DNA-based method for rationally assembling nanoparticles into macroscopic materials*. Nature, 1996. **382**: p. 607-609.
9. Alivisatos A.P., J.K.P., Peng X., Wilson T.E., Loweth C.J., Bruchez M.P., Schultz P.G., *Organization of nanocrystal molecules using DNA*. Nature, 1996. **382**: p. 609-611.
10. Meldrum F.C., H.B.R., Mann S., *Magnetoferritin: in vitro synthesis of a novel magnetic protein*. Science, 1992. **257**: p. 522-523.
11. Bulte J.W., D.T., Mann S., Frankel R.B., Moskovitz B.M., Brooks R.A., Baumgarner C.D., Vymazal J., Strub M.P., Frank J.A., *Magnetoferritin: characterization of a novel superparamagnetic MR contrast agent*. J. Magn. Reson. Imaging, 1994. **4**: p. 497-505.
12. Li Z., W.L., Gao M Y, Lei H, Adv. Mater. 2005, 17, 1001-1005, *One-pot reaction to synthesize biocompatible magnetite nanoparticles*. Adv. Mater., 2005. **17**: p. 1001-1005.
13. Hu F.Q., W.L., Zhou Z., Ran Y.L., Li M., Gao M.Y., *Preparation of biocompatible magnetite nanocrystals for in vivo magnetic resonance detection of cancer*. Adv. Mater., 2006. **18**(19): p. 2553-2556.

Results and Discussion

14. Josephson, L., et al., *High-efficiency intracellular magnetic labeling with novel superparamagnetic-Tat peptide conjugates*. *Bioconjug Chem*, 1999. **10**(2): p. 186-91.
15. Bulte J.W.M., D.T., Witwer B., Zhang S.C., Strable E., Lewis B.K., Zywicke H., Miller B., van Gelderen P., Moskowitz B.M., Duncan I.D., Frank J.A. , *Magnetodendrimers allow endosomal magnetic labelling and in vivo tracking of stem cells*. *Nat. Biotechnol.*, 2001. **19**(12): p. 1141-1147.
16. Bulte J.W., K.D.L., *Iron oxide MR contrast agents for molecular and cellular imaging*. *NMR Biomed.*, 2004. **17**: p. 484-499.
17. William W.Y., F.J.C., Cafer T.Y., Colvin V., *Synthesis of monodisperse iron oxide nanocrystals by thermal decomposition of iron carboxylate salts*. *Chem. Commun.*, 2004: p. 2306-2307.
18. Rockenberger J., S.E.C., Alivisatos A.P., *Single-precursor approach to surfactant-capped nanocrystals of transition metal oxides*. *J. Am. Chem Soc.*, 1999. **121**: p. 11595-11596.
19. Hyeon, T., et al., *Synthesis of highly crystalline and monodisperse maghemite nanocrystallites without a size-selection process*. *J Am Chem Soc*, 2001. **123**(51): p. 12798-801.
20. Cheon J, K.N.-J., Lee S-M, Lee J-H, Yoon J-H, Oh S J., *Shape evolution of single-crystalline iron oxide nanocrystals*. *J. Am. Chem Soc.*, 2004. **126**: p. 1950-1951.
21. Sun, S., et al., *Monodisperse MFe₂O₄ (M = Fe, Co, Mn) nanoparticles*. *J Am Chem Soc*, 2004. **126**(1): p. 273-9.
22. Sun S., Z.H., *Size-controlled synthesis of magnetite nanoparticles*. *J. Am. Chem Soc.*, 2002. **124**: p. 8204-8205.
23. Yin M S, O.B., *Synthesis of monodisperse nanocrystals of manganese oxides*. *J. Am. Chem Soc.*, 2003. **125**: p. 10180-10181.
24. Bloch F., H.W.W., Packard M., *Nuclear induction*. *Phys. Rev.*, 1946. **69**: p. 127.
25. Purcell E.M., T.H.C., Pound R.V., *Resonance absorption by nuclear magnetic moments in a solid*. *Phys. Rev.*, 1946. **69**: p. 37.
26. Lauterbur P.C., M.-D.M., Rudin A.M., *Augmentation of tissue water proton spin-lattice relaxation rates by in vivo addition of paramagnetic ions*. *Frontiers of biological energetics*, 1978. **1**: p. 752.
27. Lauterbur, P.C., *Image Formation by Induced Local Interactions: Examples Employing Nuclear Magnetic Resonance*. *Nature*, 1973. **242**(5394): p. 190-191.
28. Lauterbur, P.C., *Magnetic resonance zeugmatography*. *Pure Appl. Chem.*, 1974. **40**(1-2): p. 149-157.
29. Rinck, P.A., *Magnetic resonance in medicine*. Blackwell Publishing Incorporated, 2001: p. 252.
30. Merbach A.E., T.E., *The Chemistry of Contrast Agents in Medical Magnetic Resonance*. John Wiley & Son, Ltd.: West Sussex, 2001.
31. Okuhata, Y., *Delivery of diagnostic agents for magnetic resonance imaging*. *Adv Drug Deliv Rev*, 1999. **37**(1-3): p. 121.
32. Leslie LaConte, N.N., Gang Bao, *Magnetic nanoparticle probes*. *Nanotoday*, 2005. **may**: p. 32-38.

Results and Discussion

33. Ohgushi M., N.K., Wada A., *Dextran-magnetite: A new relaxation reagent and its application to T2 measurements in gel systems*. J. Magn. Reson. Imaging, 1978. **29**(3): p. 599.
34. Mendonca Dias H., L.P.C., *Ferromagnetic particles as contrast agents for magnetic resonance imaging of liver and spleen*. Magn. Reson. Med., 1986. **3**(2): p. 328.
35. Renshaw P.F., O.C.S., McLaughlin A.C., Frey T.G., Leigh J.S., *Ferromagnetic contrast agents: A new approach*. Magn. Reson. Med., 1986. **3**(2): p. 217.
36. Olsson M.B.E., P.B.R.B., Salford L.G., Schroder U., *Ferromagnetic particles as contrast agent in T2 NMR imaging*. Magn. Reson. Imag., 1986. **4**(5): p. 437.
37. Saini S., S.D.D., Hahn P.F., Wittenberg J., Brady T.J., Ferrucci J.T., *Ferrite particles: a superparamagnetic MR contrast agent for the reticuloendothelial system*. Radiology, 1987. **162**(1): p. 211.
38. Weissleder, R., et al., *Superparamagnetic iron oxide: pharmacokinetics and toxicity*. AJR Am J Roentgenol, 1989. **152**(1): p. 167-73.
39. Weissleder R., E.G., Wittenberg J., Rabito C.A., Bengele H.H., Josephson L., *Ultrasmall superparamagnetic iron oxide: characterization of a new class of contrast agents for MR imaging*. Radiology, 1990. **175**(2): p. 489.
40. Cerdan S., R.H., Künnecke L.B., Seelig J., *Monoclonal antibody-coated magnetite particles as contrast agents in magnetic resonance imaging of tumours*. Magn. Reson. Med., 1989. **12**(2): p. 151.
41. Shen T., W.R., Papisov M., Bogdanov A., Brady T., *Monocrystalline iron oxide nanocompounds (MION): Physicochemical properties*. Magn. Reson. Med., 1993. **29**: p. 599.
42. Frank H., W.R., Brady T.J., *Enhancement of MR angiography with iron oxide: preliminary studies in whole-blood phantom and in animals*. Am. J. Roentgenol., 1994. **162**(1): p. 209.
43. Weissleder R., R.P., Lee A.S., Wittenberg J., Brady T.J., *MR receptor imaging: ultrasmall iron oxide particles targeted to asialoglycoprotein receptors*. Am. J. Roentgenol., 1990. **155**(6): p. 1161.
44. Jun, Y.W., J.H. Lee, and J. Cheon, *Chemical design of nanoparticle probes for high-performance magnetic resonance imaging*. Angew Chem Int Ed Engl, 2008. **47**(28): p. 5122-35.
45. Cheon J., S.J.W., Lee J.H., *Preparation method of magnetic and metal oxide nanoparticles*. Korea Patent, 2004. **PCT WO2006/052042**.
46. Song, Q. and Z.J. Zhang, *Shape control and associated magnetic properties of spinel cobalt ferrite nanocrystals*. J Am Chem Soc, 2004. **126**(19): p. 6164-8.
47. Wang, L., et al., *Monodispersed core-shell Fe₃O₄@Au nanoparticles*. J Phys Chem B, 2005. **109**(46): p. 21593-601.
48. Lee, J.H., et al., *Artificially engineered magnetic nanoparticles for ultra-sensitive molecular imaging*. Nat Med, 2007. **13**(1): p. 95-9.
49. Markov, I.V., *Crystal Growth for Beginners: Fundamentals of Nucleation, Crystal Growth, and Epitaxi*. Word scientific, Singapore, 2003.
50. Xu, Z., Y. Hou, and S. Sun, *Magnetic core/shell Fe₃O₄/Au and Fe₃O₄/Au/Ag nanoparticles with tunable plasmonic properties*. J Am Chem Soc, 2007. **129**(28): p. 8698-9.

Results and Discussion

51. Han, Y., et al., *Reverse microemulsion-mediated synthesis of silica-coated gold and silver nanoparticles*. Langmuir, 2008. **24**(11): p. 5842-8.
52. Li J., Z.H., Sun S., Liu J.P., Wang Z.L., *Analyzing the Structure of CoFe-Fe₃O₄ Core-Shell Nanoparticles by Electron Imaging and Diffraction*. J. Phys. Chem. B, 2004. **108**: p. 14005-14008.
53. Liu, H.L., et al., *Synthesis of streptavidin-FITC-conjugated core-shell Fe₃O₄-Au nanocrystals and their application for the purification of CD₄⁺ lymphocytes*. Biomaterials, 2008. **29**(29): p. 4003-11.
54. Zhao, X., et al., *Preparation of Alkanethiolate-Functionalized Core/Shell Fe₃O₄@Au Nanoparticles and Its Interaction with Several Typical Target Molecules*. Anal Chem, 2008.
55. Casavola M., B.R., Caputo G., Cozzoli P.D., *Colloidal Strategies for Preparing Oxide-Based Hybrid Nanocrystals*. Eur. J. Inorg. Chem. , 2008: p. 837-854.
56. Shevchenko, E.V.B., M.I.; Kovalenko, M.V.; Talapin, D.V.; Smith, R.K.; Aloni, S.; Heiss, W.; Alivisatos, A.P., *Gold/Iron Oxide Core/Hollow-Shell Nanoparticles*. Advanced materials, 2008. **20**(22): p. 4323-4329.
57. Shi, W., et al., *A general approach to binary and ternary hybrid nanocrystals*. Nano Lett, 2006. **6**(4): p. 875-81.
58. Z.Y. Li, J.Y., Y. Chen, R.E. Palmer, J.P. Wilcoxon, *Direct Imaging of Core-Shell Structure in Ag-Au Nanoparticles*. Microsc Microanal, 2005. **11**(2): p. 1450-1451.
59. Dutta D., S.G., Manna P.K., Tyagi A.K., Yusuf S.M., *Room temperature ferromagnetism in CoO nanoparticles obtained from sonochemically synthesized precursors*. Nanotechnology, 2008. **19**: p. 7.
60. Zhang, J., et al., *Laser-assisted synthesis of superparamagnetic Fe@Au core-shell nanoparticles*. J Phys Chem B, 2006. **110**(14): p. 7122-8.
61. Alayoglu, S. and B. Eichhorn, *Rh-Pt bimetallic catalysts: synthesis, characterization, and catalysis of core-shell, alloy, and monometallic nanoparticles*. J Am Chem Soc, 2008. **130**(51): p. 17479-86.
62. Karel Lambert, B.D.G., Iwan Moreels, and Zeger Hens, *PbTe/CdTe Core/Shell Particles by Cation Exchange, a HR-TEM study*. Chem. Mater., 2009. **21** (5): p. 778-780.
63. Bao, N., et al., *A facile thermolysis route to monodisperse ferrite nanocrystals*. J Am Chem Soc, 2007. **129**(41): p. 12374-5.
64. Baldi, G., et al., *Cobalt ferrite nanoparticles: The control of the particle size and surface state and their effects on magnetic properties*. Journal of magnetism and magnetic materials, 2007. **311**: p. 10-16.
65. Zhichuan Xu, C.S., Yanglong Hou, Hongjun Gao, Shouheng Sun, *Oleylamine as Both Reducing Agent and Stabilizer in a Facile Synthesis of Magnetite Nanoparticles*. Chem. Mater., 2009. **21**(9): p. 1778-1780.
66. He J., G.I., Gallo J., Penades S., *A step-heating procedure for the synthesis of high-quality FePt nanostars*. Cryst. Eng. Comm., 2009. **11**: p. 2605-2607.

Results and Discussion

67. Shukla, N., et al., *FTIR study of surfactant bonding to FePt nanoparticles*. J. magn. magn. mater., 2003. **266**(1-2): p. 178-184.
68. Boal A.K., F.B.L., Uzun O., Tuominen M., Rotello V.M., *Modulation of spacing and magnetic properties of iron oxide nanoparticles through polymer mediated "bricks and mortar" self assembly*. Chem. Mater., 2004. **16**(17): p. 3252-3256.
69. Reimer, P., et al., *Clinical results with Resovist: a phase 2 clinical trial*. Radiology, 1995. **195**(2): p. 489-96.
70. Jung, C.W. and P. Jacobs, *Physical and chemical properties of superparamagnetic iron oxide MR contrast agents: ferumoxides, ferumoxtran, ferumoxsil*. Magn Reson Imaging, 1995. **13**(5): p. 661-74.
71. Mosmann, T., *Rapid colorimetric assay for cellular growth and survival: application to proliferation and cytotoxicity assays*. J Immunol Methods, 1983. **65**(1-2): p. 55-63.
72. de La Fuente, J.M., et al., *Gold Glyconanoparticles as Water-Soluble Polyvalent Models To Study Carbohydrate Interactions*. Angew Chem Int Ed Engl, 2001. **40**(12): p. 2257-2261.
73. Barrientos, A.G., et al., *Modulating glycosidase degradation and lectin recognition of gold glyconanoparticles*. Carbohydr Res, 2009. **344**(12): p. 1474-8.

Experimental part

Materials and methods

All nanocrystals were characterized before and after any step by low and high resolution TEM on a JEOL JEM 2100F microscope and the composition analysis were done by energy dispersive X-ray detector (EDX) (Oxford INCA system) and by ICP-OES (IRIS ADVANTAGE, Termo Jarrell Ash). Magnetic data from the nanoparticles were recorded with a QD magnetometer MPMS-7T. UV-Vis spectra were recorded in a Beckman-Coulter DU 800 spectrophotometer. FT-IR spectra were acquired in a Thermo Nicolet FT-IR spectrometer. ^1H NMR spectra were obtained in a Bruker 500 NMR spectrometer. Relaxivities were measured in a Bruker Minispec mq60 instrument operating at 1.47 T. MRI images were acquired in a Bruker Biospec 11.7 T with a 9 cm gradient capable of delivering 740 mT/m. Z-measurements were obtained in a Malvern Zetasizer Nano ZS. AFM images were acquired in a VEECO multimode/nanoscope IV instrument. All the chemical reagents except gold(III) acetate (99,9 % from Alfa Aesar) were purchased from Sigma-Aldrich. All solvents were analysis grade (acetone, dichloromethane, methanol, hexane and 2-propanol) and were supplied by Sharlab. All the reagents were used as received without further purification. C_5 carbohydrate derivatives were already prepared in the laboratory.

Standard preparation of $\text{Fe}_3\text{O}_4@Au$ nanoparticles

Synthesis of 4 nm Fe_3O_4 nanoparticles as magnetic seeds [1]. A thermal decomposition method was followed to synthesize these seeds. Briefly, oleic acid (6 mmol), oleylamine (6 mmol), 1,2-hexadecanediol (10 mmol), and $\text{Fe}(\text{acac})_3$ (2 mmol) were mixed into 20 mL of phenyl ether. The solution was heated, with vigorous magnetic stirring, with reflux and under Ar atmosphere in two steps: the first at 200 °C during 30 min, and the second another 30 min at 265 °C. The resulting solution had a dark brown colour. After cooling down to room temperature, 40 mL of ethanol were added into the solution to precipitate the MNPs. The nanoparticles were separated magnetically, washed 3 times with ethanol, and kept resuspended in 75 mM oleic acid and 75 mM oleylamine hexane until further use.

Experimental Part

Metallic core size (as measured by TEM) = 3.2 nm

Total size (as measured by Zsizer, 10 mM PBS pH 7.4) = 5.61 nm

UV-Vis (Hexane) = no surface plasmon resonance peak

FT-IR (ATR) = 2922.4, 2852.6 1559.2 1465.4, 1403.3 cm^{-1} .

Gold coating of 4 nm Fe_3O_4 nanoparticles [2]. In a typical synthesis, oleic acid (1.5 mmol), oleylamine (6mmol), 1,2-hexadecanediol (12 mmol), $\text{Au}(\text{OAc})_3$ (0.55 mmol) and 10 mL of the solution of magnetic cores, were mixed into 30 mL of phenyl ether. This solution was heated under vigorous stirring, Ar atmosphere, and reflux, at 190 °C during 90 min. After this procedure the solution changed its colour from dark brown to dark purple.

The purification and storage was performed as above.

The stoichiometry between the Fe and the Au reagents was varied to obtain different thickness of the outer shell.

- Stoichiometry Fe:Au 1:7

Metallic core size (as measured by TEM) = 5.8 nm

Total size (as measured by Zsizer, 10 mM PBS pH 7.4) = 11.22 nm

UV-Vis (Hexane) = surface plasmon resonance peak at 530 nm

FT-IR (ATR) = 2922.3, 2850.7, 1562.3, 1104.3, 801.2 cm^{-1}

ICP-OES \Rightarrow Fe = 3.7 %; Au = 96.3 %

- Stoichiometry Fe:Au 1:1.75

UV-Vis (Hexane) = surface plasmon resonance peak at 526 nm

FT-IR (ATR) = 2921.9, 2852.5, 1559.3, 1465.2, 1401.2, 722.3 cm^{-1}

- Stoichiometry 1:0.5 (incomplete gold coating)

UV-Vis (Hexane) = surface plasmon resonance peak at 513 nm

FT-IR (ATR) = 2919.3, 2851.4, 1720.2, 1462.9, 1100.1 cm^{-1}

Synthesis of $\text{Au}@\text{Fe}_3\text{O}_4$ nanoparticles. Briefly, oleic acid (6 mmol), oleylamine (6 mmol), 1,2-hexadecanediol (10 mmol), $\text{Fe}(\text{acac})_3$ (2 mmol) and $\text{Au}(\text{Ac})_3$ (0.55 mmol) were mixed into 20 mL of phenyl ether. The solution was heated, with vigorous

Experimental Part

magnetic stirring, with reflux and under Ar atmosphere in two steps: the first at 200 °C during 30 min, and the second another 30 min at 265 °C. The resulting solution was cooled down to room temperature and purified like before. In a final step, the sample was centrifuged at 13400 rpm for 30 min. and the supernatant was discarded. The pellet was resuspended in 75 mM oleic acid and 75 mM oleylamine solution of hexane.

Metallic core size (as measured by TEM) \Rightarrow Au = 5.0 nm; Au@Fe₃O₄ = 9.5 nm

UV-Vis (Hexane) = no surface plasmon resonance peak

FT-IR (ATR) = 2912.5, 2853.4, 1700.9, 1464.4, 1409.1, 1243.5 cm⁻¹

Preparation of XFe₂O₄@Au nanoparticles

Synthesis of 6 nm CoFe₂O₄ and MnFe₂O₄ magnetic nanoparticles [1]. In a typical reaction, Fe(acac)₃ (1 mmol), Co(acac)₂ (0.5 mmol) or Mn(acac)₂ (5.0 mmol), 1,2 hexadecanediol (7.5 mmol), oleic acid (4.5 mmol), and oleylamine (4.5 mmol) were added into 15 mL of benzyl ether in a two necked flask with reflux system. This mixture was argonized while stirring for 20 min and after that, this heating protocol was followed: 200 °C for 2 h, 300 °C for 1 h and slow cooling down to room temperature. The purification and storage was performed as above.

- CoFe₂O₄

Metallic core size (as measured by TEM) = 6.2 nm

UV-Vis (Hexane) = no surface plasmon resonance peak

FT-IR (ATR) = 2922.3, 2850.9, 1462.4, 1410.6, 795.5 cm⁻¹

- MnFe₂O₄

Metallic core size (as measured by TEM) = 6.1 nm

UV-Vis (Hexane) = no surface plasmon resonance peak

FT-IR (ATR) = 2921.4, 2852.1, 1459.3, 1411.6, 1379.0, 793.5 cm⁻¹

Gold coating of XFe₂O₄ nanoparticles. 0.5 mL of either nanocrystal were added into 5 mL of phenyl ether with oleic acid (1 mmol) in a three necked flask. This mixture was argonized for 20 min while rising the temperature to 190 °C. Once at this temperature, a mixture of Au(Ac)₃ (0.25 mmol for CoFe₂O₄, and 0.19 mmol for MnFe₂O₄) and

Experimental Part

oleylamine (6 mmol) in phenyl ether (13 mL) was added drop by drop into the mixture. After the addition the temperature was maintained at 190 °C for 1.5 h, and then slowly cooled down to room temperature. The same procedure as above was used for the purification and the storage of these products.

- **CoFe₂O₄@Au**

Metallic core size (as measured by TEM) = 12.5 nm

UV-Vis (Hexane) = surface plasmon resonance peak at 537 nm

FT-IR (ATR) = 2920.2, 2851.3, 1710.5, 1459.7, 1409.6 cm⁻¹

ICP-AES ⇒ Co = 2.9 %; Fe = 6.7 %; Au = 90.4 %

- **MnFe₂O₄@Au**

Metallic core size (as measured by TEM) = 13.5 nm

UV-Vis (Hexane) = surface plasmon resonance peak at 524 nm

FT-IR (ATR) = 2919.3, 2852.2, 1465.4, 1411.8, 796.3 cm⁻¹

ICP-AES ⇒ Mn = 2.5 %; Fe = 6.1 %; Au = 91.4 %

Synthesis of Au@MnFe₂O₄ nanoparticles. Briefly, oleic acid (4.5 mmol), oleylamine (4.5 mmol), 1,2-hexadecanediol (7.5 mmol), Fe(acac)₃ (1 mmol), Mn(acac)₂ (0.5 mmol) and Au(Ac)₃ (0.75 mmol) were mixed into 15 mL of benzyl ether. The solution was heated, with vigorous magnetic stirring, with reflux and under Ar atmosphere in two steps: the first at 200 °C during 2 hours, and the second another hour at 300 °C. The resulting solution was cooled down to room temperature and purified like before. The final product was resuspended in 75 mM oleic acid and 75 mM oleylamine solution of hexane.

Metallic core size (as measured by TEM) ⇒ Au = 3.8 nm; Au/Fe₃O₄ = 12.2 nm, flower-like structure.

UV-Vis (Hexane) = no surface plasmon resonance peak

FT-IR (ATR) = 2910.2, 2849.4, 1712.5, 1459.6, 1409.7, 1245.5 cm⁻¹

Preparation of bigger size Fe₃O₄@Au nanoparticles

Experimental Part

Synthesis of 6 nm Fe₃O₄ magnetic nanoparticles [1]. Briefly, oleic acid (6 mmol), oleylamine (6 mmol), 1,2-hexadecanediol (10 mmol), and Fe(acac)₃ (2 mmol) were mixed into 20 mL of benzyl ether. The solution was heated, with vigorous magnetic stirring, with reflux and under Ar atmosphere in two steps: the first at 200 °C during 150 min, and the second another 60 min at 300 °C. The resulting solution had a dark brown colour.

After cooling to room temperature, 40 mL of ethanol were added into the solution to precipitate the MNPs. The nanoparticles were separated magnetically, washed 3 times with ethanol, and kept resuspended in 75 mM oleic acid and 75 mM oleylamine hexane until further use.

Metallic core size (as measured by TEM) ⇒ different populations centred at 2.8, 6.0 and 10.0 nm

UV-Vis (Hexane) = no surface plasmon resonance peak

FT-IR (ATR) = 2922.0, 2852.5, 1464.3, 1411.2, 1373.9, 798.8 cm⁻¹

Synthesis of 10 nm Fe₃O₄ nanoparticles via 6 nm seeds (adapted from [1]). 1 mL of the solution of 6 nm magnetic nanoparticles was dissolved in a two necked flask in 10 mL of octylether. 0.35 g (0.5 mmol) of Fe(acac)₃, 0.75 mL (2.25 mmol) of oleic acid, 1 mL of oleylamine (2 mmol) and 1 g of 1,2 hexadecanediol (3.9 mmol) were also added into the flask. The mixture was heated under Ar in three steps: 100 °C for 40 min, 200 °C for 70 min, and finally, 300 °C for 40 min. After this protocol the reaction was allowed to cool down to room temperature and the nanoparticles were purified with ethanol and magnetic decantation.

The final product was stored in the fridge, solved in 75 mM oleylamine 75 mM oleic acid hexane until further use.

Metallic core size (as measured by TEM) ⇒ different populations centred at 4.2, 8.0 and 10.2 nm

UV-Vis (Hexane) = no surface plasmon resonance peak

FT-IR (ATR) = 2923.3, 2849.4, 1709.8, 1455.1, 1410.1, 725.9 cm⁻¹

Synthesis of 8 nm Fe₃O₄ magnetic nanoparticles [3]. 1.06 g of iron (III) acetylacetonate (Fe(acac)₃, 3 mmol) were solved in a mixture of 20 mL of oleylamine

Experimental Part

and 10 mL of benzylether in a two necked flask. The solution was heated to 110 °C while degassing (cycles of Ar/vacuum) for 1 hour and then the system was quickly heated to 300 °C. The reaction was allowed to continue at this temperature for 1 hour more before it was allowed to cool down to room temperature. Finally 50 mL of ethanol were added and the nanoparticles were washed three times with magnetic decantation. The final product was stored in the fridge, solved in 75 mM oleylamine hexane until further use.

Metallic core size (as measured by TEM) = 7.2 nm

UV-Vis (Hexane) = no surface plasmon resonance peak

FT-IR (ATR) = 2921.6, 2850.1, 1560.3, 1450.3, 1400.9 cm^{-1}

Gold coating of 8 nm Fe_3O_4 nanoparticles I [2]. In a typical synthesis, oleic acid (1.5 mmol), oleylamine (6 mmol), 1,2-hexadecanediol (12 mmol), $\text{Au}(\text{OAc})_3$ (0.55 mmol) and 1.67 mL of the solution of magnetic cores, were mixed into 30 mL of phenyl ether. This solution was heated under vigorous stirring, Ar atmosphere, and reflux, at 190 °C during 90 min. After this procedure the solution changed its colour from dark brown to dark purple.

The purification was performed as above, adding ethanol and washing with magnetic decantation.

Ligand exchange in 8 nm Fe_3O_4 nanoparticles. 3 mL of 8 nm Fe_3O_4 magnetic nanoparticles hexane solution were mixed in a 15 mL Falcon tube with 2.5 mL (7.5 mmol) of oleic acid. The tube was shaken under atmospheric condition for 72 h after which the nanoparticles were purified as usual by the addition of 5 mL of ethanol (3x) and magnetic decantation. Finally the resulting nanoparticles were resuspended in 75 mM OA 75 mM OAm hexane, and kept refrigerated until further use.

Gold coating of 8 nm Fe_3O_4 nanoparticles II [4]. 1.5 mL of the hexane solution of 8 nm Fe_3O_4 nanoparticles and 1 mL of oleylamine (2 mmol) were solved in 10 mL of chloroform. In another pot, 0.34 g of $\text{HAuCl}_4 \cdot 3\text{H}_2\text{O}$ (1 mmol) and 0.5 mL of oleylamine (1 mmol) were solved in 10 mL of chloroform. This Au solution was then added drop by drop over the solution of magnetic nanoparticles under magnetic stirring. After the addition the reaction was allowed to continue for 20 hours. To purify the final particles

Experimental Part

20 mL of ethanol were added over the reaction and the nanoparticles were washed three times with magnetic decantation. The final product was dissolved in 10 mL of hexane. The solution had a bright brown colour instead of the expected dark purple one.

Synthesis of 4.5 nm Fe₃O₄ magnetic nanoparticles [1]. A thermal decomposition method was followed to synthesize these nanoparticles. Briefly, 2 mL of oleic acid (6 mmol), 3 mL of oleylamine (6 mmol), 2.58 g of 1,2-hexadecanediol, and 0.71 g of Fe(acac)₃ were mixed into 20 mL of phenyl ether. The solution was heated **with the temperature sensor inside the solution**, with vigorous magnetic stirring, with reflux and under Ar atmosphere in two steps: the first at 200 °C during 30 min, and the second another 30 min at 265 °C. The resulting solution had a dark brown colour. After cooling down to room temperature, 40 mL of ethanol were added into the solution to precipitate the MNPs. The nanoparticles were separated magnetically, washed 3 times with ethanol, and kept resuspended in hexane 75mM in oleic acid and 75 mM in oleylamine until further use.

Metallic core size (as measured by TEM) = 4.3 nm

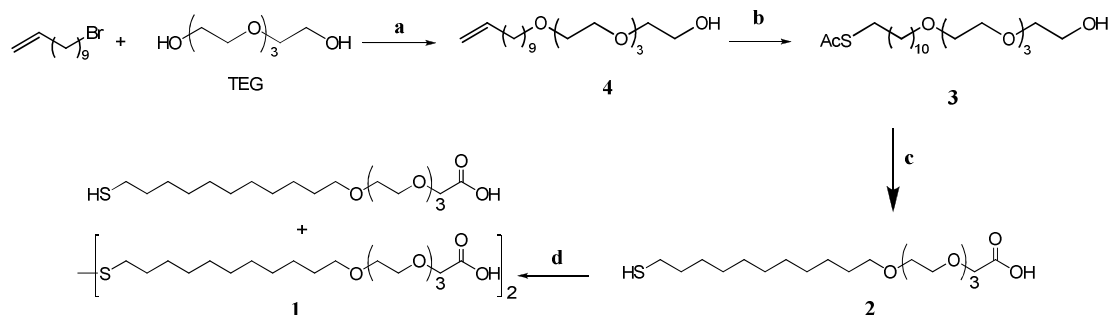
UV-Vis (Hexane) = no surface plasmon resonance peak

FT-IR (ATR) = 2924.4, 2852.1, 1560.7, 1455.6, 1401.1 cm⁻¹

ICP-OES ⇒ Fe = 5.3 %; Au = 94.7 %

Preparation and characterization of water soluble magnetic *glyco-ferrites*

Synthesis of the amphiphilic linker SH-C₁₁-TEG-CO₂H



Scheme 5. Reagents and conditions. **a**, NaOH (50 %), 100 °C, 16 hours. **b**, AcSH, AIBN, dry THF, reflux, 3 hours. **c**, Jones reagent, acetone, 1 hour. **d**, MeONa, MeOH, amberlite IR-120.

Undecen-1-en-11-yltetra(ethylen glycol) (4). A mixture of tetraethylenglycol (TEG) (35.6 g, 183.5 mmol) and NaOH (50%) (2.7 ml, 43.7 mmol) were stirred for ½ hour at 100 °C. The reaction was cooled down to room temperature and 11-Br-undecene (10.2 g, 43.7 mmol) was added. The reaction was heated at 100 °C and left over night under stirring. The mixture was diluted with CH₂Cl₂ (20 ml), washed with water (40 ml) and extracted with hexane (3 x 40 ml). The hexane fractions were collected, dried over Na₂SO₄, filtered and the solvent evaporated at low pressure. The crude product (16 g) was purified by flash column chromatography on silica gel (eluent: EtOAc) to give **4** (10.46 g, 69 %) as a yellow oil.

R_f = 0.31 (EtOAc). ¹H RMN (CDCl₃, 500 MHz) 1.26-1.36 (m, 14H); 1.57-1.653 (m, 2H); 2.01 (m, 2H). 2.7 (bs, 1H), 3.43 (t, 2H, *J* = 6.8 Hz); 3.72-3.55 (m, 16H), 4.97 (dd, 1H, *J* = 17.1, 2.1), 4.90 (dd, 1H, *J* = 10.2, 9.1), 5.78 (m, 1H).

1-(Thioacetylundec-11-yl)tetra(ethylen glycol) (3). To a solution of **4** (9.6 g, 27.7 mmol) in dry THF, AcSH (10.49 g, 138 mmol) and AIBN (cat.) were added. The mixture was left under reflux for 3 hours. The reaction was diluted with 30 ml of EtOAc and a saturated solution of NaHCO₃ was added until neutral pH. The organic phase was washed with brine, dried over Na₂SO₄ and the solvent was removed at low pressure. The residue was purified by flash column chromatography on silica gel (eluent:

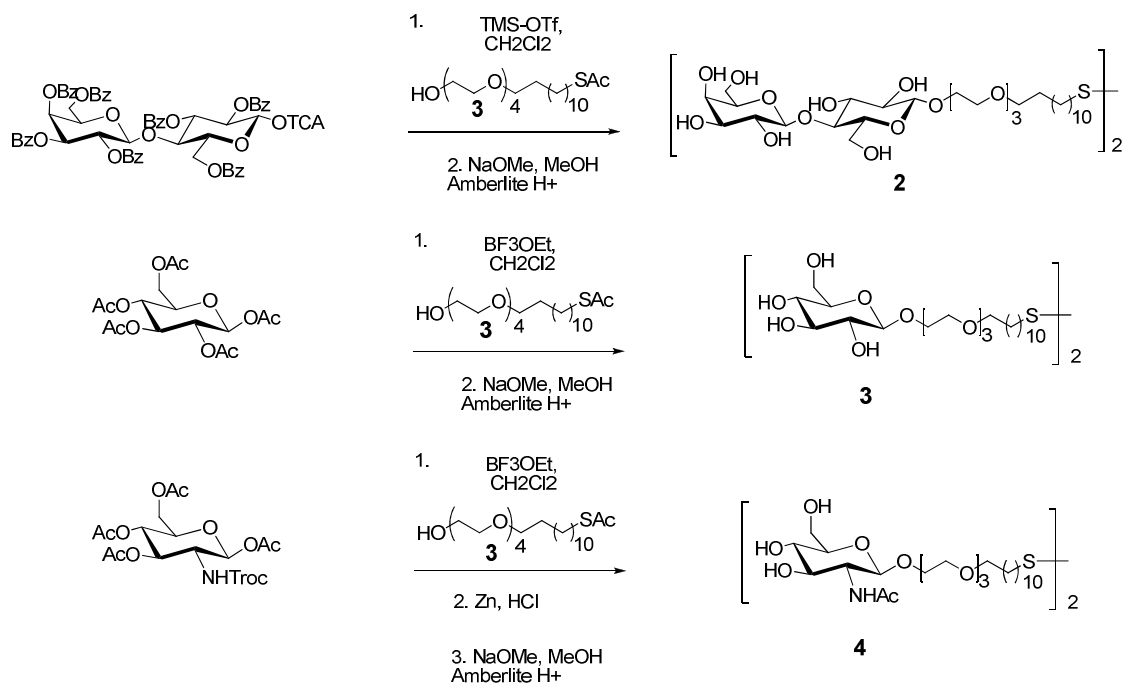
Experimental Part

EtOAc:hexane 9:1 to EtOAc) to obtain **3** as a colourless oil (7.8 g, 67 %). **Rf** = 0.28 (EtOAc). ¹H RMN (CDCl₃, 500 MHz) 1.24-1.36 (m, 14H); 1.53-1.67 (m, 4H); 2.66 (t, 2H); 3.42 (t, 2H); 3.55-3.71 (m, 16H).

22-(Thioacetyl)-2,5,8,11-tetraoxadocosan-1-oic acid (2). 1 g of **3** was dissolved in 5 mL acetone and Jones reagent was added drop by drop until red colour persisted. Then, the reaction was stirred for 30 more min and then it was stopped with 2-propanol, diluted with EtOAc, washed twice with water, and dried in the rotary evaporator. The purification was performed by column chromatography (CH₂Cl₂: MeOH 19:1) (69 % final yield). ¹H NMR (500 MHz, CDCl₃), δ 1.2-1.4 (m, 14H), 1.55 (qui, 4H, *J* = 7.0 Hz), 2.3 (s, 3H), 2.84 (t, 2H, *J* = 7.0 Hz), 3.4 (t, 2H, *J* = 7.0 Hz), 3.5-3.8 (m, 12H), 4.0 (s, 2H).

22-Mercapto [2,5,8,11- tetraoxadocosan]-1-oic acid and 23,23'-Dithio bis [2,5,8,11-tetraoxadocosan]-1-oic acid (1). 0.712 g of the protected product **1** were dissolved in 34 mL methanol and 0.088 g of sodium methoxide were added. The solution was stirred for 6 hours and then the pH was neutralized with Amberlite IR120. The reaction was filtrated, dried in the rotary evaporator and washed several times with diethyl ether. The final product **1** was obtained as a mixture of thiol and disulfide (39:61). 82 % yield. ¹H NMR (500 MHz, CDCl₃), δ 1.3-1.7 (m, 18H), 2.5 (t, 2H thiol, *J* = 7.0 Hz), 2.7 (t, 2H disulfide, *J* = 7.0 Hz) 3.5 (t, 2H, *J* = 14.0 Hz), 3.6-3.8 (m, 12H), 4.15 (s , 2H disulfide), 4.19 (s, 2H thiol).: **HR-MS** (pos., ionization phase MeOH) *m/z*: 416.2213 [M + 2Na]⁺² (C₃₈H₇₂O₁₂S₂Na₂ requires 416.2209).

Synthesis of glycoconjugates (1), (3) and (5) from the corresponding protected monosaccharides



Scheme 6. Synthesis of glycoconjugates of lactose (2), glucose (3) and N-acetyl-glucosamine (4).

11,11-Dithiobis[3,6,9,12-tetraoxaundecanyl-(β -D-galactopyranosyl)(1 \rightarrow 4)- β -D-

glucopyranoside (2). Reaction of the trichloroacetimidate of lactose (0.433 g, 0.36 mmol) and the acceptor (3) (0.23 g, 0.54 mmol) in 8.7 mL of dry CH₂Cl₂ with 18 μ L of TMSOTf (0.072 mmol) at 0 °C. The mixture was stirred at this temperature and monitored by TLC (hexane:AcOEt 1:1). After 210 min the pH was adjusted to 7 with Et₃N (50 μ L), the solvent was removed at low pressure and the residue was purified by flash column chromatography (hexane:AcOEt 1:1) to give the glycosylated product as a syrup. Yield 30 %. ¹H NMR (500 MHz, CDCl₃): δ 1.15-1.60 (m, 16H); 2.24 (s, 3H); 2.78 (t, 2H, *J* = 7.5 Hz); 3.2-3.9 (m, 18H); 4.17 (t, 1H, *J* = 9.5 Hz); 4.40 (dd, 1H, *J* = 12, 4 Hz); 4.52 (dd, 1H, *J* = 12.0, 1.5 Hz); 4.73 (d, 1H, *J* = 8.0 Hz); 4.79 (d, 1H, *J* = 8 Hz); 5.28 (dd, 1H, *J* = 10.5, 3.5 Hz); 5.37 (dd, 1H, *J* = 10.0, 8.0 Hz); 5.64 (m, 2H); 5.72 (t, 1H, *J* = 9.5); 7-8 ppm (m, 35H). The previous glycosylated product (150 mg) was treated with 1 N methanolic solution of NaOMe (2 mL). The mixture was stirred for 3 hours under Argon atmosphere and left for 24 without the argon atmosphere to complete the oxidation of the thiol group. After 24 hours, TLC (Hexane:AcOEt 1:1) showed the appearance of a new product (R_f 0.7). The reaction was neutralised with Amberlist IR-120, filtered and evaporated to dryness. Yield 90 %. ¹H NMR (500 MHz,

Experimental Part

D₂O): δ 1.3-1.5 (m, 12H); 1.57 (m, 2H); 1.67 (q, 2H, $J = 7.5$ Hz); 2.48 (t, 2H, $J = 7.5$ Hz); 2.68 (t, 2H, $J = 7.5$ Hz); 3.2-4 (m, 30H); 4.34 (dd, 1H, $J = 9.5, 8.0$ Hz) ppm; ¹³C NMR (500 MHz, D₂O): δ 21.5, 23.2, 26.0, 26.2, 28.5, 28.7, 29.3, 29.6, 29.8, 30.0, 30.9, 35.5, 39.0, 55.2, 60.2, 61.0, 68.5, 68.7, 69.8, 71.0, 71.1, 72.6, 72.8, 74.3, 74.8, 75.4, 78.5, 102.2, 103.0 ppm; MALDI-TOF: m/z : 726.3955 [M + 2Na]⁺² (C₆₂H₁₁₈O₃₀S₂Na₂ requires 726.3472); 727.3987 [M + Na]⁺ (C₃₁H₆₀O₁₅SNa requires 727.3550).

11,11-Dithiobis[3,6,9,12-tetraoxaundecanyl(β -D-glucopyranoside) (3). Reaction of β -D-glucose pentaacetate (98 %) (0.250 g, 0.64 mmol) and the acceptor (3) (0.367 g, 0.96 mmol) in 5 mL of dry CH₂Cl₂ in the presence of 230 μ L of BF₃OEt (1.92 mmol). The mixture was stirred at 0 °C and monitored by TLC (hexane:AcOEt 1:4). After 210 min the pH was adjusted to 7 with Et₃N, the solvent was removed at low pressure and the residue was purified by flash column chromatography (hexane:AcOEt 1:3) to yield the glycosylated product as a syrup (0.158 g, 63 % taking into account recovered material). ¹H NMR (500 MHz, CDCl₃): δ 1.06 (s, 3H); 1.29-1.55 (m, 16H); 1.98 (s, 3H); 1.99 (s, 3H); 2.04 (s, 3H); 2.27 (s, 3H); 2.83 (t, 2H, $J = 7.5$ Hz); 3.35 (1H, m), 3.39 (2H, t, $J = 6.8$ Hz), 3.57-3.71 (m, 18H); 3.89 (m, 1H), 4.07 (dd, 1H, $J = 12.3, 2.1$ Hz); 4.20 (dd, 1H, $J = 12.3, 4.6$ Hz), 4.55 (d, 1H, $J = 8$ Hz); 4.93 (dd, 1H, $J = 9.5, 8.0$ Hz), 5.03 (t 1H, $J = 9.8$ Hz), 5.15 (t, 1H, $J = 9.5$ Hz). The glycosylated product (150 mg, 0.21 mmol) was treated with 1 N methanolic solution of NaOMe (5 mL). The mixture was stirred for 3 hours under Argon atmosphere and left for 24 without the argon atmosphere to complete the oxidation of the thiol group. After 24 hours, TLC (CH₂Cl₂:MeOH 4:1) showed the appearance of a new product (R_f 0.7). The reaction was neutralised with Amberlist IR-120, filtered and evaporated to dryness. Yield 98 %. ¹H NMR (500 MHz, D₂O): δ ; 1.16-1.53 (m, 14 H), 2.53 (bs, 2H); 3.12 (t, 1 H, $J = 8.5$ Hz), 3.24 (q, 1H, $J = 9.4$ Hz); 3.28-3.33 (m, 4H); 3.42-3.53 (m, 1H); 3.65 (m, 1H); 3.73 (d, 1H; $J = 12.1$ Hz); 3.89 (m, 1H); 4.29 (d, 1H, $J = 7.8$ Hz); ¹³C NMR (500 MHz, D₂O): 26.1, 28.6, 29.3, 29.5, 29.7, 29.8, 29.9, 38.9, 60.8, 68.6, 69.6, 69.7, 69.8, 69.9, 71.1, 73.1, 75.7, 76.0, 102.3.

11,11-Dithiobis[3,6,9,12-tetraoxaundecanyl-2-acetamido(β -D-glucopyranoside) (4). To a solution of 1,3,4,6-Tetra-O-aceyl-2-deoxy -2-(2,2,2-trichloroethoxycarbonylamino) - β -D-gluco-pyranose (2 g, 3.83 mmol) and the acceptor 1-(Thioacetylundec-11-yl)tetra(ethylen glycol) (3) (1.75 g, 4.6 mmol) in dry CH₂Cl₂ (50 mL) TMS-OTf (0.194

Experimental Part

mL, 1.5303 mmol) was added. The mixture was stirred for 4 hours under argon. After addition of Et₃N, the organic layer was separated and washed with a saturated solution of NaHCO₃ and brine solutions. The solution was then dried over Na₂SO₄, filtered and concentrated under low pressure. The residue was purified by column chromatography (Hexane:EtOAc 1:2) to yield 0.5 g of glycosylated product as a syrup (0.813 g, 60 % taking into account recovered material). ¹H NMR (500 MHz, CDCl₃): δ 1.20 (m, 10H), 1.55 (m, 4H), 1.98 (s, 3H), 2.01 (s, 3H), 2.09 (s, 3H), 2.32 (s, 3H), 2.67 (t, 2H, *J* = 7.0 Hz), 3.45 (t, 2H, *J* = 6.5 Hz), 3.57-3.89 (m, 17H), 4.12 (dd, 1H, *J* = 12.0, 2.0 Hz); 4.26 (dd, 1H, *J* = 12.5, 5.0 Hz), 4.73 (s, 2H), 4.84 (d, 1H, *J* = 8.5 Hz), 5.10 (dt, 2H, *J* = 19.5, 9.5 Hz), 6.50 ppm (d, 1H, *J* = 9.0 Hz). To a solution of the previous glycosylated compound (0.507g, 0.6 mmol) in dichloromethane:Ac₂O (1:1, 15 mL) freshly activated Zn powder (196 mg, 3 mmol) was added. The mixture was stirred at room temperature overnight. The organic phase was evaporated and the residue was dissolved in pyridine:acetic anhydride (1:1) in the presence of a catalytic amount of 4-dimethylaminopyridine and stirred at room temperature for 5 hours. After strong washings with saturated aqueous NaHCO₃ solutions, and saturated NaCl solutions, the solution was dried (MgSO₄) and the organic phase was concentrated. The residue was directly deacetylated under Zemplén conditions (1 N methanolic solution of NaOMe). The resulting deacetylated product **4** was isolated after purification by flash chromatography with 1:1 hexane:ethyl acetate. Global yield 30 %. ¹H NMR (500 MHz, D₂O): δ 1.3-1.5 (m, 14H); 1.59 (q, 2H, *J* = 7.0 Hz); 1.70 (q, 2H, *J* = 7.0 Hz); 2.01 (s, 3H); 2.70 (t, 2H, *J* = 7.0 Hz); 3.33 (m, 3H); 3.49 (t, 1H, *J* = 6.5 Hz); 3.59-3.76 (m, 16H); 3.90 (dd, 1H, *J* = 11.5, 2.0 Hz); 3.95 (dt, 1H, *J* = 11.5, 3.5 Hz); 4.50 (d, 1H, *J* = 8.5 Hz) ppm. ¹³C NMR (500 MHz, D₂O): δ 23.4, 27.2, 29.7, 30.3, 30.5, 30.6, 30.8, 31.0, 40.0, 56.6, 61.8, 69.8, 70.7, 70.9, 71.0, 72.1, 75.0, 77.0, 102.1, 172.0 ppm. MALDI-TOF: m/z: 605.8813 [M + 2Na]⁺ (C₅₄H₁₀₆NO₂₀S₂Na₂ requires 605.3209).

Ligand exchange reaction. In a general procedure, 2 mL of the solution of gold coated magnetic glyconanoparticles (0.033 mmol) were washed three times with ethanol, one with acetone, and were suspended in 8 mL of hexane. For each transfer reaction: 500 μL of this solution (aprox 2 · 10⁻³ mmol of MGNPs) were placed in a falcon tube and diluted to 2 mL. To this falcon tube were also added 2 mL of water containing 0.055 mmol of a mixture with a proportion of 1:1 of the linker and the glycoconjugate, or 0.055 mmol of either the glycoconjugate or the linker for the case of the 100 % density nanoparticles.

Experimental Part

The tube was shaken overnight and the colours of the two phases changed completely indicating that the transfer was completed. In some cases it was necessary to add 0.5 mmol of NaBH₄ to break the disulfur linkages between the ligands. To remove large contaminants (micelles), the solutions were passed through a 0.2- μ m Nylon syringe filter. To purify the nanoparticles, they were first lyophilized, dissolved in water, washed three times (usually ethanol or methanol) with magnetic separation and purified by dialysis. This solution was loaded into 5-10 cm segments of SnakeSkin[®] pleated dialysis tubing (Pierce, 10000 MWCO), placed in a 3 L beaker of water, and stirred slowly, recharging with distilled fresh water every 3-4 hours over the course of 72 h. The final solution inside the membrane was lyophilised to render the MGNP. The composition of the ligands on the resulting magnetic nanoparticles was determined by integration of the ¹H-NMR spectrum before and after the ligand exchange. The presence of the ligands on the shell was confirmed treating MGNPs with NaCN and registering ¹H-NMR spectra of the destroyed nanoparticles mixture.

- Fe₃O₄@Au@GlcNAcC₁₁

GlcNAc C₁₁ = 10.0 mg

Hexane solution of Fe₃O₄ = 1.0 mL

Final MGNPs mass = 3.9 mg

Total size (as measured by Zsizer, H₂O) = 8.7 nm

FT-IR (KBr) = 3440.5, 2919.9, 2850.3, 1605.0, 1120.6 cm⁻¹

- Fe₃O₄@Au@Linker

Link = 10.0 mg

Hexane solution of Fe₃O₄ = 1.0 mL

Final MGNPs mass = 8.0 mg

FT-IR (KBr) = 2919.1, 2850.0, 1597.2, 1469.5, 1122.3 cm⁻¹

Surface charge (as measured by Zsizer, H₂O) = -46.0 mV

- Fe₃O₄@Au@GlcNAcC₁₁/Linker

GlcNAc C₁₁ = 10.0 mg

Experimental Part

Link = 6.4 mg

Hexane solution of Fe_3O_4 = 1.0 mL

Final MGNPs mass = 11.1 mg

Total size (as measured by Zsizer, H_2O) = 13.5 nm

FT-IR (KBr) = 3422.0, 2924.0, 2852.9, 1654.6, 1100.9 cm^{-1}

- $\text{Fe}_3\text{O}_4@Au@LactC_{11}$

Lact C_{11} = 10.2 mg

Hexane solution of Fe_3O_4 = 0.5 mL

Final MGNPs mass = 3.9 mg

FT-IR (KBr) = 3364.5, 2925.1, 2900.8, 1635.6, 1065.8 cm^{-1}

- $\text{Fe}_3\text{O}_4@Au@LactC_{11}/Linker$

Lact C_{11} = 6.6 mg

Link = 6.3 mg

Hexane solution of Fe_3O_4 = 0.5 mL

Final MGNPs mass = 20.7 mg

Total size (as measured by Zsizer, H_2O) = 15.7 nm

FT-IR (KBr) = 3373.2, 2923.6, 1616.5, 1338.5, 1016.2 cm^{-1}

- $\text{Fe}_3\text{O}_4@Au@LactC_5$

Lact C_5 = 22.0 mg

Hexane solution of Fe_3O_4 = 2.0 mL

Final MGNPs mass = 5.7 mg

FT-IR (KBr) = 3355.6, 2922.6, 2852.7, 1595.7, 1417.9 cm^{-1}

Surface charge (as measured by Zsizer, H_2O) = -8.0 mV

- $\text{Fe}_3\text{O}_4@Au@GlcC_5$

Glc C_5 = 28.0 mg

Experimental Part

Hexane solution of $\text{Fe}_3\text{O}_4 = 2.0 \text{ mL}$

Final MGNPs mass = 1.7 mg

FT-IR (KBr) = 3421.8, 2919.8, 2850.5, 1384.2, 1078.2 cm^{-1}

Surface charge (as measured by Zsizer, H_2O) = -29.1 mV

- $\text{Fe}_3\text{O}_4@ \text{Au}@ \text{GlcC}_5/\text{Linker}$

Glc C₅ = 8.0 mg

Link = 10.0 mg

Hexane solution of $\text{Fe}_3\text{O}_4 = 2.0 \text{ mL}$

Final MGNPs mass = 7.9 mg

Total size (as measured by Zsizer, H_2O) = 12.7 nm

FT-IR (KBr) = 3368.5, 2923.3, 2853.4, 1596.5, 1406.1, 1378.6, 1066.2 cm^{-1}

- $\text{Fe}_3\text{O}_4@ \text{Au}@ \text{LactC}_5/\text{Linker}$

Lact C₅ = 18.8 mg

Link = 18.5 mg

Hexane solution of $\text{Fe}_3\text{O}_4 = 2.0 \text{ mL}$

Final MGNPs mass = 8.8 mg

Total size (as measured by Zsizer, H_2O) = 21.4 nm

FT-IR (KBr) = 3384.3, 2922.6, 2852.6, 1595.0, 1417.9, 1106.7 cm^{-1}

- $\text{Fe}_3\text{O}_4@ \text{Au}@ \text{GlcNAcC}_5$

GlcNAc C₅ = 22.0 mg

Hexane solution of $\text{Fe}_3\text{O}_4 = 2.0 \text{ mL}$

Final MGNPs mass = 2.5 mg

FT-IR (KBr) = 3284.5, 2921.0, 2851.3, 1559.6, 1406.4, 1041.7 cm^{-1}

- $\text{Fe}_3\text{O}_4@ \text{Au}@ \text{GlcNAcC}_5/\text{Linker}$

GlcNAc C₅ = 19.2 mg

Experimental Part

Link = 18.0 mg

Hexane solution of Fe_3O_4 = 2.0 mL

Final MGNPs mass = 18.2 mg

FT-IR (KBr) = 3420.3, 2920.1, 2850.3, 1565.5, 1113.7 cm^{-1}

- $\text{CoFe}_2\text{O}_4@Au@Linker$

Link = 18.4 mg

Hexane solution of Fe_3O_4 = 1.0 mL

Final MGNPs mass = 5.0 mg

FT-IR (KBr) = 2918.9, 2853.2, 1703.2, 1108.3 cm^{-1}

- $\text{CoFe}_2\text{O}_4@Au@LactC_{11}/Linker$

Lact C_{11} = 9.0 mg

Link = 9.0 mg

Hexane solution of Fe_3O_4 = 1.0 mL

Final MGNPs mass = 4.9 mg

FT-IR (KBr) = 3441.4, 2920.9, 2848.2, 1605.9, 1120.1 cm^{-1}

- $\text{CoFe}_2\text{O}_4@Au@GlcNAcC_{11}$

GlcNAc C_{11} = 20.5 mg

Hexane solution of Fe_3O_4 = 1.0 mL

Final MGNPs mass = 3.9 mg

FT-IR (KBr) = 3340.7, 2919.2, 2853.3, 1615.0, 1107.6 cm^{-1}

- $\text{MnFe}_2\text{O}_4@Au@Linker$

Link = 18.0 mg

Hexane solution of Fe_3O_4 = 2.0 mL

Final MGNPs mass = 1.8 mg

Experimental Part

FT-IR (KBr) = 2920.1, 2848.3, 1726.4, 1112.8 cm^{-1}

- $\text{MnFe}_2\text{O}_4@Au@LactC_{11}/Linker$

Lact C_{11} = 20.0 mg

Link = 22.5 mg

Hexane solution of Fe_3O_4 = 1.0 mL

Final MGNPs mass = 6.8 mg

FT-IR (KBr) = 3441.8, 2919.7, 2853.3, 1605.3, 1020.7 cm^{-1}

Reaction of MGNPs with NaCN. In a general procedure, to a solution of magnetic glyconanoparticles (1 mg) in water (500 μl) NaCN (2 mg) was added at room temperature. The mixture was stirred until dark purple colour disappeared. After decantation, the supernatant was lyophilized and the resultant residue was dissolved in 600 μl of D_2O and $^1\text{H-NMR}$ spectra was registered without any purification.

Contact mode AFM MGNPs imaging. For the AFM imaging NPS tips were used. The tips were cleaned first with ethanol and then subjected to UV irradiation for 20 min previous to the imaging. The images were taken over mica surfaces recently cleaved. Over this surface, 1 μL of 1 mM NiCl_2 solution in distilled and sonicated water was added. It was incubated for 1 min previous to the addition of 6 μL of a diluted solution (10 $\mu\text{g}/\text{mL}$) of $\text{Fe}_3\text{O}_4@Au@LactC_{11}/Link$. This solution was allowed to adsorpt for 5 min, and then was washed gently with water. The images were acquired in liquid (distilled water) under contact mode conditions.

Cellular viability. $1.5 \cdot 10^4$ cells (80 μL) were seeded in a 96 well plate, and cultured at 37 $^\circ\text{C}$ and 5% CO_2 . 24 hours later 20 μL of solution of nanoparticles at the desired concentration was added and the cells were incubated in the same conditions. After 20 hours, 20 μL of MTT solution (5 mg/mL) were added to each well and the cells were still incubated for 4 hours. Finally, before the measurement, the culture media was removed and 200 μL of DMSO were added to each well to break up cells. The solution

Experimental Part

was resuspended vigorously to dissolve formazan crystals, and the samples were measured at 550 nm in the spectrophotometer.

Silver-staining of internalized MGNPs in cells. For the staining of gold inside cells a modified commercial protocol for immunogold staining in tissues was used.

$5 \cdot 10^3$ cells were seeded in a 24 well plate. The cells were incubated with a solution of 25 $\mu\text{g}/\text{mL}$ of biofunctional water soluble MNPs for different times (from 1 to 24 hours). After fixation with paraformaldehyde and permeation of the cells with Triton X-100, these cells were stained by adding 1 mL of each solution of the Silver Enhancer Kit, incubating 10 min, and washing three times with water. This incubation was repeated twice. To finish, the staining was fixed for 5 min with a solution 2.5% $\text{Na}_2\text{S}_2\text{O}_3$, and the cells were observed under the microscope.

For the control experiments, $5 \cdot 10^3$ cells were incubated without MNPs and stained like before.

T_1 and T_2 measurements. For the measurement of the transversal and longitudinal relaxivity times of the *glyco*-ferrites, 6 different concentrations of each sample, ranging from 0 to 0.1 mM of magnetic material were measured. The samples were dissolved in 500 μL of 10 mM PBS pH 7.4 and measured at 37 $^\circ\text{C}$.

MR imaging $\text{XFe}_2\text{O}_4@Au$ nanoparticles. For the phantom measurements, the samples were dissolved in 100 μL of 10 mM PBS pH 7.4 buffer and deposited inside 500 μL eppendorf tubes. All data for T_2 -weighted MR imaging of the phantoms were acquired with 256 x 256 points and a resolution of 250 μm in plane, with a slice thickness of 1.5 mm. The T_E values were varied in 32 steps ranging from 50 ms to 1600 ms and the T_R was 10 secs. The images were fitted into Levenberg-Margardt method to calculate T_2 values using Bruker's Paravision 5 software.

References

1. Sun, S., et al., *Monodisperse $M\text{Fe}_2\text{O}_4$ ($M = \text{Fe}, \text{Co}, \text{Mn}$) nanoparticles*. J Am Chem Soc, 2004. **126**(1): p. 273-9.
2. Wang, L., et al., *Iron oxide-gold core-shell nanoparticles and thin film assembly*. Journal of Materials Chemistry, 2005. **15**: p. 1821-1832.

Experimental Part

3. Zhichuan Xu, C.S., Yanglong Hou, Hongjun Gao, Shouheng Sun, *Oleylamine as Both Reducing Agent and Stabilizer in a Facile Synthesis of Magnetite Nanoparticles*. *Chem. Mater.*, 2009. **21**(9): p. 1778-1780.
4. Xu, Z., Y. Hou, and S. Sun, *Magnetic core/shell Fe₃O₄/Au and Fe₃O₄/Au/Ag nanoparticles with tunable plasmonic properties*. *J Am Chem Soc*, 2007. **129**(28): p. 8698-9.

CHAPTER 2

Preparation and characterization of CdTe- based quantum dots

Preparation and characterization of CdTe-based Quantum Dots

Introduction

Fluorescent semiconductor nanocrystals (CdSe, CdTe, InP, etc), otherwise included in the term “quantum dots” (QDs), have attracted much attention in different research fields since more than 20 years due to their chemical and physical properties which markedly differ from those of the bulk solid (quantum size effect). Quantum dots have size and mater tuneable light emission (usually with a narrow emission band), bright luminescence (high quantum yield), long emission stability (photobleaching resistance), and broad absorption spectra for simultaneous excitation of multiple fluorescence colours compared with classical organic fluorescent dyes (figure 18).

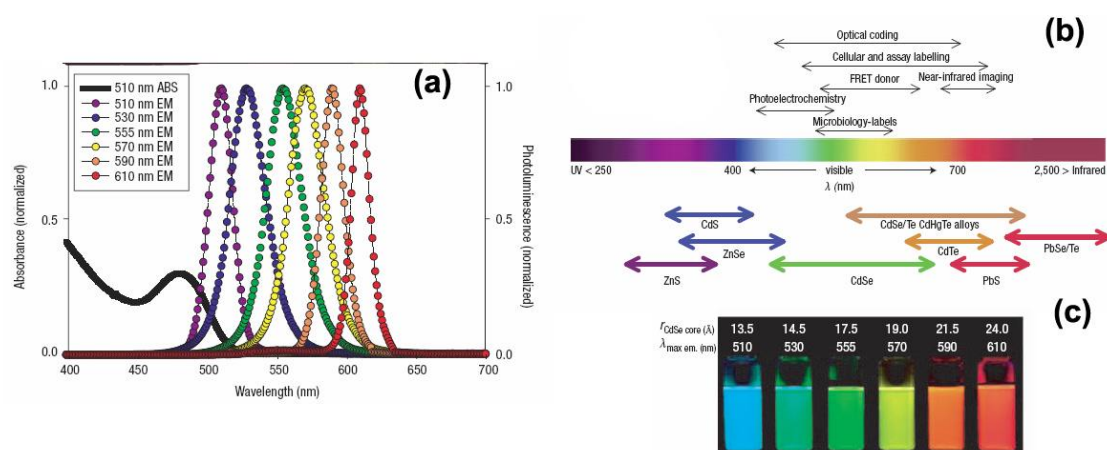


Figure 18. A, emission spectra of six different QDs dispersions. The black line shows the absorption of the 510 nm-emitting QDs. B, representative QDs’ core materials scaled as a function of their emission wavelength superimposed over the spectrum. Representative areas of biological interest are also presented corresponding to the pertinent emission highlighting how most biological usage falls in the visible–near infrared region. C, photograph demonstrating the size-tunable fluorescence properties and spectral range of the six QDs dispersions plotted in A versus CdSe core size. All samples were excited at 365 nm with a UV source. Image adapted from [1].

Research on QDs has evolved from electronic materials science to biological applications. A broad variety of synthetic methods have been developed for the preparation of QDs, conjugation with biomolecules and application as bioluminescent

probes for live-cell and/or *in vivo* animal imaging. In general, capping of the outer surface of core semiconductor prevents aggregation and oxidation, stabilizes nanoparticles in solution, and improves the particles' fluorescence emission by surface passivation. Trioctylphosphine oxide (TOPO), in tandem with trioctylphosphine (TOP) or tributylphosphine (TBP), is commonly used as capping agent of the crystallites, but many other compounds have been employed.

The synthesis of QDs was first reported in 1982 by Efros and Ekimov [2] [3] who built semiconductor nano and microcrystals in glass matrices. Since these discoveries great effort has been devoted to the development of QD technology; but the real step forward in this field did not appear until 1993 when Bawendi *et al.* reported the synthesis of high quality colloidal CdS, CdSe and CdTe QDs with narrow size distributions [4]. In their protocol high temperatures in combination with selenium in coordinating ligands (mixture of TOP and TOPO) were used to achieve the pyrolysis of organometallic compounds of cadmium (CdMe_2), and so to yield final CdSe QDs with high crystallinity and size distributions of 8-10%. The same method was used to prepare CdS and CdTe QDs. This same approach was later used with appropriate precursors to coat CdSe cores with a shell of wider-bandgap semiconducting material (the most important is ZnS [5] [6]). This second step has proven necessary for two main reasons. First, due to the high surface area to volume ratios of QDs a large fraction of their constituent atoms are exposed to the surface and not completely bonded [7]. This results in defects that reduce strongly the photoluminescence efficiency. Second, the material from the shell provides protection for the core from oxidation and degradation increasing the chemical stability of the QD, at the same time that it prevents the leakage of Cd^{2+} ions reducing the toxicity. Since these reports the synthetic chemistry of CdSe QDs quickly advanced, generating brightly fluorescent QDs that can span the visible spectrum. As a result CdSe@ZnS has become the most common chemical composition for QDs synthesis, especially for biological applications. Several types of QDs, mainly core@shell, are nowadays commercially available and routinely used either as starting materials or for various applications.

As-synthesized QDs can not be directly used in bio-applications as due to their hydrophobic surface they are not soluble in aqueous media. After modification of the capping molecules to render water soluble QDs, the photoluminescence is considerably decreased [8] [9]. This is the main reason why in the last few years direct aqueous synthesis methodologies are gaining attention. The main problem with this kind of

methods is that in their beginning the photoluminescent properties of the final QDs were poor compared with non-aqueous procedures [10]. Nowadays this problem seems to be solved [11] [12] [13]. Aqueous protocols rely on the reaction at around 100 °C between a Cd^{2+} salt and HTe^- in the presence of thiol molecules (3-mercaptopropionic acid, MPA, and others) as capping agents to yield highly stable and fluorescent CdTe QDs.

Aqueous preparation of CdTe quantum dots

The aim of our work is to prepare, directly in water, biofunctional and biocompatible QDs with high quantum yields to be used as visible and near-infrared (NIR) fluorescent probes for molecular imaging both *in vitro* and *in vivo*.

According to bibliography [8] [9] and also to previous experiences in our laboratory (in the last years InP@ZnS , CdSe_xTe_y and CdTe@CdSe QDs have being prepared according to classical apolar solvent methodologies), one of the main problems of *traditional* QDs synthetic protocols is the transfer of the nanocrystals from organic media to water without a decrease on their emission properties. This is the main reason why in this work we have attempted to prepare QDs directly in water instead of following high boiling point apolar solvent protocols. We have chosen CdTe based QDs because according to literature, the emission of CdTe QDs can be tuned to cover nearly the whole visible spectra, from blue-green to red emission, and even to enter into the near infrared region of the spectra where the interferences from the autofluorescence from cells and tissues decreases [14].

Taking into account that MPA-capped CdTe QDs are toxic even at low doses [15], we have tried to reduce their cytotoxicity either modifying the organic capping or building an inorganic shell over the CdTe core. Concerning the organic capping two strategies were tried. First, MPA was substituted by L-cystein (L-cys), a natural aminoacid that will be more biocompatible. Secondly, MPA-capped QDs were modified with carbohydrates to try to reduce their toxicity. Our other choice to improve the biocompatibility, was the deposition of a ZnTe shell over the CdTe core. This possibility apart from reducing the toxicity, in theory, would also increase the QY of the final QDs. In the core@shell strategy also two different organic cappings, MPA and L-cys, were compared.

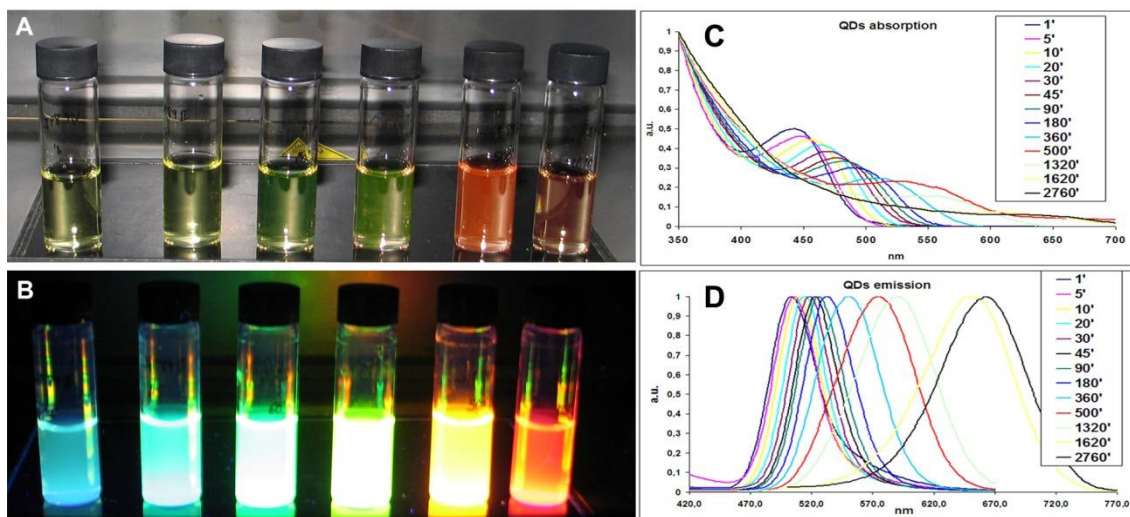
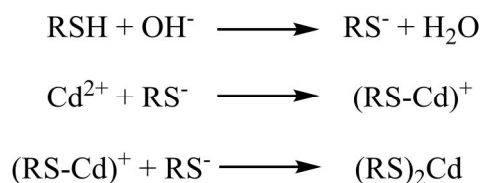


Figure 19. **A**, water solutions of CdTe-MPA QDs obtained at different reaction times under ambient light. **B**, the same water solutions under UV light. **C**, different reaction time QDs normalized absorption spectra. **D**, different reaction time QDs normalized emission spectra.

Our efforts in this field began reproducing the aqueous synthesis of CdTe QDs by Zou *et al.* [13]. The main challenge in this synthesis is the preparation of Te reagent (NaHTe) by reaction between solid Te powder and NaBH₄ in water at high temperature (around 85 °C) and in the complete absence of O₂. Once this reagent is ready (it has to be prepared immediately before use) it is added over a water solution of Cd²⁺ salts (chlorides) and 3-mercaptopropionic acid (MPA) as capping agent. The mixture is then heated to reflux and depending on the reaction time QDs with different emission wavelength can be obtained (figure 19). If the reaction is carried out under atmospheric conditions, the reaction rate is much slower than the one from the reaction under Ar atmosphere (red emission after 120 h vs. red emission after 20 h under Ar). There are other important parameters that should be controlled in this synthesis to obtain high quality QDs (with the highest quantum yield, QY, possible). These parameters are mainly pH, and temperature of the reaction. For the reaction to take place the pH of the cadmium salts solution must be basic. According to the proposed mechanism [13], the complexes Cd-MPA in their molecular state are the Cd source for the formation of CdTe monomers for nucleation and growth of the nanocrystals (scheme 7). Depending on the final emission desired, the initial pH must be adjusted carefully. If the desired final emission of the QDs is around the red (600-700 nm) the optimal pH is 9.4. Above this pH the reaction proceeds faster but the resulting QY is lower. With the refluxing temperature the effect is similar. If T is increased the reaction rate also increases but a

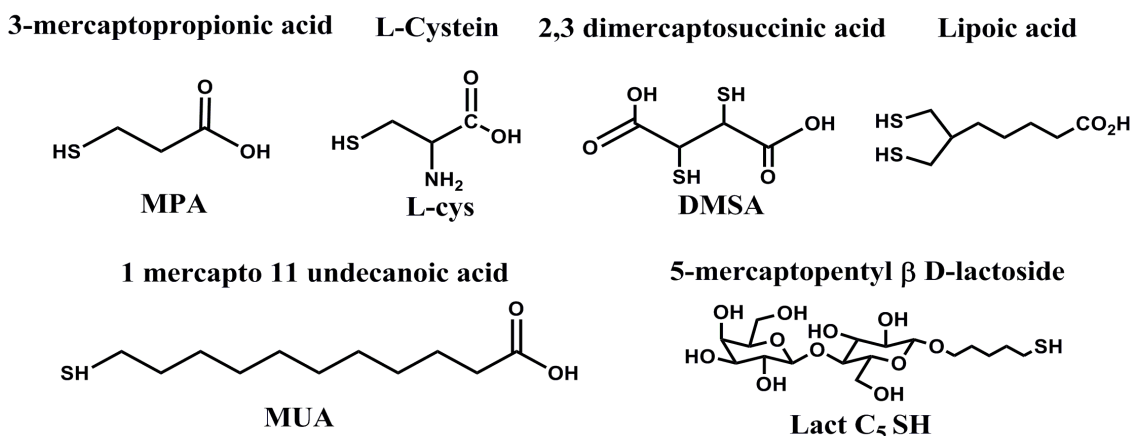
compromise has to be reached because finally QY decreases at high temperatures (above 150 °C). Under the conditions of pH 9.4 and refluxing T of 140 °C reproducible QYs [16] of 30-40 % for red emitting QDs were obtained.



Scheme 7. Proposed formation of 1:1 and 1:2 complexes of Cd^{2+} with thiol molecules under basic conditions, as Cd sources for CdTe synthesis.

To speed up this reaction, microwave assisted protocols based on the same synthetic scheme have been proposed [11] [17]. We have tried to reproduce these syntheses in our laboratory without good results. The supposed enhancement of reaction rate was not so in our hands and an important decrease in the final QY of the nanocrystals (final QY < 1 %) was observed.

Effect of the ligands on CdTe QDs aqueous preparation. In a next step the influence of the ligands over the final properties of CdTe QDs was investigated. Several reports have already stated an influence of the different thiol ending capping agents over the final QY of the nanocrystals [18]. To investigate the influence of ligands we chose several thiol ending molecules with different chain lengths (Scheme 8): 1, 2 dimercaptosuccinic acid (DMSA), L-cystein (L cys), lipoic acid and 11-mercaptopundecanoic acid (MUA). We also tried to use a thiol ending glycoconjugate as capping agent: 5-mercaptopentyl β D-lactoside (Lact C₅).



Scheme 8. Structures of the different thiol ended molecules used in QDs synthesis.

The synthesis using L-cys as capping agent was very similar to our previous experience with MPA, both in QY and in reaction rate. The only difference was that the final purified QDs in solution were much less stable with time, precipitating after a few days. The solubility of DMSA, Lipoic acid and MUA in water was very low so in order to solubilise them we had to reduce them first with NaBH₄ to remove possible disulfur linkages, put them in the basic conditions needed for the later reaction and finally heat their solutions to 70 °C. Once we had a clear solution we followed with the reactions in the same way than with MPA. The behaviour of the reaction with DMSA as capping agent was very similar to the one with MPA, but the final QY of the semiconductor nanoparticles was much worse (0.5 - 1 %). With lipoic acid and MUA, with longer alkyl chains than MPA, the reaction was completely different. With lipoic acid the reaction began and yellow emitting QDs could be isolated after the addition of NaHTe (with very low QY, < 1%) but the reaction did not evolve with time. In the case of the longest thiol molecule, MUA, the reaction did not even begin after the addition of the Te reagent and no QDs could be obtained. The problem with the lactose conjugate was different. Lactose acts as a chelating agent in the presence of Cd²⁺ ions and the final chelates precipitate. In this case it was impossible to go on with the reaction.

After checking out that the direct synthesis of carbohydrate protected QDs (*glyco*-QDs) was not possible, we decided to synthesise first MPA-capped QDs and then functionalise them with an amine ended glycoconjugate. In this case 2-aminoethyl α-D-mannopiranoside (Mann-NH₂) was chosen as ligand, and the same coupling strategy used for the functionalization of the MGNPs (see chapter 3) was applied. Basically acid groups of MPA were reacted with the amine group of the glycoconjugate in the

Results and Discussion

presence of EDC to create peptide bonds. To follow this reaction we performed Z-potential measurements. The initial Z-potential of the QDs was highly negative (around -27 mV, due to the CO_2^- groups from MPA), and upon the coupling of the glycoconjugate this charge was removed. We made serial additions of the glycoconjugate and EDC, and checked the Z-potential of purified aliquots until its value stabilised (at around -6 mV), indication that the coupling could not go further. Along the process the QDs were purified by centrifugal filtering. Both CdTe-MPA and CdTe-Mann QDs were characterised by TEM and HRTEM (figure 20). From HRTEM micrographs different lattice spacings, indication of different growth directions, were measured. Examples of two clear growth directions are illustrated in the insets of figure 20.

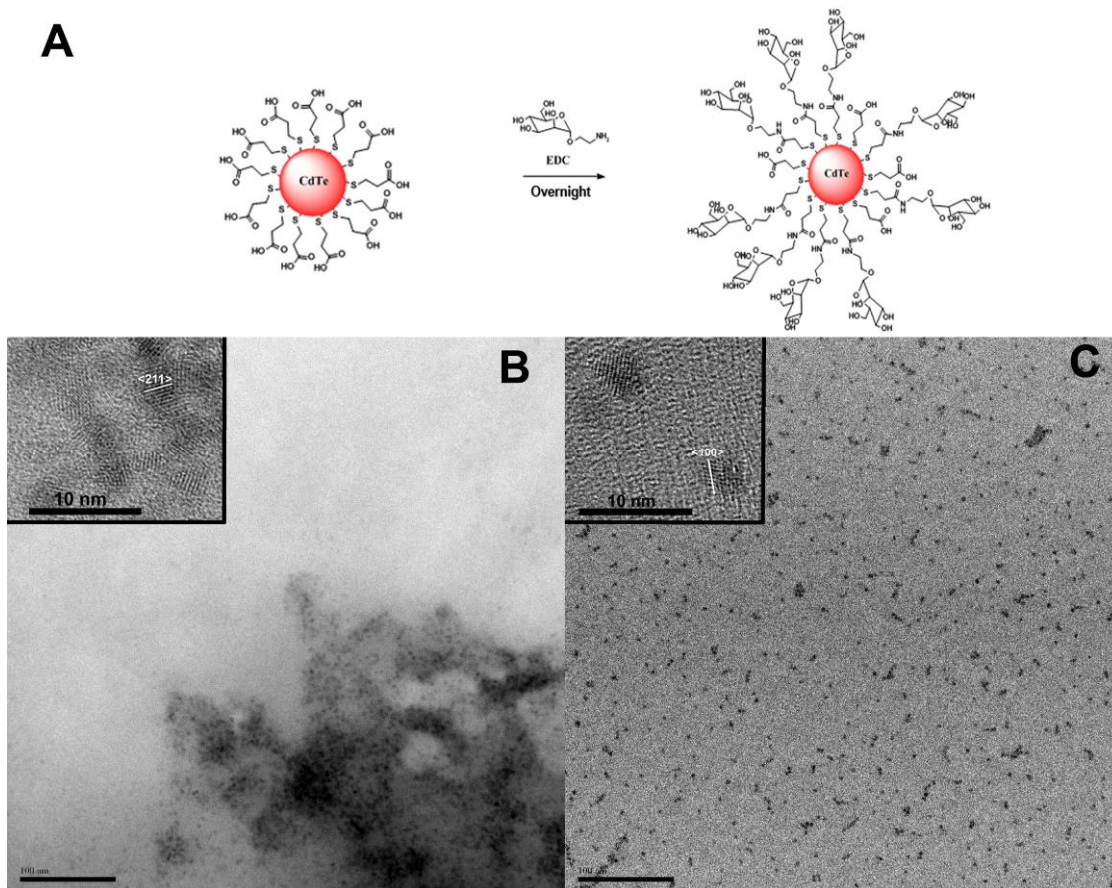


Figure 20. A, preparation of CdTe-Mann QDs. B, TEM micrograph of CdTe@MPA QDs. Inset, high resolution TEM (HRTEM) with example of lattice spacing measurement. Spacing between fringes can be measured to be 0.389 \AA , in agreement with growth along $\langle 211 \rangle$ direction. C, TEM micrograph of CdTe@Mann- NH_2 QDs. Inset, HRTEM with example of lattice spacing measurement. Spacing between fringes can be measured to be 0.324 \AA , in agreement with growth along $\langle 100 \rangle$ direction. Scale bar 100 nm.

Aqueous preparation of CdTe@ZnTe core@shell quantum dots

As has been pointed out previously in this chapter, the construction of a shell of different material around the QDs core improves greatly its fluorescence properties as well as it makes the nanocrystal more stable. One more advantage of core@shell structure is that the nature of the shell can be chosen to be more biocompatible than the materials from the core, as cytotoxicity of these constructs seem to be a major drawback [15]. The most commonly used shell material for bioapplications, ZnS, is not suitable in the case of CdTe cores as there is a large lattice mismatch between CdTe and ZnS lattice parameters (lattice constant of ZnS 5.41 Å vs 6.48 Å for CdTe, difference of around 20%). This mismatch is the reason why if the thickness of the ZnS shell exceeds 2 monolayers there appears an interfacial strain that leads to the formation of dislocations or defects that will adversely affect both the QY and the colloidal stability of the QDs [19].

One option for the protection of CdTe QDs, is the less explored ZnTe (lattice constant of 6.10 Å). Recently, the aqueous synthesis of CdTe@ZnTe core@shell QDs has been described [19], although the characterization in this paper is scarce and equivocal. According to this report, the final properties of these CdTe@ ZnTe QDs are promising for biological applications. Possible biological applications are the reason why we have tried to reproduce this synthesis. Basically, this protocol is the same than the one we used for the synthesis of CdTe QDs, but there are three main differences. First, the NaHTe reagent is added over an aqueous mixture of Cd²⁺ and Zn²⁺ salts. Second, in [19] the Cd²⁺ and Zn²⁺ salts are perchlorates instead of chlorides. And third, the organic molecule used to protect the metallic core of the QDs is L-cystein (L-cys) instead of MPA we have previously used. Using the conditions reported in [19], a white precipitate, not reported in [19], appeared after the addition of the Te reagent. However, the reaction went on as described. Once the solution had reached the desired emission wavelength (λ_{em} 600 nm), the reaction mixture was allowed to cool down to room T and then centrifuged at low speed (aprox. 1500 g) to remove the precipitate. The CdTe@ZnTe@L-cys QDs were purified by addition of acetone, centrifugation (3x), dialysis and lyophilisation to give red emitting QDs with a reproducible QY of 30-40 %. The solubility in water of the isolated QDs decreases greatly indicating probably that L-

cys is not as good capping agent as MPA. So the synthetic protocol was modified either using MPA as ligand or chloride salts instead of perchlorate. None of these two attempts allowed us to obtain more stable core@shell CdTe@ZnTe QDs nor to avoid the presence of the precipitate.

Cytotoxicity studies on CdTe and CdTe@ZnTe quantum dots

Regardless the outstanding properties of QDs [20] [1] [21] their use in biological applications nowadays still faces some problems. For the moment the main problem for the *in vivo* use of QDs is their cytotoxicity. Cytotoxicity of QDs has been observed in a large number of *in vitro* studies affecting both cell growth and viability [20] [21] [15] [22]. A number of mechanisms have been proposed to be responsible of this cytotoxicity, from desorption of free Cd²⁺, to free radical formation, or QDs interaction with intracellular components. Also, a number of factors have been probed to affect the toxicity of these nanomaterials: core and capping materials, size, surface chemistry, coating bioactivity and processing parameters [21]. Anyway, there is no agreement on the cytotoxicity of these nanocrystals as also a great number of reports claim that QDs are safe for their *in vitro* and *in vivo* use [19] [23] [24] [25]. This controversy arises from the dose-dependent toxic effect of QDs and more important from the fact that there is not a unified way to measure the cytotoxicity, each group does it with their organism, incubation times and doses of interest. So previous to any bioapplication of QDs their cytotoxicity has to be assessed individually.

We have performed a systematic study on CdTe QDs toxicity in *in vitro* cell cultures. For this purpose two human cellular lines (one adherent and one non-adherent), C33 from cervix carcinoma, and Raji cells, lymphocytes from Burkitt' lymphoma, were used. A series of previously prepared CdTe based QDs were tested (figure 21). All these cytotoxicity experiments were performed using standard viability tests, MTT for adherent C33 cells [26] and MTS [27] for non-adherent Raji ones following incubation in the presence of the QDs for 24 h.

Results and Discussion

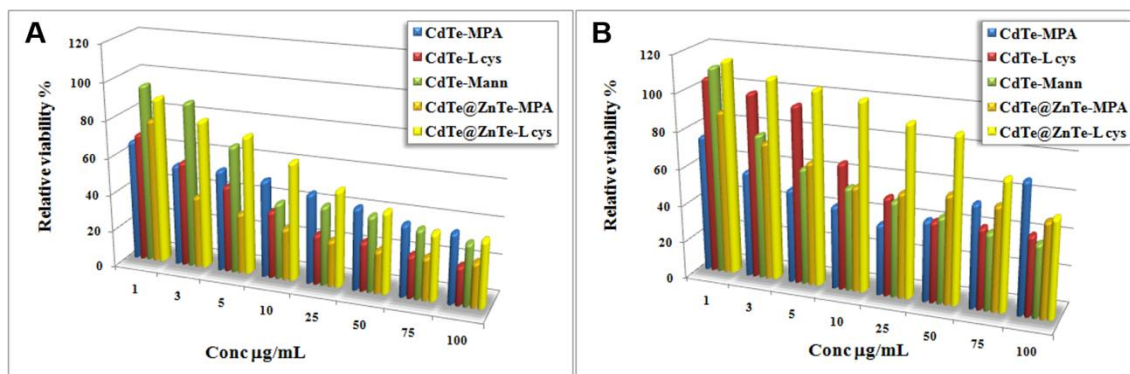


Figure 21. A, results from the MTT cytotoxicity tests performed over C33 cells with different concentrations of QDs. B, results from the MTS cytotoxicity tests performed with Raji cells at different concentrations of QDs.

The results of the viability tests are shown in figure 21. All QDs are cytotoxic at high concentrations. The cytotoxic effect of CdTe at high concentrations can not be removed or decreased by the modification of neither the inorganic shell nor the organic coating. Two remarkable features can be observed in these graphs (figure 21). First, the combination of a ZnTe shell together with an L-cys coating seems to reduce the toxicity of the QDs for both cell lines. This result may be not reliable as the colloidal stability of these core@shell QDs in water is low, making the final concentration of QDs in solution lower than expected. Second, and more interesting, at low concentrations (below 5 µg/mL) the presence of biocompatible carbohydrates (mannose) reduces the adverse effects of the semiconducting core. This behaviour is even more significant if we consider that according to tests performed with magnetic glyconanoparticles (figure 17, chapter 1) and QDs (figure 22), carbohydrate coated nanocrystals are internalised by cells more easily than acid-coated ones. This would result in a final concentration of *glyco*-QDs inside the cells higher than that of MPA or L-cys QDs, so that the reduction of the cytotoxicity may be even more important.

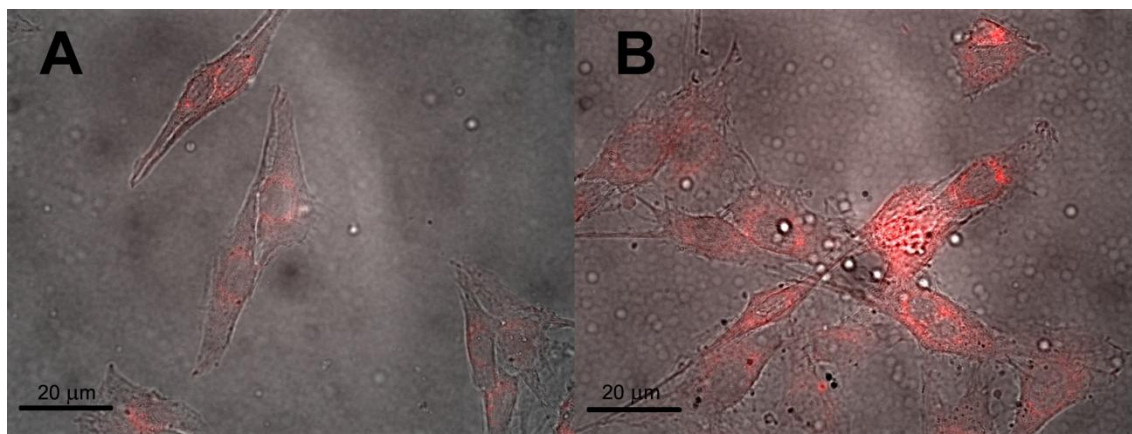


Figure 22. Overlapped bright field and fluorescence image of C33 cells incubated for 1 hour at 37 °C and 5 % CO₂ in the presence of 5 µg/mL of (A) CdTe-MPA QDs and (B) CdTe-Mann QDs. The fluorescent signal under the same imaging conditions is much higher in the case of mannose-functionalised QDs indicating higher uptake by the cells.

References

1. Medintz, I.L., et al., *Quantum dot bioconjugates for imaging, labelling and sensing*. Nat Mater, 2005. **4**(6): p. 435-46.
2. Efros, A.L., *Interband absorption of light in a semiconductor sphere*. Sov. Phys. Semicond., 1982. **16**: p. 772-775.
3. A. I. Ekimov, A.A.O., *Quantum size effect in the optical spectra of semiconductor-microcrystals*. Sov. Phys. Semicond., 1982. **16**: p. 775-778.
4. Murray, C.B., D.J. Norris, and M.G. Bawendi, *Synthesis and Characterization of Nearly Monodisperse Cde (E = S, Se, Te) Semiconductor Nanocrystallites*. Journal of the American Chemical Society, 1993. **115**(19): p. 8706-8715.
5. B. O. Dabbousi, J.R., F. V. Mikulec, J. R. Heine, H. Mattoussi, R. Ober, K. F. Jensen, M. G. Bawendi, *(CdSe)ZnS core-shell quantum dots: synthesis and optical and structural characterization of a size series of highly luminescent materials*. J. Phys. Chem. B, 1997. **101**: p. 9463-9475.
6. M. A. Hines, P.G.-S., *Synthesis and characterization of strongly luminescent ZnS-capped CdSe nanocrystals*. J. Phys Chem. B, 1996. **100**: p. 468-471.
7. Smith, A.M., et al., *Bioconjugated quantum dots for in vivo molecular and cellular imaging*. Adv Drug Deliv Rev, 2008. **60**(11): p. 1226-40.
8. Bruchez, M., Jr., et al., *Semiconductor nanocrystals as fluorescent biological labels*. Science, 1998. **281**(5385): p. 2013-6.
9. H. Mattoussi, J.M.M., E. R. Goldman, G.P. Anderson, V. C. Sundar, F. V. Mikulec, M. G. Bawendi, *Self-Assembly of CdSe-ZnS Quantum Dot Bioconjugates Using an Engineered Recombinant Protein*. J. Am. Chem. Soc., 2000. **122**: p. 12142-12150.

Results and Discussion

10. A. L. Rogach, L.K., A. Kornovsky, D. Su, A. Eychmüller, H. Weller *Synthesis and characterization of thiol-stabilized CdTe nanocrystals*. Ber. Bunsen-Ges. Phys. Chem., 1996. **100**: p. 1772-1778.
11. Li, L., H. Qian, and J. Ren, *Rapid synthesis of highly luminescent CdTe nanocrystals in the aqueous phase by microwave irradiation with controllable temperature*. Chem Commun (Camb), 2005(4): p. 528-30.
12. L. Li, H.Q., N. Fang, J. Ren, *Significant enhancement of the quantum yield of CdTe nanocrystals synthesized in aqueous phase by controlling the pH and concentrations of precursor solutions*. Journal of Luminescence, 2006. **116**: p. 59–66.
13. Zou, L.G., Z.; Zhang, N.; Zhang, Y.; Fang, Z.; Zhu W.; Zhong, X., *Ultrafast synthesis of highly luminescent green- to near infrared-emitting CdTe nanocrystals in aqueous phase*. Journal of Materials Chemistry, 2008. **18**: p. 2807–2815.
14. Frangioni, J.V., *In vivo near-infrared fluorescence imaging*. Curr Opin Chem Biol, 2003. **7**(5): p. 626-34.
15. Lovric, J., et al., *Unmodified cadmium telluride quantum dots induce reactive oxygen species formation leading to multiple organelle damage and cell death*. Chem Biol, 2005. **12**(11): p. 1227-34.
16. Y. Zheng, Z.Y., J. Y. Ying, *Aqueous Synthesis of Glutathione-Capped ZnSe and Zn_{1-x}CdxSe Alloyed Quantum Dots*. Adv. Mater., 2007. **19** p. 1475–1479.
17. Y. He, H.L., L. Sai, Y. Su, M. Hu, C. Fan, W. Huang, L. Wang, *Microwave Synthesis of Water-Dispersed CdTe/CdS/ZnS Core-Shell-Shell Quantum Dots with Excellent Photostability and Biocompatibility*. Adv. Mater., 2008.
18. Blum, A.S., M.H. Moore, and B.R. Ratna, *Quantum dot fluorescence as a function of alkyl chain length in aqueous environments*. Langmuir, 2008. **24**(17): p. 9194-7.
19. Law, W.C., et al., *Aqueous-phase synthesis of highly luminescent CdTe/ZnTe core/shell quantum dots optimized for targeted bioimaging*. Small, 2009. **5**(11): p. 1302-10.
20. Michalet, X., et al., *Quantum dots for live cells, in vivo imaging, and diagnostics*. Science, 2005. **307**(5709): p. 538-44.
21. Jamieson, T., et al., *Biological applications of quantum dots*. Biomaterials, 2007. **28**(31): p. 4717-32.
22. Kirchner, C., et al., *Cytotoxicity of colloidal CdSe and CdSe/ZnS nanoparticles*. Nano Lett, 2005. **5**(2): p. 331-8.
23. Gao, X., et al., *In vivo molecular and cellular imaging with quantum dots*. Curr Opin Biotechnol, 2005. **16**(1): p. 63-72.
24. Kim, S., et al., *Near-infrared fluorescent type II quantum dots for sentinel lymph node mapping*. Nat Biotechnol, 2004. **22**(1): p. 93-7.
25. Chen, L.D., et al., *The biocompatibility of quantum dot probes used for the targeted imaging of hepatocellular carcinoma metastasis*. Biomaterials, 2008. **29**(31): p. 4170-6.
26. Mosmann, T., *Rapid colorimetric assay for cellular growth and survival: application to proliferation and cytotoxicity assays*. J Immunol Methods, 1983. **65**(1-2): p. 55-63.

Results and Discussion

27. Cory, A.H., et al., *Use of an aqueous soluble tetrazolium/formazan assay for cell growth assays in culture*. *Cancer Commun*, 1991. **3**(7): p. 207-12.

Experimental part

Materials and methods

All nanocrystals were characterized before and after any step by low and high resolution TEM on a JEOL JEM 2100F microscope and the composition analysis were done by energy dispersive X-ray detector (EDX) (Oxford INCA system). UV-Vis spectra were recorded in a Beckman-Coulter DU 800 spectrophotometer. FT-IR spectra were acquired in a Thermo Nicolet FT-IR spectrometer. Fluorescence spectra were acquired in a Perkin-Elmer LS55 fluorimeter. Z-measurements were obtained in a Malvern Zetasizer Nano ZS. Fluorescence images were acquired in a Leica DMI 6000B inverted epifluorescence microscope. All the chemical reagents were purchased from Sigma-Aldrich and were used as received without further purification. All solvents were analysis grade (acetone, dichloromethane, methanol, hexane and 2-propanol) and were supplied by Sharlab.

Aqueous preparation of CdTe quantum dots

Preparation of NaHTe reagent. 25 mg of Te were mixed with 19 mg of NaBH₄ in 5 mL of deoxygenated nanopure H₂O under Ar. With a high flow of Ar through the solution and under magnetic stirring the reaction was heated to 85 °C and maintained at this temperature for 45 min. During this time the reaction changed from turbid black to clear purple colour. The reaction was allowed to cool down to room temperature before it was ready to use in the QD synthesis.

Preparation of MPA (1-mercaptopropionic acid) protected CdTe QDs. In a three-necked flask, 40 mL of a solution 5 mM of CdCl₂ in deoxygenated nanopure H₂O were mixed with 30 µL of MPA (1-mercaptopropionic acid). The pH was adjusted to be 9.6 with NaOH 1N and the solution was bubbled with Ar for 30 min. After that, 500 µL of recently prepared NaHTe were added into the Cd²⁺ solution and the temperature of mixture was raised and maintained at 160 °C. Varying the reaction time samples with fluorescent emission covering from green to dark red can be obtained. To purify the QDs, the solution was allowed to cool down to room temperature and then 80 mL of acetone were added to precipitate the NPs. The nanocrystals were separated by

Experimental Part

centrifugation, washed twice with EtOH, dialyzed 48 hours against 10 mM PBS and 8 hours against water, and finally stored lyophilized until further use.

- CdTe@MPA:

FT-IR (KBr) = 1560.6, 1396.9, 1152.3, 1068.2, 966.7, 860.0, 673.5, 651.8 cm^{-1} .

Surface charge (as measured by Zsizer, 10 mM PBS) = -26.9 mV.

Preparation of L-cystein (L-cys) protected CdTe QDs. In a three-necked flask, 0.5 g of $\text{Cd}(\text{ClO}_4) \cdot \text{H}_2\text{O}$ ($1.60 \cdot 10^{-3}$ moles), and 0.42 g of L-cystein ($3.50 \cdot 10^{-3}$ moles) were solved in 125 mL of deoxygenated nanopure water. The pH of this solution was modified with NaOH 1N to be 10.4 and Ar was bubbled for 20 min. Then 5 mL of a 3 mM water solution of NaHTe were injected swiftly and the temperature of the system was raised to 100 °C maintaining the temperature sensor inside the solution. Varying the reaction time, samples with fluorescent emission covering from green to dark red can be obtained. To purify the QDs, the solution was allowed to cool down to room temperature and then 80 mL of acetone were added to precipitate the NPs. The nanocrystals were separated by centrifugation, washed twice with EtOH, dialyzed 48 hours against 10 mM PBS and 8 hours against water, and finally stored lyophilized until further use.

- CdTe@L-cys:

FT-IR (KBr) = 3463.6, 2920.4, 1793.8, 1637.5, 1396.1, 1363.1, 1163.2, 1073.7, 981.6, 948.3, 860.1, 546.1, 523.7, 464.0 cm^{-1} .

Surface charge (as measured by Zsizer, 10 mM PBS) = -14.4 mV.

Preparation of 1,2 dimercaptosuccinic acid (DMSA) protected CdTe QDs. In a three-necked flask, 40 mL of a solution 5 mM of CdCl_2 in deoxygenated nanopure H_2O were mixed with 63.7 mg of DMSA (1,2 dimercaptosuccinic acid). To solubilise the DMSA 40 mg of NaBH_4 were added, the pH was adjusted to 10 with NaOH 1N and finally the solution was heated to 70 °C. When the solution was clear the heat was turned off. Once at room temperature, 500 μL of recently prepared NaHTe were added into the Cd^{2+} solution and the temperature of mixture was raised and maintained at 160 °C. To purify the QDs, the solution was allowed to cool down to room temperature and then 80 mL of acetone were added to precipitate the NPs. The nanocrystals were

Experimental Part

separated by centrifugation, washed twice with EtOH, dialyzed 48 hours against 10 mM PBS and 8 hours against water, and finally stored lyophilized until further use.

Preparation of lipoic acid protected CdTe QDs. In a three-necked flask, 40 mL of a solution 5 mM of CdCl₂ in deoxygenated nanopure H₂O were mixed with 72.2 mg of lipoic acid. To solubilise the lipoic acid 40 mg of NaBH₄ were added, the pH was adjusted to 10 with NaOH 1N and finally the solution was heated to 70 °C. When the solution was clear the heat was turned off. Once at room temperature, 500 µL of recently prepared NaHTe were added into the Cd²⁺ solution and the temperature of mixture was raised and maintained at 160 °C.

Preparation of 1 mercapto 11 undecanoic acid (MUA) protected CdTe QDs. In a three-necked flask, 40 mL of a solution 5 mM of CdCl₂ in deoxygenated nanopure H₂O were mixed with 70 mg of MUA. To solubilise the MUA 40 mg of NaBH₄ were added, the pH was adjusted to 10 with NaOH 1N and finally the solution was heated to 70 °C. When the solution was clear the heat was turned off. Once at room temperature, 500 µL of recently prepared NaHTe were added into the Cd²⁺ solution and the temperature of mixture was raised and maintained at 160 °C.

Preparation of lactose-C₅-SH protected CdTe QDs. In a three-necked flask, 40 mL of a solution 5 mM of CdCl₂ in deoxygenated nanopure H₂O were mixed with 76 mg of lactose-C₅-SH. The pH was adjusted to 10 with NaOH 1N and when shifting to basic there appeared a white precipitate. The solution was bubbled with Ar for 30 min and then, 500 µL of recently prepared NaHTe were added into the Cd²⁺ solution and the temperature of mixture was raised and maintained at 160°C.

QDs modification with mannose glyconjugates. In a typical reaction 5.2 mg (aprox. $5.60 \cdot 10^{-8}$ moles) of CdTe QDs previously obtained were solved in 2 mL of 10 mM PBS buffer and to this solution 7.1 mg of EDC ($4.5 \cdot 10^{-5}$ moles) and 7.7 mg of NHS ($6.7 \cdot 10^{-5}$ moles) were added. The solution was shaken for 90 min and then 50 mg of mannose neoglycoconjugate (Mann-(CH₂)₂-NH₂) were added. After 180 more min the sample was purified filtering through amicon 30000 MWCO filters.

- CdTe@MPA@Mann:

FT-IR (KBr) = 3422.7, 1637.7, 1560.5, 1400.2, 1265.2, 1123.5, 1055.8, 997.5, 970.8, 892.4, 545.7 cm^{-1} .

Surface charge (as measured by Zsizer, 10 mM PBS) = -7.2 mV.

Aqueous preparation of CdTe@ZnTe core@shell quantum dots

Preparation of MPA protected CdTe@ZnTe QDs. In a three-necked flask, 40 mL of a solution 5 mM of CdCl_2 in deoxygenated nanopure H_2O were mixed with 30 μL of MPA (1-mercaptopropionic acid) and 28 mg of ZnCl_2 . The pH was adjusted to be 9.6 with NaOH 1N and the solution was bubbled with Ar for 30 min. After that, 500 μL of recently prepared NaHTe were added into the Cd^{2+} solution. After the addition of the Te reagent there appears a white precipitate. The temperature of mixture was raised and maintained at 160 $^\circ\text{C}$. Varying the reaction time samples with fluorescent emission covering from green to dark red can be obtained. To purify the QDs, the solution was allowed to cool down to room temperature and then it was centrifuged for 15 min at 1500 g to remove the white precipitate. To the supernatant 80 mL of acetone were added to precipitate the NPs. The nanocrystals were separated by centrifugation, washed twice with EtOH, dialyzed 48 hours against 10 mM PBS pH 7.4 and 8 hours against water, and finally stored lyophilized until further use.

- CdTe@ZnTe@MPA:

FT-IR (KBr) = 1555.8, 1400.7, 1058.7, 956.1, 856.9, 668.5 cm^{-1} .

Surface charge (as measured by Zsizer, 10 mM PBS) = -29.9 mV.

Preparation of L-cys protected CdTe@ZnTe QDs. In a three-necked flask, 0.5 g of $\text{Cd}(\text{ClO}_4)\cdot\text{H}_2\text{O}$ ($1.60\cdot 10^{-3}$ moles), 1.20 g of $\text{Zn}(\text{ClO}_4)\cdot 6\text{H}_2\text{O}$ ($3.20\cdot 10^{-3}$ moles), and 0.42 g of L-cystein ($3.50\cdot 10^{-3}$ moles) were solved in 125 mL of deoxygenated nanopure water. The pH of this solution was modified with NaOH 5 N until it was 'optically clear' and Ar was bubbled for 20 min. Then 5 mL of a 3 mM water solution of NaHTe were injected swiftly and the temperature of the system was raised to 100 $^\circ\text{C}$ maintaining the temperature sensor inside the solution. After the addition of the Te reagent there appeared a white precipitate. Varying the reaction time, samples with

Experimental Part

fluorescent emission covering from green to dark red can be obtained. To purify the QDs, the solution was allowed to cool down to room temperature and centrifuged at 1500 g for 15 min to remove the white precipitate. Then 80 mL of acetone were added to precipitate the NPs. The nanocrystals were separated by centrifugation, washed twice with EtOH, dialyzed 48 hours against 10 mM PBS and 8 hours against water, and finally stored lyophilized until further use.

- CdTe@ZnTe@L-cys:

FT-IR (KBr) = 3378.3, 2918.1, 1448.3, 1793.9, 1655.1, 1395.5, 1360.0, 1263.3, 1162.7, 1069.6, 951.2, 860.3, 640.7, 545.5, 517.3, 466.1 cm^{-1} .

Surface charge (as measured by Zsizer, 10 mM PBS) = -12.3 mV.

Cytotoxicity studies on CdTe and CdTe@ZnTe quantum dots

Cytotoxicity measurements. The biocompatibility of each QD was studied at a range of concentrations covering from 0.1 to 100 $\mu\text{g/mL}$, with C33 cell line using a MTT standard protocol, and with Raji cell line using MTS standard protocol.

$8 \cdot 10^3$ cells for C33, or $0.5 \cdot 10^4$ cells for Raji (80 μL) were seeded in a 96-well plate, and cultured at 37 °C and 5 % CO_2 . 24 hours later 20 μL of solution of nanoparticles at the desired concentration were added to the cells and they were incubated in the same conditions again. After 20 hours, 20 μL of MTT solution (5 mg/mL) were added to each well and the cells were still incubated for 4 hours. Finally, before the measurement, the culture media was removed and 200 μL of DMSO were added to each well to break up cells. The solution was resuspended vigorously to dissolve crystals, and the samples were measured in the spectrophotometer.

CHAPTER 3

Water soluble DNA-magnetic glyconanoparticles

Water soluble DNA-magnetic glyconanoparticles

Introduction

Based on the water-soluble magnetic glyconanoparticles previously described (see chapter 1) we have prepared DNA-functionalized magnetic glyconanoparticles. The idea was to induce a controlled aggregation of the MGNPs by molecular recognition, and sense this process by means of opto-magnetic detection.

The group of Fernando Briones at the Instituto de Microelectronica de Madrid (CSIC) is developing an opto-magnetic biosensor based on the formation, upon molecular recognition, of anisotropic magnetic aggregates that are susceptible of being aligned by an external magnetic field. This alignment will interfere with the polarization of a polarised laser going through the sample and from the measurement of this interference the hydrodynamic radius of the aggregates can be measured.

A number of inorganic materials including various metal nanoparticles have been utilized to develop DNA detection schemes because of the unique physical properties of these materials, including their large extinction and scattering coefficients, catalytic activity and surface electronic. Magnetic nanoparticles have been used in immunoassays and in various reactions involving enzymes, proteins, and DNA, for magnetically controlled transport, and targeted delivery of anti-cancerous drugs [1]. Their reduced size and ability to be transported in biological systems and reacting media is an advantage over conventional support systems. Iron oxide nanoparticles owe their popularity to their numerous attributes such as their magnetic properties that enable them to be directed by an external magnetic field, the possibility to separate them from a reaction mixture, in addition to their low toxicity and biocompatibility.

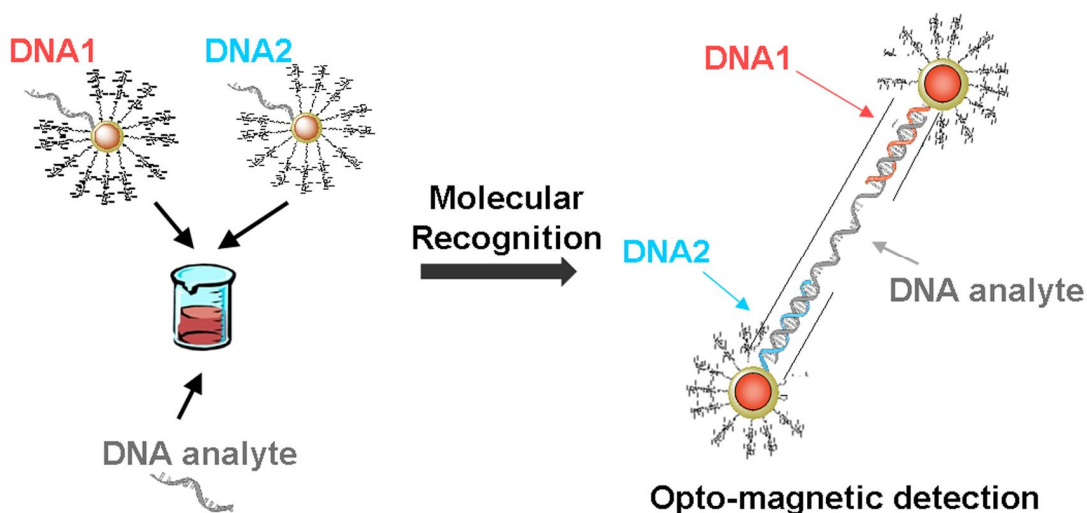
On the other hand, considerable interest over the past two decades has been directed towards the functionalization of gold nanoparticles because of their excellent biocompatibility, stability, and established synthesis protocols [2] [3] [4] [5]. Furthermore, the use of thiol chemistry on a gold surface allows the attachment of molecules with a relative ease using a variety of thiol linked biomolecules including nucleotides [6] [7] [8] [9]. Hence, if the magnetic nanoparticles are provided with a gold coating, then the combined benefits of the robust chemistry for gold surfaces and the uniqueness of magnetic nanoparticles could be realized [10] [11] [12]. Recently, Fan *et*

al. [13], taking advantage of a magnetic separation/mixing process and the amplification feature of colloidal gold label, used gold-coated magnetic beads for immunoassay development. If DNA is labelled with appropriate fluorophores, then their fluorescence quantum yields could be strongly enhanced upon hybridization, which can thus be imaged against a weakly fluorescing background [13].

The development of assemblies of inorganic materials with biomolecules has emerged as a novel approach to the controlled fabrication of functionalized nanostructures and networks. In the last years, the practice of DNA sequence detection has become more and more ubiquitous in genetics, pathology, criminology, food safety, and many other fields [14]. For example, single-strand DNA (ssDNA) probes immobilized to solid materials has proven to be a fundamental process in a variety of biotechnological [15] and biomedical applications [16], including DNA-driven assembly of nanoparticles [14] [17] [18] and biosensors [19]. The interest for this last example, biosensors, is increasing in biomedicine but also in completely different areas as can be in traffic safety (detection of drugs of abuse in saliva). Lower detection limits are demanded each day and currently well-established sensing methodologies are not the best suited to achieve so. For example, enzyme-based assay technology underlying the glucose sensor (commercially in use by diabetic patients) is well suited for analytes in the millimolar concentration range, but cannot be applied with the same results to analytes that are present in the picomolar range. The case of genetic material probes is different. The detection limit provided by current technologies (for example DNA/RNA amplification PCR) is already low enough, but in this case a purification step has to be introduced as this kind of processing is not possible in complex biological media. These reasons altogether make new sensing approaches necessary. Among the possibilities, the magnetic nature of our nanoparticles can be exploited also in this field. In recent years a few different prototypes of optomagnetic biosensors have appeared in the literature with promising features [20] [21] [22] [23]. Among them, detection of low concentrations of analyte, fast assay speed and possibility of analyte multiplexing are the most interesting ones.

DNA-functionalised magnetic glyconanoparticles as probes for biosensors

In this study we have prepared $\text{Fe}_3\text{O}_4@Au$ magnetic nanoparticles coated with 100 % lactose glycoconjugates and functionalised with a controlled number of specific ssDNA molecules to be used as sensing probes to detect DNA disease markers in biological fluids. In collaboration with Briones's group and the company Progenika S.A. (Bilbao) we designed a proof of concept. We hypothesize that MGNPs functionalised with selected strands of DNAs, complementary to the DNA to be detected in the biological sample, would form aggregates by hybridization of the DNA analyte with the complementary DNAs onto the MGNPs, and be detected by the opto-magnetic sensor (scheme 9).



Scheme 9. Representation of the molecular recognition process required for the detection of the DNA analyte.

To functionalise the MG-NP, two different non-complementary DNA strands were selected which are modified either in the 5' or 3' positions with a 5-mercaptopentyl chain to attach them to the gold surface:

BS_1SH_5 : 5'-HS-C₅-AAAAAGGAGTGAGATGAGAA-3'

BS_2SH_3 : 5'-GAAGGGTTGGTCTGTAAAAA-C₅-SH-3'

The DNA analyte was an ssDNA oligomer complementary in the 3' position to BS_1SH_5 and in 5' position to BS_2SH_3 . Both sequences were separated by a variable number (33

Results and Discussion

nt, 17 nt, or 1 nt) of non-complementary nucleotide bases to test the influence of the distance in the molecular recognition (hybridization process) between the complementary strands. As control a 47 nucleotide non-complementary sequence was chosen:

Complementary 33 nt:

5'-ACAGACCAACCCTTCAGTTCAAAGGATACAAAGAATGTTACACGACAGTTCTCATCTCACTCC-3'

Complementary 17 nt:

5'-ACAGACCAACCCTTCAGCAAAGGATACAAAGATTCTCATCTCACTCC-3'

Complementary 1 nt:

5'-ACAGACCAACCCTTCATTCTCATCTCACTCC-3'

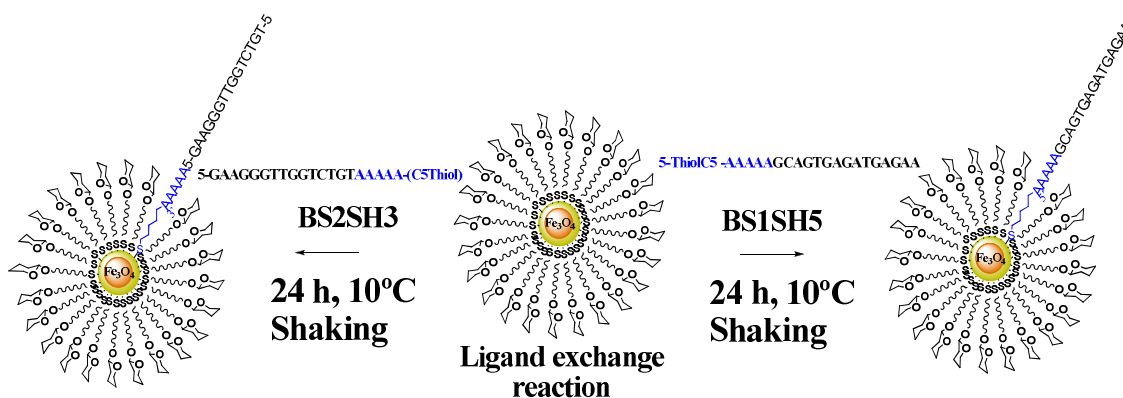
Non-complementary:

5'-ATAATAGGTCAAAGGATACAAAGAATGTTACACGCCTCTATCGCAA-3'

The surface modification of the LactC₅ gold-coated magnetic nanoparticles with DNA oligomers was carried out by ligand exchange chemistry. The hybridization of the target oligonucleotides was evaluated by melting point measurements, electrophoretic mobility, transmission electron microscopy, and atomic force microscopy to assess the amount of bound targets. Besides, the specificity with respect to non-complementary strands was also analysed.

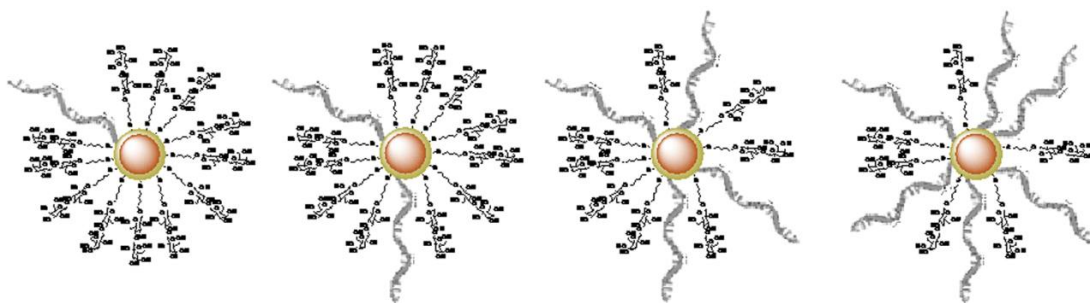
Preparation and characterization of DNA-functionalised magnetic glyconanoparticles

The ligand exchange reaction between the 100 % functionalised LactC₅-MGNPs and the BS₁SH₅ or BS₂SH₃ DNA oligomers was performed in buffer at 10°C during 24 h (scheme 10).



Scheme 10. DNA attachment to magnetic nanoparticle

After a reductive pretreatment with dithiothreitol (DTT) to disassemble disulfur linkages, ssDNA chains were incubated with MGNPs to get a ligand exchange. Different DNA oligomer ratios were used for the functionalization of the MGNPs. The stoichiometries between the MGNPs and the ssDNA were controlled and varied (MGNPs:ssDNA 1:1, 1:2, 1:4 and 1:6) to obtain final nanoparticles with an average amount of one, two, four or six DNA chains (scheme 11).



Scheme 11. Schematic representation of the DNA-nanoparticles obtained at different stoichiometries by ligand exchange reaction.

The final products were purified by centrifugal filtering and washing, and stored frozen at $-20\text{ }^{\circ}\text{C}$ until needed.

For the characterization of the DNA-MGNPs structures, agarose gel electrophoresis (AGE) was chosen. In this kind of gels, particles run towards positive or negative electrode at a speed dependent on both their mass and their charge. The attachment of ssDNA molecules do not change significantly the mass of the nanoparticle, but the variation in charge (DNA is a highly negatively charged biopolymer under physiological conditions) can be really noticeable. The MGNPs show negative Z-potential due to the negative charge coming out from the gold coating (figure 23 B). As the stoichiometry of DNA with respect to MGNPs increases, the front of the resulting band runs faster towards the positive electrode, supporting the presence of an increased number of DNA chains per nanoparticle (figure 23). There is a linear correlation between the R_f of the DNA-MGNPs and the number of DNA molecules on their surface (figure 23 C).

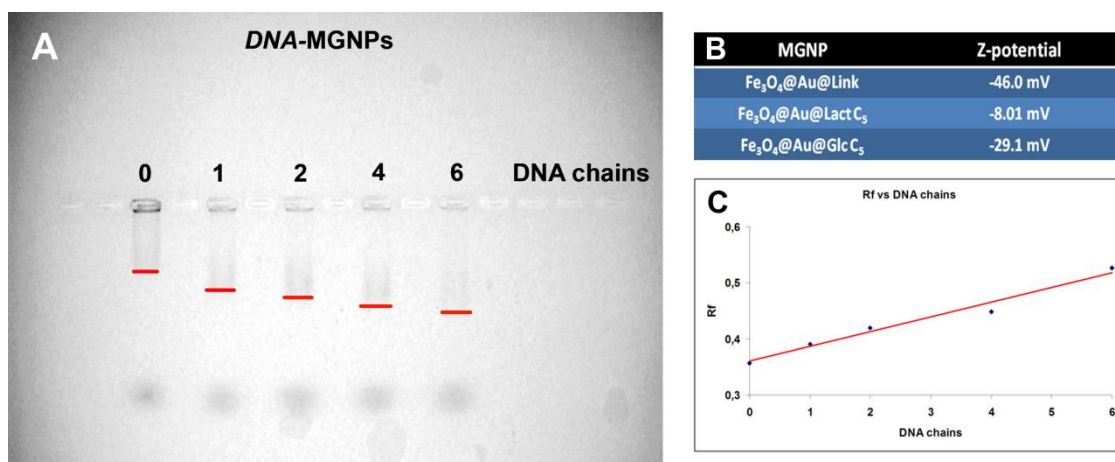


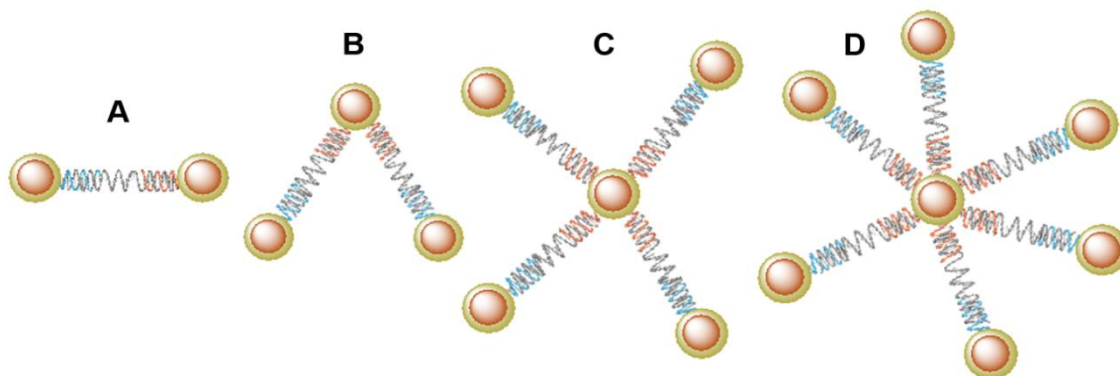
Figure 23. **A**, AGE of the different constructions; line 1: MGNPs; line 2: (BS₁SH₅)₁-MGNPs; line 3: (BS₁SH₅)₂-MGNPs; line 4: (BS₁SH₅)₄-MGNPs; line 5: (BS₁SH₅)₆-MGNPs. **B**, Z-potential measurements from different 100% density MGNPs. **C**, plot of the Rf of the (BS₁SH₅)_x-MGNPs conjugates versus the amount of DNA chains per nanoparticle showing a linear relationship between both.

Hybridization of DNA-magnetic glyconanoparticles

To further assess the presence of DNA molecules on the MGNPs, hybridization experiments were carried out. Once the hybridised products were obtained we analysed changes in the absorption properties of the nanoparticles. The deshybridization was followed by UV spectroscopy (melting experiments), and the formation of dimers/multimers of nanoparticles was followed also by TEM and AFM.

The ssDNA sequences (BS₁SH₅ and BS₂SH₃) onto the MGNPs were not complementary to avoid aggregation of DNA-MGNPs in the absence of the analyte. The ssDNA analyte has one end (3') complementary to BS₁SH₅ and the other end (5') to BS₂SH₃. The length of the rest of the DNA molecule between the two complementary ends was 33 nt, 17 nt or 1 nt to test its influence on the formation of the final complexes. The complementary ssDNA was suspended in TE buffer and mixed with an equimolar solution of both (BS₁SH₅)₁- and (BS₂SH₃)₁-MGNPs. This solution was then subjected to a standard hybridization protocol, in which the final step of cooling down to room temperature was performed slowly to reduce the possibility of self-folding of DNA chains. Following this protocol, we have tried to obtain dimers of nanoparticles (Scheme 11 A). To obtain tri, penta, and hepta discrete structures, the nanoparticles bearing two, four, or six DNAs have been hybridized with nanoparticles bearing only

one DNA chain (scheme 12). Following the same protocol, big aggregates can also be obtained using $(\text{DNA})_x$ -MGNGPs with x higher than 1 in both cases.



Scheme 12. Possible discrete structures of DNA-MGNGPs complexes; **A**, $(\text{BS}_1\text{SH}_3)_1$ -MGNGPs 1:1 $(\text{BS}_2\text{SH}_3)_1$ -MGNGPs; **B**, $(\text{BS}_1\text{SH}_3)_2$ -MGNGPs 1:2 $(\text{BS}_2\text{SH}_3)_1$ -MGNGPs; **C**, $(\text{BS}_1\text{SH}_3)_4$ -MGNGPs 1:4 $(\text{BS}_2\text{SH}_3)_1$ -MGNGPs; **D**, $(\text{BS}_1\text{SH}_3)_6$ -MGNGPs 1:6 $(\text{BS}_2\text{SH}_3)_1$ -MGNGPs.

Annealing any DNA-MGNGPs with $(\text{DNA})_1$ -MGNGPs, produced no visible change in colour. However, when both of the starting nanoparticles had more than one DNA chains, there was a great shift of the plasmon resonance peak towards the blue (figure 24 C). This translates in a colour change from purple-red to grey-blue. With time precipitation of aggregates is observed and colour disappears due to the precipitation of the big aggregates formed.

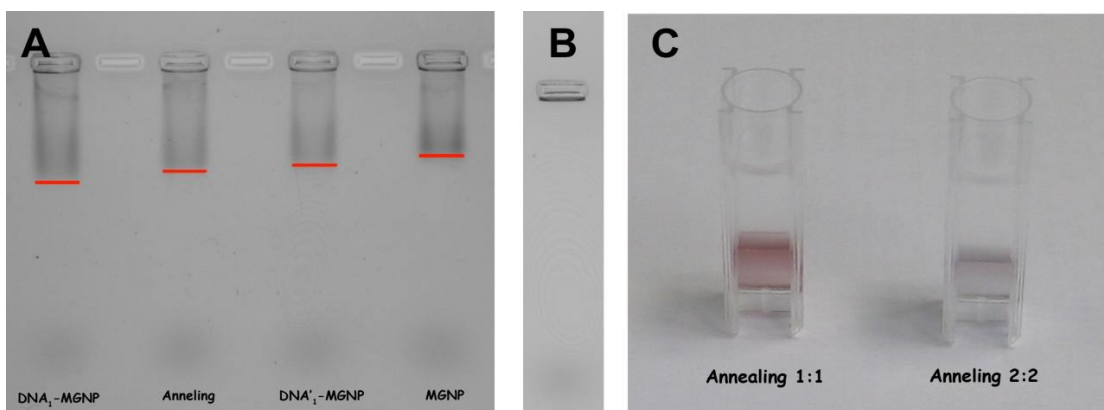


Figure 24. **A**, AGE of annealed complex in comparison to its mother samples; line 1: $(\text{BS}_1\text{SH}_3)_1$ -MGNGPs; line 2: $(\text{BS}_1\text{SH}_3)_1$ -MGNGPs:33 nt: $(\text{BS}_2\text{SH}_3)_1$ -MGNGPs; line 3: $(\text{BS}_2\text{SH}_3)_1$ -MGNGPs. **B**, complex $(\text{BS}_1\text{SH}_3)_2$ -MGNGPs: $(\text{BS}_2\text{SH}_3)_2$ -MGNGPs is too big to enter into the gel remaining stacked in the well. **C**, solution of complex $(\text{BS}_1\text{SH}_3)_1$ -MGNGPs:33 nt: $(\text{BS}_2\text{SH}_3)_1$ -MGNGPs (right) and complex $(\text{BS}_1\text{SH}_3)_2$ -MGNGPs:33 nt: $(\text{BS}_2\text{SH}_3)_2$ -MGNGPs (left). A shift to the blue (of 20 nm in the gold surface plasmon) is clearly visible when nets are formed.

Results and Discussion

The specificity of this hybridization was tested using a non-complementary ssDNA strand. An experiment using both (DNA)₂-MGNPs and the non-complementary strand was carried out and neither precipitation nor shift to the blue was observed.

Agarose gel of the product from the hybridization of DNA₁-MGNPs, the starting nanoparticles, and the control MGNNPs without DNAs was run (figure 24). In this case the result was more difficult to interpret than before as now both factors (mass and charge) change significantly. The mass of the hybrids is 2 times that of the starting DNA-MGNNPs and so is the charge. The effect of these two factors is opposite. An increase of the mass of the particles in a gel makes the complex run slower towards the corresponding electrode. Otherwise, an increase in charge makes the particles move faster to the electrode. In figure 24 A, we can clearly see that the hybridised product runs slightly different than the starting nanoparticles. This same agarose gels could not be repeated with hybridised products coming from (DNA)₂-MGNNPs as these aggregates are already too big to enter into the gel pores and they stay stacked in the well (figure 24 B).

Transmission electron microscopy (TEM) and contact mode Atomic Force Microscopy (AFM) were used to better characterise the hybridized products. Figure 25 A shows the result of the hybridization of DNA₁-MGNNPs with the 33nt DNA analyte without further purification. In the overview TEM micrographs, dimmers of nanoparticles are clearly visible. There are also trimmers and nanoparticles standing alone. From a statistical point of view, it is not possible to obtain in the ligand exchange reaction nanoparticles bearing only one DNA chain each. The formation of trimmers and the presence of isolated nanoparticles can be explained in terms of the production, in the ligand exchange reaction, of a noticeable proportion of nanoparticles bearing 2 and 0 chains. Then, nanoparticles bearing two DNAs can anneal simultaneously with two nanoparticles and two DNA analytes to form the trimmers.

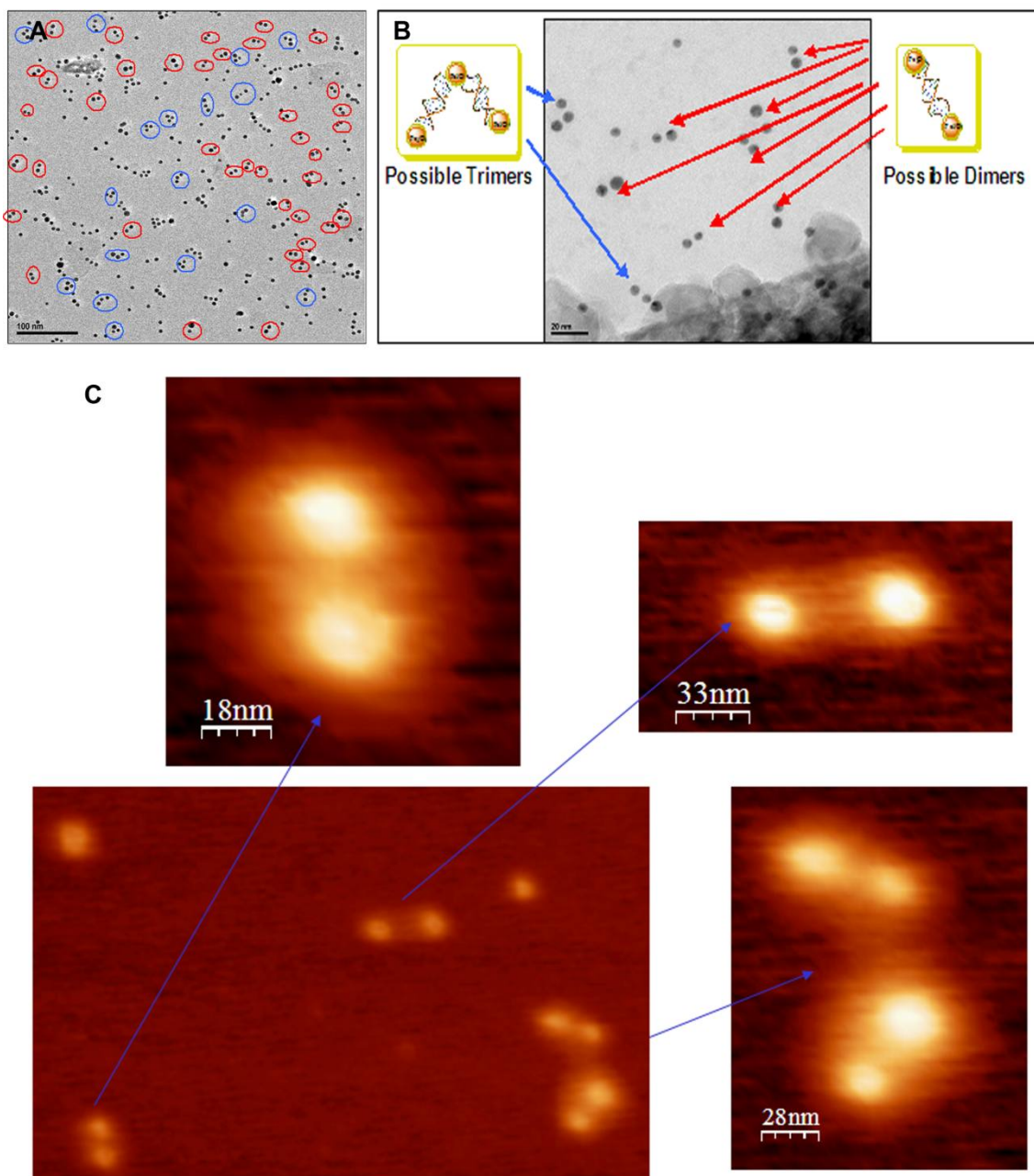


Figure 25. **A**, TEM image of hybridised $(BS_1SH_5)_1$ -MGNPs:33 nt: $(BS_2SH_3)_1$ -MGNPs sample before centrifuging. **B**, TEM image of same sample after centrifuging at 13400 rpm for 10 mins. **C**, low-magnification AFM image and magnified views of several nanoparticle dimers $(BS_1SH_5)_1$ -MGNPs:33 nt: $(BS_2SH_3)_1$ -MGNPs deposited in a drop over recently cleaved mica and slowly allowed to dry before imaging.

To separate dimmers and trimmers from isolated nanoparticles, the sample was centrifuged at 14000 g for 10 mins and the supernatant was discarded. TEM micrographs of the precipitated nanoparticles show mainly dimmers and trimmers and most *lonely* nanoparticles were washed away (figure 25 B). Similar results were obtained in the hybridization with the 17 nt DNA. AFM confirmed that the dimmers

Results and Discussion

observed in TEM are constituted by two magnetic cores of DNA-MGNPs coupled by a softer organic shell (figure 25 C).

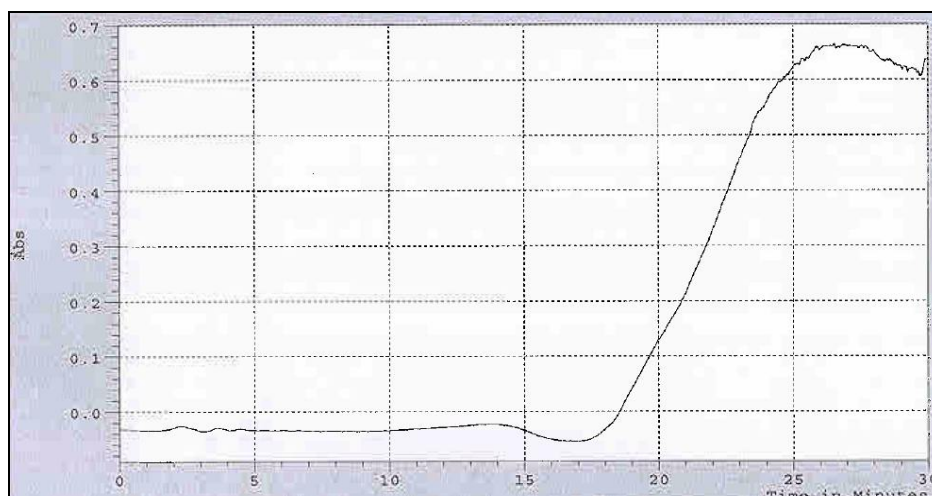


Figure 26. UV-Vis melting point graph of the annealed product of 1:1:1 ratio of $(BS_1SH_3)_1$ -MGNPs:33 nt: $(BS_2SH_3)_1$ -MGNPs.

To further assess the hybridization of the DNA strands, we profited from the changes in the absorption spectra at 260 nm when DNA goes from double strand to single strand (melting process). This change from double to single chain can be forced an increase of the temperature over the so called melting temperature (T_m) which is sequence specific and can be related to the proportion of G-C pairs in the double stranded DNA. The experiment consists on the monitoring of the absorption at 260 nm over time as the temperature of the sample is increased from room temperature to 90 °C. The result obtained is shown in figure 26 and was exactly the expected one.

Attempts to detect the hybridization aggregates with the opto-magnetic sensor under development by Briones' group failed. The magnetic core sizes and the distance between them in the aggregates may be the cause of the unsuccessful detection.

References

1. Niemeyer, C.M. and B. Ceyhan, *DNA-Directed Functionalization of Colloidal Gold with Proteins*. *Angew Chem Int Ed Engl*, 2001. **40**(19): p. 3685-3688.
2. Barrientos, A.G., et al., *Gold glyconanoparticles: synthetic polyvalent ligands mimicking glycolyx-like surfaces as tools for glycobiological studies*. *Chemistry*, 2003. **9**(9): p. 1909-21.

Results and Discussion

3. de La Fuente, J.M., et al., *Gold Glyconanoparticles as Water-Soluble Polyvalent Models To Study Carbohydrate Interactions*. *Angew Chem Int Ed Engl*, 2001. **40**(12): p. 2257-2261.
4. de la Fuente, J.M. and S. Penades, *Understanding carbohydrate-carbohydrate interactions by means of glyconanotechnology*. *Glycoconj J*, 2004. **21**(3-4): p. 149-63.
5. Minard-Basquin, C., et al., *Gold-nanoparticle-assisted oligonucleotide immobilisation for improved DNA detection*. *IEE Proc Nanobiotechnol*, 2005. **152**(2): p. 97-103.
6. Ojeda, R., et al., *Preparation of multifunctional glyconanoparticles as a platform for potential carbohydrate-based anticancer vaccines*. *Carbohydr Res*, 2007. **342**(3-4): p. 448-59.
7. Park, S.Y., et al., *Structures of DNA-linked nanoparticle aggregates*. *J Phys Chem B*, 2006. **110**(25): p. 12673-81.
8. Hurst, S.J., A.K. Lytton-Jean, and C.A. Mirkin, *Maximizing DNA loading on a range of gold nanoparticle sizes*. *Anal Chem*, 2006. **78**(24): p. 8313-8.
9. Kim, E.Y., et al., *A real-time PCR-based method for determining the surface coverage of thiol-capped oligonucleotides bound onto gold nanoparticles*. *Nucleic Acids Res*, 2006. **34**(7): p. e54.
10. Mikhaylova M, K.K., Berry CC, Zogorodni A, Toprak M, Curtis ASG, Muhammed M, *BSA immobilization on amine-functionalized superparamagnetic iron oxide nanoparticles*. *Chem. Mater.*, 2004. **16**: p. 2344-2354.
11. Lo, C.K., D. Xiao, and M.M.F. Choi, *Homocysteine-protected gold-coated magnetic nanoparticles: synthesis and characterisation*. *Journal of Materials Chemistry*, 2007. **17**: p. 2418–2427.
12. Park, H.Y., et al., *Fabrication of magnetic core@shell Fe oxide@Au nanoparticles for interfacial bioactivity and bio-separation*. *Langmuir*, 2007. **23**(17): p. 9050-6.
13. Fan, A., C. Lau, and J. Lu, *Magnetic bead-based chemiluminescent metal immunoassay with a colloidal gold label*. *Anal Chem*, 2005. **77**(10): p. 3238-42.
14. Wolfgang Fritzsche, T.A.T., *Metal nanoparticles as labels for heterogeneous, chip-based DNA detection*. *Nanotechnology*, 2003. **14**: p. R63-R73.
15. Sekar, M.M., W. Bloch, and P.M. St John, *Comparative study of sequence-dependent hybridization kinetics in solution and on microspheres*. *Nucleic Acids Res*, 2005. **33**(1): p. 366-75.
16. Peterson, A.W., R.J. Heaton, and R.M. Georgiadis, *The effect of surface probe density on DNA hybridization*. *Nucleic Acids Res*, 2001. **29**(24): p. 5163-8.
17. Petrovykh, D.Y., et al., *Quantitative analysis and characterization of DNA immobilized on gold*. *J Am Chem Soc*, 2003. **125**(17): p. 5219-26.
18. Mir, K.U. and E.M. Southern, *Determining the influence of structure on hybridization using oligonucleotide arrays*. *Nat Biotechnol*, 1999. **17**(8): p. 788-92.
19. Kerman, K., Kobayashi, M., Tamiya, E., *Recent trends in electrochemical DNA biosensor technology*. *Meas. Sci. Technol.*, 2004. **15**: p. R1-R11.
20. Bruls, D.M., et al., *Rapid integrated biosensor for multiplexed immunoassays based on actuated magnetic nanoparticles*. *Lab on a chip*, 2009. **9**: p. 3504-3510.

Results and Discussion

21. Dittmer, W.U., et al., *Rapid, high sensitivity, point-of-care test for cardiac troponin based on optomagnetic biosensor*. Clinica Chimica Acta, 2010. **411**: p. 868-873.
22. Wilhelm, C., F. Gazeau, and J.C. Bacri, *Binding of biological effectors on magnetic nanoparticles measured by a magnetically induced transient birefringence experiment*. Physical reviews E, 2002. **65**(3): p. 031404.
23. Aurich, K., et al., *Affinity analysis for biomolecular interactions based on magneto-optical relaxation measurements*. Nanotechnology, 2008. **19**(50): p. 505102.

Experimental part

Materials and methods

All nanocrystals were characterized before and after any step by low and high resolution TEM on a JEOL JEM 2100F microscope. UV-Vis spectra were recorded in a Beckman-Coulter DU 800 spectrophotometer. All the reagents were purchased from Sigma-Aldrich. All solvents were analysis grade (acetone, dichloromethane, methanol, hexane and 2-propanol) and were supplied by Sharlab. All the reagents were used as received without further purification.

Preparation and characterization of DNA-functionalised magnetic glyconanoparticles

DNA pretreatment [1]. 28 μg of BS_2SH_3 oligomer were mixed with 500 μL of a solution 50 mM of DTT in 10 mM PBS pH 7.4 to reduce the disulfur linkages between chains. This solution was allowed to shake for 16 hour at 10 °C. After this period, the excess of DTT was removed by an extraction with ethylacetate (x3 and three times the volume of the solution of DNA).

Coupling of DNA to MGNPs. To couple the DNA to the nanoparticle a ligand exchange reaction was used. Four different stoichiometries were used, 1:1, 1:2, 1:4, and 1:6 MGNPs:DNA. Basically, four alicuots of 250 μg of functionalized MGNPs ($3.37 \cdot 10^{-10}$ moles) each, were mixed respectively with 2.2, 4.3, 8.6 and 12.96 μg of the reduced oligonucleotides. These solutions were allowed to shake at 10°C overnight. The final conjugates were purified by centrifugal filtering through Amicon filters (MWCO 100000).

Agarose gel electrophoresis (AGE) of the constructions. To prepare the agarose gel we solved 4.5 g of agarose in 150 mL of TBE buffer. Five wells were seeded with 25 μL of DNA-MGNPs solution (aprox 1 $\mu\text{g}/\mu\text{L}$) plus 6 μL of DNA loading buffer. TBE buffer was used as running buffer and finally the gel was run at 90 V for 2 hours. No

Experimental Part

staining was needed to visualize the final position of the bands as the DNA-MGNPs conjugates were coloured.

Annealing. In a 500 μL eppendorf 25 μL ($5.2 \cdot 10^{-11}$ moles of DNA) of each of the DNA modified MNPs (in 10 mM PBS pH 7.4) were mixed with 2 μL ($5.2 \cdot 10^{-11}$ moles) of the aliquot of complementary DNA. This eppendorf was heated in a thermomixer to 95 $^{\circ}\text{C}$ and maintained at this T for two minutes. Then, the T was allowed to decrease to room T during 45 minutes. This slow cooling avoids the self folding of DNA. When this procedure was completed, the samples were frozen till further use.

Melting experiment. Whole purified sample from the previous annealing was diluted to 500 mL with 10 mM PBS and loaded into a disposable UV cubette. The cubette was placed inside the UV-Vis spectrophotometer with a peltier temperature controller installed. The absorbance at 260 nm was monitored each 10 s during 30 min while the temperature was increased to 90 $^{\circ}\text{C}$.

References

1. Park, S., K. Brown, and K. Hamad-Schifferli, *Changes in Oligonucleotide Conformation on Nanoparticle Surfaces by Modification with Mercaptohexanol*. Nano Letters, 2004. 4(10): p. 1925-1929.

CHAPTER 4

Fluorescent/magnetic *immuno-* glyconanoparticles and quantum dots

Magnetic/fluorescent *immuno-*glyconanoparticles and quantum dots

Introduction

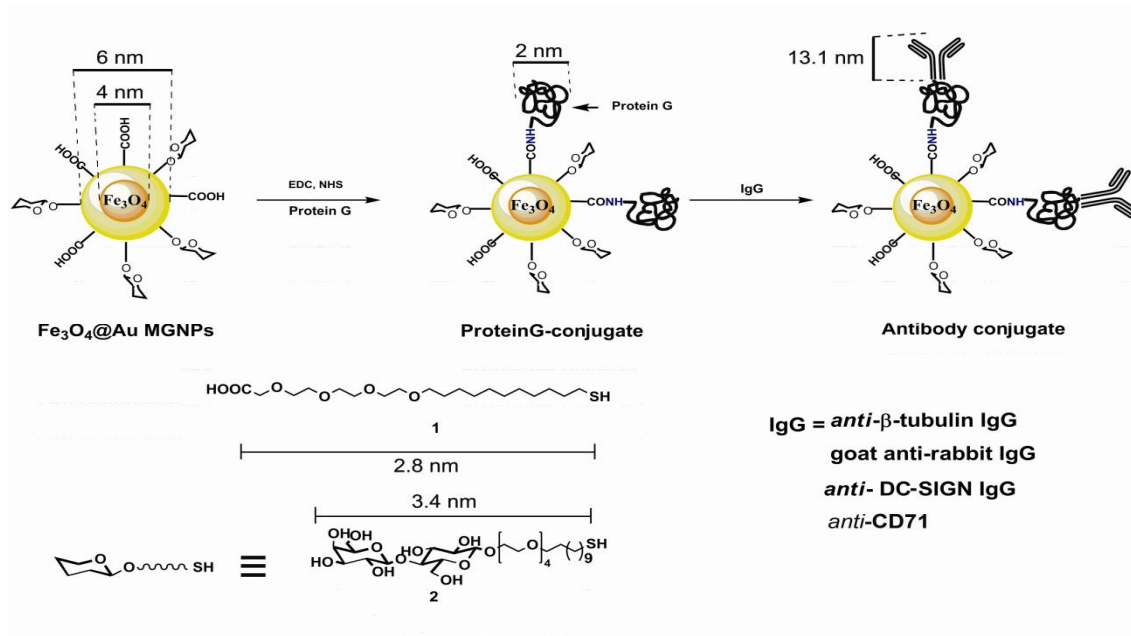
This chapter presents the biofunctionalization of previously prepared nanoparticles (magnetic glyconanoparticles and quantum dots, see chapters 1 and 2) with proteins for their further use as probes for the selective labelling and tracking of cells by magnetic resonance and optical molecular imaging.

The challenge for the specific magnetic labelling of cells is to develop well-characterized and versatile magnetic platforms conjugated with appropriate vectors that present high binding affinity and specificity for their natural target. Antibodies are highly specific biological vectors. Antibody-coated magnetic particles were first prepared as contrast agents to image tumours [1], myocardial infarct [2], and cells [3] [4] [5]. In these constructs the biomolecule was conjugated to the magnetic particles using different protocols, which do not assure the efficient orientation of the antibody. In other cases, attachment of the antibody was accomplished via Protein G coupling [6], although in this work the use of natural protein G yielded problems concerning the unspecific adsorption of proteins. Nowadays the availability of commercial recombinant protein G lacking the albumin and cell surface binding domains has solved this problem. In general, the surface coating of these magnetic platforms (dextran, PEG, polymers, surfactants or silica) avoids the aggregation of the nanoparticles, but increases significantly their sizes. Small particle size is desirable to prevent fast elimination by the reticuloendothelial system (RES) and to allow the pass through the capillary's pores in their way to the target organ.

In this chapter we describe the functionalization of gold coated magnetic glyconanoparticles coupled to protein G as scaffold over which IgG antibodies can be specifically captured and presented with a perfect orientation without loss of biofunctionality. The well-oriented capture by Protein G of any IgG converted the glyco-ferrites in targeted tools for the specific labelling of cell surface receptors.

Preparation and characterization of magnetic *immuno-glyconanoparticles*

The free carboxylic group of the hybrid water-soluble glyconanoparticles allows direct covalent immobilization of commercially available recombinant protein G by amide coupling. MGNPs were first activated with EDC/NHS, and then dissolved in 10 mM PBS (pH = 7.4) in the presence of 5 equivalents of protein G (Scheme 13).



Scheme 13. Scheme of the biofunctionalization of water soluble glyco-nanoferrites to obtain magnetic *immuno-glyconanoparticles*.

The presence of protein G was verified by MALDI-TOF spectrometry where peaks at $[M^+]$ 21830, 43754, 66718, and $[M^{2+}]$ 10925 corresponding to monomer, dimer, trimer, and doubly charged protein G, respectively were obtained (Figure 27). Protein G immobilization technique here used has shown good reproducibility. The r_2 relaxivity values ($137.44 \text{ mM}^{-1}\text{s}^{-1}$, 10 mM PBS, 25 °C, 1.4 Ts) of the Protein G-MGNP conjugate did not change remarkably related to the precursory MGNPs.

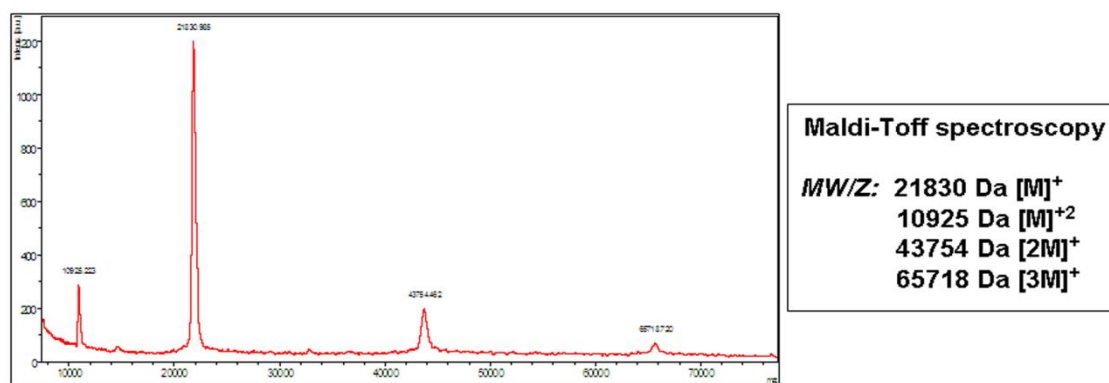
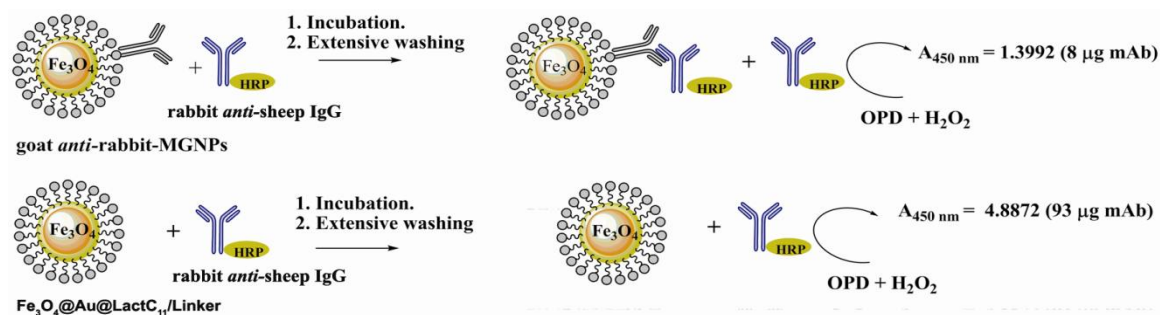


Figure 27. Maldi-Toff spectra of Protein G-MGNP conjugate showing peaks at 21830, 43754, 66718 and 10925 corresponding to [M]⁺ protein G, dimer [2M]⁺, trimer [3M]⁺ and [M]⁺² protein G respectively.

The oriented capture of antibodies by protein G has been shown to be superior for retaining their activity versus the disordered orientation of IgG molecules obtained by direct functionalization onto the nanoparticle's surface. Protein G-MGNP conjugate was incubated with different antibodies in basic 10 mM PBS for 6 h at 10 °C. The conjugates were purified by centrifugation until the washings did not show any free antibody (by SDS-page analysis). To confirm the presence of the antibody on the MGNPs, SDS-PAGE electrophoresis was carried out [7]. Although the nanoparticles are too heavy to run into this kind of gels, the bands of the antibody present on the surface were clearly visible at ~25 and ~50 kDa, which correspond to the light- and heavy-chain of the antibody, respectively (figure 29 A). The amount of antibody present on the MGNP-conjugate was also estimated by quantifying the amount of recovered antibody in the supernatant by Bradford method [8]. The result indicates that the number of antibody molecules per nanocrystal was around three.

Evaluation of the functionality of the IgG coupled magnetic immunoglyconanoparticles by different techniques. In order to quantify antibody activity, an immunoassay was performed (scheme 14) where a goat anti-rabbit IgG was coupled to the Protein G-MGNP conjugate and a HRP-labelled rabbit anti-sheep IgG was chosen as target antibody [9]. As control experiment, bare MGNPs were also subjected to the immunoassay.



Scheme 14. Principle of immunoassay for quantifying the functionality of the antibody in the conjugate goat anti-rabbit MGNPs. The binding of target antibody (rabbit anti-sheep IgG) to goat anti-rabbit MGNP conjugate was estimated in terms of horseradish peroxidase (HRP) enzymatic activity. As control MGNPs without protein G or Ab were used.

HRP-labelled rabbit anti-sheep IgG is recognized only by well-oriented goat anti-rabbit IgG. The oxidation of *o*-phenylenediamine (OPD) catalyzed by horseradish peroxidase enzyme was evaluated by the change in the absorbance at 450 nm. The different absorbance intensities obtained for the control and the goat anti-rabbit-MGNPs experiments with HRP-labelled IgG revealed that 92% of the secondary mAb was recognized by the antibody-MGNPs conjugate (scheme 14). The amount of non-specific interactions was negligible as indicated by the control experiment.

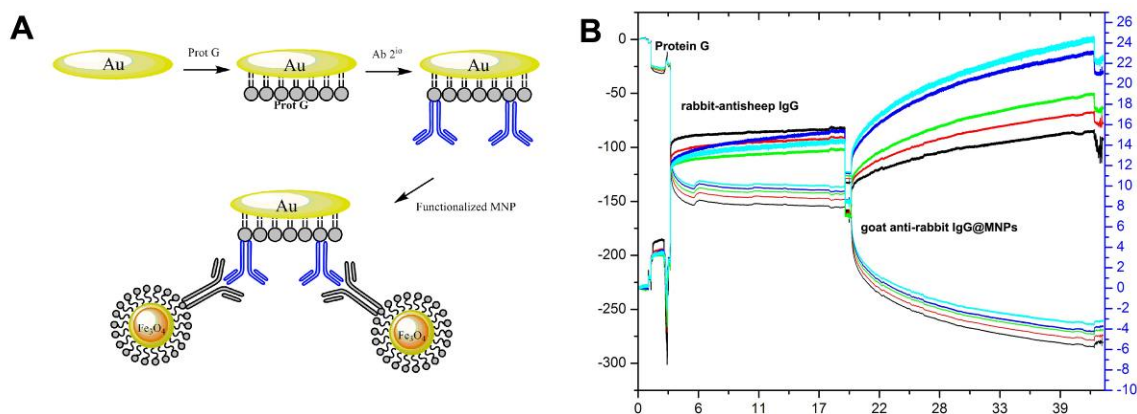


Figure 28. A, schematic representation of the QCM-D experiments to confirm the biofunctionality of goat anti-rabbit MGNPs. Rabbit anti-sheep IgG was used as target antibody. B, QCM data showing functionality of the goat anti-rabbit MGNPs. The plot shows the change of frequency Δf and dissipation ΔD (lower and upper plots, respectively) of a gold QCM sensor after the absorption of protein G (step 1), immobilization of the target antibody rabbit anti-sheep IgG (step 2) and specific recognition by MGNPs@ProtG@goat anti-rabbit IgG (step3) as a function of the time.

Results and Discussion

Quartz Crystal Microbalance with Dissipation (QCM-D) experiments also confirmed the biofunctionality of the antibody in the MGNP-conjugate. Figure 28 shows a schematic representation of the designed QCM experiment and the corresponding QCM curves. As shown by the shift in frequency with time in the first step of figure 28 B, protein G gets adsorbed rapidly onto the gold surface. Upon buffer rinsing, only a small percentage of protein gets desorbed. When the antibody is added (step 2), a much higher shift in the frequency is observed as expected from the difference of molecular size and thickness of the antibody layer ($\sim 13.1 \times 10.5 \times 7.3$ nm versus ~ 2.0 nm radius for protein G), if we assume monolayer coverage. Finally, a stronger shift in frequency, caused by the coupling of the *immuno*-MGNP conjugate (step 3) is observed. In this case, a slower binding kinetics is also observed for the complexes because of their slower diffusion due to the higher molecular weight. In the control experiment, no addition of mass to the sensor was observed when non-functionalised MGNPs were added.

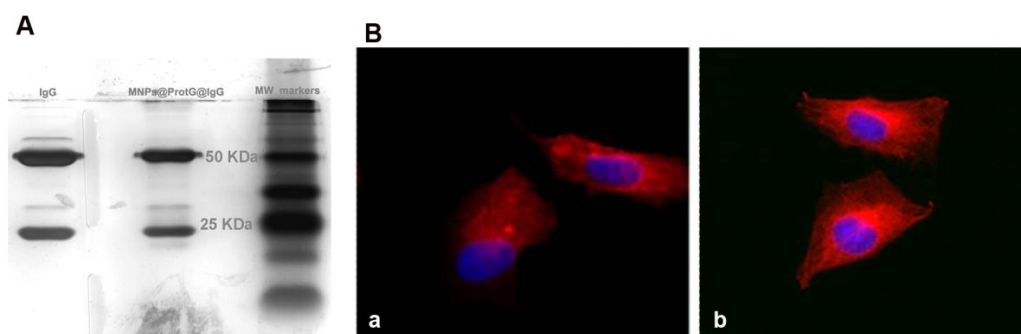


Figure 29. A, SDS-PAGE of the anti-human β -tubulin IgG (left line), anti-human β -tubulin *immuno*-MGNP conjugate (central line) and molecular weight markers (right line). B, Immunocytochemistry of C33 cells with a) free mouse anti-human β -tubulin mAb and b) anti-human β -tubulin *immuno*-MGNPs. Red: β -tubulin, blue: DAPI staining of the nucleus.

The labelling potential of our antibody-conjugated MGNPs in cells was tested by immunocytochemistry fluorescence microscopy. A monoclonal mouse anti-human β -tubulin IgG antibody was conjugated to Protein G-MGNPs and immunocytochemistry of epithelial cell line C33 was performed. The microtubules of C33 cells were stained with anti-human β -tubulin MGNPs and with the free antibody as a control. The same microtubule morphology was stained by the control (free) and the anti-human β -tubulin MGNPs, thus confirming the functionality and specificity of the complex antibody-MGNP after conjugation (figure 29 B).

Preparation and characterization of multifunctional fluorescent-magnetic *immuno*-glyconanoparticles

Magnetic resonance imaging (MRI) is gaining importance in medical diagnosis as technology improves (higher fields and stronger gradients) and also as new contrast agents are developed. Anyway there are still inherent features of the technique that unable it to compete with for example fluorescence microscopy. The resolution obtained by both methodologies is still not comparable (mm to μm for MRI *vs* ~ 200 nm for fluorescence microscopy [10]) although great efforts are being done in the development of micro-imaging systems for MRI. This reason explains why multifunctional contrast agents with both magnetic properties and fluorescence emission are attracting so much interest from the scientific community [10] [11] [12] [13]. We have tried to increase the capabilities of our magnetic platform (*immuno* magnetic glyconanoparticles, *immuno*-MGNPs) attaching to its surface organic fluorophores to achieve dual fluorescent-magnetic probes (*immuno*-FMGNPs).

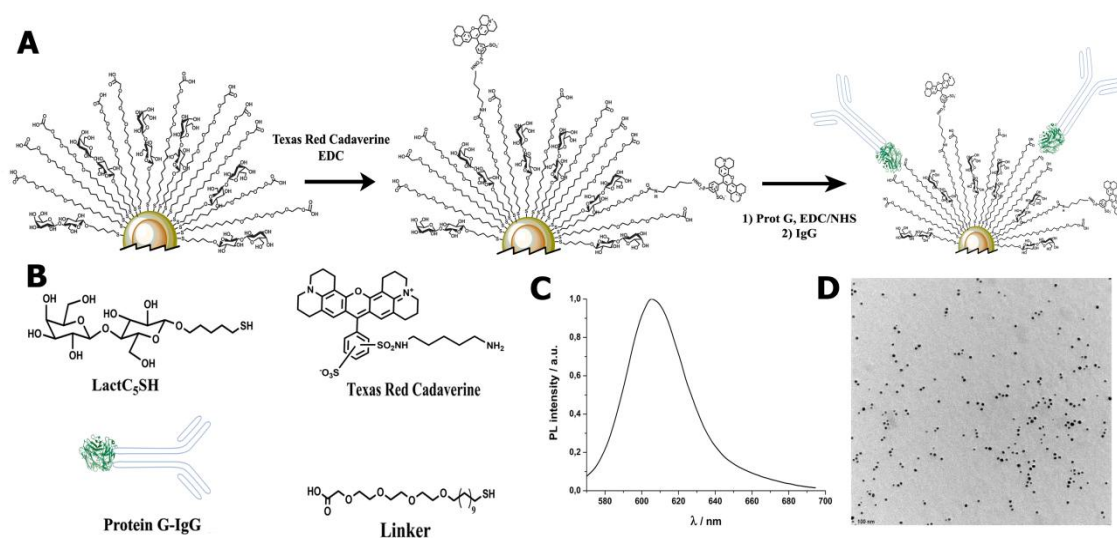


Figure 30. **A**, schematic representation of fluorescent-magnetic immuno glyconanoparticle (*immuno*-FMGNP) preparation. **B**, molecules involved in *immuno*-FMGNPs preparation. **C**, normalized emission spectra of *immuno*-FMGNPs. **D**, TEM micrograph of FMGNPs.

The coupling of the fluorescent dye was designed to be compatible with the rest of protocols developed for the functionalization of the MGNPs (see previous sections in this chapter), and the fluorophore itself was chosen with a chemical structure without

Results and Discussion

reactive groups in the chemistry applied. The chosen fluorophore was Texas Red cadaverine (λ_{exc} 595 nm, λ_{em} 615 nm). The chemical structure of this dye is available, it presents no interfering chemical groups for the later reactions, and it emits in the red region of the spectra that minimizes the interferences from the natural auto-fluorescence of cells [14]. The chemistry used for the coupling of this fluorescent dye to the nanoparticles was the same used for the protein G. An amide bond is formed between CO_2H groups of the linker onto the MGNPs and the -NH_2 group of the Texas red linker. Using a mixture 1:5 of DMSO/ H_2O as solvent, the fluorophore was attached to the nanoparticle in a controlled way. After centrifugal purification, the amount of Texas red onto the MGNPs, was determined indirectly by UV-Vis spectroscopy by measuring the amount of dye present in the washings. The fluorescence of the conjugate (F-MGNPs) was checked by fluorescence spectroscopy (figure 30 C).

We also checked these nanoparticles as fluorescent probes with cells with promising results (figure 31). F-MGNPs were incubated for 30 min under standard culture conditions with Raji cells, a line of lymphoblast-like cells. Cells were then washed three times, fixed and imaged in an epifluorescence microscope.

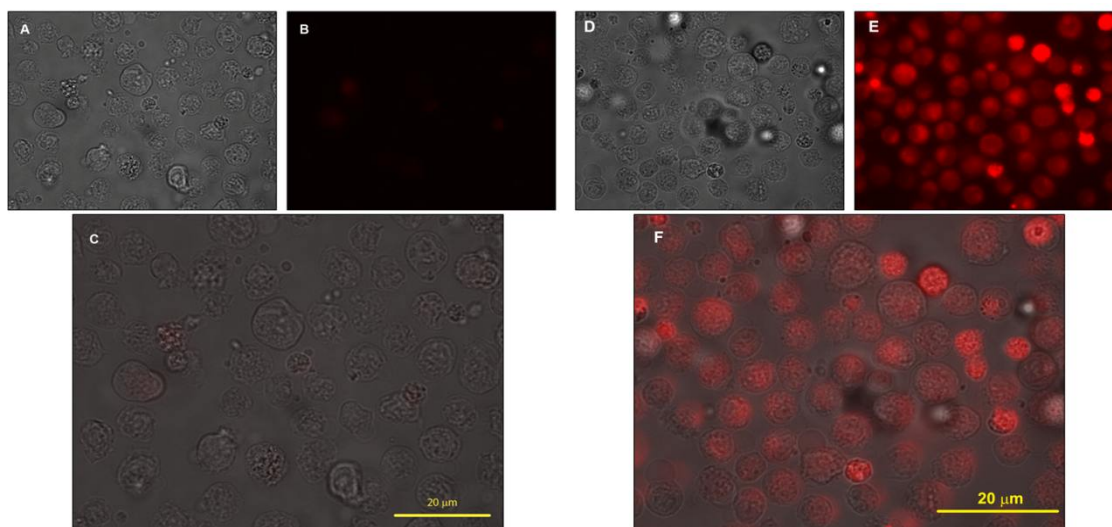


Figure 31. **A**, bright field image; **B**, red filter (TX2) fluorescence image; and **C**, superimposed image of Raji cells incubated for 30 min with 10 mM PBS as control. **D**, bright field image; **E**, red filter (TX2) fluorescence image; and **F**, superimposed image of labelled Raji cells incubated for 30 min with a 10 mM PBS solution of F-MGNPs at a concentration of 50 $\mu\text{g}/\text{mL}$.

The results shown in figure 31 demonstrate both the ability of Raji cells to internalise the nanoparticles, and the capability of the F-MGNPs to be used for the fluorescence labelling of living cells.

Immuno-FMGNPs were prepared as the next step. F-MGNPs were functionalized with protein G for the further attachment of specific antibodies. If the coupling was carried out as usual (see previous section in this chapter), only 2 proteins were attached per nanoparticle. This is the expected effect of the previous coupling of the dye, as now less free carboxylic groups are available for the coupling with the protein. The reaction conditions were forced by increasing the amount of protein G and coupling reagents to get to an average number of 4 protein molecules per NPs similar to those in the non-fluorescent MGNPs as evaluated by Bradford test. The fluorescence of the protein G F-MGNPs thus prepared was the same as the non-immuno prepared F-MGNPs. Incubation with the IgGs was performed as usual to obtain *immuno*-FMGNPs.

The interaction of the *immuno*-GNPs with living cells as well as their application as magnetic-fluorescent probes both *in vitro*, *ex vivo* and *in vivo* have been explored and the results are presented in the following chapters 5 and 6.

Preparation of *immuno*-CdTe quantum dots for fluorescent labelling of cells

An important issue for the introduction of QDs in biological applications is their functionalization and characterization. At these respect is important to note the fragile colloidal stability of QDs [15] [16] that makes their functionalization even more difficult than it already is with other nanostructures. According to Aldana et al. [17] the interaction between the thiol ligands and the surface atoms of a QD can be regarded as a special type of coordinating bond. When the concentration of hydrogen ions increases in the system (lower pH), they compete for the surface ligands with the nanocrystals. Therefore the detachment of the ligands from the QD surface not only diminishes their solubility and promotes aggregation, but also causes the formation of surface defects leading to a decrease of photoluminescence efficiency and shortening of photoluminiscence lifetime [16].

In this section, we report the preparation, from MPA-capped CdTe QDs, of biofunctional CdTe QDs conjugated to specific IgG antibodies through protein G (*immuno*-QDs).

QDs are well-suited for imaging applications as their photostability is better than the one of traditional organic dyes (figure 32), and also because of the wide excitation spectra of QDs that allows multicolour imaging with just one excitation source. Self-prepared QDs present the advantage, compared with commercial ones, that the emission wavelengths can be chosen as desired, and that, in our approach involving protein G, we can build a unique platform over which any IgG can be coupled.

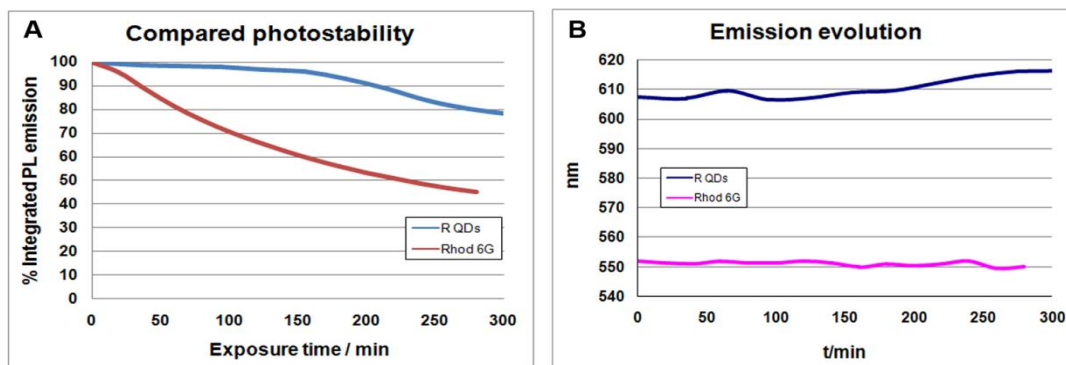


Figure 32. **A**, plot showing the improved photostability of red emitting CdTe QDs compared to the organic dye rhodamine 6G. **B**, evolution of the maximum of the emission spectra of both red QDs and rhodamine 6G.

All the QDs used from now on for these experiments had a photoluminescent emission in red area of the spectra (figure 33). In some of the images, the QDs have been coloured in green to make the visualization easier.

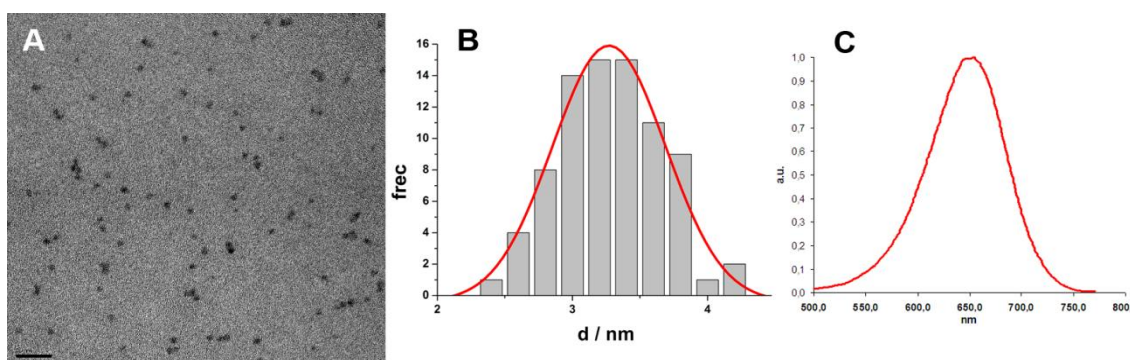


Figure 33. **A**, TEM micrograph of CdTe-ProteinG red QDs used for the staining experiments. **B**, graph showing the size distribution of the precursory red QDs. **C**, fluorescence emission spectrum obtained from the same red QDs upon excitation at 400 nm.

Functional characterization of *immuno*-CdTe QDs in standard immunostainings.

In this case the idea was to functionalize the QDs with antibodies and use them as substitutes of organic fluorophores in standard immunostainings. For this application cytotoxicity is not important as usual immunostainings are performed over fixed and permeabilised cells.

First, MPA protected QDs were used directly without modification in a staining over fixed and permeabilised cells. A great unspecific labelling of the nuclei of the cells is visible under these conditions. This phenomenon can be explained in terms of an electrostatic interaction between CO_2^- groups in the surface of QDs and NH_3^+ groups of basic proteins (histones for example) that are in high concentration in the nuclei complexing DNA (figure 34 A).

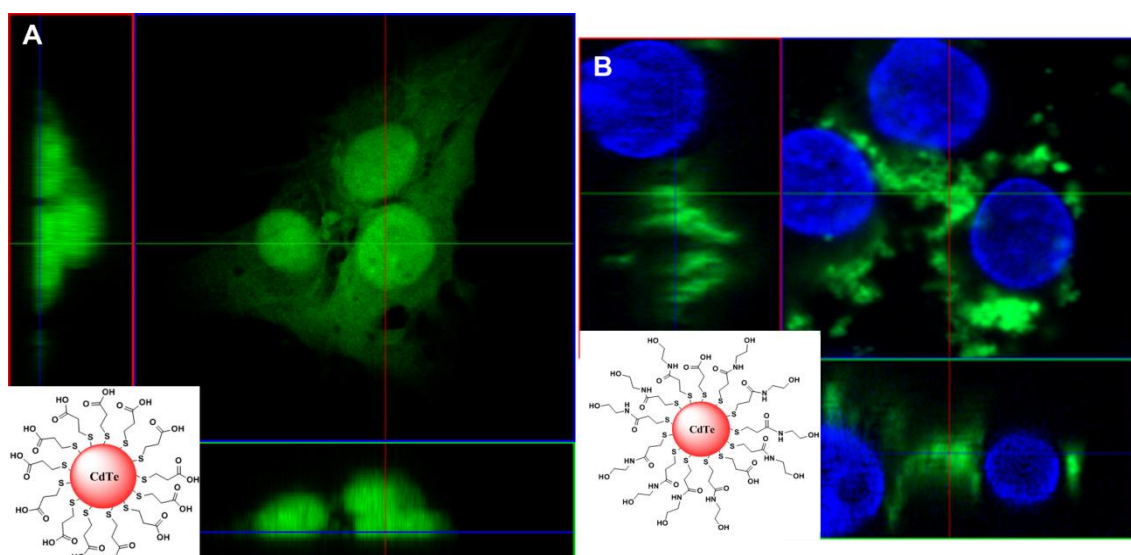


Figure 34. **A**, confocal florescent image of fixed and permeabilized C33 cells stained with unspecific MPA-protected CdTe QDs. **B**, confocal fluorescence image of fixed and permeabilized C33 cell stained with DAPI (blue) and MPA-ethanolamine protected CdTe QDs. **Insets**, scheme of the QDs used for each staining.

To try to understand this behaviour, as a first try part of the MPA molecules were capped with ethanolamine molecules, using EDC/NHS, to reduce the global negative charge of the QDs. Z-potential measurements showed an important decrease of the total surface charge of the QDs (from -26.9 mV for MPA capped QDs, to -6.4 mV after the coupling with ethanolamine). We tried again these QDs in fixed and permeabilised cells

and this time no nuclei staining was visible (figure 34 B). The problem using ethanolamine to reduce negative charges was that at the same time it reduces greatly the solubility of the QDs. According to our previous experience, the suitable candidate to reduce negative charges without decreasing the solubility of the system will be an amine ended glycoconjugate, of mannose in this case. The next step was to functionalize the QDs with protein G to further attach specific antibodies, and in the same reaction couple the amine glycoconjugate. Exactly in the same way used with MGNPs (see previous sections in this chapter), first CO_2^- groups in the QDs were activated with EDC/NHS, and then a controlled amount of protein G was added. After 1 hour of reaction when the protein G should already be coupled, the rest of activated acid groups (EDC/NHS is used in large excess) were profited to couple the amine glycoconjugate to the QDs. This reaction worked well and also the purification (that is a key point when working with QDs) by centrifugal filtering. The amount of protein G coupled to the QDs was calculated, from the washings using Bradford method [8], to be 98 % when the initial stoichiometry protein G:QDs was 5:1. Then, QDs@Prot G were incubated with a secondary goat anti-mouse IgG. After 6 hours of incubation at 10°C (the same used with MGNPs) the solution of QDs appeared turbid. There is an important lose of solubility in this step that is hard to explain as non-specific interactions in this system are not expected. Anyway we tried these *immuno*-QDs in cellular stainings using a mouse anti-human β -tubulin as primary Ab. The results (figure 35) show apart from the tubulin staining, a staining of the whole cellular body excluding the nucleus.

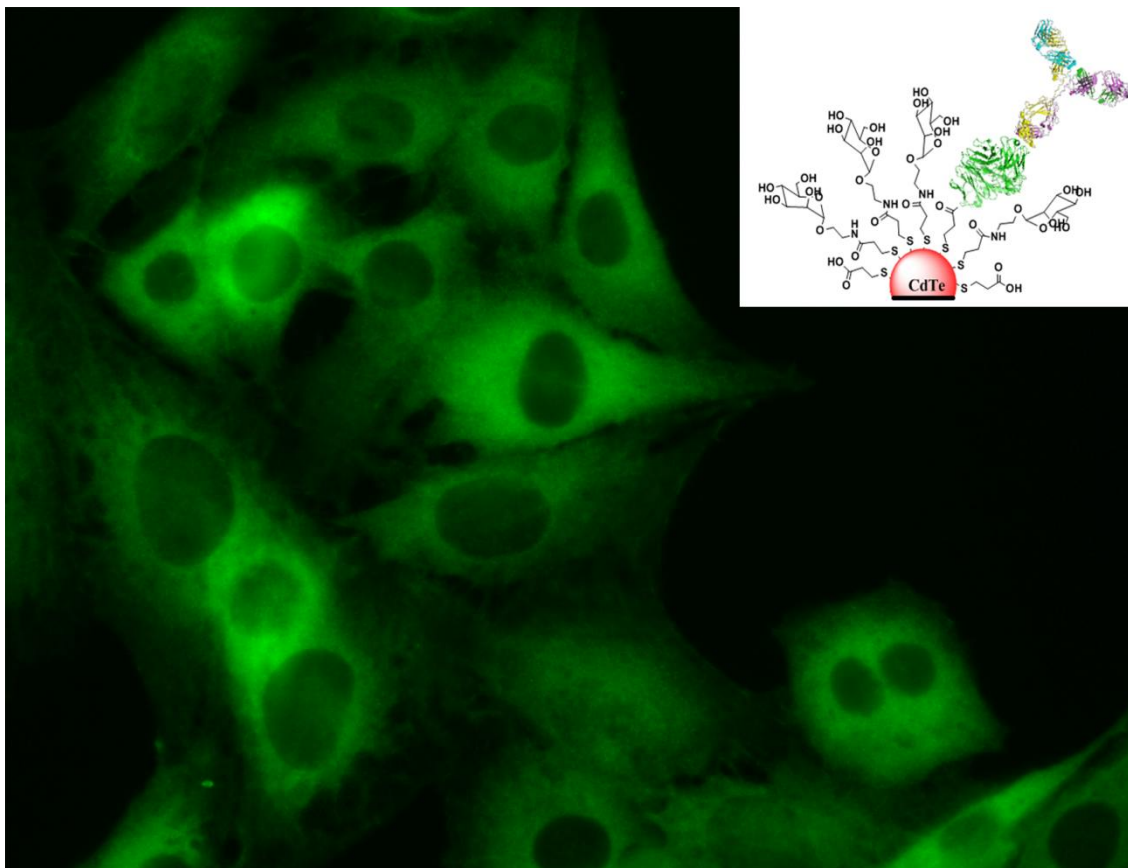


Figure 35. Fluorescence microscopy image of fixed and permeabilized C33 cells stained with CdTe QDs functionalized with mannose and protein G, and incubated with IgG anti-human β tubulin.

In this case, we had not succeeded in the preparation of a versatile QD platform to be used in substitution of traditional organic fluorophores for application in immunocytostaining protocols. More work has to be done to increase the solubility of the final QDs-ProtG-IgG complexes, and to elucidate if the staining of the whole cellular body observed when mannose is used to remove negative charges from the surface of the QDs, is specific (coming for example from the interaction between mannose and lectins), or unspecific.

References

1. Cerdan S., R.H., Künnecke L.B., Seelig J., *Monoclonal antibody-coated magnetite particles as contrast agents in magnetic resonance imaging of tumours*. Magn. Reson. Med., 1989. **12**(2): p. 151.
2. Weissleder R., L.A.S., Khaw B.A., Shen T., Brady T.J., *Antimyosin-labeled monocrystalline iron oxide allows detection of myocardial infarct: MR antibody imaging*. Radiology, 1992. **182**: p. 381-385.

Results and Discussion

3. Hermentin P., D.R., Franssen U., Bieva C., Van der.Bregghen F.J., Strycksman P., Friesen H.J., Otaczy B., Schnaider S., Ax W., Enssle K.H., Kurrle R., Seiler F., *Hinge-thiol coupling of monoclonal antibody to silanized iron oxide particles and evaluation of magnetic cell depletion*. *Bioconjugate Chem*, 1990. **1**: p. 411-418.
4. Bulte J.W.M., H.Y., Kamman R.L., Magin R.L., Webb A.G., Briggs R.W., Go K.G., Hulstaert C.E., Miltenyi S., The T.H., Deleij L., *Specific MR imaging of human lymphocytes by monoclonal antibody-guided dextran-magnetite particles*. *Magn Reson Med*, 1992. **25**: p. 148-157.
5. Ahrens E.T., F.-H.M., Xu H., Genove G., Morel P.A., *Receptor-Mediated Endocytosis of Iron-Oxide Particles Provides Efficient Labeling of Dendritic Cells for In Vivo MR Imaging*. *Magn Reson Med*, 2003. **49**: p. 1006-1013.
6. Perez, J.M., et al., *Viral-induced self-assembly of magnetic nanoparticles allows the detection of viral particles in biological media*. *J Am Chem Soc*, 2003. **125**(34): p. 10192-3.
7. Laemmli, U.K., *Cleavage of Structural Proteins during the Assembly of the Head of Bacteriophage T4*. *Nature*, 1970. **227**: p. 680-685.
8. Bradford, M.M., *A rapid and sensitive method for the quantitation of microgram quantities of protein utilizing the principle of protein-dye binding*. *Anal Biochem*, 1976. **72**: p. 248-54.
9. Grüttner, C., et al., *Synthesis and antibody conjugation of magnetic nanoparticles with improved specific power absorption rates for alternating magnetic field cancer therapy*. *Journal of magnetism and magnetic materials*, 2006. **311**: p. 181–186.
10. Cheon, J. and J.H. Lee, *Synergistically integrated nanoparticles as multimodal probes for nanobiotechnology*. *Acc Chem Res*, 2008. **41**(12): p. 1630-40.
11. Gao, J., H. Gu, and B. Xu, *Multifunctional magnetic nanoparticles: design, synthesis, and biomedical applications*. *Acc Chem Res*, 2009. **42**(8): p. 1097-107.
12. C. Fang, M.Z., *Multifunctional magnetic nanoparticles for medical imaging applications*. *J. Mater. Chem.*, 2009. **19**: p. 6258-6266.
13. Sun, C., J.S. Lee, and M. Zhang, *Magnetic nanoparticles in MR imaging and drug delivery*. *Adv Drug Deliv Rev*, 2008. **60**(11): p. 1252-65.
14. Frangioni, J.V., *In vivo near-infrared fluorescence imaging*. *Curr Opin Chem Biol*, 2003. **7**(5): p. 626-34.
15. Moon J., C.K., Kim B., Yoon KH., Seong TY., Woo K., *Aggregation-free process for functional CdSe/CdS core/shell QDs*. *J. Phys Chem. C*, 2009. **113**(17): p. 7114-7119.
16. Zhang Y., M.L., Wang PN., Ma J., Chen JY., *pH-dependent aggregation and photoluminescence behaviour of thiol-capped CdTe QDs in aqueous solutions*. *J. Lumin.*, 2008. **128**: p. 1948-1951.
17. J. Aldana, N.L., Y. Wang, X. Peng, *Size-dependent dissociation pH of thiolate ligands from cadmium chalcogenide nanocrystals*. *J Am Chem Soc*, 2005. **127**(8): p. 2496-2504.

Experimental part

Materials and methods

All nanocrystals were characterized before and after any step by low and high resolution TEM on a JEOL JEM 2100F microscope. UV-Vis spectra were recorded in a Beckman-Coulter DU 800 spectrophotometer. FT-IR spectra were acquired in a Thermo Nicolet FT-IR spectrometer. Fluorescence spectra were acquired in a Perkin-Elmer LS55 fluorimeter. QDM-D measurements were performed on a Qsense EA4 instrument. Fluorescence images were acquired in a Leica DMI 6000B inverted epifluorescence microscope or in a Zeiss LSM 510 confocal microscope. All the reagents were purchased from Sigma-Aldrich. Protein G was purchased from Pierce and Southern biotech. Secondary IgG antibodies were purchased from Santa Cruz, Invitrogen and Sigma-Aldrich. All solvents were analysis grade (acetone, dichloromethane, methanol, hexane and 2-propanol) and were supplied by Sharlab. All the reagents were used as received without further purification.

Preparation and characterization of *immuno-magnetic glyconanoparticles*

Covalent coupling of protein G to MGNPs. Usually, 1.0 mg of lyophilized MNPs was dissolved in 1 mL of 10 mM PBS pH 7.4. To activate the acidic groups, a solution of EDC/NHS in a ratio 1/2.3 in PBS was added into the solution of the MNPs (to a final concentration of 40 μg EDC/mL). This mixture was allowed to shake for 90 min, and then was diluted to 2 ml. In this moment, a solution of 1 mg/ml of Protein G (161 μg ; relationship 1/5 MGNPs/Prot G) is added to the mixture, and it is shaken for 3 hours. The purification of this product is done by centrifuging right after the three hours (to avoid adsorption and therefore the formation of nets), three times at 16400 g for 90 min at 4 °C. The resulting pellet is resuspended in 10 mM PBS pH 7.4 and kept frozen until further use.

Coupling of an antibody (IgG) to protein G functionalised MNPs. 10 μL (aprox. $7 \cdot 10^{-10}$ mol of protein G) of the previous solution were incubated for 6 hour at 10 °C with 136 μL of a solution 400 $\mu\text{g}/\text{ml}$ of any IgG (aprox. $3 \cdot 5 \cdot 10^{-10}$ mol, ratio MNP/IgG

1/5). The sample was centrifuged (three times) at 16400 g at 4 °C for 90 min to separate the unbounded antibody, resuspended in PBS, and frozen until further use.

Immunoassay with Fe₃O₄@Au@ProteinG@ Goat anti-rabbit IgG. Goat antirabbit IgG conjugate (100 µl, 1 mg/mL) and control nanoparticles MGNPs (without any antibody, 100 µl, 1 mg/mL) were incubated with (100 µl, 1 mg/mL) of rabbit antisheep IgG-HRP in 10 mM PBS pH 7.4 at 10 °C overnight. After purification by centrifugation at 16400 g at 4 °C for 90 min (three times), the presence of HRP labelled antibody in the washings was determined by enzymatic reaction with *o*-Phenylenediamine (OPD)/hydrogen peroxide (H₂O₂) at 25 °C following the protocol supplied by Aldrich. After reaction, brown solutions were measured at 450 nm and the Ab concentration was evaluated into the corresponding standards curve.

QCM-D tests of IgG functionality in the MGNPs. Gold QCM sensor chips (planar gold-coated polished 5 MHz AT-cut crystals) were used for these measurements. Gold surfaces were thoroughly cleaned immediately before use. The sensors were first sonicated in Cobax solution for 10 min, then rinsed and sonicated in Nanopure water another 10 min, and last subjected to UV-ozone treatment for 20 min. This protocol was repeated three times, and thereafter the chips were immediately mounted in the QCM cells. The QCM cell and tubing were thoroughly rinsed with Hellmanex 1%, and Nanopure water. The experiments were performed by sudden exchange of the solutions in the experimental chamber as follows: After stabilization of the QCM-D baseline first in MilliQ water and then in 10 mM PBS pH 7.4, a protein G solution, 0.05 mg/mL, was added to the clean sensor surface. Once the adsorption reached the steady state, loosely bounded molecules were rinsed off with 10 mM PBS. After rinsing the surface, a rabbit antisheep IgG solution, 0.1 mg/ml, was injected into the system. The surface was rinsed again with 10 mM PBS, and Fe₃O₄@Au@Lact-Link@ProtG@Goat antirabbit IgG solution was added to the chip. To end, the surface was rinsed again to remove any unbounded nanoparticle complex. The control experiment was performed exactly in the same conditions using MGNPs without any conjugated antibody. All experiments were performed at 37 °C and at a flow rate of 0.2 mL/min.

SDS-PAGE gel. A Laemli standard protocol [1] was used for the preparation of the gels. The gels were obtained by mixing in a ratio 37.5:1 stock solutions of acrylamide and bis-acrylamide. The crosslinking was 4 % and 12 % for the stacking and separating gels respectively. For sample preparation, 40 μL of free anti-DC-SIGN **1**, *anti*-DC-SIGN-Protein G-conjugate **2** antibody and molecular markers buffer **3** were mixed with 10 μL of sample buffer (62.5 mM Tris-HCl pH 6.8, 20 % glycerol, 2 % SDS, 5 % β -mercaptoethanol) and the mixture is heated at 95 $^{\circ}\text{C}$ for 4 min. Samples were seeded on the gel and the gel was run in SDS running buffer (25 mM Tris, 192 mM glycine, 0.1 % SDS, pH 8.3) during 45 min at 100 V and further at 250 V for 90 min. Finally, a silver staining protocol with a commercial silver staining kit was followed to reveal the bands

Immunocytostaining with MGNPs. After fixation (2 % PFA, 2 % sucrose, 10 mM PBS pH 7.4) and permeabilisation (0.5 % Triton X-100 in 10 mM PBS pH 7.4) epithelial cervix cancer cells (C33) were incubated for 1 hour with a solution of $\text{Fe}_3\text{O}_4@Au@Lact/Link@Prot\ G@mouse\ anti\beta\text{-tubulin}\ IgG$. The cells were then washed in 0.5 % Tween 20 10 mM PBS pH 7.4 several times, and then the secondary antibody, anti mouse IgG biotin labelled, was added to the sample. The same procedure was followed with a tertiary element, streptavidine labelled Texas Red. Finally the sample was washed again with 0.5 % Tween-20, mounted on a glass slide and imaged by fluorescence microscopy. The final image was compared with the same staining using free primary Ab, as control.

Preparation and characterization of multifunctional fluorescent-magnetic *immun-glyconanoparticles*

Fluorescent dye coupling to MGNPs. In a usual coupling, 47 μg of Texas Red cadaverine ($6.5 \cdot 10^{-8}$ moles) in 20 μL of a 5:1 mixture $\text{H}_2\text{O}:\text{DMSO}$, were shaken for 6 hours with 20 μL of a solution of NaOH 1N. After that, the dye solution was mixed with 500 μg of MGNP (aprox. $2.65 \cdot 10^{-10}$ moles) in 250 μL of H_2O . To this mixture, 50 mg of EDC ($3.2 \cdot 10^{-4}$ moles) were added and the solution was allowed to stir overnight. To purify the final product the nanoparticles were filtered through Amicon 100000 MWCO filters and washed three times with H_2O . Finally the fluorescent nanoparticles were

Experimental Part

resuspended in 500 mL of pH 7.4 10 mM PBS and kept at 4 °C until further use. All this protocol was performed in the absence of light as far as possible.

Protein G coupling to F-MGNPs. In a typical coupling, half of the product from the previous reaction (aprox. $1.32 \cdot 10^{-10}$ moles of F-MGNPs) was reacted for 90 min with 30 μg of EDC ($1.32 \cdot 10^{-7}$ moles) and 47 μg of NHS ($3.04 \cdot 10^{-7}$ moles) in an eppendorf tube. Then 40 μg of protein G ($1.32 \cdot 10^{-9}$ moles) were added into the tube and the sample was shaken at room temperature for 3 more hours. The purification of the sample was performed as in the previous step and the final sample were resuspended in 575 μL of pH 7.4 10 mM PBS. The washings from the centrifugal filtering were put together and dialyzed for 24 hours against 10 mM PBS to finally quantify the amount of protein G using the Bradford protocol [2].

Antibody incubation with protein G functionalized F-MGNPs. 120 μL of the previous solution were incubated overnight at 10 °C with 33 μg of IgG ($1.06 \cdot 10^{-9}$ moles). The sample was purified centrifuging at 16400 g for 90 min at 4 °C, removing the supernatant and washing the pellet twice with 10 mM PBS. The final sample was kept refrigerated until further use. The presence of IgG in the washings was stimulated by Bradford [2].

Non-specific labelling of Raji cell with fluorescent magnetic glyconanoparticles (F-MGNPs). An experiment with F-MGNP was performed in order to find the best conditions for the incubation of *immuno*-F-MGNPs with blood cells. 200 μL of Raji cell suspension in warm complete medium at $4 \cdot 10^5$ cells per well were plated in round bottom 96-well plate, and were centrifuged at 440 g, 5 min., 4 °C. Then cells were resuspended in 50 μL of F-MGNP (50 $\mu\text{g}/\text{mL}$ in 10 mM PBS) and incubated for 30 min at 37 °C. After incubation, cells were washed three times with cold 10 mM PBS and finally resuspended in 100 μL of 10 mM PBS before acquiring fluorescence images. 20 μL drops of the samples were deposited onto a thin glass slide and then mounted upwards in the microscope. After 5 min to let the cells settle, the samples were imaged using an oil-immersion 63x objective on a Leica inverted microscope with TX2 filter (a 560/40 nm band-pass excitation filter and a 645/75 nm band pass emission filter) and a Leica mercury lamp.

Applications of CdTe quantum dots in standard immunostainings

Immunofluorescence with CdTe QDs (protocol adapted from [3]). $2.5 \cdot 10^3$ C33 cells were cultured at 37 °C and 5 % CO₂ on 24-well plate. After 48 hours the cells were rinsed with 10 mM PBS buffer at 37 °C and then were fixed and permeabilized for 20 min at room temperature with a solution of 4 % paraformaldehyde and 0.1 % Triton X-100 in 10 mM PBS buffer. After three washings of 5 min each with 10 mM PBS, the cells were blocked with 10 % BSA, 10 % serum 10 mM PBS buffer for 30 min at room temperature. To stain the cells, a solution of the desired concentration of QDs was added to the cells and they were incubated for 3 hours at room temperature. Finally, the samples were washed three times for 5 min each in the shaker with 0.5 % Tween-20 10 mM PBS buffer, they were mounted and imaged in the fluorescence microscope.

Surface charge suppression of MPA protected CdTe QDs. Typically, 1 mg of MPA protected CdTe QDs (aprox. $1 \cdot 10^{-8}$ moles) were solved in 2 mL of 10 mM PBS buffer in an eppendorf tube. 20 mg of EDC ($1.3 \cdot 10^{-4}$ moles) were added to this solution together with 100 µL of ethanolamine. The reaction was allowed to shake for 5 hours and then was purified by size exclusion chromatography (Sephadex G25 as stationary phase and 10 mM PBS buffer as eluent). The final product was stored at 4 °C in the fridge until further use.

Surface charge (as measured by Zsizer) = -6.4 mV.

QDs functionalization. In a standard reaction, 500 µg of MPA protected CdTe QDs (aprox. $6.25 \cdot 10^{-9}$ moles) were solved in 500 µL of 10 mM PBS buffer in an eppendorf tube. 244 µg of EDC ($1.56 \cdot 10^{-6}$ moles) and 416 µg of NHS ($3.59 \cdot 10^{-6}$ moles) were added to this solution. 90 mins later the sample was diluted with 2 mL of 10 mM PBS and 687 µg of protein G ($3.12 \cdot 10^{-8}$ moles) were added from a PBS solution 1 mg/mL. The reaction was allowed to shake for another 90 mins and then 140 µg of mannose glycoconjugate ($6.25 \cdot 10^{-7}$ moles) (generous gift from Dr.M. Marradi) was added to the reaction. Finally after 90 more minutes the reaction was purified filtering through 50000 MWCO amicon filters. The final sample was stored at 4 °C until further use.

Antibody incubation with protein G functionalized QDs. The incubation of the functionalised QDs with the corresponding Ab was performed exactly like in the case of the magnetic nanoparticles. See previous sections.

References

1. Laemmli, U.K., *Cleavage of Structural Proteins during the Assembly of the Head of Bacteriophage T4*. Nature, 1970. **227**: p. 680-685.
2. Bradford, M.M., *A rapid and sensitive method for the quantitation of microgram quantities of protein utilizing the principle of protein-dye binding*. Anal Biochem, 1976. **72**: p. 248-54.
3. Xing, Y., et al., *Bioconjugated quantum dots for multiplexed and quantitative immunohistochemistry*. Nat Protoc, 2007. **2**(5): p. 1152-65.

PART 2:

Applications of biofunctional nanoparticles

CHAPTER 5

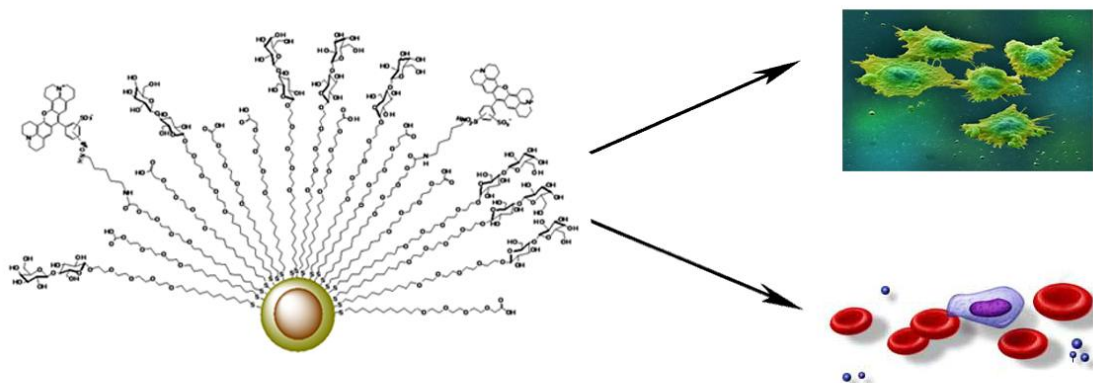
In vitro and *ex vivo* applications of *immuno-* nanoparticles

***In vitro* and *ex vivo* applications of immuno-nanoparticles**

In this chapter the results obtained on the interaction studies of the magnetic glyconanoparticles with cells and their application as labelling probes will be presented together with the application of *immuno*-QDs as labelling and potential anticancer agents. We have investigated first the way of interaction between fluorescent-magnetic glyconanoparticles and C33 cervix cancer derived line, and demonstrated the ability of the *immuno*-MGNPs platform as dual specific labelling probes for fluorescence imaging and MRI in simple *in vitro* cellular system and in complex *ex vivo* biological media as human blood. The potential of *immuno*-QDs as specific labelling probes and targeted anticancer agents has been demonstrated with an *in vitro* cellular model.

Uptake and intracellular fate of dual fluorescent-magnetic glyconanoparticles

The number of different applications of nanoparticles in the biomedical field is increasing rapidly in the last years [1-3]. For some of these applications it is crucial to characterize the behaviour of nanoparticles in the presence of living matter. For example, in the case of drug delivery or *ex vivo* magnetic labelling of cells, nanoparticles have to enter into the cells to be effective. Great efforts are being made to increase the cellular uptake of nanoparticles, ranging from the co-administration of the nanocrystals together with membrane permeabilising agents [4-5], to the modification of the particles with cellular uptake inducers (for example protein transduction domains PTDs) [6-7]. In our case, the presence of natural biocompatible saccharides in the outer organic shell of the nanoparticles facilitates the internalization of these conjugates into the cells. In previous works the importance of the carbohydrate coating over the internalization of different nanoparticles has already been explored [8]. Some of the applications mentioned above (for example drug/gene delivery) require a much deeper understanding of the internalization process and the intracellular fate of the nanoconjugates, to favour the careful design of the nanoprobe.



Scheme 15. The fluorescent-magnetic glyconanoparticle $\text{Fe}_3\text{O}_4@Au@LactC_{11}/\text{Linker}/\text{Texas red}$ and its *in vitro* and *ex vivo* applications.

The fluorescent-magnetic glyconanoparticles (FMGNP) incorporating lactose, the carboxylic linker and Texas red conjugates ($\text{Fe}_3\text{O}_4@Au@LactC_{11}/\text{Linker}/\text{Texas red}$ and $\text{Fe}_3\text{O}_4@Au@LactC_5/\text{Linker}/\text{Texas red}$,) previously prepared, were used along the work described in this chapter. According to previous results the internalization ability of the carbohydrate coated nanoparticles is straightforward. Although the internalization of hybrid lactose-carboxylic linker fluorescent-magnetic nanoparticles is expected to be similar to that of the 100 % lactose MGNPs, the effect of the negative charges arising from the non-coupled carboxyl groups of the linker should not be underestimated. Confocal micrographs from C33 cells incubated for 3 hours with hybrid FMGNPs demonstrate that these nanoparticles are internalised in considerable amount (Figure 36 A).

To keep on with the internalization experiments it is important to characterise the time frame of nanoparticle internalization by C33 cells. To do so and obtain an uptake curve, cells were incubated in the presence of 50 $\mu\text{g}/\text{mL}$ of FMGNPs for different periods of time (between 0 and 360 min) and after washing free nanoparticles, the fluorescence of the cells was measured at 612 nm (Texas red λ_{exc} 595 nm, λ_{em} 615 nm).

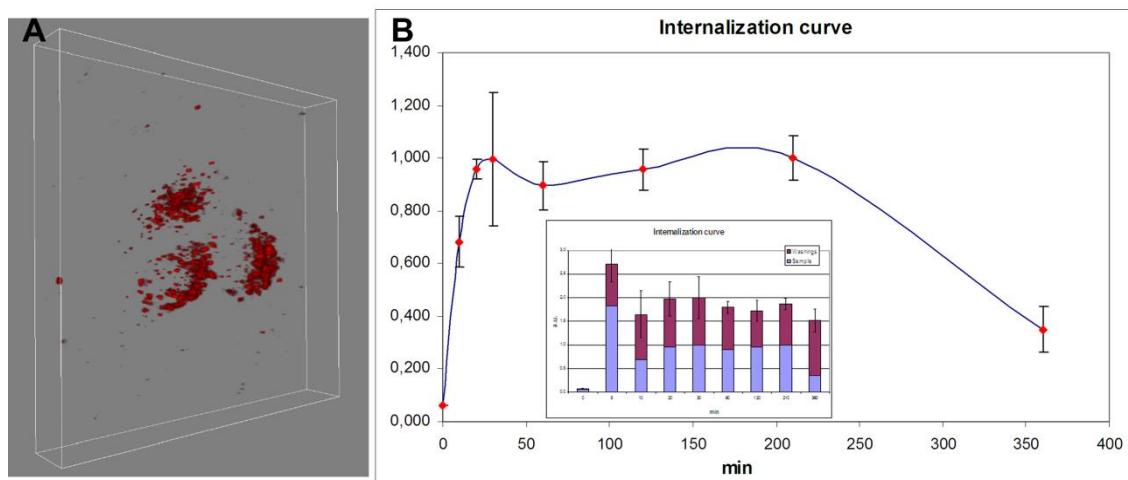


Figure 36. **A**, 3D reconstruction from a z-stack series of confocal fluorescence images of C33 cells incubated for 180 min with 50 $\mu\text{g}/\text{mL}$ of FMGNPs showing the accumulation of nanoparticles inside the cells. **B**, normalised time dependent photoluminescence of C33 cells incubated with 50 $\mu\text{g}/\text{mL}$ of FMGNPs. **Inset**, normalised photoluminescence data in each time point for the sample (blue) and the washings (purple)

From normalised photoluminescence (PL) results (Figure 36 B), some conclusions can be extracted; nanoparticles are internalised quite fast, in approximately 20-30 min the maximum of fluorescence is reached. At this time the concentration of internalised particles reaches a steady state and after 4 h part of the nanoparticles are excreted as indicated by a decrease of the PL in the cells and an increase in the washings. This behaviour seems to be quite general as it has been observed with nanoparticles of different natures and sizes, and with different cells [9].

To get a first insight into the mechanism or pathway of internalization of the nanoparticles into the cells, chemical inhibition of endocytosis was used. Traditionally the mechanisms of endocytosis have been divided mainly into three groups: clathrin-mediated, lipid raft/caveolae-mediated, and macropinocytosis/phagocytosis. Recent studies have demonstrated that internalization pathways are much more diverse (Figure 37) [10].

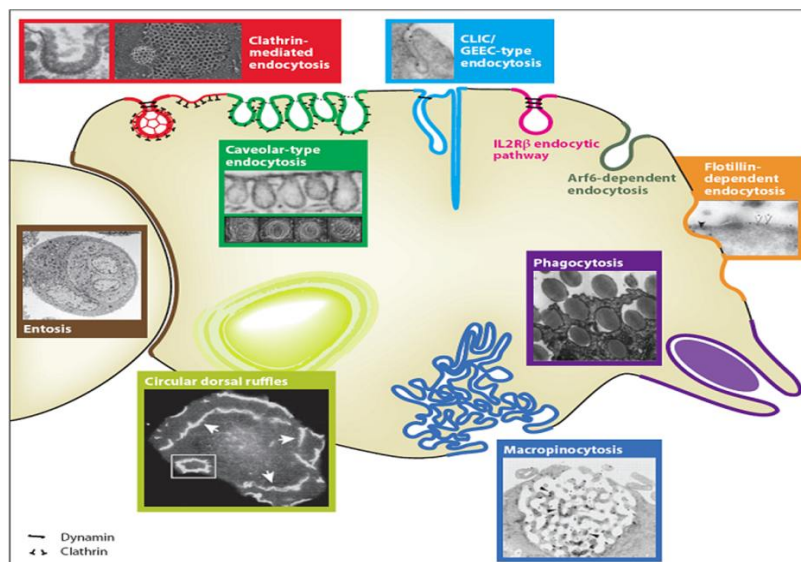


Figure 37. Putative endocytic portals into the cell. Taken from reference [10]

The chemical specific inhibitors of these internalization routes are routinely used in biological works [9, 11-13], although they are not always as specific as expected [14]. We have tried to use them as a first approach to explore the internalization of the FMGNPs. Chlorpromazine (clathrin-mediated endocytosis inhibitor), filipin III and nystatin (lipid-raft/caveolae endocytosis inhibitor), dynasore (dynamin inhibitor), cytochalasin D (phagocytosis and macropinocytosis inhibitor), and lactose (receptor/transporter specific competitor) were incubated with the cells for one hour and then a mixture of each inhibitor and the nanoparticles was added and cell fluorescence was measured after incubation (figure 38 A). The results (figure 38, B and C) indicate that the FMGNPs enter into C33 cells by different pathways. Both clathrin and lipid-raft/caveolae mechanisms are used by the nanoparticles to enter the cell under the conditions of culture. Dynasore also has an effect on the endocytosis as dynamin is somehow implicated in both mechanisms [10]. Finally, a specific receptor or transporter that recognises lactose molecules on the nanoparticle surface is involved, as indicated by the dose-dependent inhibition of entry by free lactose molecules (figure 38, C).

Results and Discussion

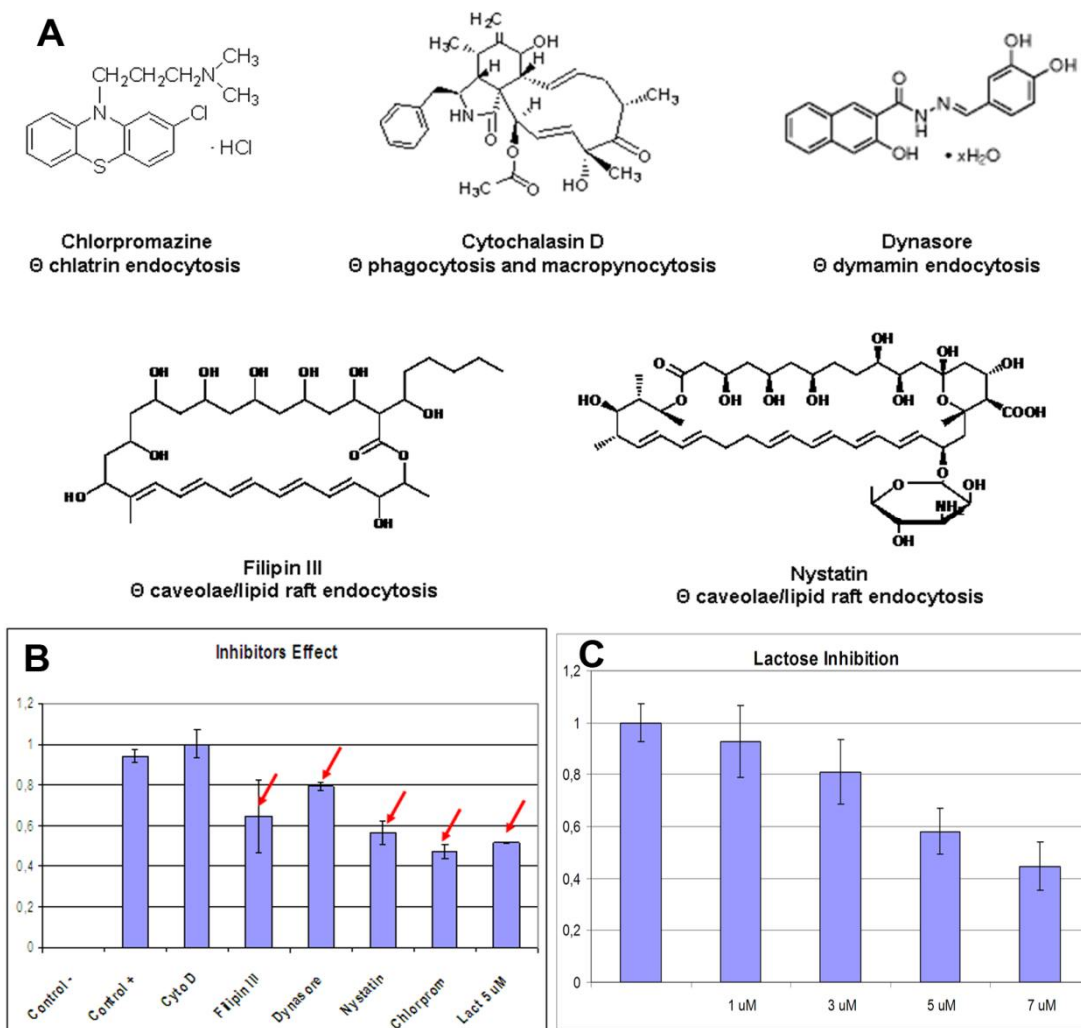


Figure 38. **A**, chemical structure of the specific endocytosis inhibitors used. **B**, normalised PL from cells treated with chemical endocytosis inhibitors. Inhibitors with a statistical effect over the internalization are marked with a red arrow. **C**, dose-dependent inhibition of FMGNPs endocytosis by free lactose.

To dig deeper into the intracellular fate of our fluorescent-magnetic nanoparticles, co-localization analysis of immunocytostaining experiments was carried out at different incubation times with the FMGNPs. In the typical experiment, C33 cells were incubated under the usual conditions in the presence of 50 $\mu\text{g}/\text{mL}$ of FMGNPs for 30, 180 or 360 mins. In general, we observed by confocal imaging a clear accumulation of the FMGNPs in the perinuclear region of the cells. These data are consistent with intracellular translocation of vesicles from the plasma membrane along microtubules in the minus direction toward the centrosome/microtubule-organising region of the cell [15].

After washing out the remaining nanoparticles, cells were co-stained in green with specific markers of different intracellular compartments. According to data from the bibliography [12, 16-18] possible final destinations for uptaken material include the endoplasmic reticulum and the Golgi apparatus. To label these two organelles ER-Tracker green (endoplasmic reticulum marker) [19] and fluorescein labelled wheat germ agglutinin (WGA) (Golgi marker) [20] were used. The path followed inside the cell, early endosomes (anti human EEA1 antibody) [18], lysosomes (Lyso-Tracker green) [11-13], chlatrin (anti human chlatrin antibody) [21], and caveolin (anti human caveolin-1 antibody) [22] was also stained. Analysis of the confocal images was performed based on co-localization coefficients according to Manders using ImageJ software (Rasband, W., 1997, US National Institutes of Health, <http://rsb.info.nih.gov/ij/>). This methodology gives us numerical values ranging from 0 to 1. Co-localization is positive for values above 0.5, and e.g. 0.6 means that 60 % of red pixels co-localize with green pixels. This analysis shows clear co-localization at any of the incubation times investigated of the FMGNPs with chlatrin coated vesicles, ER and trans-Golgi apparatus, and a less intense co-localization with lysosomes vesicles (figure 39). It does not seem to be clear co-localization with early endosomes except at 30 min incubation. At the shortest incubation time (30 min) FMGNPs are homogeneously dispersed over the whole cytoplasm and only a few brighter dots (vesicles) are visible. After 180 min, the nanoparticles seem to be mainly localised inside of vesicles. Finally, at long incubation times (360 min), a mixture of both previous situations is observed; there are clear highly fluorescent vesicles but fluorescence is also observed along the cytoplasm. It seems that after an initial burst of nanoparticle internalization, FMGNPs are cleared away from the cytoplasm and 'stored' in vesicles in the perinuclear region. At longer times the nanoparticles either escape from the reservoirs to the cytoplasm or are exocyted through the trans-Golgi network in accordance to the internalization curve previously measured (figure 36). Considering the endocytic pathway more carefully, the entrance of the FMGNPs into the cells is, at least in part, through chlatrin and caveolin dependent mechanisms in accordance with data from the inhibition experiments (figure 38) and as shown by the co-localization at any of the time points tested (figure 39).

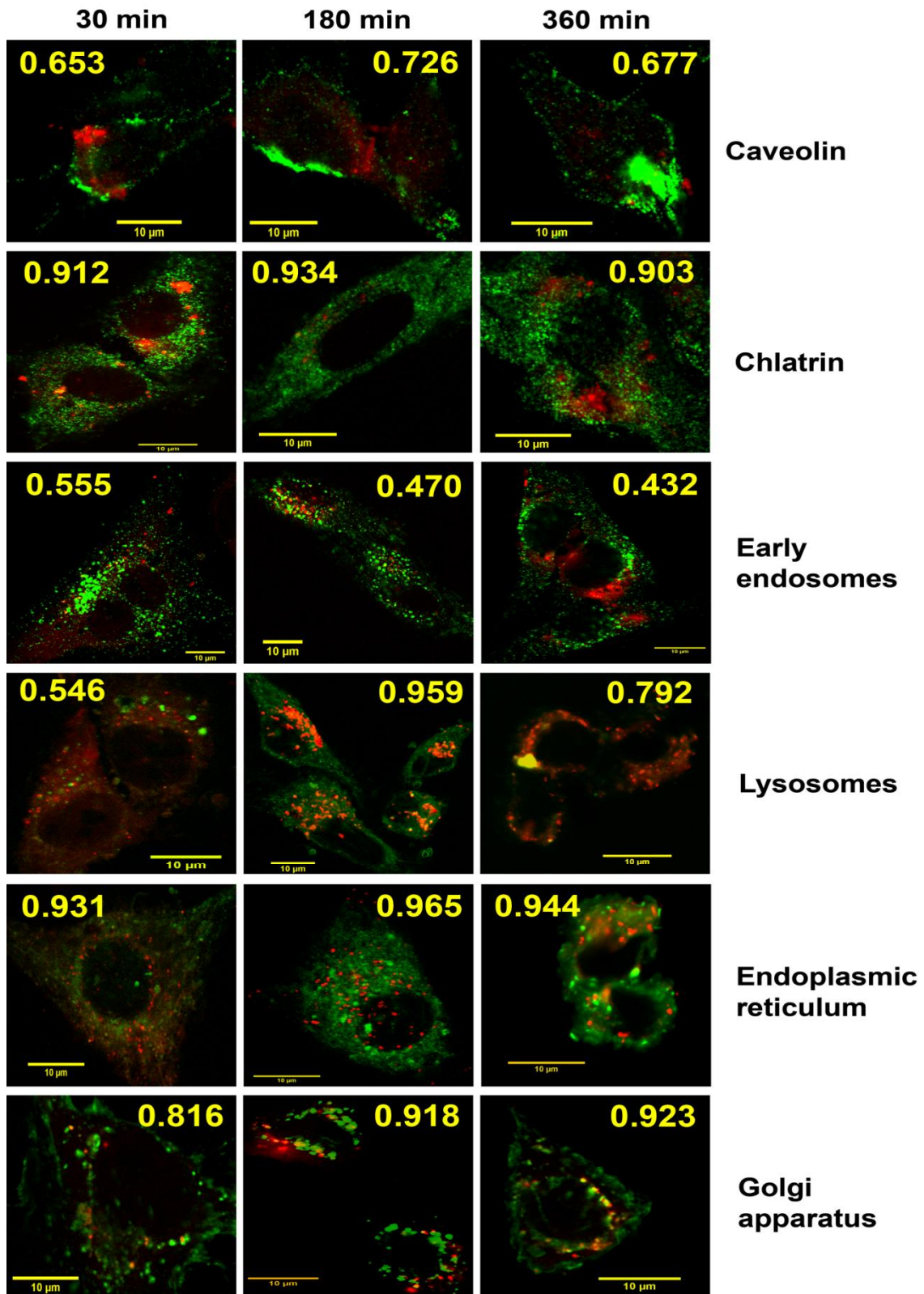


Figure 39. Confocal images of C33 cells incubated with 50 $\mu\text{g}/\text{mL}$ of FMGNPs (red) for different times (30, 180 or 360 min) and specifically co-stained (green) for different cellular compartments: Caveolin, chlatrin coated vesicles, early endosomes, lysosomes, endoplasmic reticulum and Golgi apparatus. Numbers in yellow give the value of co-localization coefficient according to Manders of red with green. Scale bar 10 μm .

From co-localization experiments we propose a pathway that would take caveolin-mediated endocytosis as the main way of entry into the cells (figure 40). Caveolin vesicles would fuse to form the caveosome and from there the nanoparticles would be directed either to the Golgi, the endoplasmic reticulum or the lysosomes without going through the early endosomes [23]. The way of the nanoparticles out of the cells would be either through trans-Golgi transport (heavy co-localization) or by other mechanisms after lysosomal escape due to changes in nanoparticle surface charge (due to acidic pH in lysosomes) [24-25].

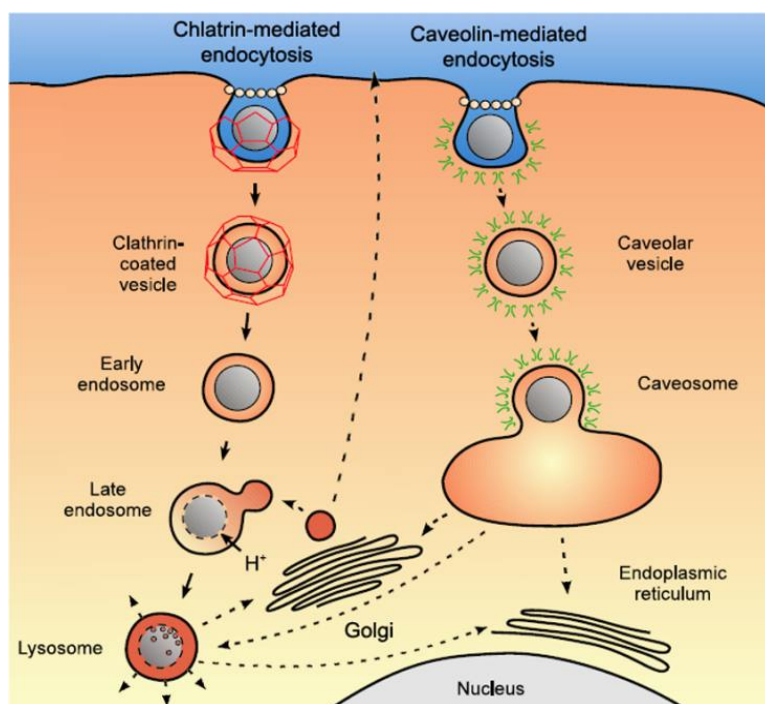


Figure 40. Proposed intracellular trafficking for FMGNPs into C33 cells. Two entry pathways have been demonstrated, clathrin-mediated endocytosis and caveolin-mediated endocytosis. We propose caveolin-dependent way as the mayor one based on co-localization images. Modified from ref.[26]

In this section we have demonstrated that hybrid lactose/linker coated fluorescent-magnetic glyconanoparticles are easily internalised by C33 human cellular line following different pathways. The time frame of this uptake has been studied, as well as the intracellular fate of the nanoparticles.

In vitro specific cellular labelling with *immuno*-magnetic glyconanoparticles

Before testing the *immuno*-MGNPs as specific probes in complex media we have demonstrated their ability to label specifically cell populations *in vitro* as a proof-of-concept. The DC-SIGN receptor expressed on the surface of immature dendritic cells (iDCs) was chosen as target. DC-SIGN is a calcium dependent human lectin that recognises high-mannose oligosaccharides expressed on the surface of bacteria, virus and other pathogens [27] [28].

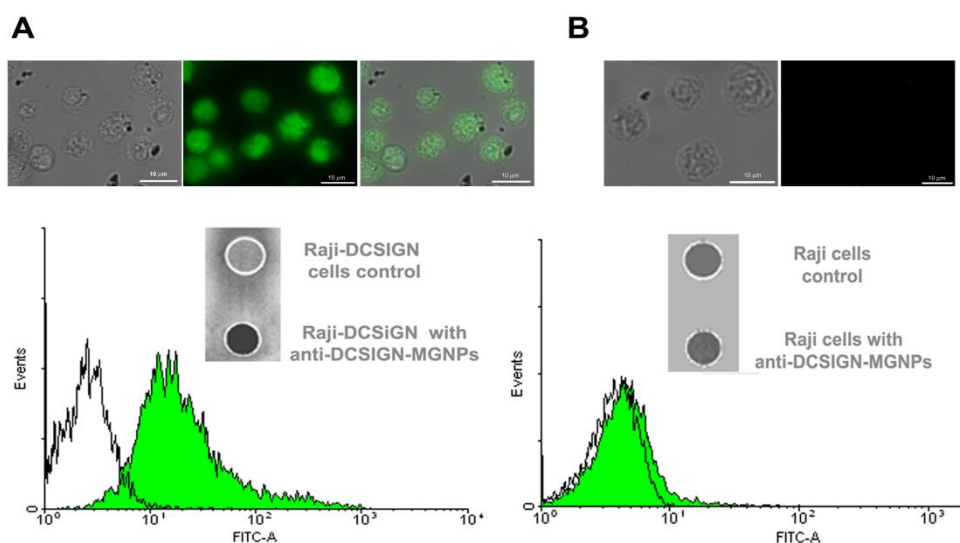


Figure 41. Fluorescence microscopy images, flow cytometer graphics and T_2 -weighted MR images obtained after incubating anti-DC-SIGN-MGNPs (conjugate) with **A**, Raji-DC-SIGN cells and **B**, Raji cells (1 hour at 4 °C for cytometry and fluorescence microscopy and 30 min at 0 °C for MRI). **Top A**, (from left to right): Bright-field, fluorescence, and bright-field-fluorescence overlay images obtained with Raji-DC-SIGN cells incubated with anti-DC-SIGN-MGNPs and Alexa-Fluor488 (green fluorescence) as secondary antibody. **Top B**, (from left to right): Bright-field and fluorescence images obtained at the same conditions with Raji cells. Scale bars represent 10 μm. No green fluorescence activity from the anti-DC-SIGN-MGNPs treated Raji cells (**top B**) is observed while intense green fluorescence is seen from treated Raji-DC-SIGN cells (**top A**). **Bottom A**, Flow cytometry analyses (**lower graphics**) and MRI phantoms (**upper images**) of anti-DC-SIGN-MGNPs treated Raji-DC-SIGN cells. **Bottom B**, Flow cytometry analyses (**lower graphics**) and MRI phantoms (**upper images**) of anti-DC-SIGN-MGNPs treated Raji cells. Data collected by flow cytometry are shown as histograms of the FITC-channel: Raji/Raji+ cells treated with the conjugate are displayed by green shaded curve, while untreated control by black curve. MR imaging of anti-DC-SIGN-MGNPs treated Raji+ cells (**A**) showed a significant darkening while no enhancement of the contrast is observed for anti-DC-SIGN-MGNPs treated Raji cells (**B**).

Anti-DC-SIGN-MGNPs conjugates were prepared to target the specific receptor DC-SIGN (CD209) on DC-SIGN-transfected cell line (Raji+). As control, Raji negative (Raji) cell line was used. First, MTS viability assay [29] showed that the anti-human DC-SIGN-MGNPs were not cytotoxic for Raji cells in a broad range of concentrations (0.002 - 1 mg/mL). The targeting efficacy and specificity of the anti-DC-SIGN-MGNPs for Raji and Raji+ cells was analysed by fluorescent microscopy, flow cytometry and MRI (figure 41). Images of Raji incubated with anti-DC-SIGN-MGNPs did not show fluorescence signals indicating no binding to the nanoparticles (upper figure 41 B), while the image of Raji+ cells showed binding of the magnetic nanoparticles over total cell surface area (upper figure 41 A). Flow cytometry analysis of Raji and Raji+ cells incubated with anti-DC-SIGN-MGNPs, using Alexa 488 rabbit antimouse IgG as secondary antibody, revealed that Raji+ cells showed a higher mean fluorescence than the non-transfected Raji control cells (bottom figure 41 A). This means that anti-DC-SIGN-MGNPs interact specifically with the DC-SIGN target receptor and not with other cell membrane components. MRI shows consistency with fluorescence and flow cytometry results. Raji and Raji+ cells were incubated with anti-DC-SIGN-MGNPs under the same conditions (2.4 $\mu\text{g/ml}$ of Fe, 30 min, 0 °C). T₂-weighted images of Raji+ cells treated with anti-DC-SIGN-MGNPs present a significant contrast enhancement versus Raji+ cells non treated (bottom, Figure 41 A) while in the T₂-weighted images of Raji negative cells no differences were observed (bottom, Figure 41 B). A 2.4 $\mu\text{g/ml}$ of Fe content was sufficient to selectively label 10⁴ Raji+ cells confirming our nanoplatform as ultra-sensitive magnetic probe for image enhancement.

Specific dual labelling of blood cell populations

In general, for targeting-mediated imaging and especially in the case of intravenous injection, the following two prerequisites must be fulfilled by the contrast agent: reticuloendothelial system (RES) evading properties, and preservation of the bioactivity of the targeting molecule. In addition, interaction of nanoparticles with blood cells (platelets, red blood cells, peripheral blood mononuclear cells PBMCs) and other blood components (plasma proteins) within the first moments after injection may dictate the biodistribution of the nanoparticles. Opsonisation remains an obstacle for nanoparticles gaining access to the blood stream. This interaction of nanoparticles with

plasma proteins results in facilitated uptake by the RES, or blocking of the delivery to the intended target sites. Studies about aggregation of the particles caused by protein adsorption and the physico/chemical nature of the nanoparticles in complex biological media are particularly important [30] [31] [32]. Unspecific uptake of nanoparticles by immune cells in the bloodstream (such as monocytes, platelets, leukocytes, and dendritic cells) may cause the nanoparticles to be routed away from their expected pathway [33] [34]. Little is known of the interaction of nanoparticles and blood and about their transport through the blood stream to their target tissues or organs.

In this part of the work, we have used our dual *immuno*-fluorescent magnetic glyconanoparticles (*immuno*-FMGNP) for the specific labelling *ex-vivo* of red blood cells (RBCs) or leukocytes in whole human blood samples from healthy donors as complex cellular system. The *immuno*-FMGNPs were prepared based on water-soluble gold-coated magnetite nanoparticles bearing lactose conjugate and the carboxyl ended linker (see chapters 1) that have shown excellent properties *in vitro* as T₂ contrast agents in MRI (figure 28). To these magnetic glyconanoparticles a fluorophore (Texas Red) and protein G were sequentially conjugated (see chapter 4). The oriented coupling of an antibody to the protein G-fluorescent-magnetic glyconanoparticles, converts the glyconanoparticles in dual targeted probes (*immuno*-FMGNPs) for the specific labelling of cell populations within a complex biological medium. Protein G guaranties the perfect orientation of antibodies on the *immuno*-complexes maximizing the efficiency of targeting and labelling of specific cells present at very low concentrations. Carbohydrates confer the nanoparticles water solubility and biocompatibility, and prevent nonspecific binding of proteins (opsonisation) that is critical in the complex biological environment of blood. The specific labelling of leucocytes (0.10-0.17 % of total blood cells) and erythrocytes (RBCs) in whole blood was further assessed by both fluorescence microscopy at cellular resolution and magnetic resonance imaging (MRI). To label erythrocytes glycophorin A (GpA, CD 235a), major sialoglycoprotein fraction of the human red cell membrane (figure 42 left) was chosen. GpA is a relatively simple erythrocyte membrane protein composed of 131 amino acid residues found in three domains: a short hydrophilic cytosolic domain, a hydrophobic transmembrane domain (of ~25 residues), and a more substantial extracellular domain that bears extensive carbohydrate modification [35]. By control experiments we tested the high expression of this protein on RBCs. On the other side, to label leukocytes (a subpopulation of PBMCs) a leukocyte specific transmembrane glycoprotein (CD 45), which is a receptor-

Results and Discussion

like protein tyrosine phosphatase (PTPase 1B in this case) (figure 42 right) was the chosen. CD45 comprise a family of high molecular weight glycoproteins which are expressed in lymphoid and myeloid cells except erythrocytes and plasma cells as several alternatively spliced isoforms, that differ in the extracellular domain [36] [37]. To target these two molecules the corresponding mouse anti human IgGs were selected and coupled to our fluorescent magnetic glyconanoparticles (F-MGNPs) (see chapter 4).

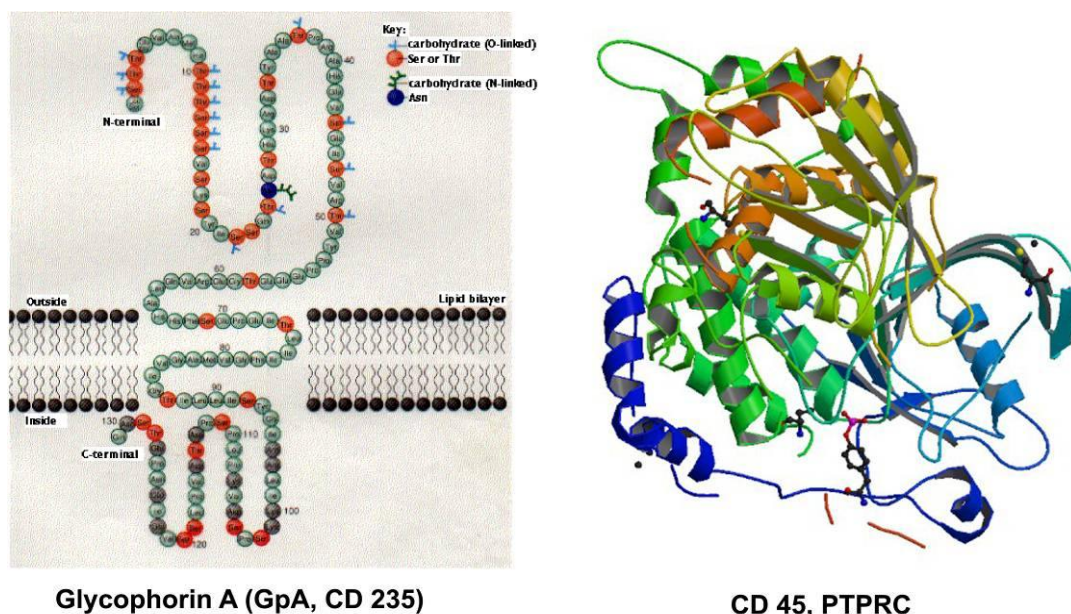


Figure 42. Left, schematic structure of erythrocyte transmembrane protein Glycophorin A (obtained from <http://users.rcn.com/jkimball.ma.ultranet/BiologyPages/G/Glycoproteins.html>). Right, structure of leukocyte transmembrane protein CD 45 (obtained from <http://molecularstructure.org>).

Evaluation of the cytotoxicity and haemolytic effect of the dual fluorescent-magnetic glyconanoparticles. Before the labelling experiments, the toxicity of the FMGNPs was evaluated against Raji cellular line and whole blood. First, a MTS assay [29] with Raji cells was carried out to test the cytotoxicity of our FMGNPs in the concentration range between 0 and 50 $\mu\text{m}/\text{mL}$. The results clearly indicate that FMGNPs were not cytotoxic for Raji cells even at concentrations of 50 $\mu\text{g}/\text{mL}$ (Figure 43 A). Then the toxicity and haemolytic effect of the FMGNPs were tested in whole blood. The measurement of any possible toxicity over blood cells is especially important as it has been recently described that nanoparticle systems can have an adverse effect over red blood cells integrity [32] [34] [38]. Blood samples were analysed before and after the incubation with different concentrations of nanoparticles

Results and Discussion

with the help of a commercial blood analyser. Comparison of 16 standard blood parameters showed no significant differences between blood and blood incubated with increasing concentration of FMGNPs (Figure 43 B)

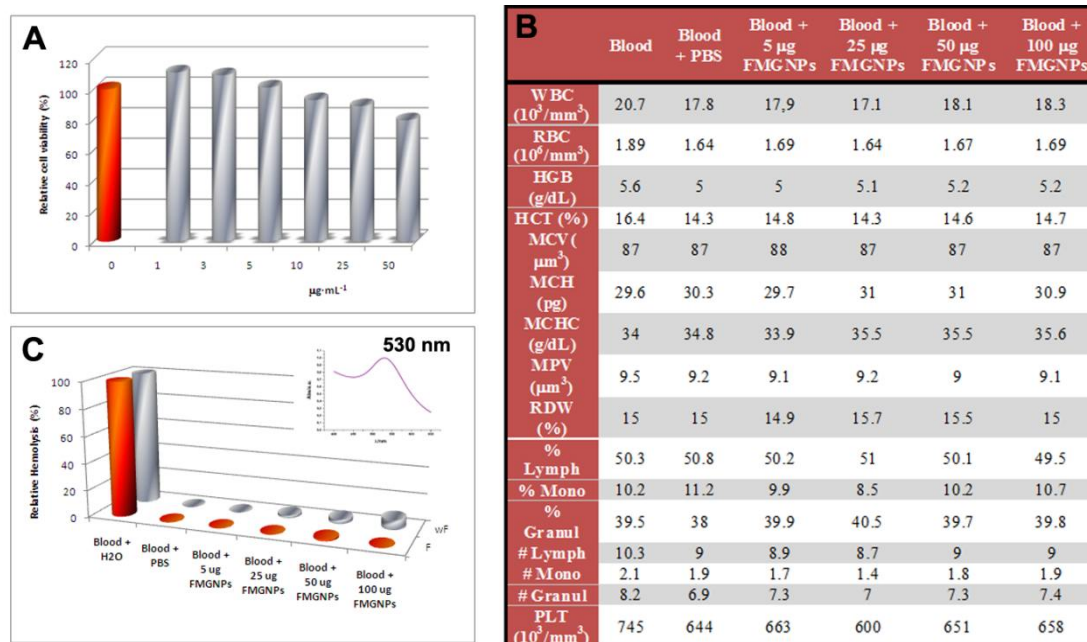


Figure 43. A, viability assay of Raji cells incubated with different concentrations of FMGNs (1, 3, 5, 10, 25 and 50 $\mu\text{g}/\text{mL}$) for 24 h at 37 $^{\circ}\text{C}$ and 5 % CO_2 atmosphere. B, results from blood analyses before and after the incubation with 100 μL of 10 mM PBS buffer containing different concentrations of FMGNPs. WBC, white blood cells; RBCs, red blood cells; HGB, haemoglobin; HCT, haematocrit; MCV, mean corpuscular volume; MCH, mean corpuscular haemoglobin; MCHC, mean corpuscular haemoglobin concentration; PLT, platelets; MPV, mean platelet volume; RDW, red blood cells distribution width; %Lym, %lymphocytes; %Mono, %monocytes; %Gran, %granulocytes; #Lym, ; #Mono, ; #Gran. C, haemolytic assay over 750 μL of whole blood incubated for 90 min at 37 $^{\circ}\text{C}$ with 750 μL of 10 mM PBS buffer containing different concentrations of FMGNPs. In gray, raw results; in red results after filtering the lysates through 100000 MWCO Amicon filters to remove the interfering nanoparticles. Inset, UV-Vis spectrum of a 10 mM PBS buffer solution of FMGNPs showing important absorption at 560 nm from the surface resonance plasmon of the nanoparticle that could interfere in haemolytic measurements.

Finally, an analytical colorimetric method was followed [39] to measure the haemolytic effect of different concentrations of FMGNPs over erythrocytes. Whole blood was incubated either with H_2O , or 10 mM PBS solutions of the FMGNPs. Under hypotonic conditions (H_2O) erythrocytes are lysed and haemoglobin can be detected at 560 nm in the supernatant after centrifugation. In the case of the samples containing FMGNPs a filtration step was introduced to remove the FMGNPs from the supernatants as their

Results and Discussion

surface Plasmon (530 nm) and the absorption peak of Texas Red (595 nm) interfered in the measurement (Figure 43 C inset). The final results (Figure 43 C) show that our FMGNPs do not have any haemolytic effect on the erythrocytes.

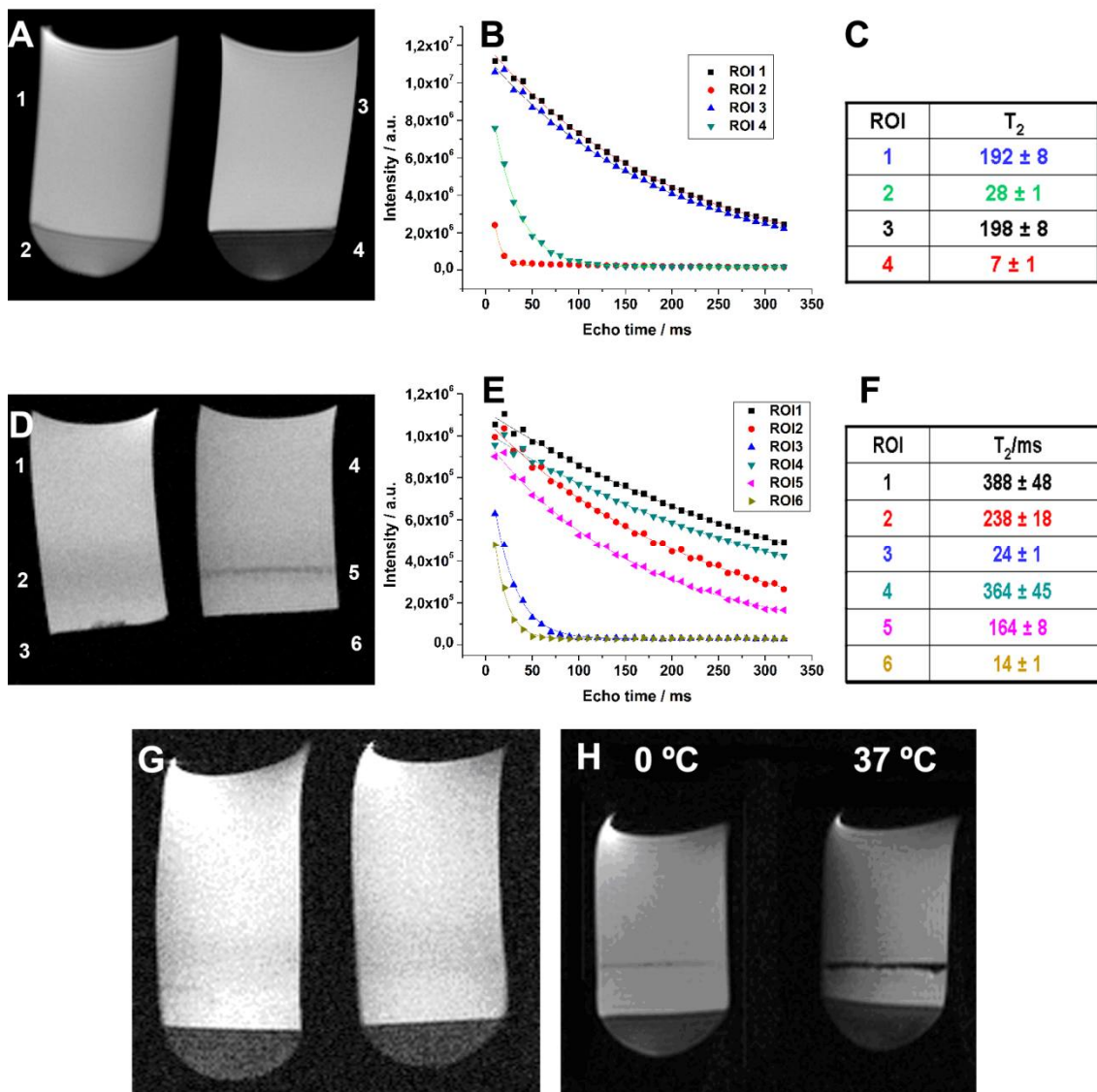


Figure 44. MRI T_2 -weighted image of the labelling of (A) red cells without nanoparticles (left) and with 50 $\mu\text{g}/\text{mL}$ of anti-CD235a *immuno*-FMGNPs (right), and (D) white cells without nanoparticles (left) and with 50 $\mu\text{g}/\text{mL}$ of anti-CD45 *immuno*-FMGNPs (right), and the corresponding T_2 plots and fits of ROIs from the labelling of the red (B) and white (E) bands. T_2 relaxation times of the ROIs from the labelling of the red (C) and white (F) bands. (G), MRI T_2 -weighted image of whole blood incubated with PBS (left) or 50 $\mu\text{g}/\text{mL}$ of non-functionalised FMGNPs. (H), MRI T_2 -weighted image of whole blood incubated with 50 $\mu\text{g}/\text{mL}$ of anti-CD45 functionalised FMGNPs at 0 °C (left) or 37 °C (right).

Specific blood populations labelling with fluorescent-magnetic *immuno-glyconanoparticles*. Blood aliquots were incubated at 4° C with 50 µg/mL of either anti-CD235a antibody *immuno*-FMGNPs or anti-CD45 antibody *immuno*-FMGNPs and after centrifugal washing, blood was added over Ficoll and separated into four bands (RBCs, Ficoll, PBMCs, and plasma) by density gradient centrifugation inside cryovials.

Right after centrifugation, the vials were placed into the MRI scanner and the T₂ weighed images and T₂ values from the regions of interest (ROIs) were obtained. Figure 44 A shows the MRI T₂ weighted images of the blood samples with (right) and without (left) anti CD235a *immuno*-MGNPs, both treated in the same way. Both images show two well defined and separated regions, characterized by a dark and a clearer colour, respectively. As erythrocytes contain iron-coordinated haemoglobin, an important decrease in the T₂ relaxation time is observed for those areas with higher accumulation of erythrocytes. The shortening of the T₂ value is a consequence of the magnetic nature of the iron present in the haemoglobin, which provokes changes in the local magnetic field, leading to a dephasing of the MRI signal. This effect is clearly observed in the T₂ weighted image from the control tube (Figure 44 A left), where the bottom part of the vial is remarkably darker (T₂ of 28 ms) than the upper part (T₂ 192 ms) with a 85% decrease in signal strength. In the presence of CD235a *immuno*-FMGNPs the differences in T₂ between the two regions (Figure 44 A right) are even bigger (96%) indicating that the cells are labelled with the *immuno*-nanoparticles. More important is the difference between both dark areas (control vial left *vs* sample vial right) where a 25% decrease in signal is observed, while the difference between the upper parts of the vials is negligible (figure 44 B and C). No labelling of the white band is observed. These results confirm a selective labelling of the erythrocytes by the magnetic nanoparticles as planned while leaving the rest of the blood's cells barely affected or completely unaffected.

The second type of *immuno*-magnetic nanoparticles synthesised are targeted against leukocytes (CD45 *immuno*-FMGNPs). As opposed to the control sample, in the T₂ weighted image (Figure 44 D right) a band is observed (marked as ROI 5, Figure 44 D) with a 55% loss of signal intensity with respect to the surrounding area. The T₂ map shows that the T₂ value of this band (ROI 5) is lowered to 164 ms, which represents a 30% decrease with respect to its mirror area (ROI 2) (figure 44 E, F). This difference is assigned to the selective labelling of leukocytes by the nanoparticles through the

antibody. Control experiments with untreated blood samples and blood incubated with the FMGNPs without antibodies, did not show any difference in the T_2 values of the different regions (figure 44 G).

In all the MRI experiments described until here, the incubations of the blood with the *immuno*-FMGNPs were performed at 4 °C to remove the potential contribution of internalised particles (the chosen targets CD235a and CD45 are membrane proteins). But in *in vivo* biological conditions blood temperature can be an important feature to be considered, so the specific labelling was repeated under the same conditions than above but at 37 °C. The results (figure 44 H) show that the *immuno*-FMGNPs can label efficiently blood cell populations independently of the temperature.

We want to remark that these results indicate that after the interaction of the *immuno*-nanoparticles with whole blood, they retain their activity to label specifically two different populations of cells. It seems that they are not masked by protein adsorption as has been described for many kinds of nanoparticles, even PEGylated ones [40] [41] [32]. This can be attributed to the carbohydrate coating that protects the nanoparticles from unspecific protein adsorption.

To further assess the specific labelling at cellular scale, the fluorescence of the *immuno*-FMGNPs was used to label either RBCs or leukocytes isolated from whole blood samples by fluorescence microscopy. For the labelling of 10^5 cells, concentrations of 50 $\mu\text{g}/\text{mL}$ of the corresponding antibody (anti CD45 for leukocytes or anti CD235a for RBCs) were used.

In the case of leukocytes the labelling was visible after 90 min incubation. However, in the case of RBCs no fluorescence was visible even using Ab concentrations of up to 300 $\mu\text{g}/\text{mL}$.

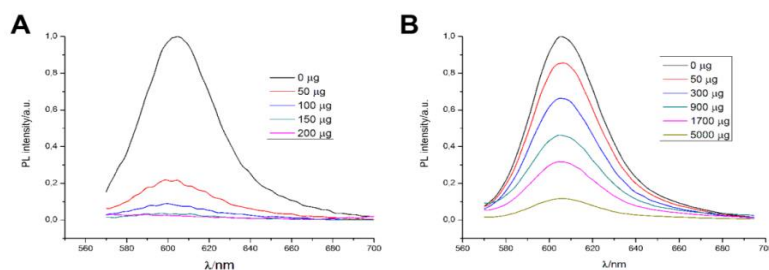


Figure 45. **A**, normalized photoluminescence spectra of a solution 100 $\mu\text{g}/\text{mL}$ of *immuno*-FMGNPs before (0 μg) and after the addition of different amounts of haemin. **B**, normalized photoluminescence spectra of a solution 100 $\mu\text{g}/\text{mL}$ of *immuno*-FMGNPs before (0 μg) and after the addition of different amounts of haemoglobin.

Results and Discussion

After bibliography revision we learnt that fluorophores quenching in RBCs is a common effect due to haemin, haemoglobin and other membrane biomolecules [42] [43] [44] [45] [46] [47]. Quenching experiments carried out with the *immuno*-FMGNPs and increasing amounts of haemin or haemoglobin showed a strong decrease in the emission band of nanoparticles (Figure 45 A and B). These phenomena can give an explanation to the lack of fluorescence emission in the RBCs observed by fluorescence microscopy.

As fluorescence results could not confirm or exclude the presence of the *immuno*-nanoparticles in the RBCs, we tried to confirm their presence on these cells by transmission electron microscopy (TEM).

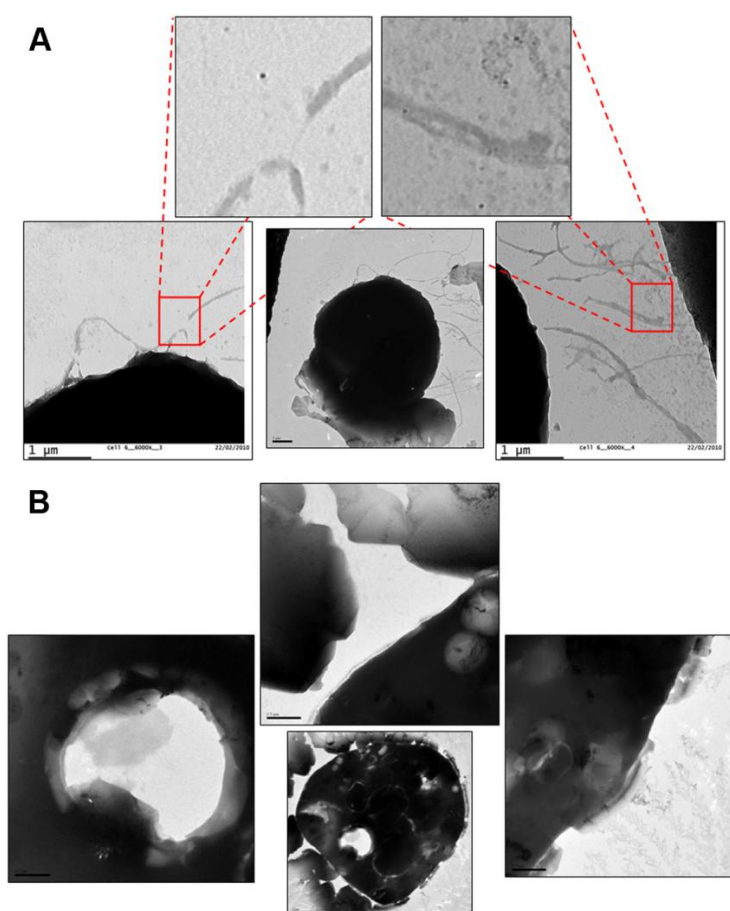


Figure 46. **A**, TEM micrograph of a RBC (central) incubated with a solution of *immuno*-FMGNPs anti-CD235a at a concentration of 25 μg/mL for 90 min, and magnifications of different areas of this image. *Immuno*-FMGNPs are clearly visible in the magnifications. **B**, TEM micrograph of a RBC (central) incubated with a solution of *immuno*-FMGNPs anti-CD45 at a concentration of 25 μg/mL for 90 min as control, and magnifications of different areas of this image.

Results and Discussion

The same samples that did not give a signal in previous fluorescence experiments were imaged by TEM and we observed some nanoparticles surrounding the cells (Figure 46 A) while TEM micrographs of RBCs incubated with the antiCD45-FMGNPs did not show the presence of nanoparticles (figure 46 B). The lack of emission of the *immuno*-FMGNPs in the cell medium supports the quenching effect of the red cells.

The next step was to label specifically leukocytes with anti-CD45 FMGNPs within a mixture of blood-isolated PBMCs and RBCs. PBMCs and RBCs can be distinguished by means of shape and size but there is another intrinsic characteristic that can be profited to differentiate unequivocally both of them. RBCs do not have nuclei while PBMCs are nucleated cells; thus DAPI dye was used to label the genetic material. Figure 47 shows the result of these stainings and it is clear that red (coming from the nanoparticles) and blue (coming out from the nuclei) signals co-localize in the same cells, confirming the specific labelling of leukocytes via anti-CD45 receptors.

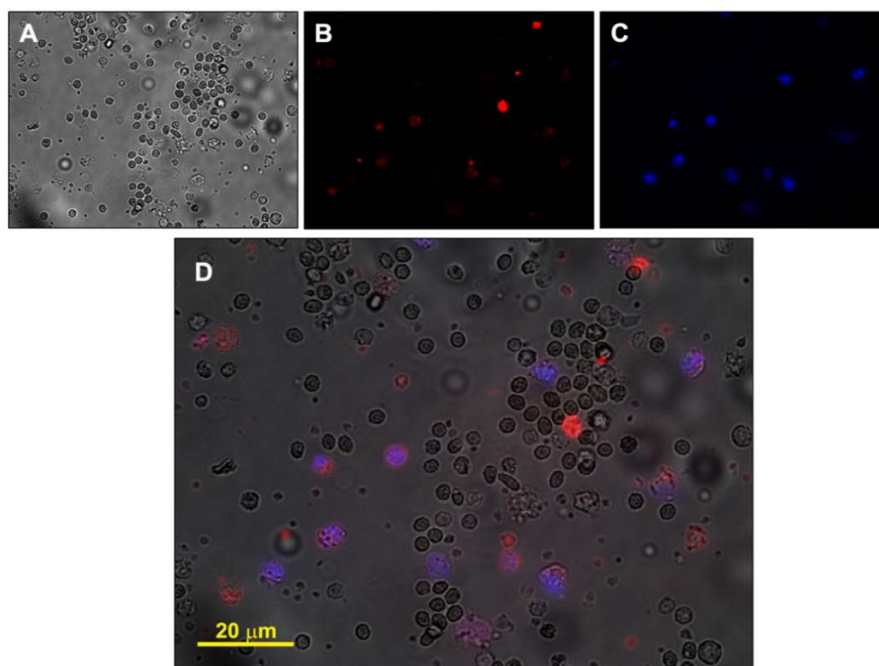


Figure 47. **A**, bright field image; **B**, red filter (TX2) fluorescence image; **C**, blue filter (A) fluorescence image; and **D**, superimposed image of the labelling of leukocytes within a mixture with RBCs, with *immuno*-FMGNPs at a concentration of 25 $\mu\text{g/mL}$ in antibody for 90 min.

Fluorescence images are not as clean as if working with cell lines because here whole blood samples were used as source of RBCs (erythrocytes make 92.9-96.6 % of total cell bloods). This means that different blood components such as plasma proteins as well

as platelets, which are small and quite numerous (135000-450000 per mm^3) will 'interfere' in the images. Moreover, since blood cells are non adherent, taking clean perfect images becomes difficult as floating or moving cells appear unfocused.

Application of *immuno*-quantum dots as potential anti-cancer agents

We have previously shown that QDs exhibit strong cytotoxic effects due to the CdTe cores and good optical properties in water. We thought that the combination of these two features make them potential candidates for the specific optical labelling of cells as well as for targeting and destruction of tumour cells.

To investigate the potential of QDs as anti-cancer agents, MPA-coated CdTe QDs were functionalised with an anti CD71 antibody. CD71 or TfR is a transferrin receptor that is known to be overexpressed in tumoural cells [48] [49]. This receptor is needed for the import of iron into the cell and maintains iron homeostasis. Overexpression of TfR in malignant cells mediates higher iron uptake required for cell division. To target these receptors, the same strategy used previously with the magnetic glyconanoparticles (MGNPs) was followed. First, protein G was bound to the QDs in a controlled way by conjugation to the carboxyl groups of the MPA using EDC/NHS as coupling agents. This reaction was performed under the same conditions as in the case of MGNPs, but keeping always the pH of the aqueous solution basic to protect the emission of the QDs. These constructions were incubated with an immunoglobulin G (IgG) anti-human transferrin receptor overnight (anti-CD71) to obtain the specific QDs to target the tumoural cells. The purification of the final functionalised QDs (*immuno*-QDs) was performed by centrifugal filtering through 100000 MWCO filters to remove non-functionalised QDs. The emission at 647 nm was the same as that of MPA coated QDs. The prepared QDs are water soluble and stable and contain an average of 3 protein G molecules per QD and 1.5 Ab molecules as determined by Bradford [50].

The cells chosen for this experiment were erythrocytes isolated from whole blood of healthy donors and as tumour cells C33 cellular line from cervix cancer. Such a mixture of cells would be a good model as for any *in vivo* application of the QDs. Erythrocytes (RBCs) will be the first cells that the QDs encounter after injection. One more

Results and Discussion

advantage of this model is that morphologically C33 and RBCs are completely different and can be distinguished easily at the microscope.

To perform the experiment, C33 cells were first incubated overnight in a sterile Petri dish. Then over these cells a population of recently isolated RBCs was added. This cellular mixture was incubated for a couple of hours in C33 culture medium to let them settle and then, a solution of the anti CD71-QDs was added. The Petri dish was then imaged every 3 mins in a cell observer semi-confocal microscope both in bright and fluorescence field for 12 h (figure 48; see also videos 1 and 2).

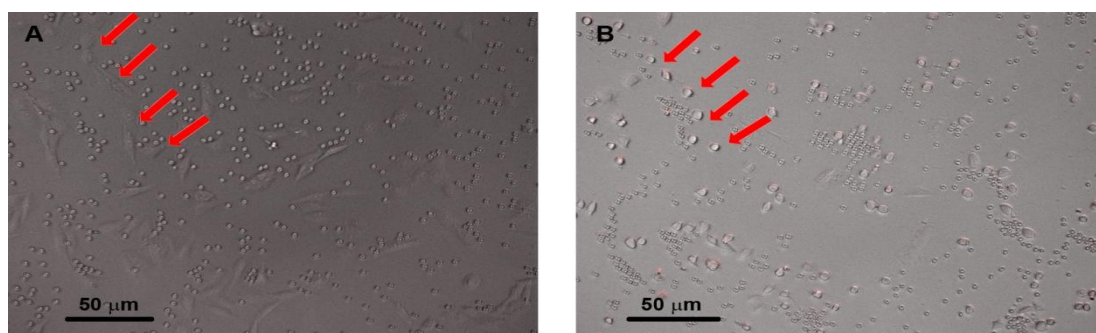


Figure 48. **A**, overlapped bright field and fluorescence image taken from a mixture of C33 cells and erythrocytes before the addition of anti-CD 71 functionalized QDs. **B**, overlapped bright field and fluorescence image taken over the same cell population after 16 h incubation with anti-CD 71 functionalized QDs. C33 cells are clearly affected by QDs (important morphological changes) and also red fluorescence signal is visible inside these cells, indicating QD uptake. Red arrows have been introduced to facilitate the comparison of the morphology of C33 cells.

The results from this experiment are shown in figure 48 and videos 1 and 2. It is clearly visible that C33 cells are damaged by *immuno*-QDs cytotoxic effect, while RBCs are not affected. Also, a red labelling coming from the emission of the immuno-QDs is observed in C33 cells, while RBCs appeared unlabelled. A control experiment with the same CdTe QDs but without further functionalization was also performed in which neither RBCs nor C33 cells are damaged in 12 hours by raw QDs.

References

1. De, M.G., P.S.; Rotello, V.M., *Application of nanoparticles in biology*. Adv. Mater., 2008. **20**: p. 1-17.

Results and Discussion

2. Gao, J., H. Gu, and B. Xu, *Multifunctional magnetic nanoparticles: design, synthesis, and biomedical applications*. *Acc Chem Res*, 2009. **42**(8): p. 1097-107.
3. Boisselier, E. and D. Astruc, *Gold nanoparticles in nanomedicine: preparations, imaging, diagnostics, therapies and toxicity*. *Chem Soc Rev*, 2009. **38**(6): p. 1759-82.
4. Vreys, R., et al., *MRI visualization of endogenous neural progenitor cell migration along the RMS in the adult mouse brain: validation of various MPIO labeling strategies*. *Neuroimage*. **49**(3): p. 2094-103.
5. Hoehn, M., et al., *Monitoring of implanted stem cell migration in vivo: a highly resolved in vivo magnetic resonance imaging investigation of experimental stroke in rat*. *Proc Natl Acad Sci U S A*, 2002. **99**(25): p. 16267-72.
6. Khalil, I.A., et al., *Octaarginine-modified multifunctional envelope-type nanoparticles for gene delivery*. *Gene Ther*, 2007. **14**(8): p. 682-9.
7. Josephson, L., et al., *High-efficiency intracellular magnetic labeling with novel superparamagnetic-Tat peptide conjugates*. *Bioconjug Chem*, 1999. **10**(2): p. 186-91.
8. de la Fuente, J.M., D. Alcántar, and S. Penadés, *Cell Response to magnetic glyconanoparticles: Does the carbohydrate matter?* *IEEE Trans Nanobio*, 2007. **6**(4): p. 275-281.
9. Gratton, S.E., et al., *The effect of particle design on cellular internalization pathways*. *Proc Natl Acad Sci U S A*, 2008. **105**(33): p. 11613-8.
10. Doherty, G.J. and H.T. McMahon, *Mechanisms of endocytosis*. *Annu Rev Biochem*, 2009. **78**: p. 857-902.
11. Nam, H.Y., et al., *Cellular uptake mechanism and intracellular fate of hydrophobically modified glycol chitosan nanoparticles*. *J Control Release*, 2009. **135**(3): p. 259-67.
12. Fujiwara, T., H. Akita, and H. Harashima, *Intracellular fate of octaarginine-modified liposomes in polarized MDCK cells*. *Int J Pharm*. **386**(1-2): p. 122-30.
13. Lu, C.W., et al., *Bifunctional magnetic silica nanoparticles for highly efficient human stem cell labeling*. *Nano Lett*, 2007. **7**(1): p. 149-54.
14. Ivanov, A.I., *Pharmacological inhibition of endocytic pathways: Is it specific enough to be useful?* *Methods in molecular biology*, 2008. **440**: p. 15-33.
15. Matteoni, R. and T.E. Kreis, *Translocation and clustering of endosomes and lysosomes depends on microtubules*. *J Cell Biol*, 1987. **105**(3): p. 1253-65.
16. Saftig, P. and J. Klumperman, *Lysosome biogenesis and lysosomal membrane proteins: trafficking meets function*. *Nat Rev Mol Cell Biol*, 2009. **10**(9): p. 623-35.
17. Grant, B.D. and J.G. Donaldson, *Pathways and mechanisms of endocytic recycling*. *Nat Rev Mol Cell Biol*, 2009. **10**(9): p. 597-608.
18. Cartiera, M.S., et al., *The uptake and intracellular fate of PLGA nanoparticles in epithelial cells*. *Biomaterials*, 2009. **30**(14): p. 2790-8.
19. Cole, L., et al., *ER-Tracker dye and BODIPY-brefeldin A differentiate the endoplasmic reticulum and golgi bodies from the tubular-vacuole system in living hyphae of *Pisolithus tinctorius**. *J Microsc*, 2000. **197**(Pt 3): p. 239-49.

Results and Discussion

20. Virtanen, I., P. Ekblom, and P. Laurila, *Subcellular compartmentalization of saccharide moieties in cultured normal and malignant cells*. J Cell Biol, 1980. **85**(2): p. 429-34.
21. Pearse, B.M., *Clathrin and coated vesicles*. Embo J, 1987. **6**(9): p. 2507-12.
22. Xia, T., et al., *Comparison of the mechanism of toxicity of zinc oxide and cerium oxide nanoparticles based on dissolution and oxidative stress properties*. ACS Nano, 2008. **2**(10): p. 2121-34.
23. Chiu, Y.L., et al., *The characteristics, cellular uptake and intracellular trafficking of nanoparticles made of hydrophobically-modified chitosan*. J Control Release. **146**(1): p. 152-9.
24. Panyam, J., et al., *Rapid endo-lysosomal escape of poly(DL-lactide-co-glycolide) nanoparticles: implications for drug and gene delivery*. Faseb J, 2002. **16**(10): p. 1217-26.
25. Singh, S., et al., *Unveiling the mechanism of uptake and sub-cellular distribution of cerium oxide nanoparticles*. Mol Biosyst. **6**(10): p. 1813-20.
26. Hillaireau, H. and P. Couvreur, *Nanocarriers' entry into the cell: relevance to drug delivery*. Cell. Mol. Life Sci., 2009. **66**: p. 2873-2896.
27. Engering, A., et al., *The dendritic cell-specific adhesion receptor DC-SIGN internalizes antigen for presentation to T cells*. J Immunol, 2002. **168**(5): p. 2118-26.
28. Cambi, A., et al., *Microdomains of the C-type lectin DC-SIGN are portals for virus entry into dendritic cells*. J Cell Biol, 2004. **164**(1): p. 145-55.
29. Cory, A.H., et al., *Use of an aqueous soluble tetrazolium/formazan assay for cell growth assays in culture*. Cancer Commun, 1991. **3**(7): p. 207-12.
30. Lacerda S.H., P.J.J., Meuse C., Pristiniski D., Becker M.L., Karim A., Douglas J.F., *Interaction of gold nanoparticles with common human blood proteins*. ACS Nano, 2010. **4**(1): p. 365-379.
31. LL. Ma, P.J., SS. Venkatraman, *Block Copolymer Stealth Nanoparticles for Chemotherapy: Interactions with Blood Cells In Vitro*. Adv. Func. Mater., 2008. **18**(5): p. 716-725.
32. Dobrovolskaia, M.A., et al., *Interaction of colloidal gold nanoparticles with human blood: effects on particle size and analysis of plasma protein binding profiles*. Nanomedicine, 2009. **5**(2): p. 106-17.
33. Hall, J.B., et al., *Characterization of nanoparticles for therapeutics*. Nanomedicine (Lond), 2007. **2**(6): p. 789-803.
34. Dobrovolskaia, M.A. and S.E. McNeil, *Immunological properties of engineered nanomaterials*. Nat Nanotechnol, 2007. **2**(8): p. 469-78.
35. Tomita, M., H. Furthmayr, and V.T. Marchesi, *Primary structure of human erythrocyte glycophorin A. Isolation and characterization of peptides and complete amino acid sequence*. Biochemistry, 1978. **17**(22): p. 4756-70.
36. Charbonneau, H., et al., *The leukocyte common antigen (CD45): a putative receptor-linked protein tyrosine phosphatase*. Proc Natl Acad Sci U S A, 1988. **85**(19): p. 7182-6.
37. Julius M. Cruse, R.E.L., Huan Wang, *Immunology Guidebook*. Elsevier Academic Press, London, UK, 2004.

Results and Discussion

38. Dobrovolskaia M.A., C.J.D., Jeffrey D., Neun B.W., Hall J.B., Patri A.K., McNeil S.E., *Method for analyses of nanoparticle hemolytic properties in vitro*. Nano Letters, 2008. **8**(8): p. 2180-2187.
39. Koziara J.M., O.J.J., Skers W:S., Ferraris S.P., Mumper R.J., *Blood compatibility of cetyl alcohol/polysorbate-based nanoparticles*. Pharmaceutical research, 2005. **22**(11): p. 1821-1828.
40. Mu Q., L.Z., Li X., Mishra S.R., Zhang B., Si Z., Yang L., Jiang W., Yan B., *Characterization of protein clusters of diverse magnetic nanoparticles and their dynamic interactions with human cells*. J Phys Chem C, 2009. **113**(14): p. 5390-5395.
41. Lacerda, S.H., et al., *Interaction of gold nanoparticles with common human blood proteins*. ACS Nano. **4**(1): p. 365-79.
42. Lissi, E.A. and T. Caceres, *Oxygen diffusion-concentration in erythrocyte plasma membranes studied by the fluorescence quenching of anionic and cationic pyrene derivatives*. J Bioenerg Biomembr, 1989. **21**(3): p. 375-85.
43. Stokke, T., et al., *Quenching of Hoechst 33258 fluorescence in erythroid precursors*. Cytometry, 1990. **11**(6): p. 686-90.
44. Jumi Kim, J.-M.K., *Fluorescence Quenching of a Partially Conjugated Polymer by Hemoglobin*. Macromolecular Research, 2007. **15**(1): p. 90-92.
45. Michel Deumie, M.E.B., Edwin Quinones, *Fluorescence quenching of pyrene derivatives by iodide compounds in erythrocyte membranes: an approach of the probe location*. Journal of Photochemistry and Photobiology A: Chemistry 1995. **87**: p. 105-113.
46. Crowley, J.B., R.C. Birkmeyer, and A.L. Tan-Wilson, *Additional antigenic sites on human hemoglobin evident upon separation of antibody populations*. Mol Immunol, 1980. **17**(12): p. 1449-57.
47. Wilson, D.H., et al., *Fully automated assay of glycohemoglobin with the Abbott IMx analyzer: novel approaches for separation and detection*. Clin Chem, 1993. **39**(10): p. 2090-7.
48. R. Sutherland, D.D., C. Schneider, R. Newman, J. Kemsheard, M. Greaves, *Ubiquitous cell-surface glycoprotein on tumour cells id proliferation-associated receptor for transferrin*. Proc. Natl. Acad. Sci. U.S.A., 1981. **78**(7): p. 4515-4519.
49. I.S. Trowbridge, M.B.O., *Human cell surface glycoprotein related to cell proliferation is the receptor for transferrin*. Proc Natl Acad Sci U S A, 1981. **78**(5): p. 3039-3043.
50. Bradford, M.M., *A rapid and sensitive method for the quantitation of microgram quantities of protein utilizing the principle of protein-dye binding*. Anal Biochem, 1976. **72**: p. 248-54.

Experimental part

Materials and methods

All chemical reagents were purchased from Sigma-Aldrich or Invitrogen and were used as received without further purification. Fluorescence images were acquired on a Leica DMI 6000B epifluorescence inverted microscope. Confocal imaging was performed on a Zeiss LSM 510 instrument. Fluorescence data from 96-well plates were obtained in a Tecan Genius pro instrument. FSC experiments were carried out on a BD FACS Canto II instrument. MRI images were acquired in a Bruker Biospec 11.7 T with a 9 cm gradient capable of delivering 740 mT/m. Blood samples from healthy donors were obtained from the Basque Blood Bank in San Sebastian. Blood samples were analysed with the help of ABX Micros 60 blood analyzer (Horiba). Fluorescence spectra were obtained in a Perkin Elmer LS55 fluorimeter.

Uptake and intracellular fate of dual fluorescent-magnetic glyconanoparticles

Fluorescent-magnetic glyconanoparticles uptake. $6 \cdot 10^3$ cells were seeded per well and incubated in 200 μ L of minimum essential medium Eagle for 24 hours at 37 °C and 5 % CO₂ in a 96-well dark plate. The media was removed and 200 μ L of culture media containing 50 μ g/mL of FMGNPs were added to each well. The cells were further incubated at 37 °C and 5 % CO₂ and at different incubation times (0, 10, 20, 30, 60, 120, 210 and 360 min) the cells were washed three times with 10 mM PBS buffer to remove free nanoparticles, and the fluorescence of each well was measured at 612 nm. Each experiment was repeated three times and the fluorescence of the first washing was also measured as a quality control of the measurements.

Effect of endocytosis inhibitors. $6 \cdot 10^3$ cells were seeded per well and incubated in 200 μ L of medium for 24 hours at 37 °C and 5 % CO₂ in a 96-well dark plate. The media was removed and 200 μ L of culture media containing either 20 μ g/mL of chlorpromazine, 50 μ g/mL of nystatin, 3 μ g/mL of filipin III, 5 μ g/mL of cytochalasin D, 25 μ g/mL of dynasore, or 5 μ M of lactose were added and cells were incubated for 1 hour at 37 °C and 5 % CO₂. The media was removed and 200 μ L of culture media

Experimental Part

containing 50 µg/mL of FMGNPs and the corresponding inhibitor were added. After 1 more hour the cells were washed three times with 10 mM PBS buffer to remove free nanoparticles, and the fluorescence of each well was measured at 612 nm. Each experiment was repeated three times and the fluorescence of the first washing was also measured as a quality control of the measurements.

The data obtained from the inhibition studies were analysed using Student's *t* test for paired samples with $p = 0.05$.

Dose-dependent endocytosis inhibition by lactose. $6 \cdot 10^3$ cells were seeded per well and incubated in 200 µL of medium for 24 hours at 37 °C and 5 % CO₂ in a 96-well dark plate. The media was removed and 200 µL of 10 mM PBS buffer containing different concentrations of lactose (1, 3, 5, 7 and 10 µM) were added and cells were incubated for 1 hour at 37 °C and 5 % CO₂. The media was removed and 200 µL of 10 mM PBS buffer containing 50 µg/mL of FMGNPs and the corresponding concentration of inhibitor were added. After 1 more hour the cells were washed three times with 10 mM PBS buffer to remove free nanoparticles, and the fluorescence of each well was measured at 612 nm. Each experiment was repeated three times and the fluorescence of the first washing was also measured as a quality control of the measurements.

Wheat germ agglutinin labelling with FITC. 2290 µg ($6.4 \cdot 10^{-8}$ moles) of wheat germ agglutinin (WGA) were resuspended in an eppendorf in 1.0 mL of 50 mM borate buffer pH 9.3. Separately 750 µg ($9.6 \cdot 10^{-7}$ moles) of fluorescein isothiocyanate (FITC) were dissolved in DMF at a concentration of 10 mg/mL. Both solutions were mixed and shaken. After 1 hour the reaction was purified by size exclusion chromatography and final product was stored at -20 °C until further use.

FMGNPs intracellular fate. To get an insight into the fate of the nanoparticles once internalized into the cells different markers against organelle specific indicators were used: IgG mouse anti human EEA1 (5µg/mL) as a marker of early endosomes, IgG mouse anti human chlatrin (5 µg/mL) as a marker of chlatrin coated vesicles, WGA (50 µg/mL) as a marker of trans-Golgi, ERTracker (5 µM) as marker of endoplasmic reticulum, and LysoTracker (1 µM) as marker of lysosomes.

$5 \cdot 10^4$ cells were seeded per well in 24-well plate. After 24 hours of incubation at 37 °C and 5 % CO₂ the media was exchanged by fresh media containing 50 µg/mL of

MGNPs. The cells were incubated under the same conditions for 30, 180 or 360 more min and then they were fixed and permeabilized (4 % PFA, 0.1 % Triton X-100 in 10 mM PBS for 20 min at room temperature). After a 30 min blocking step (10 % BSA, 10 % horse serum, 0.025 % NaN_3 , 10 mM PBS buffer) the specific marker was added and incubated for 60 min (IgGs) or 30 min (WGA, ER and LysoTracker) at 37 °C. In the case of the antibodies after washing, a secondary anti mouse green-labelled antibody at 2.5 $\mu\text{g}/\text{mL}$ was incubated for 60 min at 37 °C. Finally all samples were mounted and imaged in a confocal microscope.

Zen LE (Zeiss) and ImageJ software (Rasband, W., 1997, US National Institutes of Health, <http://rsb.info.nih.gov/ij/>) were used for the co-localization analysis [1] of the acquired data.

Specific *in vitro* cellular labelling with *immuno-magnetic glyconanoparticles*

Cell culture. The Raji line of lymphoblast-like cells, established from a Burkitt's lymphoma were a generous gift from Dr. José Alcamí, Instituto de Salud Carlos III, Madrid. This line was grown in RPMI-1640 medium supplemented with 10 % Fetal Bovine Serum (Gibco), 2 mM L-glutamine and streptomycin/penicillin (100 U/mL penicillin and 100 $\mu\text{g}/\text{mL}$ streptomycin). Cells were subcultured following ATCC recommendations.

Cytotoxicity experiments. The biocompatibility of antiDC-SIGN *immuno*-MGNPs was studied at a range of concentrations (0.002-1 $\mu\text{g}/\text{mL}$) with Raji cells using a MTS standard protocol. $1 \cdot 10^4$ cells in 80 μL of media were seeded into a 96 well plate. Then, the conjugate solution (20 μL) at desired concentration was added and incubated at 37 °C, 5 % CO_2 atmosphere. After 20 hours, 20 μL of MTS solution (5 mg/mL) was added to each well and the cells were still incubated for 4 hours at 37 °C, 5 % CO_2 atmosphere. Finally the absorbance of samples was measurement at 490 nm by a microplate reader.

Flow Cytometry Analysis of Raji and Raji DC-SIGN. Raji and Raji DC-SIGN ($2 \cdot 10^5$ cells) were seeded into BD Falcon tubes in 300 μL of medium. After the addition of 500 μL of 10 mM PBS buffer, the solution was centrifuged twice at 440 g, 4 °C for 5 min.

Experimental Part

Then cells were fixed adding 200 μL of 2 % paraformaldehyde 10 mM PBS for 10 min at room temperature. After two washings with 500 μL of 10 mM PBS, the cells were blocked with 200 μL of blocking buffer (0.025 % $\cdot\text{NaN}_3$, 10 % horse serum, 10 % BSA, 10 mM PBS) and incubated 15 min at 37 $^\circ\text{C}$. After another washing step, the cells were incubated with 10 μL of a solution of the conjugate (1 $\mu\text{g}/\mu\text{L}$ of antibody) in 50 μL (final volume) of blocking buffer for 1 hour at 4 $^\circ\text{C}$. Two washing steps with 0.5 % Tween-20 10 mM PBS and incubation with 50 μL of a solution of secondary antibody alexa-Fluor488 rabbit antimouse IgG (5 $\mu\text{g}/\text{mL}$) in blocking buffer for 30 min at 4 $^\circ\text{C}$ were performed. After three washes with 0.5 % Tween-20 10 mM PBS, finally the cells were suspended in 300 μL of 10 mM PBS buffer before the measurement by flow cytometry.

In vitro MR imaging of Raji and Raji DC-SIGN. Raji and Raji DC-SIGN (10^4 cells) were seeded in an eppendorf tube in 300 μL of culture media. Then, the conjugate (120 μL , 0.4 $\mu\text{g}/\mu\text{L}$ in nanoparticle) was added and incubated for 30 min at 0 $^\circ\text{C}$. After fixing with 4 % paraformaldehyde 10 mM PBS solution for 30 min at room temperature, the cells were washed and centrifuged and the resulting cell pellet was mixed with 1 % agarose solution. For T_2 -weighted MR imaging of in vitro cells the following parameters were adopted: all data were acquired with 256 x 256 points and a resolution of 250 μm in plane, with a slice thickness of 1.5 mm. The T_E values were varied in 16 equally spaced steps ranging from 20 ms to 320 ms and T_R 5 s. The images were fitted into Levenberg-Margardt method to calculate T_2 values using Bruker's Paravision 5 software.

Fluorescence microscopy studies of Raji and Raji DC-SIGN. Raji and Raji DC-SIGN ($2 \cdot 10^5$ cells) were seeded in 200 μL of culture medium into BD Falcon tubes. After the addition of 500 μL of 10 mM PBS, the solution was centrifuged at 440 g at 4 $^\circ\text{C}$ for 5 min. Then cells were fixed adding 200 μL of 2 % formaldehyde 10 mM PBS for 15 min at 4 $^\circ\text{C}$. After two washes with 500 μL of 10 mM PBS, cells were blocked incubating with 200 μL of 0.025 % $\cdot\text{NaN}_3$, 10 % horse serum, 10 % BSA in 10 mM PBS buffer for 15 min at 37 $^\circ\text{C}$. After another washing step, the cells were incubated with 50 $\mu\text{g}/\mu\text{L}$ of $\text{Fe}_3\text{O}_4@Au@Lact/Link@ProtG@antiDC-SIGN$ in 50 μL (final volume) of

blocking buffer for 1 hour at 4 °C. Two washing steps with 0.5 % Tween-20 10 mM PBS were performed and cells were incubated with 50 µL of a solution of the secondary antibody, alexa-Fluor488 rabbit antimouse IgG (12.5 µg/mL) in blocking buffer for 1 hour at 4 °C. After three washes with 0.5 % Tween-20 10 mM PBS, finally, cells were suspended in 150 µL of 10 mM PBS and 20 µL of the cell suspension were dropped onto a thin microscope slide before taking images with a fluorescence microscope. In vitro studies were conducted using an oil-immersion 63x objective on a Leica inverted microscope with L5 green filter (a 480/40nm band-pass excitation filter and a 527/30nm band pass emission filter) and a Leica mercury lamp. Images were taken using a charge-coupled Hamamatsu camera.

Specific dual labelling of blood cell populations with *immuno-fluorescent magnetic glyconanoparticles*

Cell viability assay. The biocompatibility of the FMGNPs with Raji cells was studied at 0-50 µg/mL concentration range using a MTS standard protocol [2]. Cells suspensions ($1 \cdot 10^4$ in 80 µL of media) were seeded into a 96-well plate. Then, the conjugate solution (20 µL) at desired concentration was added and incubated at 37 °C, 5 % CO₂ atmosphere. After 20 h, 20 µL of MTS solution (5 mg/mL) were added to each well and cells were still incubated for 4 hours at 37 °C, 5 % CO₂ atmosphere. Finally the absorbance of the samples was measured at 490 nm in a multiplate reader.

Standard blood analyses. 750 µL of whole blood samples were incubated for 90 min at 37 °C with 100 µL of a 10 mM PBS buffer solution of the nanoparticles at 5 different concentrations (from 0 to 100 µg, of FMGNPs). After the 90 min the samples, together with a sample of untreated whole blood, were analysed with the help of ABX Micros 60 blood analyzer (Horiba) and 16 standard parameters were obtained for each sample.

Haemolysis assay. 750 µL of whole blood were incubated for 90 min at 37 °C in an orbital shaker with 750 µL of either H₂O or a 10 mM PBS buffer solution of the nanoparticles at 5 different concentrations (from 0 to 100 µg of FMGNPs). Then the samples were centrifuged at 600 g for 5 mins, the pellet was discarded and the

Experimental Part

supernatant was incubated at room temperature for 30 more min to allow haemoglobin oxidation. Finally the absorbance of the samples was recorded at 560 nm. The samples containing nanoparticles were then filtered through 100000 MWCO Amicon filters to remove the remaining nanoparticles that could interfere in the absorbance measurements, and their absorbance was recorded again.

Blood cell populations separation. In a typical blood cell separation from buffy coat packs, four bands were obtained by Ficoll-Paque (GE Healthcare) gradient density centrifugation: Red Blood Cells (RBCs) band, Ficoll band, Peripheral Blood Mononuclear Cells (PBMCs) band and plasma band (bottom to top). Buffy coat packs from healthy donors were obtained from the Basque Center for transfusions and human tissues. Briefly, blood contained in buffy coat was diluted with Hank's Balanced Salt Solution (HBSS, Gibco), supplemented with 1 % Fetal Bovine Serum (FBS) in a 1:1 ratio. Carefully, 750 μ L of diluted blood were loaded onto 250 μ L Ficoll in CryoTube vials (Nunc). Vials were centrifuged for 25 min at 400 g, 4 °C without brake to achieve cell separation. After density gradient centrifugation, PBMCs were collected from the interface, washed three times with 10 mM PBS/2mM EDTA/0.5 % BSA/pH 7.2 (spin for 10 min, at 3000 g, 4 °C) and counted with Neubauer Chamber. RBCs collected from this blood separation will not be used for our experiments as they are agglutinated by Ficoll.

Red Blood Cells purification from whole blood. Blood contained in buffy coat was diluted with Hank's Balanced Salt Solution (Gibco) supplemented with 1% Fetal Bovine Serum in a 1:1 ratio and centrifuged for 10 min at 350 g, 20 °C. The supernatant was discarded and pellet was washed twice in the same way with 10 mM PBS.

Specific labelling of blood populations by MRI using functionalized fluorescent magnetic glyconanoparticles (*immuno-FMGNPs*). According to the method described above, after diluting blood from buffy coats with HBSS + 1 % FBS, 750 μ L of diluted blood were incubated for 90 min at 0 °C on ice with 50 μ g of *immuno-FMGNPs* (IgG anti human Glycophorin A for red cells) or 50 μ g of *immuno-FMGNPs* (IgG anti human CD45 for white cells). After incubation, 5 mL 10 mM PBS were added and vials were centrifuged for 15 min at 900 g, 4 °C. Then, the blood pellet was

completed to 750 μL with 10 mM PBS, and finally blood separation was achieved following exactly the previous protocol.

MRI imaging of the previous separations. All MRI experiments were performed with a Bruker Biospec 11.7 T horizontal scanner operating at a proton frequency of 500 MHz (Bruker Biospin GmbH, Ettlingen, Germany) with a 9 cm gradient capable of delivering 740 mT/m and a rise time of 100 ms. T_2 -weighted multi-spin-echo sequences were measured with the following parameters: All data were acquired with 256 x 256 points and a resolution of 155 μm in plane, slice thickness of 1 mm, (TR: 3000 ms, TE: 10-320 ms in 10 ms steps), number of averages 1-4. T_2 maps were generated based by fitting the images into Levenberg-Margardt method using Bruker's Paravision 5 software.

Specific labelling of blood populations by fluorescence microscopy using functionalized fluorescent magnetic glyconanoparticles (*immuno*-FMGNPs). $2 \cdot 10^6$ blood cells (either whole blood-RBCs, or PBMCs) were fixed with 2.5 % formaldehyde, 10 min at 4 °C following a standard protocol. After fixation, 10^5 fixed cells (whole blood-RBCs, PBMCs, or a mixture 1:1 of both) were incubated for 90 min at 0 °C on ice with 50 μL of 10 mM PBS buffer containing a concentration of *immuno*-FMGNPs of 50 μg of $\text{Ab} \cdot \text{mL}^{-1}$ (25 μg $\text{Ab} \cdot \text{mL}^{-1}$ in the case of 1:1 cell mixtures). After the incubation, cells were washed three times with 500 μL of cold 10 mM PBS, and finally were resuspended in 80 μL of the same buffer. 20 μL drops of the samples were deposited onto a thin glass slide and then mounted upwards in the microscope. After 5 min to let the cells settle, the samples were imaged using an oil-immersion 63x objective on a Leica inverted microscope with TX2 filter (a 560/40 nm band-pass excitation filter and a 645/75 nm band pass emission filter), an A filter with a 340-380 nm band-pass excitation and 425 nm long-pass emission, and a Leica mercury lamp.

Fluorescence quenching experiments. 150 μg of FMGNPs were solved in 1500 μL of 10 mM PBS buffer in a quartz cubette. The cubette was placed in the fluorimetre with magnetic stirring and a spectrum was acquired from 570 to 700 nm with an excitation wavelength of 550 nm and a scan speed of 500 nm/min. Then, 10 μL of a solution either of haemin 5 mg/mL in 1.4 M NH_4OH H_2O or human haemoglobin 5 mg/mL in 10 mM PBS buffer were added into the cubette and the spectrum was acquired again. This procedure was repeated after the different additions.

Cellular sample preparation for TEM imaging. Carbon only TEM copper grids were hydrophilised by glow discharge at 15 mA for 2 min just before sample deposition. 4 μL of the same cell samples prepared for fluorescence imaging were deposited over the hydrophilised grids and after 3 min the remaining liquid was sucked away with a filter paper. The grids were then placed inside a vacuum chamber for 12 h before imaging.

Application of CdTe quantum dots in specific cell labelling and as potential anti-cancer agents

QDs functionalization. 1 mg of lyophilized CdTe QDs (aprox. $1 \cdot 10^{-8}$ moles) were dissolved in 1 mL of 10 mM PBS in an eppendorf tube. To this solution, 469 μg of EDC ($3 \cdot 10^{-6}$ moles) and 795 μg of NHS ($6.9 \cdot 10^{-6}$ moles) were added and the solution was shaken for 90 min. Then, 659 μg of protein G ($3 \cdot 10^{-8}$ moles) were added and the reaction continued for 60 min previous to the addition of 30 μg of mannose- $\text{C}_2\text{-NH}_2$ neoglycoconjugate. The reaction was shaken 120 min more and then purified using Amicon centrifugal filters (MWCO 30000). Finally the ProtG-QDs (Protein G functionalized QDs) were resuspended in basic 10 mM PBS pH 9.4 and stored at 4 $^\circ\text{C}$, -20 $^\circ\text{C}$ or lyophilized.

Antibody incubation with protein G functionalized QDs. 120 μL of the previous solution were incubated for 6 hours at 10 $^\circ\text{C}$ with 33 μg of IgG ($1.06 \cdot 10^{-9}$ moles). The sample was purified centrifuging at 16400 g for 90 min at 4 $^\circ\text{C}$, removing the supernatant and washing the pellet twice with 10 mM PBS. The final sample was kept refrigerated until further use.

RBCs purification from whole blood. 10 mL of whole blood from buffy coat were mixed with 10 mL of HBSS medium without Ca^{2+} nor Mg^{2+} (to prevent coagulation) and centrifuged for 10 min at 350 g. The supernatant was discarded and the pellet was washed twice in the same way with 10 mM PBS buffer.

Specific cell targeting with functionalised CdTe QDs. 10^6 C33 cells were incubated in a sterile 5.5 cm \varnothing petri dish at 37 $^\circ\text{C}$ and 5 % CO_2 . After 24 hours 10^6 erythrocytes

Experimental Part

were added with 1.5 mL of C33 culture medium. The petri dish was mounted in the fluorescence microscope (Cell observer) and then 1.5 mL of medium containing 50 μg of IgG anti human CD71 functionalised QDs (aprox. $2.2 \cdot 10^{-10}$ moles) were added. The sample was imaged with a 10x objective for 12 hours during which two images (bright field image and fluorescence image) were taken each 4 min.

Control experiment with non-functionalised CdTe QDs. 10^6 Raji cells were seeded together with 10^5 erythrocytes in a sterile 5.5 cm \varnothing petri dish in a total volume of 1.5 mL of Raji culture medium. The petri dish was mounted in the fluorescence microscope (Cell observer) and then 1.5 mL of medium containing 500 μg (aprox. $2.2 \cdot 10^{-9}$ moles) of non-functionalised QDs were added. The sample was imaged during 12 hours during which two images (bright field image and fluorescence image) were taken each 4 min.

References

1. Li, Q., et al., *A syntaxin 1, Galpha(o), and N-type calcium channel complex at a presynaptic nerve terminal: analysis by quantitative immunocolocalization*. J Neurosci, 2004. **24**(16): p. 4070-81.
2. Cory, A.H., et al., *Use of an aqueous soluble tetrazolium/formazan assay for cell growth assays in culture*. Cancer Commun, 1991. **3**(7): p. 207-12.

CHAPTER 6

***In vivo* tracking of endogenous neural progenitor migration towards brain damaged sites with *immuno*-magnetic glyconanoparticles**

***In vivo* tracking of endogenous neural progenitors in response to damage**

Introduction

Mammalian brain has been long considered to have poor, if any, neuronal regenerative capacity. It is now clearly established that neurogenesis is maintained in discrete brain regions during mammal's lifespan. This cellular differentiation occurs primarily in two regions of the adult brain, the dentate gyrus of the hippocampus and the subventricular zone (SVZ) of the lateral ventricles. However, in rodents (the main subjects of study in brain studies), the main source of adult neural stem cells is the SVZ [1]. Under normal conditions progenitors formed in the SVZ migrate rostrally along a well defined pathway known as the rostral migratory stream (RMS) [2] to the olfactory bulb (OB) where they differentiate not only into neurons but also into astrocytes and oligodendrocytes [3].

Recent studies have shown that neural progenitor cells arising from the SVZ can also migrate towards damaged brain regions and subsequently differentiate into the phenotype of the destroyed cells [4-5]. These studies indicate that the adult brain has the capacity for neuronal self-repair. Disturbed adult neurogenesis has been reported in neurodegenerative diseases [6]. An increase in cell proliferation in the SVZ has been observed in Alzheimer patients, as well as in a mouse model for Alzheimer's disease [7]. Conversely, in a rat model for Parkinson's disease, experimental depletion of dopamine resulted in decreased cell proliferation in the SVZ [8]. This reduction was also demonstrated in human Parkinson's disease [9]. However, all these studies have been only done *ex vivo* and little is known about these cell migrations and differentiations *in vivo*.

To date, fluorescence imaging and electron microscopy (EM) have been principally used to identify migrating cells derived from cells in the SVZ. Due to the number of antibodies specific to these cells, immunohistochemistry has been used to detect groups of cells in well-defined areas. Bromodeoxyuridine has also been used to specifically label these cells because they divide in the SVZ before migrating. Additionally, transgenic cells expressing green fluorescent protein have been successfully used to

study cell migration [10]. However, none of these techniques enable migration throughout the brain within living animals to be studied.

Bioluminescence and optical fluorescent imaging have been employed as non-invasive methods to track neural stem cell migration and monitor therapeutic efficacy in animal models [11]. However, the clinical utility of these imaging modalities is limited by poor tissue penetration and low spatial resolution, making them impractical for use in patient trials. Although positron emission tomography is commonly used in preclinical and clinical studies for visualization of various tumours and drug interactions and for understanding tumour metabolism with high specificity, its low spatial resolution (>3–4 cm), radiation dose, and relatively short-term signal production make it a non-ideal technique for clinical tracking of cells [12], which requires extended periods of observation.

Numerous works have been done recently using MRI to characterize this pathway *in vivo* [13-16]. Clinical Magnetic Resonance Imaging (MRI) has high spatial resolution (approximately 1 mm³) with excellent soft tissue contrast for non-invasive, dynamic *in vivo* assessment of cellular trafficking at multiple time points. One more mayor advantage of MRI is that the migration can be directly followed onto the anatomy maps available from MRI. In addition, functional activity can be available from fMRI or neuronal tract tracing [17]. MRI-based neural cell tracking in intact animals was first described in 1990 [18] with transplanted iron-oxide labelled cells, and has been further developed in a number of laboratories (see ref [19] for recent review of this field).

Recently, the group of Augusto Silva at the Centre of Biological Research (CSIC) has been able to generate monoclonal antibodies Nilo1 and Nilo2 (Neural Identification Lineage from Olfactory Bulb) highly specific to neural stem and early progenitor cell surface antigens [20]. In the SVZ, Nilo1 identifies an early neural precursor subpopulation lining the ventricle, whereas Nilo2 detects more differentiated neural progenitors associated with the anterior horn of the SVZ at the beginning of the RMS.

In collaboration with this group, we have coupled Nilo2 antibody to our previously prepared protein G functionalised magnetic glyconanoparticles (*immuno*-MGNPs) to be used as specific labelling probes to study *in vivo* the migration of neural progenitor cells towards brain injuries by magnetic resonance imaging.

Neural stem cells tracking with *immuno*-magnetic glyconanoparticles

We have coupled Nilo2 Ab to the glyconanoparticles following our standard protocol and the ability of these *immuno*-MGNPs to recognize its target cells was tested *in vitro* with olfactory bulb derived mouse neurospheres that were generated by Dr. Silva group (Figure 49). Both flow cytometry and immunocytochemistry experiments confirmed that the labelling capacity and the labelling extension of Nilo2 capped nanoparticles are very similar to that of free Nilo2 Ab.

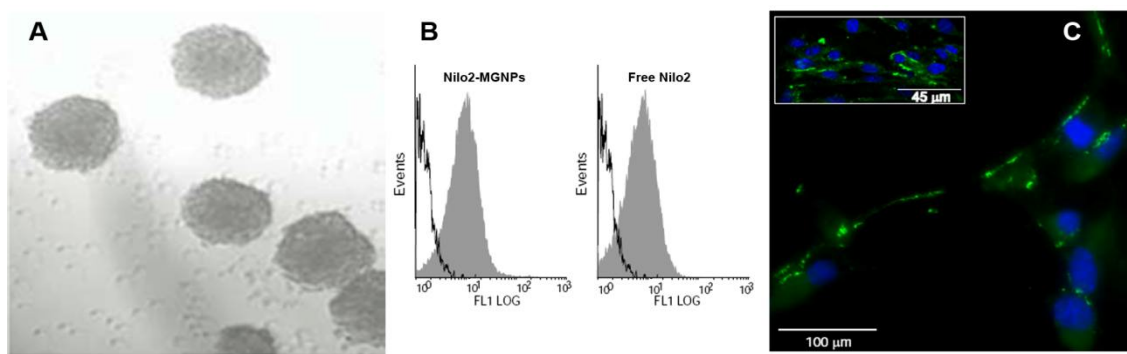


Figure 49. A, olfactory bulb-derived mouse neurospheres used for the *in vitro* tests. B, flow cytometry analyses of Nilo2 positive cells from SVZ neurospheres incubated either with MGNP-ProtG-Nilo2 or free Nilo2. C, immunocytochemistry of MGNP-ProtG-Nilo2 labelled neurosphere cells (green) grown in Matrigel and detected with traditional or confocal microscopy (inset). Dapi (blue) was used to stain nuclei.

With this confirmation, we went a step further to the *in vivo* tests. In a first experiment mice were injected intracranially with green fluorescent protein transfected astrocytoma cells (GFP-CT-2A) in the left hemisphere to generate a tumour, and then, 13 days later they were contralaterally injected in a more rostral position with Nilo2 *immuno*-MGNPs (figure 50, A). T_2^* -weighed MRI images of the brain were acquired one day before (d+12) MGNP injection (as background image), and one (d+14) and five days (d+20) after MGNP injection. The obtained images (figure 50, B) demonstrated a migration from the injection site of the nanoparticles towards the contralateral damaged area. At d+14, the contrast agent has already arrived at the site of the tumour and after 4 days more (d+18) accumulation of MGNP was clear. A control experiment with MGNP

Results and Discussion

coupled to a human Ab against p53 protein (hp53) demonstrated specificity as the contrast agent did not move from the injection site.

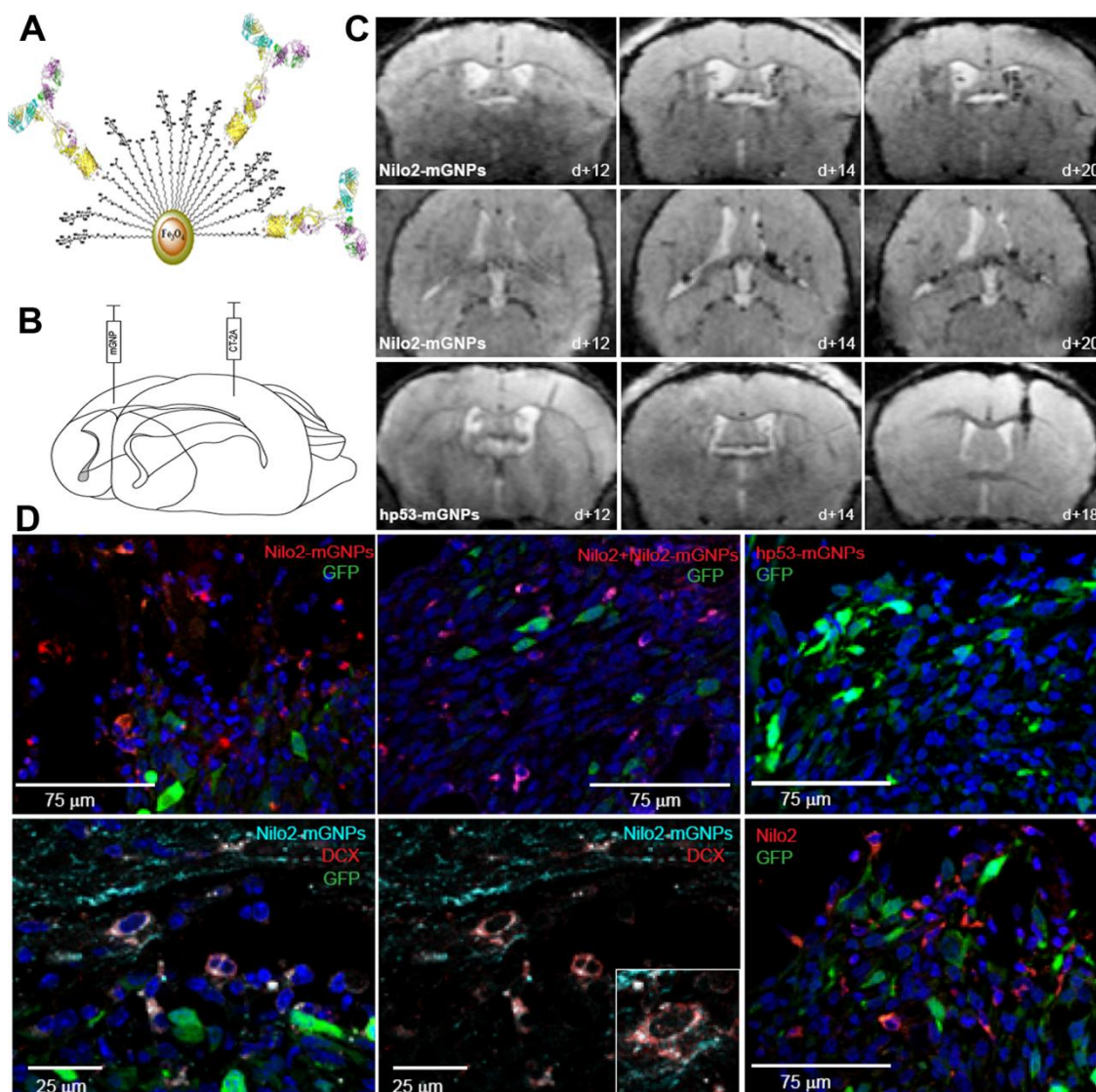


Figure 50. A, schematic representation of the *immuno*-MGNPs used in these studies. B, brain injection sites for GFP-CT-2A astrocytoma cells and Nilo2 functionalised nanoparticles. C, MRI analyses of the brain of representative mice injected with GFP-CT-2A cells (day 0) and Nilo2 functionalised nanoparticles (axial and coronal views) or hp53 functionalised nanoparticles (axial view) as control, before (day +12), one day after (day +14) and 5 or 7 days after (day +18 or +20) nanoparticles injection. D, immunohistochemistry analyses using confocal microscopy of fixed mice brains labelled with Nilo2-functionalised or hp53-functionalised nanoparticles and sacrificed after MRI measurements. GFP-CT-2A astrocytoma cells were identified in green. Anti-hamster biotin and Texas red- (red) or Alexa Fluor 647-labelled streptavidin (cyan) was used to identify free Nilo2 or Nilo2-functionalised nanoparticles. Cy3-labelled (red) anti-rabbit polyclonal antibody was used to detect hp53-functionalised nanoparticles.

The results of the MRI experiments were later confirmed by immunohistochemistry. The brains of the mice were fixed, sliced and stained with specific Abs against Nilo2, doublecortin (DCX, for the specific labelling of neuroblasts), or hp53. The tumoural cells were identified from the GFP staining (figure 50, C). This staining confirmed that Nilo2 positive cells surrounding the tumour were type 1 neuroblasts. In the case of hp53 no staining was observed near the tumour.

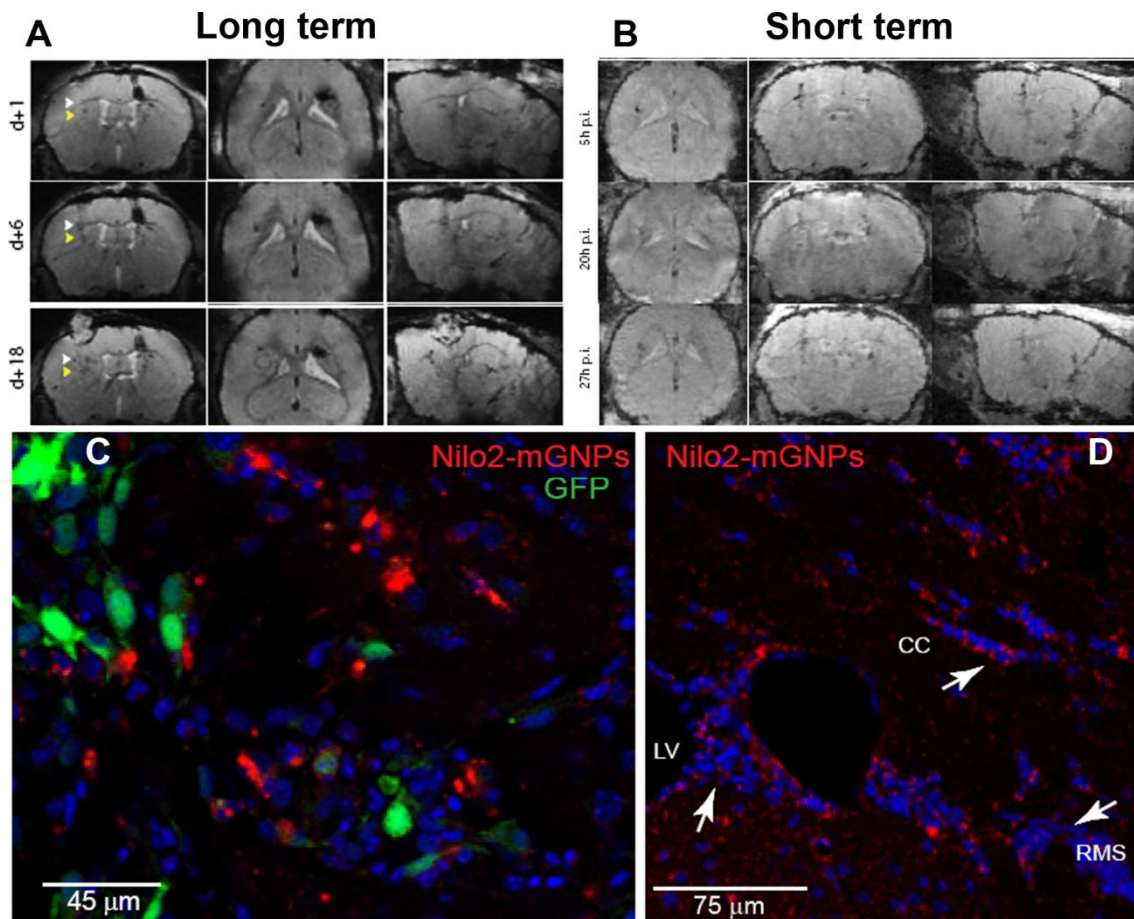


Figure 51. A, long term and B, short term MRI analyses (axial, coronal and sagittal views) of Nilo2 positive cells migrating towards the tumour site, one day (d +1), six days (d +6) and eighteen days (d +18) after Nilo2-functionalised nanoparticles injection in the right hemisphere. At day 0 a tumour was generated by the injection of GFP-CT-2A cells in the left hemisphere. C and D, immunohistochemistry of brain sections fixed after MRI, C, at the tumour site or D at the *corpus callosum* and the ventricle contralateral to the tumour site. Nilo2-functionalised nanoferrites were identified with an anti-hamster biotin-streptavidin-Alexa Fluor 647 (red) antibody. Nuclei were stained with Dapi (blue) and tumour cells are identified in green.

In a second set of experiments, the protocol was changed so that Nilo2-nanoparticles were injected before the induction of the damage to favour the labelling of neuroblasts in their niches. Three days later, the tumour was generated in the contralateral hemisphere and the *in vivo* short- and long-term migration of endogenous Nilo2 positive cells from the SVZ was followed by MRI. After the MRI experiments, the same mice were sacrificed and immunohistochemical analyses of their fixed brains was performed (figure 51, A-D). The results show that Nilo2⁺ cells migrate towards the injury even in the very first hours (5 h) after the injection of the tumour cells. Chain-like formations of labelled cells were visible in the immunostainings moving from the lateral ventricles towards the tumour through the highly dense *corpus callosum*. Reproducible results were obtained with different animals.

The recruitment of neural stem cells by different kinds of brain injuries was also investigated. Following demyelination or a mechanical injury, Nilo2⁺ neuroblasts also migrated to the damage site with equivalent kinetics. Lysophosphatidilcholine (LPC) injected in the left CC induced a demyelination that was analyzed by MRI on mice previously injected with Nilo2-MGNPs in the right SVZ. Hypointense signals in the lateral ventricles were detected twenty-four hours after LPC injection, being higher in the lateral ventricle closer to the damage site (figure 52). In the absence of injury, however, Nilo2-MGNPs remained at the injection site for at least twenty-five days (figure 52, a-d). Although the initial LPC effect was a localized demyelination [21], at latter times (d+25) triggered an inflammatory response of the white matter, leading to an accumulation of Nilo2-MGNPs near the hippocampus demyelinated region (figure 52, h). Indeed, immunohistochemical analyses showed that Nilo2⁺ cells were adjacent to oligodendrocytes (O4⁺) and myelin producing cells (myelin⁺) present in the damaged white matter (figure 52, i-n).

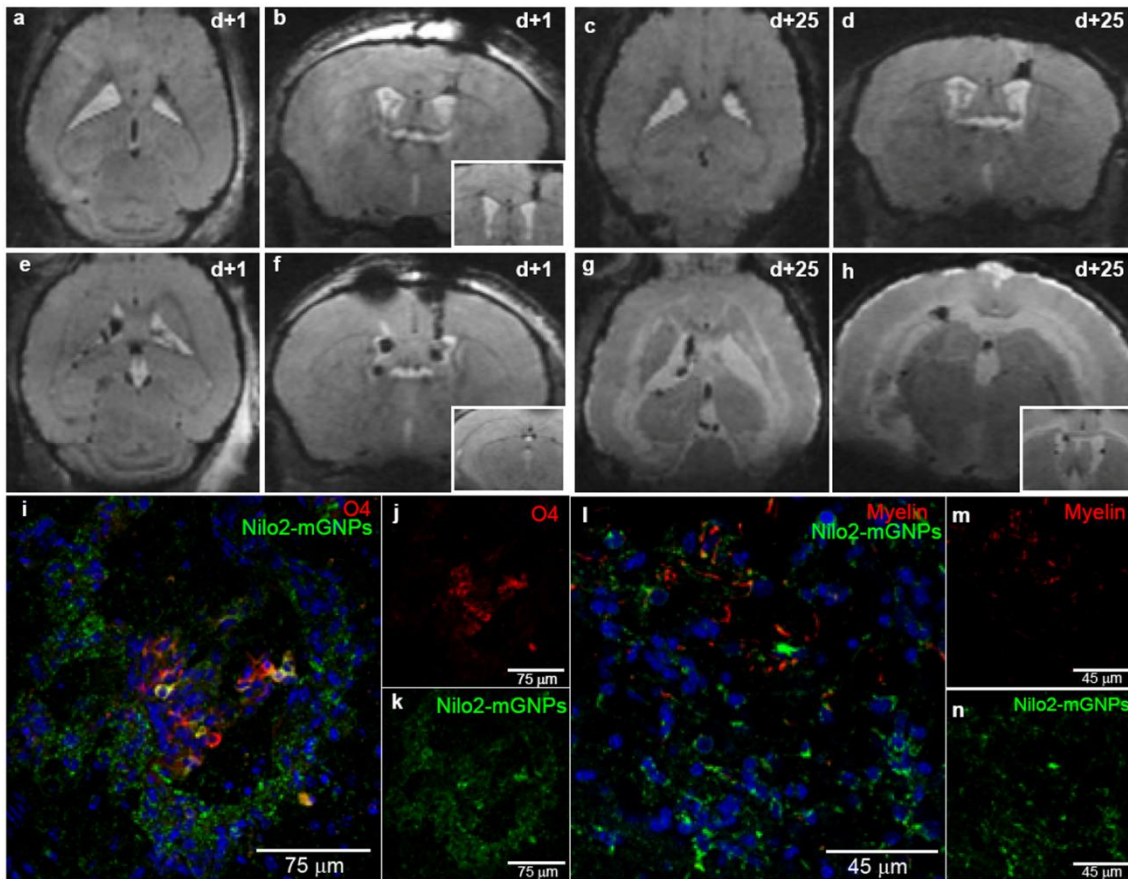


Figure 52. Migration of endogenous Nilo2 positive cells in a demyelination model. **a-h**, coronal and axial MRI views of mice brains injected with Nilo2-functionalised nanoferrites in the right hemisphere **a-d**, alone or **e-h**, after injection of lysophosphatidylcholine in the left *corpus callosum*, one (**a, b, e, f**) or twenty five (**c, d, g, h**) days after the day of damage. **i-n**, representative immunohistochemical analyses of fixed brains from sacrificed mice twenty five days after the brain injury, showing the double staining of Nilo2 (green) and O4 (**i-k**, red) or Nilo2 and myelin (MAB328, **l-n**, red) positive cells.

In response to a mechanical lesion induced by puncture with the stereotaxic needle, Nilo2⁺ cells also migrated to the damage site within less than 24 hours. In this model, migration of Nilo2⁺ cells preceded tissue repair, as the puncture started to be filled one day after the damage and wound healing was completed three days later (figure 53).

These data show for the first time a cellular link between neuroblast migration to a damage site and tissue repair. The repair was not restricted to a mechanical damage since the presence of myelin producing cells surrounded by Nilo2⁺ cells in LPC suggest that this was also the situation in demyelinating models.

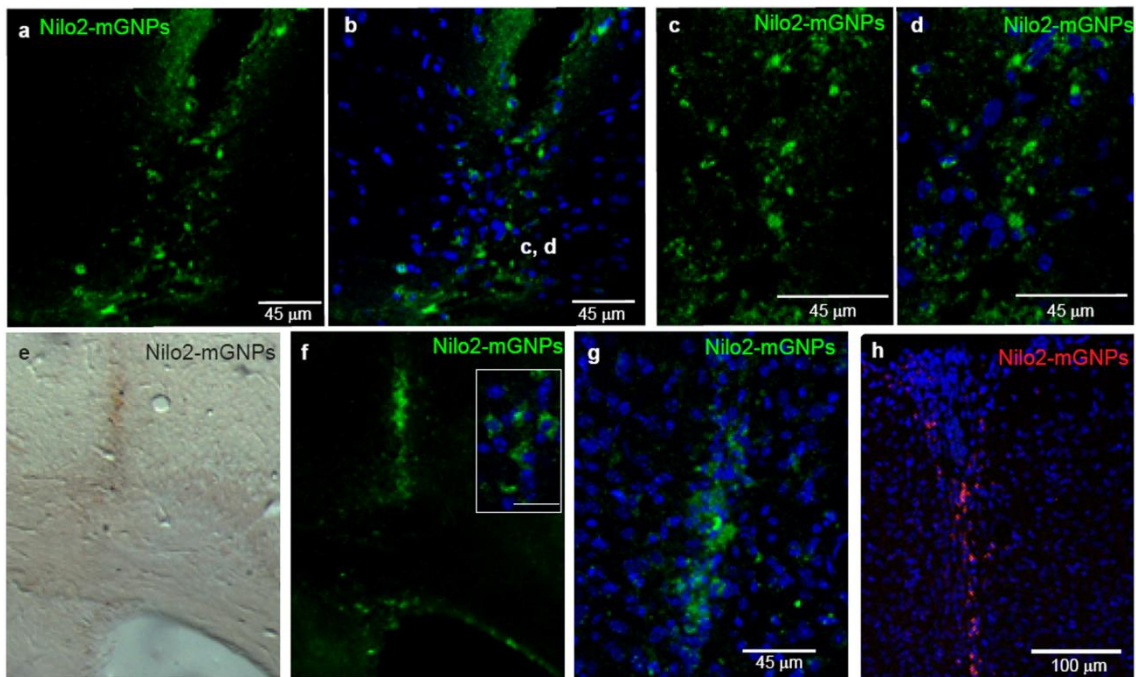


Figure 53. Damage repair by Nilo2 positive cells in response to a mechanical lesion. A mechanical lesion was produced by intracranial injection of GFP-CT-2A cells **a-d, h**, or Nilo2-functionalised nanoferrites **e-g**. Fixed brain sections were incubated with a FITC-labelled anti-hamster antibody **a-g**, or with anti-hamster biotin antibody, Texas red-sterptavidin, **h**. Fluorescence and DIC (**e**) confocal microscopy images from immunohistochemistry of fixed brain section of mice one day (**a-d**), or three days (**e-h**) after mechanical lesion. Details of the regenerated tissue from **a** and **f** are shown in **c-d**, and **g** respectively. Scale bar of inset in **f** corresponds to 20 μm .

In conclusion, we have demonstrated that our *immuno*-MG NPs are versatile tools for *in vivo* specific labelling and tracking of endogenous neural cells. The *in vivo* tracking of a small and defined endogenous cell subpopulation within the brain (neuroblasts), migrating from their niches towards a lesion in response to brain insults, was possible with MG NPs coupled to an antibody specific to neuroblasts (Nilo2-MG NPs) and MRI analyses. In response to an insult, neuroblasts migrated fast and orderly from their niches, accumulating at the lesion site and promoting tissue repair in the analyzed models. These data represent the first report on *in vivo* detection of the movement of a specific minority endogenous precursor population within the brain and its consequences. Furthermore, this work reinforces the hypothesis that an active neurogenesis participates in adult tissue repair.

References

1. D.N. Abrous, M.K., M. Le Moal, *Adult neurogenesis: from precursors to network and physiology*. *Physiol. Rev.*, 2005. **85**(2): p. 523-569.
2. F. Doetsch, A.A.-B., *Network of tangential pathways for neuronal migration in adult mammalian brain*. *Proc. Natl. Acad. Sci. U.S.A.*, 1996. **96**: p. 11619-11624.
3. A. Alvarez-Buylla, J.M.G.-V., *Neurogenesis in Adult Subventricular Zone*. *The journal of neuroscience*, 2002. **22**(3): p. 629-634.
4. A. Arvidsson, T.C., D. Kirik, Z. Kokaia, O. Lindvall, *Neuronal replacement from endogenous precursors in the adult brain after stroke*. *Nat. Med.*, 2002. **8**: p. 963-970.
5. N. Picard-Riera, L.D., C. Delarasse, K. Goude, B. Nait-Oumesmar, R. Liblau, D. Pham-Dinh, A.B. Evercooren, *Experimental autoimmune encephalomyelitis mobilizes neural progenitors from the subventricular zone to undergo oligodendrogenesis in adult mice*. *Proc. Natl. Acad. Sci. U.S.A.*, 2002. **99**: p. 13211-13216.
6. M.A. Curtis, R.L.F., P.S. Erikson, *The effect of neurodegenerative diseases on the subventricular zone*. *Nat. Rev. Neurosci.*, 2007. **8**: p. 712-723.
7. K. Jin, V.G., L. Xie, X.O. Mao, O.F. Gorostiza, D.E. Bredesen, D.A. Greenberg, *Enhanced neurogenesis in Alzheimer's disease transgenic (PDGF-APP^{Sw/Ind}) mice*. *Proc. Natl. Acad. Sci. U.S.A.*, 2004. **101**: p. 13363-13367.
8. S.A. Baker, K.A.B., T. Hagg, *Dopaminergic nigrostriatal projections regulate neural precursors proliferation in the adult mouse subventricular zone*. *Eur. J. Neurosci.*, 2004. **20**: p. 575-579.
9. G.U. Höglinger, P.R., M.P. Muriel, C. Duyckaerts, W.H. Oertel, I. Caille, E.C. Hirsch, *Dopamine depletion impairs precursor cell proliferation in Parkinson disease*. *Nat. Neurosci.*, 2004. **7**: p. 726-735.
10. S.O. Suzuki, J.E.G., *Multiple cell populations in the early postnatal subventricular zone take distinct migratory pathways: a dynamic study of glial and neuronal progenitor migration*. *J. Neurosci.*, 2003. **23**: p. 4240-4250.
11. K. Shah, E.B., D.E. Kim, K. Yang, Y. Tang, *et al.*, *Glioma therapy and real time imaging of neural precursor cell migration and tumor regression*. *Ann. Neurol.*, 2005. **57**: p. 34-41.
12. Modo, M., *Understanding stem cell-mediated brain repair through neuroimaging*. *Curr Stem Cell Res Ther*, 2006. **1**: p. 55-63.
13. E. M. Shapiro, O.G.-P., J. M. García-Verdugo, A. Alvarez-Buylla, A. P. Koretsky, *Magnetic resonance imaging of the migration of neuronal precursors generated in the adult rodent brain*. *Neuroimage*, 2006. **32**: p. 1150-1157.
14. J. P. Sumner, E.M.S., D. Maric, R. Conroy, A. P. Koretsky, *In vivo labeling of adult neural progenitors for MRI with micron sized particles of iron oxide: Quantification of labeled cell phenotype*. *Neuroimage*, 2009. **44**: p. 671-678.
15. B. J. Nieman, J.Y.S., J. J. Rodriguez, A. D. Garcia, A. L. Joyner, D. H. Turnbull, *In vivo MRI of neural cell migration dynamics in the mouse brain*. *Neuroimage*, 2010. **50**: p. 456-464.

Results and Discussion

16. R. Vreys, G.V.V., O. Krylychkina, M. Vellema, M. Verhoye, J-P. Timmermans, V. Baekelandt, A. Van der Linden, *MRI visualization of endogenous neural progenitor cell migration along the RMS in the adult mouse brain: Validation of various MPIO labeling strategies*. Neuroimage, 2010. **49**: p. 2094-2103.
17. R.G. Pautler, A.C.S., A.P. Koretski, *In vivo neuronal tract tracing using manganese-enhanced magnetic resonance imaging*. Magn. Reson. Med., 1998. **40**: p. 740-748.
18. P. Ghosh, N.H., J. Broadus, W.T. Greenough, P.C. Lauterbur, *NMR imaging of transplanted iron-oxide labelled cells in the brain*. Proceedings of the 9th ISMRM, 1990: p. 1193.
19. Bulte J.W., K.D.L., *Iron oxide MR contrast agents for molecular and cellular imaging*. NMR Biomed., 2004. **17**: p. 484-499.
20. I. delValle, G.E., L. García, A. Armesilla, L. Kremer, J.A. Garcia-Sanz, S. Martinez, A. Silva, *Characterization of novel monoclonal antibodies able to identify neurogenic niches and arrest neurosphere proliferation and differentiation*. Neuroscience, 2010.
21. Nait-Oumesmar, B., et al., *Progenitor cells of the adult mouse subventricular zone proliferate, migrate and differentiate into oligodendrocytes after demyelination*. Eur J Neurosci., 1999. **11**(12): p. 4357-4366.

Experimental part

Materials and methods

All chemical reagents were purchased from Sigma-Aldrich or Invitrogen. Primary and secondary antibodies are described in table 5. Fluorescence images were acquired on a Leica DMI 6000B epifluorescence inverted microscope. Confocal imaging was performed on a Zeiss LSM 510 instrument. FSC experiments were carried out on a BD FACS Canto II instrument. All experiments were performed in compliance with the European Union and Spanish laws (Council Directive 86/609/EEC) and approved by the Committee of animal experimentation of the CSIC.

Animals. Experiments were performed in compliance with the European Union and Spanish laws (Council Directive 86/609/EEC) and approved by the Committee of Animal Experimentation of the CSIC.

Table 5. Primary and secondary antibodies used in this study.

PRIMARY ANTIBODIES				
Antibody	Host	Source	Clone or Cat. #	Ab Dilution
Ki-67	Rabbit, monoclonal	Neomarkers	RM-9106-S1	1:200
PDGFRα	Rabbit, polyclonal	Santa Cruz Biotech	Sc-338	
DCX	Goat, polyclonal	Santa Cruz Biotech	Sc-8066	1:200
PSA-NCAM	Mouse, monoclonal	Chemicon	MAB5324	1:400
CD4	Rat, monoclonal	BD Pharmingen	553043	
CD4FITC+CD8FITC	Rat, monoclonal	BD Pharmingen		
CD11b	Rat, monoclonal	BD Pharmingen	553308	1:100
GFAP	Rabbit, polyclonal	Neomarkers		1:200
O4	Mouse, monoclonal	Abcam	Ab64547	1:1000
Myelin	Mouse, monoclonal	Chemicon	MAB328	
hup53	Rabbit, polyclonal	Cell Signalling Tech.	2521S	-
CD3ϵ	Hamster, monoclonal	BD Pharmingen	553058	-
SECONDARY ANTIBODIES AND REAGENTS				
Anti-Hamster IgG-HRP	Mouse	BD Pharmingen	554012	1:100
Anti-hamster-FITC	Mouse	BD Pharmingen	554011	1:100
Anti-mouse IgG-TxRed		Molecular Probes		1:200
Anti-rat AlexaFluor 647	goat			1:400
Anti-Rabbit IgG-Cy3	Goat	Jackson ImmunoRes	111-165-003	1:400
Anti-Goat 594	Chicken	Invitrogen	A21468	1:400
Anti-hamster biotin	Mouse	BD Pharmingen	550335	1:100
Streptavidin AlexaF 647	-	Invitrogen	S32357	0.25 μ g/ μ l

Experimental Part

Antibodies. Nilo2 was obtained from hybridoma as previously described [1]. Purification of Nilo2 was from Immunostep Inc. (Salamanca, Spain).

Neurosphere preparations and cell culture. Adult neurospheres were prepared from the SVZ of 6- to 8-week old FVB mice as described [1]. CT-2A mouse astrocytoma (gift from Prof. T.N. Seyfried, Boston, MA, USA), and GFP-CT-2A (gift from A. Martinez, I. Cajal, CSIC, Madrid, Spain) [2], were grown in RPMI medium, 10% heat-inactivated foetal bovine serum in 5 % CO₂ at 37 °C.

Intracranial surgery. C57BL/6J mice were anaesthetized intraperitoneally with 100 mg/Kg of ketamine and 10 mg/Kg of xylazine. The heads of the mice were immobilized in stereotaxic frame and intracranially injected with 1 µl of Nilo2-functionalised nanoparticles in striatum, +0.9 mm anterior, + 0.75 mm lateral, -2.75 mm ventral. As control, PBS buffer was used. Brains fixation was performed on anesthetized mice by transcardiac perfusion with 4% (w/v) paraformaldehyde (PFA) in 0.1 M phosphate buffer (fixation buffer). Brains were extracted and post-fixed overnight at 4 °C in fixation buffer and cryo-protected in fixation buffer with 30 % (w/v) sucrose for two days at 4 °C before freezing at -80 °C. Fixed brains were cut in cryostat at 25 µm and slices maintained at -20 °C in glycerol/ethylenglycol buffer until analyzed.

Mice demyelinated model was performed injecting 1 µl of lysophosphatidylcholine (LPC) 2 % in PBS near *corpus callosum* (CC), stereotaxic positions +1mm anterior, -1 mm lateral, -2 mm ventral, from bregma as reference.

Tumour mice model was performed by grafting 10² to 2x10⁵ CT-2A or GFP-CT-2A cells intracranially at stereotaxic coordinates +0.1 mm anterior, -2.25 mm lateral, -2.70 mm ventral into the right caudate *putamen*, in 1 µl of cell suspension.

Immunological analyses and staining procedures. Neurosphere adherent cultures were performed on Matrigel Basement Membrane Matrix Growth Factor Reduced (BD Pharmingen) pre-coated coverslips with 1:20 dilution in culture media. Cells were fixed with 4 % PFA in 10 mM PBS buffer for 15 min at RT. Quenching was performed by the addition of 0.1 M glycine pH 7.4 for 15 min. at RT. After three 10 mM PBS washes, blocking was performed by incubating the coverslips with 10 % mouse serum in PBS during 1 hour at RT. Fixed cells were incubated overnight with Nilo2-functionalised nanoparticles (5 µL/well) mAb at 4 °C. After 3x PBS washings, cells were incubated

Experimental Part

with the secondary antibody (anti-Ha-FITC 1:100, BD, Anti-Ha-Cy5.5 1:500 Abcam) for 1 hour.

For *in vivo* recognition of SVZ cells, 25 μm brain sections of mice intracranially injected with Nilo2-functionalised MGNPs were blocked with 10 % mouse serum in PBS during 1 hour at RT and stained with anti-Ha-FITC (1:100). Coverslips were mounted in Dapi/Mowiol and analyzed in a Nikon Eclipse 80i fluorescence microscope and LEICA TCS-SP2-AOBS confocal microscope.

For *in vivo* identification of Nilo2 positive cells surrounding the brain tumour, mice were intraperitoneally injected with Nilo2 ascites at 10 $\mu\text{g/g}$ of body weight one week after cell injection (100 CT-2A cells). Next day, mice were sacrificed and 25 μm sections of fixed brains were analyzed using Cy5.5-labelled anti-hamster antibody.

Magnetic resonance imaging. MRI studies were performed in a Bruker Biospec 70/20 scanner using a combination of a linear coil (for transmission) with a mouse head phase array coil (for reception). Animals were anesthetized with sevoflurane (5 % for induction and 2 % for maintenance) and placed in an MRI-adapted stereotaxic holder. Respiration and body temperature were continuously monitored. MRI acquisition protocol included an initial flash sequence (repetition time: 100 ms, echo time: 6 ms, field of view: 4 cm, matrix: 128 x 128) to centre the Field of View (FOV), followed by a shimming procedure applied to a region of interest covering the head (FOV = 3 x 2 x 2 cm, matrix = 64 x 64 x 64) and based on a Field Map sequence ($T_R = 20$ ms, $T_E = 1.43$ and 5.42 ms).

As an anatomical reference we used a T_2 -weighted coronal image ($T_R = 2500$ ms; T_E , 33 ms; $\alpha = 180^\circ$; FOV = 2 x 2 cm; matrix = 256 x 256; slice thickness = 0.5 mm) and nanoparticles were detected and tracked with a 3D multi gradient echo (MGE) sequence ($T_R = 200$ ms; 8 echoes, $T_E = 10$ to 45 ms; echo spacing = 5 ms; $\alpha = 15^\circ$; FOV = 1.6 x 1.6 x 1.5 cm; matrix = 192 x 96 x 96).

In order to increase signal-to-noise ratio (SNR) and improve image contrast, the different echo images were added (in magnitude). To display the results, the tumour area was manually segmented on the T_2 scans and spatially aligned with the MGE image.

References

1. I. delValle, G.E., L. García, A. Armesilla, L. Kremer, J.A. Garcia-Sanz, S. Martinez, A. Silva, *Characterization of novel monoclonal antibodies able to identify neurogenic niches and arrest neurosphere proliferation and differentiation*. Neuroscience, 2010.
2. Martinez-Murillo, R.M., A., *Standardization of an orthotropic mouse brain tumor model following transplantation of CT-2A astrocytoma cells*. Histol. Histopathol., 2007. **22**: p. 1309-1326.

Concluding remarks

Concluding Remarks

Concluding remarks

- In this thesis we have optimised the preparation protocols of different nature nanocrystals, magnetic $X\text{Fe}_2\text{O}_4$ ($X = \text{Fe}, \text{Mn}, \text{or Co}$) nanoparticles and CdTe quantum dots.
- We have coated these magnetic/fluorescent cores with an inorganic shell (Au or ZnTe) in the search of complementary properties for the final nanoparticles: basically chemical stability, biocompatibility and in the case of gold a way for further chemical functionalization.
- We have developed a general protocol for the transfer of apolar solvent soluble nanoparticles into water. This protocol, based on modified glycoconjugates and thiol chemistry has been used successfully with gold coated magnetic nanoparticles, but also with FePt, CdSe_xTe_y , CdS and InP/ZnS nanocrystals.
- We have designed and demonstrated a versatile and universal methodology for the oriented coupling of IgG antibodies onto the nanoparticle surface. Protein G has been covalently bounded to the organic shell of the nanocrystals with a controlled stoichiometry, and subsequently IgG antibodies were captured in a well oriented manner. In this way specific targeting nanoparticles can be obtained.
- The ability of these *immuno*-nanocomplexes to recognise their target has been demonstrated both with analytical methods, in *in vitro* experiments and in *ex vivo* tests.
- Before the application of any of the obtained nanoprobcs with living cells their cytotoxicity has been evaluated. In the case of the *ex vivo* tests the haemolytic potential of the nanoparticles has been also tested before hand.

Concluding Remarks

- The magnetic *immuno-glyconanoparticles* have been used as probes for tracking neural stem cells *in vivo*. MRI experiments with these probes using Nilo2 (Neural Identification Lineage from Olfactory Bulb), a highly specific IgG antibody of neuroblast cell surface antigens, have revealed an implication of neural stem cells in brain injury reparation processes.
- Finally, in the case of *immuno-quantum dots*, their cytotoxicity has been profited to demonstrate their potential to produce a selectives cellular death in a mixed population with model *in vitro* experiments.

To sum up, we have not only designed and prepared versatile biofunctional nanoparticles for the specific targeting at sub-cellular level of organs, tissues or cells, investigated their potential as *in vitro* and *in vivo* probes by means of molecular imaging techniques, but we have also demonstrated their utility to help in the understanding of relevant biological issues.

Contributors

- **Chapter 1 J. Gallo, I. Garcia, D. Padro, B. Arnaiz, S. Penadés**
Laboratory of GlycoNanotechnology, Biofunctional Nanomaterials, CIC
biomaGUNE/CIBER-BBN, San Sebastian, Spain.

- **Chapter 2 J. Gallo, N. Genicio, I. García, S. Penadés**
Laboratory of GlycoNanotechnology, Biofunctional Nanomaterials, CIC
biomaGUNE/CIBER-BBN, San Sebastian, Spain.

- **Chapter 3 J. Gallo, I. García, S. Penadés**
Laboratory of GlycoNanotechnology, Biofunctional Nanomaterials, CIC
biomaGUNE/CIBER-BBN, San Sebastian, Spain.
M. Köber, F. Briones
Instituto de Microelectrónica de Madrid (IMM), Consejo Superior de
Investigaciones Científicas, Madrid, Spain.

- **Chapter 4 J. Gallo, N. Genicio, I. Garcia, E. Martínez, S. Penadés**
Laboratory of GlycoNanotechnology, Biofunctional Nanomaterials, CIC
biomaGUNE/CIBER-BBN, San Sebastian, Spain.

- **Chapter 5 J. Gallo, N. Genicio, D. Padro, I. Garcia, S. Penadés**
Laboratory of GlycoNanotechnology, Biofunctional Nanomaterials, CIC
biomaGUNE/CIBER-BBN, San Sebastian, Spain.

- **Chapter 6 J. Gallo, I. Garcia, S. Penadés**
Laboratory of GlycoNanotechnology, Biofunctional Nanomaterials, CIC
biomaGUNE/CIBER-BBN, San Sebastian, Spain.
G. Elvira, J. A. Garcia-Sanz, A. Silva
Centro de Investigaciones Biológicas (CIB), Consejo Superior de
Investigaciones Científicas, Madrid, Spain.
M. Benito, M. Desco
Hospital Universitario Gregorio Marañón, Madrid, Spain.

Acknowledgements

I want to thank first of all my boss during the last four years, Prof. Soledad Penadés, for the opportunity to develop this research project and for giving me freedom to work on it in the borderline between organic chemistry, materials science and biochemistry. I have to thank here also my thesis supervisor Dr. Isabel García.

I also want to remember all present and past members of the laboratory of glyconanotechnology in which I have been working for their support during these years, not only in matters related to research. I want to thank especially Nuria Genicio, among other things, because she is the one that has been working more closely with me giving me support in any biological issue.

I want to thank also, all other contributors to this Thesis: The group of Dr. Augusto Silva, especially Dr. Gemma Elvira, from the CIB (CSIC) in Madrid, and the group of Dr. Manuel Desco from the Hospital Universitario Gregorio Marañón, also in Madrid, for their work in the project to track endogenous neural progenitors; the group of Dr. Fernando Briones, especially Mariana Köber, from the IMM (CSIC) in Madrid, for their work in the development of an optomagnetic sensor.

My gratitude goes also to the centre in which this Thesis has been developed, CIC biomaGUNE, for its financial support.

Appendix (publications)

- Shengtai He, Isabel Garcia, Juan Gallo and Soledad Penadés, A step-heating procedure for the synthesis of high-quality FePt nanostars, *Crys. Eng. Comm.*, **2009**, 11, 2605-2607.
- Juan Gallo, Isabel García, Daniel Padro, Blanca Arnáiz and Soledad Penadés, Water-soluble magnetic glyconanoparticles based on metal-doped ferrites coated with gold: Synthesis and characterization, *J. Mater. Chem.*, **2010**, 20, 10010-10020.
- Isabel García, Juan Gallo, Nuria Genicio, Daniel Padro, and Soledad Penadés, Magnetic Glyconanoparticles as a Versatile Platform for Selective Immunolabeling and Imaging of Cells, *Bioconjugate Chem.*, **2011**, DOI: 10.1021/bc1003923.
- Isabel García, Juan Gallo, Marco Marradi, and Soledad Penadés, Engineered Carbohydrate-Based Materials for Biomedical Applications: Polymers, Surfaces, Dendrimers, Nanoparticles, and Hydrogels. *Chapter 6: Glyconanoparticles: new nanomaterials for biological applications*, Ed. R. Narain, John Wiley & Sons Inc., **2011**, in press.
- Gema Elvira, Isabel García, Mariana Benito, Juan Gallo, Manuel Desco, Soledad Penadés, José A. Garcia-Sanz, and Augusto Silva, *In vivo* tracking of endogenous neural progenitors in response to damage, **2010**, submitted.

Appendix (curriculum vitae)

PERSONAL DATA:

- Family Name: Gallo Páramo
- First Name: Juan
- Date of Birth: 03-12-1979
- Place of Birth: Burgos (Spain)
- Nationality: Spanish
- Permanent address: C/ Petronila Casado N° 18, 2ºF
CP: 09005 BURGOS
- Mobile tel.: 00 34-678632377
- E-mail: Juanillogallo@yahoo.es

EDUCATION:

- 2009 Master degree in Nanoscience, University of the Basque Country.
- 2005 Master degree in Chemistry. University of Valladolid.
- 2004 Master degree in Biochemistry. University of Salamanca.
- 1997 International Baccalaureate. “IES Cardenal López de Mendoza”, Burgos.

LANGUAGES:

- **Mother Tongue:** Spanish
- **English**
 - Certificate in Advanced English (CAE), University of Cambridge
 - First Certificate in English (First), University of Cambridge
 - Preliminary English Test (PET), University of Cambridge
 - 3rd Course Official School of Languages, Burgos
 - Levels 6 and 7, General foundation of the University of Valladolid
 - Course of English Language (Upper-intermediate), Nord Anglia International, Nottingham (England)
- **French**
 - 3 Courses of French, IES Cardenal Lopez de Mendoza, Burgos
 - 2 months in Bordeaux (France)
- **German**
 - Initial German Course, Summer Courses “Merimee de Sebastian”

WORKING EXPERIENCE:

- March 2007 – up to date PhD student. Biofunctional nanomaterials unit, laboratory of glyconanotechnology. **CIC biomaGUNE**.
Thesis: Design and synthesis of biofunctional magnetic/fluorescent glyco-nanoparticles and quantum dots and their application as specific molecular imaging probes.
- March 2006 – March 2007 Research assistant in organic materials, R&D building, **GRUPO ANTOLÍN S.A.**, Burgos.
- July 2004 – October 2004 Laboratory assurance; quality control of drinkable and waste waters, and biological sludges; laboratory performance. **AQUAGEST Palencia**.

PROFESSIONAL SKILLS:

- Practical and theoretic experience in modern instrumental techniques (FT-IR, UV, ...), biological methods (PAGE, AGE, ELISA, protein quantification protocols, cellular stainings, ...)
- Preparation, purification and characterization of nanoparticles (magnetic nanoparticles, quantum dots, gold and silica nanoparticles).
- Functionalization of nanoparticles.
- Advanced user knowledge of electron microscopies TEM, STEM, EDX (element scanning, mapping, ...)
- User knowledge of light microscopy, epifluorescence microscopy, confocal microscopy, SEM, QCM.

Appendix (curriculum vitae)

- Good knowledge of Windows environment and main software (Office, ChemOffice, Origin, ImageJ, Photoshop and related programs, Internet)

PUBLICATIONS:

- A step-heating procedure for the synthesis of high-quality FePt nanostars, He J., Garcia I., Gallo J., Penadés S., *Cryst. Eng. Comm.*, **2009**, 11, 2605-2607.
- Water-soluble magnetic glyconanoparticles based on metal-doped ferrites coated with gold: Synthesis and characterization, Gallo J., Garcia I., Padro D., Arnaiz B., Penades S., *J. Mater. Chem.*, **2010**, 20, 10010-10020.
- Glyconanoparticles: new nanomaterials for biological applications, Garcia I., Gallo J., Marradi M., Penadés S., Chapter contribution for Engineered carbohydrate-based materials for biomedical applications: Polymers, surfaces, dendrimers nanoparticles and hydrogels. Ed. Narain R., John Wiley & sons, in press.
- Magnetic glyconanoparticles as a versatile platform for selective immunolabelling and imaging of cells, Garcia I., Gallo J., Genicio N., Padro D., Penades S., *Bioconjugate Chem.*, **2011**, DOI: 10.1021/bc1003923.
- *In vivo* tracking of endogenous neural progenitors in response to damage, Elvira G., García I., Benito M., Gallo J., Desco M., Penades S., Garcia-Sanz JA., Silva A., **2010**, submitted for publication.
- Immuno-fluorescent magnetic glyco-nanoparticles as specific blood labelling agents, Gallo J., Genicio N., Garcia I., Padro D., Penadés S., in preparation.
- CdTe based quantum dots: synthesis, cytotoxicity and applications, Gallo J., Genicio N., Garcia I., Penades S., in preparation.

PATENTS:

- Gold-coated magnetic glyconanoparticles functionalised with proteins for use as diagnostic and therapeutic agents. S. Penadés, I. García, J. Gallo. **2009**. EP09382185.8. PCT/EP2010/064012.

CONFERENCE PROCEEDINGS:

- Gallo J., Garcia I., Penadés S., 'Synthesis of novel glycosuperparamagnetic nanoparticles as potential contrast agents', *NanoBioEurope*, 9-13 jun, Barcelona **2008**.
- Garcia I., Gallo J., Penadés S., 'Biofunctional magnetic nanoparticles for labeling stem cells', *NanoBioEurope*, 9-13 jun, Barcelona **2008**.
- Gallo J., Garcia I., Penadés S., 'Nanopartículas magnéticas como biomateriales para marcar células progenitoras', *X Congreso Nacional de Materiales*, 18-20 Jun, San Sebastián, **2008**. Award best work young researcher.
- García I., Gallo J., Elvira G., Silva A., Penadés S., 'Biofunctional Magnetic Glyconanoparticles for labelling stem cells', *IV Iberian Carbohydrate Meeting*, 10-12 sept, Santiago de Compostela, **2008**.
- Martines E., Martínez-Avila O., Marradi M., Di Gianvincenzo P., Arnaiz B., García I., Gallo J., and Penadés S. 'Glyconanoparticles: New Multivalent Systems to Understand and Interfere in Biological Recognition'. *Advanced Microscopy Techniques for Immunonanoscopy*, 15-16 Oct Barcelona **2008**.
- Rodríguez-Ruano A, Benito M, Elvira G, Gallo J, Garcia I, Penadés S, Silva A, Garcia-Sanz JA, Desco M., 'Tracking *in vivo* migration of small cell populations during brain damage by MRI', *4th European Molecular Imaging Meeting*, 27-30 May Barcelona **2009**.
- Marradi M., García I., Gallo J., Irure A., Penadés S., 'Magnetic Glyconanoparticles as MRI Probes', *NanoSpain2010*, 23-26 March Malaga **2010**.
- Gallo J., Garcia I., Penades S., 'Synthesis and structural characterization of water soluble bimetallic magnetic glyconanoparticles', *Microscience2010*, 28 jun-1 jul London **2010**.
- Gallo J., Garcia I., Genicio N., Padro D., Penadés S., 'Core@shell fluorescent magnetic glyco-ferrites as specific targeted contrast agents for magnetic resonance imaging', *TNT2010*, 6-10 sept Braga **2010**. Organization award.

eman la zabal zazu



Universidad
del País Vasco

Euskal Herriko
Unibertsitatea



Biomaterialetako Ikerkuntza Kooperatiboko Zentroa
Centro de Investigación Cooperativa en Biomateriales